FZR-423

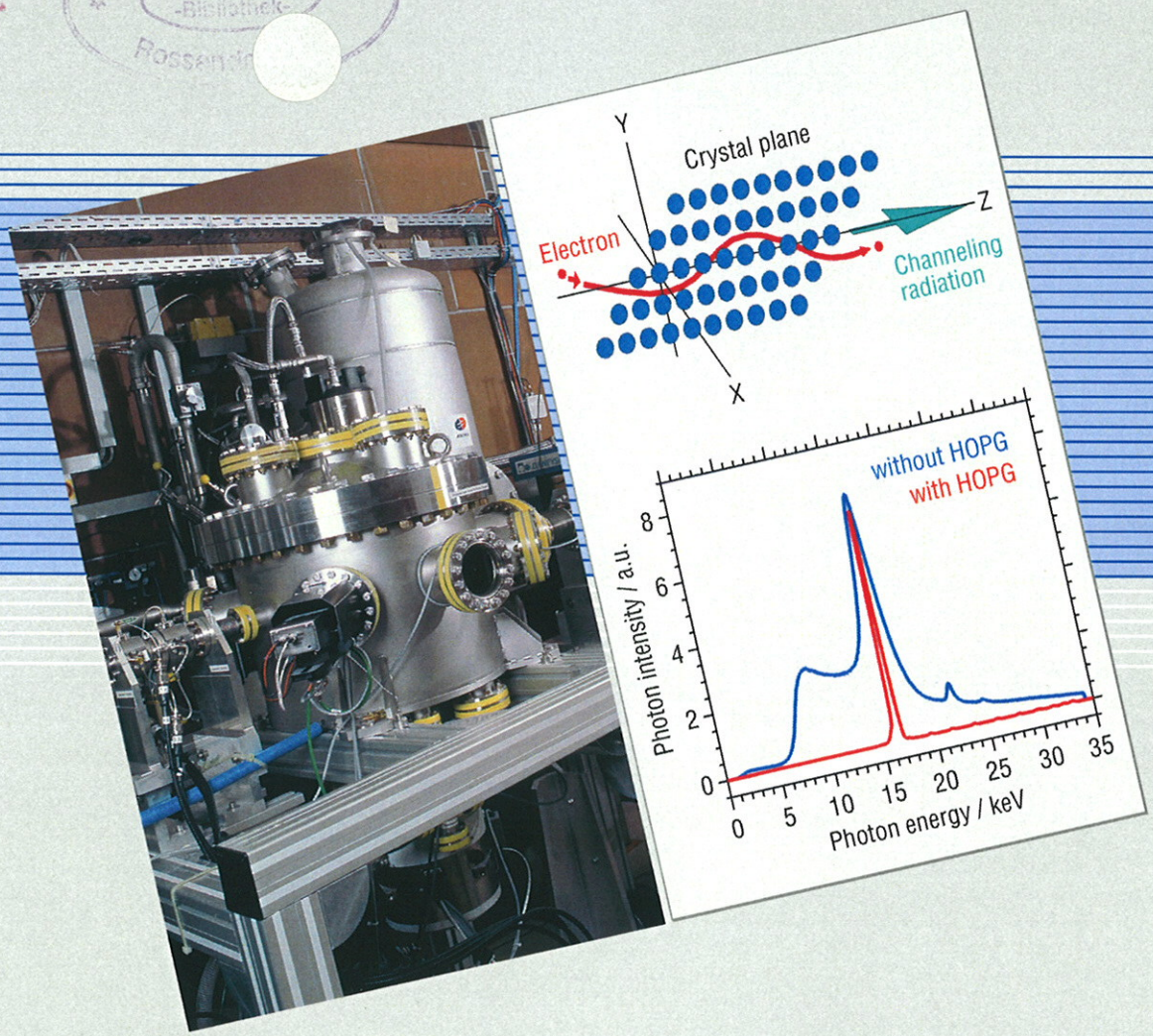

Wissenschaftlich-Technische Berichte
FZR-423 2005 · ISSN 1437-322X

Annual Report 2004

Institute of Nuclear and Hadron Physics

Forschungszentrum
Rossendorf

Wissenschaftlich-Technische Berichte
FZR-423
April 2005

Annual Report 2004

Institute of Nuclear and Hadron Physics

Editors:
W. Enghardt, K. Fahmy, E. Grosse,
B. Kämpfer, C. Schneidereit, A. Wagner

Forschungszentrum
Rossendorf

Cover Picture:

The photograph shows the target chamber of the channeling X-ray facility at the radiation source ELBE. The electron beam coming from the ELBE accelerator and entering the vacuum chamber on the left side hits a single crystal. The angle of incidence is precisely adjusted by means of a goniometer in the chamber which carries the crystal. Channeling radiation is emitted by the relativistic electrons if travelling through the crystal along a lattice plane or axis as illustrated in the upper-right scheme. The energy spectrum of (110) planar channeling in a diamond crystal at an electron energy of 14.6 MeV is presented in the lower-right figure showing the quasi-monochromatic channeling peak at 16.5 keV together with the polychromatic bremsstrahlung background (blue line). The X-rays can be further monochromized by Bragg reflection in highly oriented pyrolytic graphite (HOPG) mosaic crystals as demonstrated by the red line. The peak energy can be easily varied by changing the electron energy and the X-ray pulses are only a few picoseconds wide; thus channeling X-rays allow interesting applications which are not possible at conventional X-ray tubes.

Explanation of special symbols:

The letters given in parentheses in the following text and used as superscripts in the titles of the scientific contributions do express our grateful acknowledgement to the funding, sponsoring or grants provided by several institutions.

Research projects were funded by the Federal Ministry of Education and Research BMBF (B), by the Saxon Ministry of Education and Arts SMWK (S), by the German Research Foundation DFG (D), by the German Academic Exchange Service DAAD (A), by the European Commission (E), by the GSI Darmstadt (G), by the FZ Jülich (J), and by the special program HSP III (H) or were sponsored within Scientific agreements with eastern European countries (W).

Typeset using TEX©

Contents

Life Sciences:

Biostructures and Radiation 55

Preface

The Forschungszentrum Rossendorf (FZR) at Dresden is a multidisciplinary research centre within the Wissenschafts-Gemeinschaft G.W. Leibniz (WGL), one of the German agencies for extra-university research. The centre is active in investigations on the structure of matter as well as in the life sciences and in environmental research. **The Institute of Nuclear and Hadron Physics (IKH)** *within the FZR avails for its research the coupling of radiation to matter in subatomic dimensions as well as to tissue, to cells, and to their components. Its research in the field of* **Subatomic Physics** *is part of the FZR-program* **Structure of Matter** *and its investigations concerning the interaction of* **Biostructures and Radiation** *contribute to the* **Life Science** *program of the FZR. On the basis of these two legs the IKH exploits possibilities for transfer and introduction of experimental and theoretical techniques from particle and nuclear physics to life science projects. Much of this kind of interdisciplinary transfer is connected to the Radiation Source ELBE at the FZR. With its superconducting accelerator for relativistic electrons this large installation provides photons in the wide wavelength range from fm to mm - i.e. bremsstrahlung for the excitation of nuclei and infrared light for investigations on the structural dynamics of biomolecules. The compact bunches of the secondary beams of photons, X-rays and neutrons offer unique possibilities in laboratory studies related to cosmic processes as well as in the life sciences. The coupling to radiation not only dominates the projects in nuclear astrophysics as pursued at ELBE, it also is a central theme of the experimental and theoretical research performed by the IKH in close connection to the experimental program at the heavy ion synchrotron SIS and the upcoming FAIR facility at Darmstadt.*

In this Scientific Report each of the research projects of the Institute is presented by several articles. Other contributions describe the progress made in the production of the different kinds of secondary radiation at ELBE, and on the experimental equipment to be installed for their use. Parallel to intensive attempts to optimize the experimental conditions with respect to resolution, luminosity and background conditions several investigations on dipole strength distributions in various nuclei were performed. Interesting results were obtained for isotopes of Molybdenum, one of the elements with largely unknown details of its generation during the cosmic element production. The experimental conditions at ELBE proved to be very favourable for photon induced processes, especially those in the excitation energy range characteristic of stellar environments. Photon or electron induced fission is of special use as the source of neutron rich nuclei whose properties are of importance for the detailed understanding of the stellar production of heavy elements. Here neutron beams in the MeV range later available at ELBE will play a role as well.

Hadron physics at the IKH - the second research activity in subatomic physics - studies the strong (nuclear) interaction within the hadronic medium. Experiments observing the consequences of increasing hadron density are performed at high energy heavy-ion accelerators and the IKH is heavily involved in research within the international HADES project at GSI. Theoretical studies refer to these experiments and to even higher energies where a phase transition to a quark gluon plasma occurs. The theory for the high density phases of hadronic matter is an important ingredient for the understanding of the Big Bang and the subsequent evolution of the universe.

In its second part this Report describes the research in the life sciences, partly performed using nuclear technology. In the past the IKH contributed considerably to the field of tumour-conform radiotherapy by employing positron emission tomography. The successful operation of a PET scanner simultaneously to the irradiation of tumors with heavy ion beams considerably improved the reliability and reproducibility of the radiation therapy with carbon ions. This in-situ PET as developed at IKH has been shown to also allow the control of irradiations performed with lighter

ions or even with photons - an important information for upcoming dedicated therapy accelerators.

In the coming years interesting biomedical investigations will be performed with beams from ELBE: Quasi-monochromatic X-rays of easily variable energy as produced in electron channeling have been observed and a strong suppression of the unwanted background continuum was achieved. Thus a probe for the study of elementary processes causing radiation induced cell damage and for investigations with respects to photon activation therapy (PAT) is available now.

The conceptual design studies for the free electron laser (FEL) at ELBE have continued with detailed calculations on a magnetic undulator for the far infrared (IR) and THz regime; they constitute a very important contribution to this FELBE project. The IKH biophysics department uses it to study biomolecular dynamics under non-destructive and native-like conditions. Fundamental aspects of the structure and conformational changes of various receptor proteins and DNA play a key role in these investigations – up to now performed with IR from other, less favourable sources. Progress has been achieved particularly with new experimental techniques that combine IR- and visual laser pulses in the spatially resolved detection of structural transition in thin biomolecular films.

The interaction between the different fields of research at IKH has led to considerable synergy effects with respect to hard- and software for performing and analyzing the experimental investigations; here the transfer of information from the large international particle and nuclear physics community to the life sciences has continued. Thus the Institute's various areas of research from laboratory studies on cosmic processes to the interaction of radiation with bio-structures have common grounds.

The scientific activities of the institute have benefited from various support. We gratefully acknowledge the close and fruitful collaboration with the Technical University (TU) Dresden and with GSI Darmstadt. These contacts and those to many other scientific institutions in Germany and abroad are of vital importance for the Institute. Specific projects were subsidized by the Federal Ministry for Education and Research (BMBF), the Saxon Ministry for Science and Art (SMWK), GSI Darmstadt and Forschungszentrum Jülich. We express our gratitude to them as well as to the Deutsche Forschungsgemeinschaft (DFG) and to the European Union (EU) for the support of several research projects initiated by the Institute.

Structure of Matter:

Nuclear and Hadron Physics

Research in nuclear physics at the Forschungszentrum Rossendorf aimed at a deeper understanding of processes involved in the synthesis of nuclei in the cosmos and related problems in nuclear structure. Experimental beam time at the new superconducting linear accelerator ELBE was devoted mainly on the investigation of interactions of photons with nuclei up to or beyond particle separation energies.
Systematic studies of the electromagnetic response covered the stable Molybdenum isotopes ^{92,98,100}Mo *including the most neutron-deficient and the most neutron-rich isotope. For these nuclei, the dipole strength distributions have been determined up to the neutron separation energies. Considerable effort has been devoted to a theoretical understanding of excitations of these nuclei in the framework of Random Phase Approximation theory. Here, a remarkable theoretical achievement has been made which will allow for a better applicability of this theory not only in nuclear physics but in descriptions of general finite fermionic systems as well. Studies of the dipole response in* $N = 50$ *nuclei continued in* $^{88}\mathrm{Sr}(\gamma,\gamma)$ *and were complemented by spherical shell model calculations.*
The astrophysical relevance of the chain of stable Molybdenum isotopes - no contemporary theory of galactical evolution is able to describe the abundance of the neutron-deficient Mo and Ru isotopes - led to the investigation of dissociation reactions using Bremsstrahlung-photons at ELBE. Here, the $^{92}\mathrm{Mo}(\gamma,\mathrm{p})^{91}\mathrm{Nb}$ *reaction rate has been been studied over a wide energy range in an activation study and comparison to theoretically predicted cross sections have been made. Cross sections from the reaction* $^{92}\mathrm{Mo}(\gamma,\mathrm{n})^{91}\mathrm{Mo}$ *have been determined in the same experiment as well.*
With ^{92}*Mo also the* (γ,α) *reaction has been studied in a pioneering experiment for the first time under stellar conditions, showing the remarkable sensitivity of the applied technique also for this very small cross section.*
The set-up of a new time-of-flight facility for neutron-induced reactions has progressed with Monte-Carlo simulations, construction, and tests of various components. The collaborative effort between the IKH, the institutes for safety research and radiochemistry of FZR and the institute for nuclear and particle physics of TU Dresden led to the design of an effective production facility for pulsed neutrons.

The research on hadron physics focuses on experiments at the complex detector system HADES installed at the heavy-ion synchrotron SIS/GSI Darmstadt. The ultimate goal is to investigate the in-medium behaviour of vector mesons via their e^+e^- *decay channels. A first series of experiments has been performed by studying di-electron production on* $C+C$ *collisions at 1 and 2 AGeV. The data analysis is in progress and goes parallel with software developments concerning improved tracking algorithms. The challenge is to achieve the designed momentum resolution and identification of* ρ *and* ω *signals. Complementary to the heavy-ion programme is the study of elementary hadron reactions, e.g. with the high-statistic run* $p(2\ \mathrm{GeV})+p$ *with the focus on* η *identification for calibration purposes and* ω *Dalitz decays for pining down the* ω *form factor.*
While the HADES installation is nearly completed (the 6 large tracking sectors consisting of multiwire chambers are built at IKH), the so-called TOFino regions have to be up-graded by resistive plate counters (RPC) to improve granularity and time resolution, needed for the heaviest ions. A test module for optimising RPC time resolution has been installed at ELBE exploiting the excellent beam time structure available there.
We also benefit from instrumental contributions to other hadron experiments like FOPI, COSY-TOF and COSY-ANKE, which are continuously delivering interesting results.
The theory group accompanies intimately the experimental activities, e.g. by studying in-medium hadron modifications on the basis of QCD sum rules. Strangeness degrees of freedom are also investigated theoretically over a wide energy range. Also nuclear astrophysics and cosmology

related aspects are investigated.
Further perspective work is devoted to the physics case of the starting Compressed Baryonic Matter (CBM) project at the future Facility of Anti-protons and Ion Research (FAIR) in Darmstadt. IKH has joined this project and a first step are developments for the use of HADES at FAIR.

A series of regular seminar talks from both the nuclear and the hadron physics fields has been started in 2004 indicating the intense collaboration of both departments. The seminar talks and the regular students days devoted to talks on their theses have become a regular part of the work at the institute.

The hadron physics results described in this report are obtained in the following international collaborations:

HADES: Univ. Frankfurt, TU München, Univ. Giessen, GSI Darmstadt, FZ Rossendorf, Institute of Physics Bratislava (Slovakia), LNS Catania (Italy), LPC and Univ. Blaise Pascal Clermont (France), Jagellonian Univ. Cracow (Poland), JINR Dubna (Russia), Univ. degli Studi di Milano (Italy), ITEP Moscow (Russia), INR Moscow (Russia), MEPhI Moscow (Russia), Univ. of Cyprus (Cyprus), Institute de Physique Nucleaire d'Orsay (France), Nuclear Physics Institute Rez (Tschechia), Univ. of Santiago de Compostela (Spain), Univ. of Valencia (Spain),

KaoS: TU Darmstadt, Univ. Frankfurt, Univ. Marburg, GSI Darmstadt, Jagellonian Univ. Cracow (Poland), FZ Rossendorf.

Some data mentioned in this report stem from the FOPI set-up at GSI, from E91916 at Jefferson Labaratory and from ANKE at FZR.

The research in nuclear physics has profited from collaborating with groups in the following institutions:

Tech. Univ. Dresden, Univ. Stuttgart, Univ. Köln, Tech. Univ. Darmstadt, GSI Darmstadt, INRE, Bulgaria, Univ. of Sofia, Bulgaria, Univ. of Notre Dame, USA, JINR, Dubna, Russia and Univ. of Washington, Seattle, USA, Inst. for Safety Research, and Inst. for Radiochemistry, FZR

First Measurement with Polarised Photons at ELBE [D]

R. Schwengner, M. Erhard, E. Grosse[1], A.R. Junghans, K. Kosev, G. Rusev, K. D. Schilling, A. Wagner

The excitation of nuclear states by linearly polarised photons in connection with the measurement of the azimuthal asymmetry of the scattered photons is one method to distinguish between electric and magnetic radiation at high photon energies ($E_\gamma > 5$ MeV) and, hence, to determine the parity of nuclear states. For the production of a beam of linearly polarised photons we use the fact that an off-axis portion of the spatial distribution of the bremsstrahlung photons is partly polarised [1, 2]. Steering magnets deflect the electron beam from the normal direction and then back on to the centre of the radiator under a selected angle [3]. As a consequence, an off-axis portion of the spatial distribution of the photons is transmitted through the collimator. The optimum deflection angle for the production of polarised bremsstrahlung is around $\theta = m_0c^2/E_e$, the ratio of the rest energy to the full energy of the electron. The steering magnets were designed such that the electron beam can be deflected at four azimuthal angles of 0°, 90°, 180° and 270°, thus defining four different polarisation planes. A cyclical use of these four directions enables us to reduce the influence of fluctuations of the electron current and of systematic uncertainties.

The applicability of polarised bremsstrahlung was tested by irradiating a ^{208}Pb target at an electron energy of 15 MeV. The deflection of the electron beam was switched between the four possible directions each hour. Fig. 1 shows the degree of polarisation deduced as $P_\gamma = (N_{p\perp} - N_{p\parallel})/(N_{p\perp} + N_{p\parallel})$, where $N_{p\perp}$ and $N_{p\parallel}$ are the intensities of protons resulting from the disintegration of deuterons [4] and measured perpendicular or parallel to the polarisation plane, respectively, assuming an analysing power of one. The energies of these protons were rescaled to the energies of the incident photons as described in Ref. [4]. Spectra measured with those detectors, which belong to the same orientation relative to the polarisation plane, were added up. The maximum degree of polarisation in this first experiment is about 12 % and has still to be optimised in further experiments. Asymmetries deduced for known transitions in ^{208}Pb as $(I_{\gamma\perp} - I_{\gamma\parallel})/(I_{\gamma\perp} + I_{\gamma\parallel})$, where $I_{\gamma\perp}$ and $I_{\gamma\parallel}$ are the intensities of γ transitions observed perpendicular or parallel to the polarisation plane, respectively, are shown in Fig. 2. Positive asymmetry values are expected for electric dipole ($E1$) transitions and negative asymmetry values for magnetic dipole ($M1$) transitions. The deduced values are consistent with those deduced in previous work [5] and hence demonstrate that the facility for polarised bremsstrahlung at ELBE can be used to measure the linear polarisations of many γ transitions in a wide energy range simultaneously.

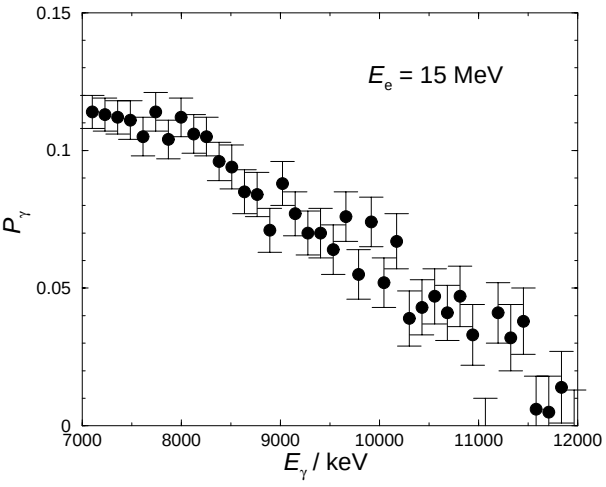

Fig. 1 *Degree of polarisation as a function of the photon energy as deduced from spectra of protons emitted from disintegrated deuterons. Data below $E_\gamma \approx 7$ MeV cannot be used because the proton spectra are at low energy contaminated by scattered photons.*

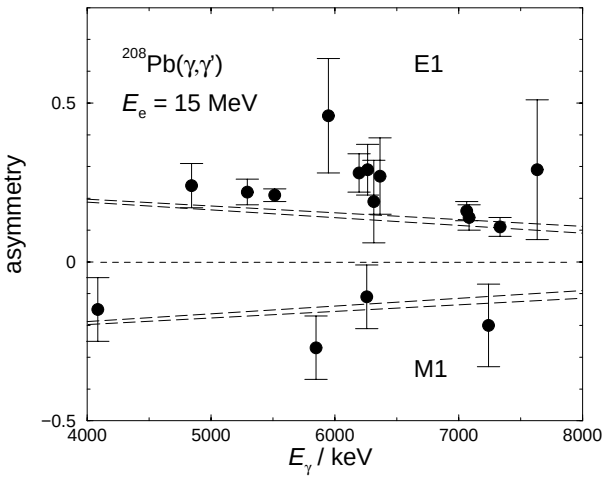

Fig. 2 *Experimental asymmetries of transitions in ^{208}Pb. The bands marked with dashed lines indicate the degree of polarisation as derived from Fig. 1. Note that the bands are extrapolations below 7 MeV.*

[1] U. Kneissl, H.H. Pitz, A. Zilges, Prog. Part. Nucl. Phys. 37 (1996) 349
[2] K. Govaert et al., Nucl. Instr. Meth. A 337 (1994) 265
[3] K.D. Schilling et al., Wiss.-Techn. Berichte FZR-272 (2003) 31
[4] R. Schwengner et al., this report, p. 16
[5] K. Wienhard et al., Phys. Rev. Lett. 49 (1982) 18

[1] *also Technische Universität Dresden*

Dipole-Strength Distribution of ^{88}Sr up to 12 MeV [D]

R. Schwengner, G. Rusev, K. D. Schilling, A. Wagner, F. Dönau,
M. Erhard, E. Grosse[1], A. R. Junghans, K. Kosev, N. Nankov

We have extended our investigation of the $N = 50$ nuclide ^{88}Sr [1] to higher energies using the photon-scattering facility at the ELBE accelerator. The experiment was carried out with bremsstrahlung produced with an electron beam hitting a niobium radiator of 7 μm thickness. The kinetic energy of the electrons was 13.2 MeV and the average electron current was 400 μA. A 10 cm thick aluminium absorber was placed behind the radiator in order to reduce the low-energy part of the bremsstrahlung spectrum. The target consisted of 2731.8 mg of $^{88}SrCO_3$ with an enrichment of 99.9 %, combined with 455.5 mg of ^{11}B used for the calibration of the photon flux. γ rays were measured with four high-purity germanium detectors of 100 % efficiency relative to a 3" $\times$ 3" NaI detector. All detectors were surrounded by escape-suppression shields of bismuth germanate scintillation detectors. Two detectors were placed at 90° relative to the photon-beam direction while the other two were positioned at 127° to deduce angular distributions of the γ rays. About 150 γ transitions in the energy range from 7 to 12 MeV were observed for the first time. Fig. 1 shows ratios of integrated cross sections obtained from the present measurement at $E_e^{kin} = 13.2$ MeV and from our previous measurement at 6.8 MeV [2] for states with excitation energies E_x between 3.5 and 6.5 MeV. Ratios of 2 to 10 for states below 6 MeV indicate a considerable feeding of these states by transitions from higher-lying states in the measurement at 13.2 MeV. However, the feeding becomes small for states with $E_x > 6$ MeV.

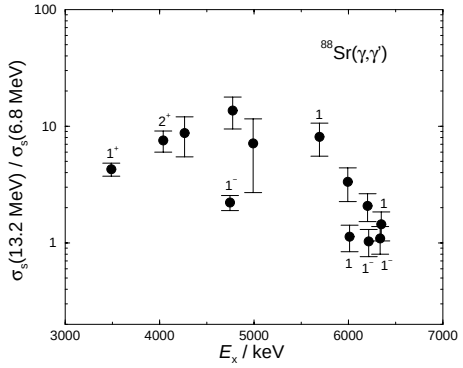

Fig. 1 *Ratios of integrated cross sections obtained in measurements at electron energies of 13.2 and 6.8 MeV.*

The reduced partial widths Γ_0/E_γ^3 deduced from the γ-ray intensities under the assumption, that all transitions are ground-state transitions, are shown in Fig. 2. These reduced partial widths are proportional to the reduced transition strengths of dipole transitions ($B(E1)$ or $B(M1)$). The dipole-strength distribution is characterised by little strength below 6 MeV and few prominent transitions accompanied by many transitions of small strength at higher energies. The transition with large strength at 7088 keV may be related to the $\nu(g_{9/2} \rightarrow g_{7/2})$ spin-flip transition which is predicted at about this energy by shell-model calculations [3].

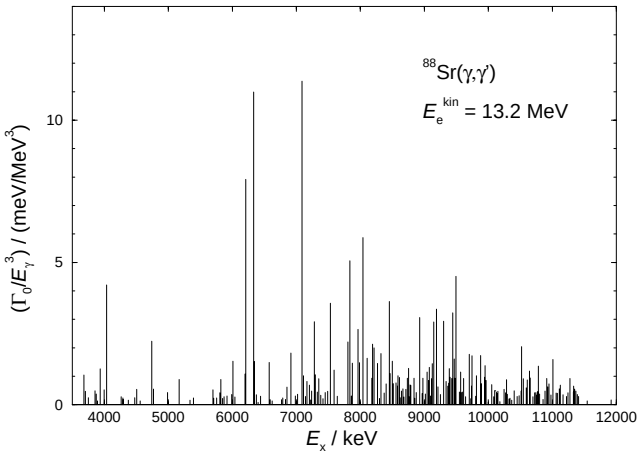

Fig. 2 *Reduced partial widths for transitions in ^{88}Sr.*

The sum of the $B(E1)\uparrow$ strengths for transitions from states between 6 MeV and the highest observed level in ^{88}Sr is compared with the one obtained for the $N = 50$ isotone ^{92}Mo [4] in Fig. 3. This sum seems to increase with the ratio of neutron number to proton number, N/Z. However, the study of further $N = 50$ isotones is necessary to learn about this tendency of dipole strength which has implications for the synthesis of nuclei in explosive stellar events [5].

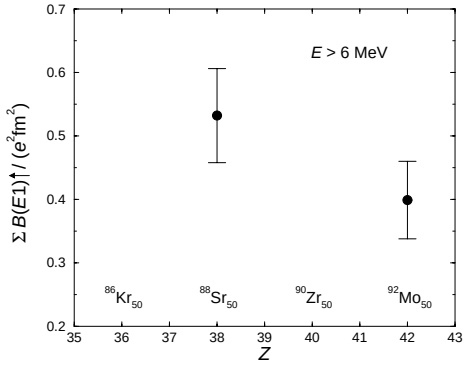

Fig. 3 *Sums of $B(E1)\uparrow$ values for the $N = 50$ isotones ^{88}Sr and ^{92}Mo.*

[1] R. Schwengner, G. Rusev et al., Wiss.-Techn. Berichte FZR-401 (2004) 9
[2] L. Käubler, H. Schnare et al., Phys. Rev. C 70 (2004) 064307
[3] R. Schwengner, this report, p. 6
[4] G. Rusev, R. Schwengner et al., Wiss.-Techn. Berichte FZR-401 (2004) 7
[5] S. Goriely, Phys. Lett. B 436 (1998) 10

[1] *also Technische Universität Dresden*

Comparison of the Dipole-Strength Distribution of ^{88}Sr with Shell-Model Predictions[D]

R. Schwengner

We have studied the nuclide ^{88}Sr in a photon-scattering experiment at ELBE. The dipole-strength distribution obtained from this experiment is shown in Ref. [1]. So far, we cannot distinguish between electric dipole ($E1$) and magnetic dipole ($M1$) transitions and, consequently, we cannot assign parities to the newly found $J = 1$ states.

To learn about the structure of the $J = 1$ states we have performed shell-model calculations using the code RITSSCHIL [2]. The model space used in our calculations includes the active proton orbitals $\pi(0f_{5/2}, 1p_{3/2}, 1p_{1/2}, 0g_{9/2})$ and neutron orbitals $\nu(0g_{9/2}, 1d_{5/2}, 0g_{7/2})$ relative to a hypothetic ^{68}Ni core. Since an empirical set of effective interactions for this model space is not available up to now, various empirical interactions have been combined with results of schematic nuclear interactions applying the surface delta interaction. Details of this procedure are described in Ref. [3] and Refs. therein. In order to make the calculations feasible, a truncation of the occupation numbers was necessary. At most three protons are allowed to occupy the $(1p_{1/2}, 0g_{9/2})$ subshell and at most one $0g_{9/2}$ neutron can be lifted to either the $1d_{5/2}$ orbital or the $0g_{7/2}$ orbital. With these restrictions, a configuration space with a dimension of 4929 has been obtained for the 1^+ states. For the calculation of $B(M1)$ transition strengths, effective g factors of $g_s^{\rm eff} = 0.7 g_s^{\rm free}$ have been used. $B(E1)$ strengths cannot be calculated in the present model space.

We have calculated the first twenty-five 1^+ states, which cover an excitation-energy range up to 8.5 MeV. The spacings between the states drop to less than 100 keV above 8 MeV. The corresponding $B(M1, 0^+ \rightarrow 1^+)$ values are compared with experimental $B(M1)\uparrow$ values in Fig. 1. The experimental values include transitions of all $J = 1$ states observed in the considered energy range except for the known 1^- states.

As can be seen in Fig. 1, the shell-model calculations predict two 1^+ states with large $B(M1, 0^+ \rightarrow 1^+)$ values. One is the 1_1^+ state at 3692 keV which includes mainly the spin-flip configuration $\pi(1p_{3/2}^{-1}\, 1p_{1/2})$. The second one is the 1_{16}^+ state at 7646 keV containing mainly the spin-flip configuration $\nu(0g_{9/2}^{-1}\, 0g_{7/2})$. For the other twenty-three 1^+ states small values of $B(M1)\uparrow \leq 0.1\mu_N^2$ have been obtained. The calculated 1_1^+ state corresponds to the first experimental 1^+ state at 3487 keV. The calculated 1_{16}^+ state may be related to the experimental $J = 1$ state at 7089 keV. However, the experimental $B(M1)\uparrow$ value is by a factor of two smaller than the predicted one. In contrast, there are many more experimental dipole transitions with considerable strengths in the energy region from 7.0 to 8.5 MeV than predicted by the shell-model calculations. This discrepancy between experiment and calculation implies that (i) there may be 1^+ states that are not reproduced within the present model space and (ii) a considerable part of the observed dipole-strength distribution comprises $E1$ transitions. In order to clarify this problem, the measurement of the linear polarisation of the dipole transitions is needed.

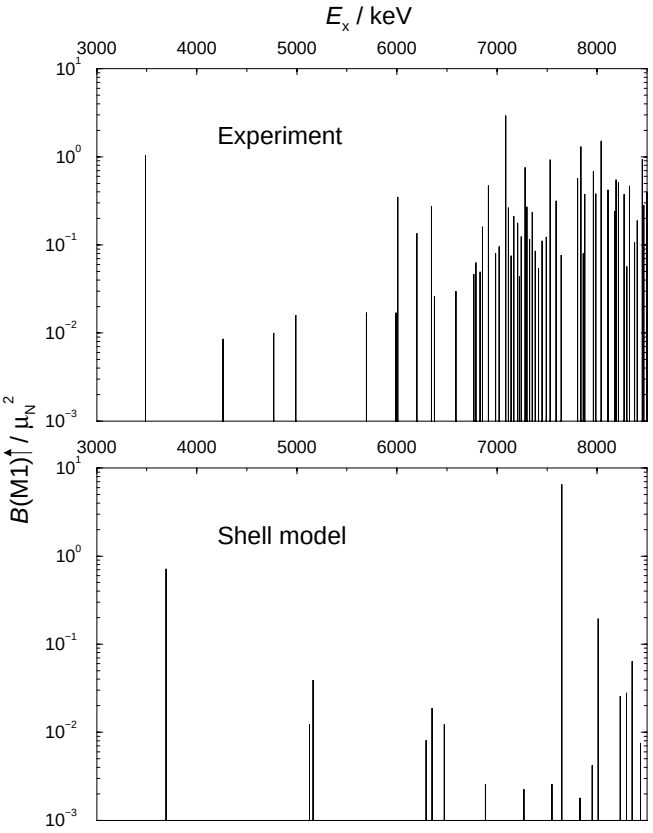

Fig. 1 *$B(M1, 0^+ \rightarrow 1^+)$ values for excitation energies of the 1^+ states between 3.0 and 8.5 MeV. Upper panel: all experimental $J = 1$ states except known 1^- states are included. Lower panel: 1^+ states predicted by shell-model calculations.*

[1] R. Schwengner, G. Rusev et al., this report, p. 5
[2] D. Zwarts, Comput. Phys. Commun. 38 (1985) 365
[3] R. Schwengner, G. Rainovski et al., Phys. Rev. C 66 (2002) 024310

Feeding of Intermediate States in Photon Scattering from ^{100}Mo [D]

G. Rusev, R. Schwengner, K.D. Schilling, A. Wagner, F. Dönau, S. Frauendorf[1], M. Erhard, A.R. Junghans, K. Kosev, N. Nankov[2], E. Grosse[3]

The investigation of the dipole-strength distribution of ^{100}Mo [1] was extended with a measurement at E_e = 13.2 MeV. An electron-beam energy above the neutron threshold S_n = 8.3 MeV was chosen in order to provide a high photon flux close to S_n. The improved detector setup [2] and an intense photon beam led to the observation of more than 250 transitions in ^{100}Mo in the range between 4 MeV and S_n. The level widths Γ_0 were obtained under the assumption that all transitions decay only to the ground state. The distribution of the ratio Γ_0/E_γ^3 proportional to the reduced transition probability $B(E1)$ is presented in Fig. 1.

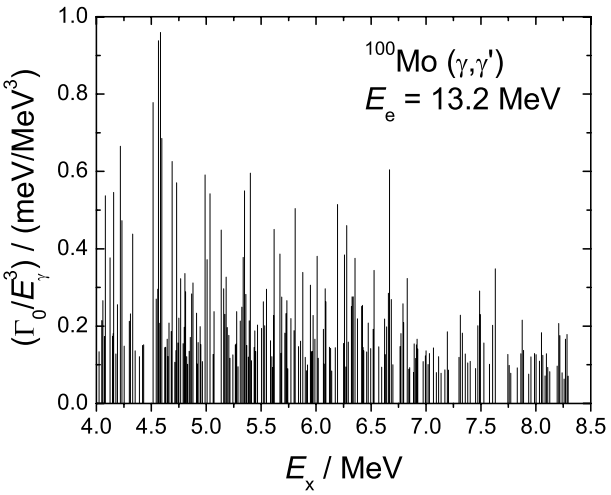

Fig. 1 *Distribution of the ratio Γ_0/E_γ^3 for the observed transitions in ^{100}Mo.*

The high-lying excited levels E_x may decay not only to the ground state but feed also states E_f with intermediate energy. In this case the considered width Γ_0 is only part of the total width Γ of a level. The fed levels, however, show a higher photon-scattering cross section than the one obtained from measurements at lower electron-beam energies [3] where the levels are directly excited but not fed from higher-lying levels.

In order to investigate the distribution of the fed levels we performed an additional measurement on ^{100}Mo at E_e = 7.8 MeV. The electron energy was chosen such that levels in a 500 keV range between 7.8 and S_n = 8.3 MeV are not excited. Therefore, transitions linking states between 7.8 and S_n = 8.3 MeV with intermediate states were observed only in the spectrum measured at E_e = 13.2 MeV. The energy of the fed levels is defined by the Ritz principle as $E_f = E_x - E_{link}$, where E_{link} is the energy of a transition linking the levels E_x and E_f. A distribution of the number of levels with E_f fed from the excited levels at E_x in the range between 7.8 and 8.3 MeV and satisfying the Ritz principle is presented in Fig. 2. The used criterion does not exclude counting of more fed levels because of a random matching of E_{link} with energy spacing (E_x - E_f) for different pairs of levels.

An estimate of the feeding can be obtained from a statistical model. A level scheme of ^{100}Mo containing only dipole states was created using the back-shifted Fermi-gas model and the Wigner level-spacing distribution [4]. The level-density parameter was set to $a = 15.5$ MeV^{-1}. The probability for the decay of a level was assumed to depend only on E_γ^3. The decay of the excited levels between 7.8 and 8.3 MeV to the ground state as well as to the intermediate levels can be simulated and the number of fed levels can be obtained. The results from the statistical model are compared with the experimental ones in Fig. 2. The obtained histogram is normalized to the number of populations of one particular excited level E_x.

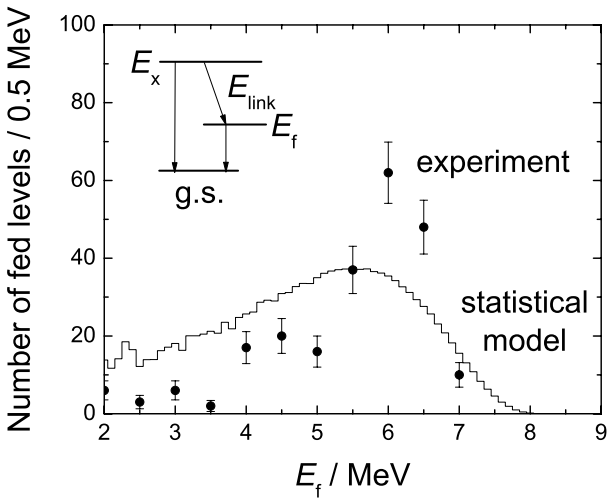

Fig. 2 *Distribution of the number of fed levels from excited states between 7.8 and 8.3 MeV obtained from the experiment and the back-shifted Fermi-gas model.*

The comparison in Fig. 2 shows that the interplay between the high level density and the transition probability causes a decay of excited levels in the range between 7.8 and 8.3 MeV to many low-lying intermediate levels with a distribution with a maximum at about 6 MeV.

[1] G. Rusev, R. Schwengner et al., Wiss.-Techn. Berichte FZR-401 (2004) 7

[2] K.D. Schilling, F. Dönau et al., Wiss.-Techn. Berichte FZR-401 (2004) 5

[3] G. Rusev, R. Schwengner et al., Wiss.-Techn. Berichte FZR-372 (2003) 34 and 35

[4] T. von Egidy, H.H. Schmidt and A.N. Behkami, Nucl. Phys. A 481 (1988) 189

[1] *also Department of Physics, University of Notre Dame, IN 46556, USA*
[2] *also INRNE Sofia, Bulgaria*
[3] *also Technische Universität Dresden*

The Decay of 1^+ States as a New Probe of the Structure of 0^+ Shape Isomers[D]

G. Rusev, R. Schwengner, F. Dönau, S. Frauendorf[1], L. Käubler, L.K. Kostov[2], S. Mallion, K.D. Schilling, A. Wagner, E. Grosse[3], H. von Garrel[4], U. Kneissl[4], C. Kohstall[4], M. Kreutz[4], H.H. Pitz[4], M. Scheck[4], F. Stedile[4], P. von Brentano[5], J. Jolie[5], A. Linnemann[5], N. Pietralla[6], V. Werner[7]

We have studied the nuclides ^{98}Mo and ^{100}Mo in photon-scattering experiments by using bremsstrahlung produced from electron beams with kinetic energies from 3.2 to 3.8 MeV [1]. A specific feature of both nuclides is the deexcitation of one state with spin $J = 1$ to both the 0^+ ground state and to the first excited 0^+ state. Such peculiar transitions from $J = 1$ to excited 0^+ states have not been quantitatively discussed so far because common interpretations like two-phonon mixed-symmetry states in terms of the Interacting Boson Approximation (IBA) or the interpretation in terms of the Random Phase Approximation (RPA) do not take shape coexistence into account. We have developed a model based on one-particle-one-hole (1p1h) excitations, which allows us to estimate the mixing of the two 0^+ shape isomers from experimental transition strengths.

For the case of ^{98}Mo, the two 0^+ states correspond to two minima of the deformation energy as a function of the quadrupole deformation parameter ε_2 and of the triaxiality parameter γ. The shell-correction method without BCS pairing field predicts two minima: The lowest minimum (a) corresponds to a triaxial equilibrium shape with the proton configuation $(fp)^{-2}g^4_{9/2}$. Due to a level crossing at the Fermi surface there is an additional minimum (b) at a prolate shape with the proton configuration $(fp)^{-4}g^6_{9/2}$.

We assume a two-state mixing scenario for the description of the $M1$ transitions. Employing orthogonality of the equilibrium configurations a and b the two coexisting 0^+ states are written as

$$\begin{aligned} |0^+_1\rangle &= c_a(0^+)|0a\rangle + c_b(0^+)|0b\rangle \\ |0^+_2\rangle &= -c_b(0^+)|0a\rangle + c_a(0^+)|0b\rangle \end{aligned} \quad (1)$$

Analogously we define the 1^+ states that decay by $M1$ transitions through a two-state mixing from the 1p1h configurations ($1a$) and ($1b$):

$$\begin{aligned} |1^+_1\rangle &= c_a(1^+)|1a\rangle + c_b(1^+)|1b\rangle \\ |1^+_2\rangle &= -c_b(1^+)|1a\rangle + c_a(1^+)|1b\rangle \end{aligned} \quad (2)$$

It is important to notice that the particle-hole excitations of the configuration changes $0a \leftrightarrow 1a$ and $0b \leftrightarrow 1b$, respectively, involve the same orbitals. Only in this case the configuration change $1a \leftrightarrow 1b$ is not of higher type than the 2p2h transfer which can be bridged by the pairing interaction.

The $M1$ operator manages the 1p1h transitions $1a(1b) \leftrightarrow 0a(0b)$ but can not connect configurations of the a type with the ones of the b type. Hence, the matrix elements connecting the 1^+_1 state with the two 0^+ states are

$$\begin{aligned} \langle 1^+_1|\mathcal{M}(M1)|0^+_1\rangle = \; & c_a(1^+)c_a(0^+)\langle 1a|\mathcal{M}(M1)|0a\rangle \\ & + c_b(1^+)c_b(0^+)\langle 1b|\mathcal{M}(M1)|0b\rangle \quad (3) \\ \langle 1^+_1|\mathcal{M}(M1)|0^+_2\rangle = \; & -c_a(1^+)c_b(0^+)\langle 1a|\mathcal{M}(M1)|0a\rangle \\ & + c_b(1^+)c_a(0^+)\langle 1b|\mathcal{M}(M1)|0b\rangle \quad (4) \end{aligned}$$

The matrix elements of the 1^+_2 state are given by the replacements $c_a(1^+) \rightarrow -c_b(1^+)$ and $c_b(1^+) \rightarrow c_a(1^+)$. For a minor group of 1^+ states that involve one of the crossing orbitals in the 1p1h excitation only one of the configurations, either $1a$ or $1b$, exists because a particle can be neither added to nor removed from the same orbital which is filled in a and empty in b. Hence we may take e.g. $c_a(1^+) = 1$ and $c_b(1^+) = 0$ in eqs. (3,4). For this type of 1^+_1 states the $1a$ configuration is strongly excited and the corresponding state decays into both 0^+ states. The relation between the mixing coefficients and $B(M1)$ values becomes:

$$\frac{B(M1, 1^+_1 \rightarrow 0^+_2)}{B(M1, 1^+_1 \rightarrow 0^+_1)} = \left[\frac{c_b(0^+)}{c_a(0^+)}\right]^2 \quad (5)$$

The branching ratio is a direct measure of the relative contributions of the minima a and b in each of the two 0^+ states. The experimental intensities of the 2816.9 and 3551.2 keV transitions in ^{98}Mo result in 0.28(5) for the ratio (5). Using normalization one obtains $c_b(0^+)^2 = 0.22(3)$ and $c_a(0^+)^2 = 0.78(3)$. An analogous argument applies to the 1^+_2 state and results in the inverse ratio (5), i.e., $B(M1, 1^+_2 \rightarrow 0^+_2)/B(M1, 1^+_2 \rightarrow 0^+_1) = 3.6(6)$. The $1b$ state is not observed in this experiment, because it is expected at about 500 keV above the $1a$ state. In the case of ^{100}Mo the intensities of the 2595.2 and 3290.1 keV transitions lead to $B(M1, 1^+_1 \rightarrow 0^+_2)/B(M1, 1^+_1 \rightarrow 0^+_1) = 0.45(13)$. The obtained mixing coefficients are $c_b(0^+)^2 = 0.31(6)$ and $c_a(0^+)^2 = 0.69(6)$.

The presented model is generally valid for analogous cases in other nuclides. Consequently, the observation of decay branches to excited 0^+ states in connection with the presented model provides a new means to investigate the structure of shape-isomeric states.

[1] G. Rusev, R. Schwengner et al., Wiss.-Techn. Berichte FZR-372 (2003) 34 and 35

[1] *Department of Physics, University of Notre Dame, Notre Dame, Indiana 46556, USA*
[2] *Institute for Nuclear Research and Nuclear Energy, BAS, 1784 Sofia, Bulgaria*
[3] *also Technische Universität Dresden*
[4] *Institut für Strahlenphysik, Universität Stuttgart, 70569 Stuttgart, Germany*
[5] *Institut für Kernphysik, Universität Köln, 50937 Köln, Germany*
[6] *Nuclear Structure Laboratory, Dept. of Physics & Astronomy, SUNY, Stony Brook, NY 11794-3800, USA*
[7] *Wright Nuclear Structure Laboratory, Yale University, New Haven, CT 06520-8124, USA*

An RPA Code for Deformed Nuclei

F. Dönau

The shell-model calculation of the vibrational excitations and their electromagnetic decay properties is for non-spherical nuclei a challenging but yet unsolved task because of the untractable large configuration space necessary for such a diagonalization. The Random Phase Approximation (RPA) [1] is known to describe these vibrational excitations in both spherical and deformed nuclei but at the expense of restricting the configuration mixings to the ones of two-quasiparticle excitations and their ground-state correlations. In spite of this simplification, the RPA calculations for deformed shapes require a considerable numerical effort when using non-separable effective interactions like Skyrme- or Gogny-type interactions. In the following we present a more versatile RPA code based on Nilsson-like single-particle wave functions and separable interaction terms which was developed mainly as a handy tool for interpreting the recently measured dipole excitations in the photon-scattering experiments at ELBE.

The RPA Hamiltonian of this code is

$$H_{\rm RPA} = h_{2qp} + \sum_i \kappa_i (Q_i)^2 \qquad (1)$$

where the part h_{2qp} contains the unperturbed two-quasiparticle excitations which are coupled by a series of factorized residual interaction terms composed of squared operators Q_i and corresponding strength parameters κ_i.

The present version of the RPA code is using the quasiparticle wave functions as obtained from the Rossendorf TAC code [2] which allows us to treat quadrupole-deformed shapes, a monopole-pair potential as well as a rotational cranking term. The available TAC code enables the selfconsistent calculation of the equilibrium shapes by means of the shell-correction method.

Concerning the residual interaction the following operator types Q_i are implemented into the RPA code:

- the particle number operator N
- the spin operators $S_{\mu=0,\pm1}$
- the angular momentum operators $J_{\mu=0,\pm1}$
- the quadrupole operators $r^2 Y^2_{\mu=0,\pm1,\pm2}$

for the calculation of $I^\pi = 1^+, 2^+$ vibrational excitations with positive parity and

- the momentum operators $P_{\mu=0,\pm1}$
- the coordinate operators $R_{\mu=0,\pm1}$
- the octupole operator $r^3 Y^3_{\mu=0,\pm1,\pm2,\pm3}$
- the octupole-dipole operators $r^3 Y^1_{\mu=0,\pm1}$

for the calculation $I^\pi = 1^-$ vibrational excitations with negative parity.

Using the strength-function method [3] the code yields the strength distribution of transitions between the ground state and the vibrational states. The transition strength can be obtained for the electric and magnetic dipole operators $(E1)_{\mu=0,\pm1}$ and $(M1)_{\mu=0,\pm1}$, respectively, as well as for any selected operator type listed above. The interaction constants κ_i can be chosen such that the corresponding interaction operators get separated according to their isoscalar and isovector parts or alternatively to their proton and neutron components. In this way any mixture with regard to the isospin character of the residual interaction can be studied. Similarly the different isospin parts of the transition operators can be distinguished.

As a particular advantage we mention that our RPA code includes the the full suppression of spurious modes as described in [4]. For illustration we show the $E1$ strength distribution for the axially deformed nucleus ^{156}Gd obtained for a dipole-plus-octupole interaction.

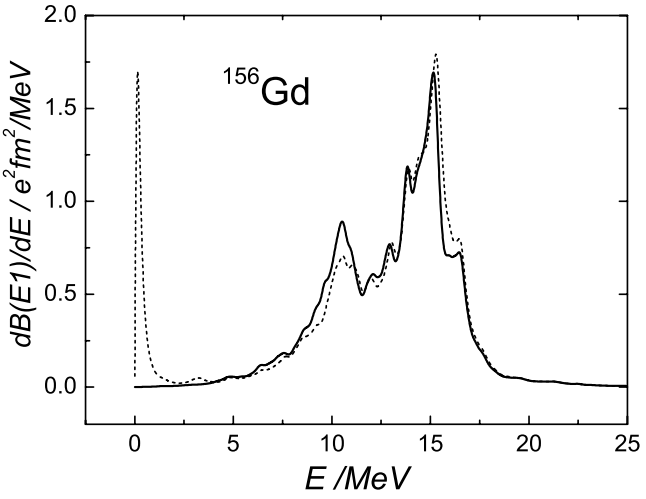

Fig. 1 *Calculated RPA strength $dB(E1)/dE$ $(efm)^2/MeV$ as a function of the excitation E (MeV). A constant width Γ = 0.5 MeV is applied for plotting the Lorentzian shaped lines of the $E1$ strength function. Solid curve: Spurious c.m. effects fully excluded. Dashed curve: approximate removal of c.m. effects by effective charges $e_p = N/A,\ e_n = -Z/A$.*

[1] P. Ring and P. Schuck, *The Nuclear Many Body Problem*, Springer, New York, 1980
[2] D.G. Jenkins, C.J. Chiara et al., TAC Manual, unpublished
[3] V. O. Nesterenko, J. Kvasil and P.-G. Reinhardt, Phys. Rev. C 66 (2002) 044307
[4] F. Dönau, this report, p. 12

$E1$ and $M1$ Strength in ^{92,98,100}Mo Calculated by RPA

F. Dönau

The photon beam of the bremsstrahlung facility at ELBE has been used to measure the spin $I = 1$ (dipole) excitations between 4 to 9 MeV excitation energy in ^{92,98,100}Mo in a high resolution experiment. Due to the magic $N = 50$ neutron configuration in the ground state the ^{92}Mo nucleus is spherical whereas the occupation of open neutron shells in ^{98,100}Mo is known to lead to deformed shapes [1]. An interesting question is how the distribution of the dipole excitations changes when considering this isotopic series. A further question concerns the suggestion of possible Pygmy resonances for growing neutron excess, i.e. whether the dipole-excitation strength in the vicinity of the neutron threshold increases with the neutron number.

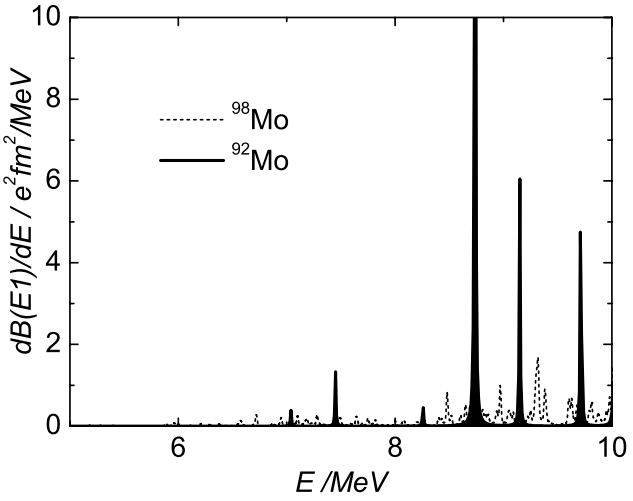

Fig. 1 *Calculated strength for an $E1$ excitation from the the ground state to a vibrational state at the energy E in ^{92}Mo (solid lines) and ^{98}Mo (dashed lines), respectively. A Lorentzian width $\Gamma = 10$ keV is used in both nuclei. The strength distribution in ^{100}Mo which is not shown here is qualitatively quite similar to the one in ^{98}Mo.*

The RPA code [2] has been applied to investigate what the mean field plus RPA is predicting for this case. In Fig. 1 we present the calculated $E1$-strength distribution for ^{92}Mo and ^{98}Mo as obtained for an isovector dipole-plus-octupole interaction. The strength of the residual interaction was chosen to fit the position of the giant dipole resonance. The selfconsistently calculated shape of the Nilsson potential changes from $\varepsilon = \gamma = 0$ in ^{92}Mo to $\varepsilon = 0.19, \gamma = 16°$ in ^{98}Mo. The resulting $E1$ strengths found in the RPA calculation are shown in Fig 1. The transition strength in the spherical ^{92}Mo is distributed into a few strong lines corresponding to the degeneracy of the spherical shells and their strong selection rules for $E1$ transitions. In contrast, the transition strength in ^{98}Mo appears strongly fragmented due to the shell splitting in a deformed field.

Defining the energy-weighted sum rule $EWSR(E)$ as the integrated $E1$ strength up to the energy E, the ratio $EWSR(E)/EWSR(E_{\max}{=}30\,\mathrm{MeV})$ as a function of the energy is shown in Fig. 2. The function $EWSR(E)/EWSR(E_{\max})$ provides a more quantitative measure of the fragmentation effect of the transition strength originated by the structural change in the isotopic series ^{92,98,100}Mo. One notices the stepwise increase of the ratio in ^{92}Mo reflecting again the spherical degeneracy which is modified in ^{98}Mo to a more regular curve in accordance with the more smooth level density in the deformed ^{98}Mo which is seen also in the ratio for ^{100}Mo. The same tendency was found for the analogous ratio of the $M1$ transition strengths.

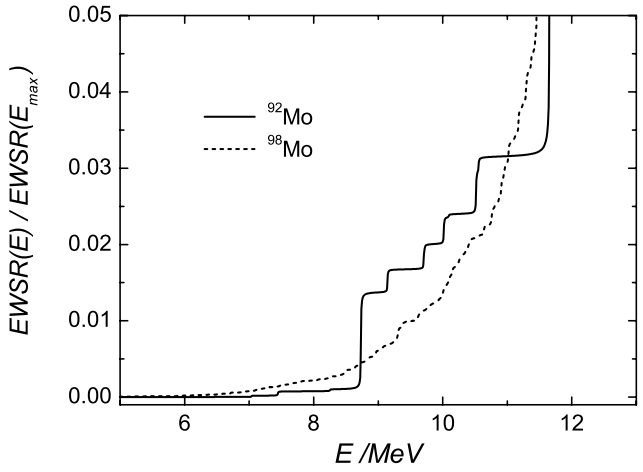

Fig. 2 *Ratio of the calculated energy-weighted sum rule $EWSR(E)/EWSR(E_{\max} = 30\ MeV)$ as a function of the energy E. Note, that $EWSR(E)$ amounts at $E = 10$ MeV only to about 2 % of the total $EWSR$.*

Comparing the $EWSR$ ratios in detail one finds that the values in the spherical case are fluctuating with a large period about the more smoothed values in the deformed case. It seems suggestive to perform a similar analysis of the experimental data by extracting the fractional $EWSR$s in order to obtain information about the shell structure in the isotopic series which can be compared with the calculation. It is evident that for such a comparison the experimental transition strength needs to be measured for a large enough energy interval in order to obtain a sensitive $EWSR$ ratio. A comparison of such ratios at an arbitrarily selected excitation energy E is probably not very conclusive because of the fluctuating character of this ratio.

[1] P.F. Mantica, A.E. Stuchbery et al., Phys. Rev. C 63 (2001) 034312
[2] F. Dönau, this report, p. 10

Removal of Spurious Modes in the RPA

F. Dönau

The Random Phase Approximation (RPA) [1] is a powerful standard approach to calculate microscopically the variety of vibrational excitations and giant resonances in nuclei and in other finite fermion systems. The RPA is derived from the mean-field approach and might be infected from the same symmetry violations as the mean-field concept. Thus, for example, the translational symmetry and the rotational symmetry are broken for deformed mean-field potentials which in the RPA is reflected by the unwanted appearance of spurious center-of-mass (c.m.) motion and angular-momentum fluctuations. These spurious modes contaminate the transition strength calculated in RPA in a complicated manner.

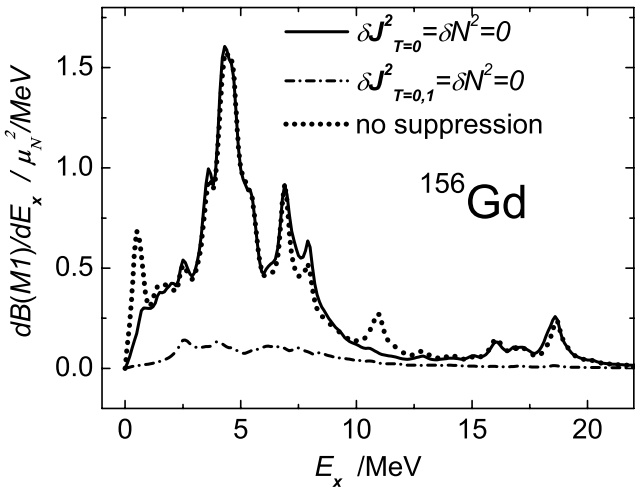

Fig. 1 *Mode suppression in the $M1$-strength function for ^{156}Gd. A constant Lorentzian width $\Gamma = 0.5$ MeV is used in the strength functions shown. Solid curve: Fluctuations of both the isoscalar ($T = 0$) a.m. $\boldsymbol{J_\pi + J_\nu}$ and of the particle numbers N_π, N_ν suppressed. Dotted curve: without any suppression. Dashed-dotted curve: Like the solid curve but additionally the fluctuations of the isovector ($T = 1$) a.m. part $\boldsymbol{J_\pi - J_\nu}$ suppressed. Note, that in the latter curve the dramatic effect might be not realistic because of the simple interaction.*

We present in [2] a simple method which gives for the first time a rigorous solution for this very old problem within the RPA [3, 4]. The underlying idea of our method is quite simple: A restoring force $\kappa \cdot \boldsymbol{F^2}$ for the considered spurious mode $\boldsymbol{F}$ is supplemented to the RPA Hamiltonian in order to freeze this unwanted spurious motion by taking a large enough strength parameter κ. In this way a forced damping of the corresponding spurious motion is achieved such that the RPA fluctuations for this mode can be completely suppressed. If, for instance, the RPA fluctuations of the angular momentum $\boldsymbol{J}$ are to be eliminated, then a term $\kappa \cdot \boldsymbol{J^2}$ with a sufficiently large strength constant κ is included in the RPA Hamiltonian. Our method of mode suppression requires only a minor additional effort in the practical performance of the RPA since the equations of motion can be treated as usual [1].

In Fig. 1 the mode-suppression effects are illustrated in a schematic RPA calculation of the $M1$ strength function for nucleus ^{156}Gd. The RPA Hamiltonian consists of a two-quasiparticle part resulting from a rotating axially deformed Nilsson-plus-pairing potential and a residual interaction of spin-plus-quadrupole type.

The suppression of the c.m. mode recovers also the Galilean invariance on the RPA level. Therefore, the $E1$-transition strength can be calculated more precisely than the hitherto approximate c.m. correction by taking effective proton and neutron charges, i.e. $e_p = N/A$ and $e_n = -Z/A$, respectively.

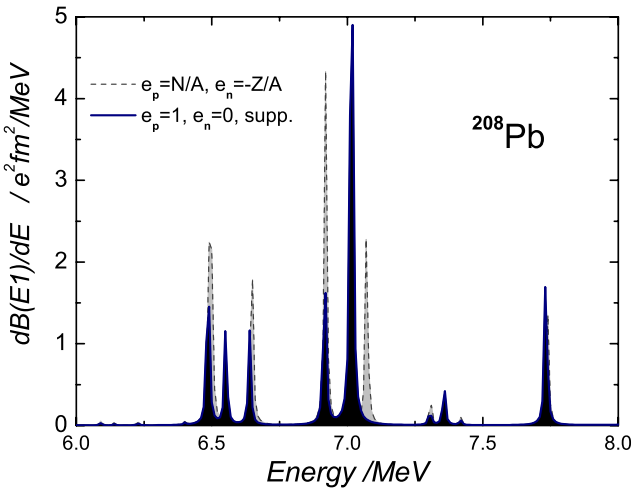

Fig. 2 *$E1$ strength for ^{208}Pb calculated with a schematic dipole interaction. Note, here a constant Lorentzian width $\Gamma = 10$ keV is applied. Solid lines: correct removal of c.m. fluctuation by the suppression method. Dashed lines: approximate c.m. removal by effective charges.*

In Fig. 2 the effect of an exact c.m. removal is demonstrated in the $E1$ strength for ^{208}Pb comparing the result of an ordinary RPA calculation where effective charges are used with the one where the c.m. fluctuations are completely suppressed. The latter is achieved by a supplementary term $\kappa \cdot \boldsymbol{R^2}$ where $\boldsymbol{R}$ is the c.m. coordinate and $\kappa = 10^6$. The freezing of the c.m. fluctuations is obviously redistributing the peak strength as well as is partially shifting the peak position. Hence, the application of our suppression method is demanding for a reliable calculation of transition strengths within the RPA. This is an absolutely necessary ingredient for the comparison with the experimental data obtained at ELBE in high-spectroscopic resolution.

[1] P. Ring and P. Schuck, The Nuclear Many Body Problem, Springer, New York, 1980
[2] F. Dönau, Phys. Rev. Lett. 94 (2005) 092593
[3] D.J. Thouless, Nucl. Phys. 21 (1960) 225 (1960), ibid. 22 (1961) 78
[4] E.R. Marshalek and J. Weneser, Ann. Phys. (N.Y.) 53 (1969) 569

Measurements of the Photodisintegration Yield of Mo and Au at Different Energies

M. Erhard, E. Grosse[1], A.R. Junghans, K. Kosev, C. Nair, N. Nankov, G. Rusev, K.D. Schilling, R. Schwengner, A. Wagner

The aim of photoactivation studies with bremsstrahlung at ELBE is the investigation of p-nuclei like ^{92}Mo [1] to determine photodisintegration cross sections of astrophysical interest [2]. The measured photoactivation yield is proportional to the integral of the photon flux times the photodisintegration cross section. The γ decay of the photodisintegration products is used to identify the number of nuclei produced. The photon flux can be deduced from the known ^{11}B transition strengths and from the activation of Au samples irradiated together with natural molybdenum.

In ^{92}Mo, the proton-separation energy is $S_p = 7.456$ MeV, and the (γ, p) process populates the 105 keV state ^{91m}Nb with a half-life $T_{1/2} = 60.86$ d [1]. The neutron-separation energy is $S_n = 12.672$ MeV, and the (γ, n) process decays to the 64.6 s isomer of ^{91}Mo. Calculations with TALYS [3] show that the direct population of the ground states (g.s.) for both, ^{91}Mo and ^{91}Nb, is strongly reduced due to the high spin difference between the decaying ^{92}Mo continuum states and the corresponding g.s. If the activation energy is below S_n, a unique signature of the (γ, p) process is the electron-capture decay of ^{91m}Nb (branching ratio $K = 2.9\,\%$) into an excited level of ^{91}Zr, which deexcites into the stable g.s. by emitting a 1205 keV γ quantum.

From the intensity of the full-energy peak measured with an HPGe detector [4], the photoactivation yield was derived by taking into account the total deposited beam charge, target mass, isotopic abundance, decay and measurement time, full-energy peak efficiency, and dead time as well as coincidence-summing corrections.

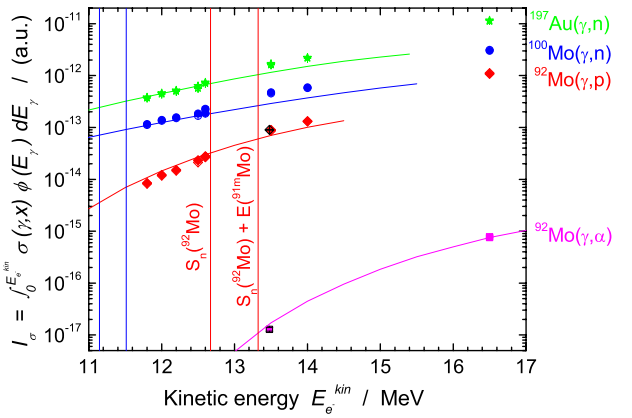

Fig. 1 *Integrated excitation functions of photodisintegration processes in Mo isotopes (points) and theoretical predictions from a Hauser-Feshbach model [5] folded with the photon-energy distribution [6] up to the endpoint energy E_e^{kin}. Theoretical curves are adjusted to the low-energy points in $^{197}Au(\gamma, n)$.*

In Fig. 1, the measured photoactivation yields are compared to model calculations. The theoretical curves are normalised to fit the simultaneously measured ^{197}Au(γ, n) data at low energies. At the highest activation energy at ≈ 16.5 MeV, we observed the ^{92}Mo$(\gamma, \alpha)^{88}$Zr reaction for the first time [$T_{1/2}(^{88}\mathrm{Zr}) = 83.4$ d; $E_\gamma = 393$ keV; $K = 97.24\,\%$]. The photoactivation of enriched ^{92}Mo (97.31 %) at 13.48 MeV was used to get a second value for the (γ, α) yield. This value was normalised relative to the yield of the 1205 keV transition from ^{92}Mo(γ, p). The reaction ^{100}Mo(γ, n) was observed by analysing the transition at 740 keV.

Photoactivation of ^{92}Mo at energies above the neutron threshold plus the excitation energy of the isomeric state of ^{91m}Mo leads to a contribution of the (γ, n) channel in the measured yield, since ^{91m}Mo decays to ^{91m}Nb via β^+ decay with a probability of 50 %. Because of the short half-life this contribution cannot be separated by measuring γ quanta from the ^{91m}Mo decay. The ^{91}Mo g.s. decay branch, however, can be used to separate the (γ, n) contribution. The g.s. itself decays with a half-life of $T_{1/2} = 15.5$ min predominantly to the g.s. of ^{91}Nb via β^+ decay. The decay of the Mo sample was measured in several short runs directly after the irradiation, the result is shown in Fig. 2. The transitions at 1582 and 1637 keV in ^{91}Nb allow to deduce the number of ^{91}Mo nuclei produced from ^{92}Mo(γ, n).

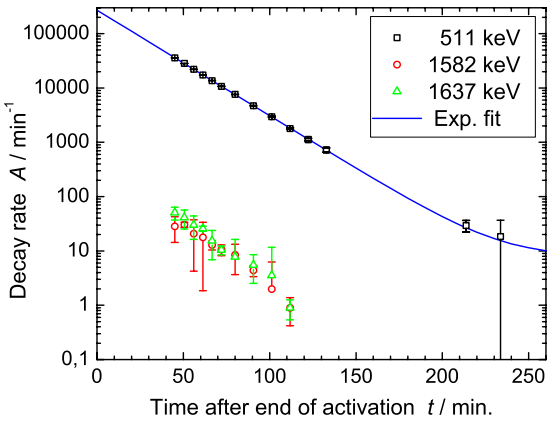

Fig. 2 *Decay of ^{91}Mo. Photoactivation of 677 mg ^{nat}Mo ($E_e^{kin} \approx 16.5$ MeV, $t_{irr} \approx 7$ h, $I_e \approx 350\,\mu$A). The data point of the 511 keV annihilation peak measured after 234 min gives an upper limit of the background contribution. The half-life $T_{1/2} = (15.49 \pm 0.04)$ min [statistical error] deduced from the fit reproduces exactly the literature value of $T_{1/2} = (15.49 \pm 0.01)$ min.*

[1] M. Erhard, A. Wagner et al., Wiss.-Techn. Berichte FZR-401 (2004) 13
[2] M. Arnould, S. Goriely, Phys. Rep. 384 (2003) 11
[3] A.J. Koning et al., program TALYS-0.64 (Dec 2004), NRG Report 21297/04.62741/P FAI/AK/AK
[4] M. Erhard, E. Grosse et al., this report, p. 14
[5] T. Rauscher, F.-K. Thielemann, Atom. Data and Nucl. Data Tables 88 (2004) 1
[6] L.I. Schiff, Phys. Rev. 83 (1951) 252

[1] *also Technische Universität Dresden*

The Photoactivation Setup at ELBE

M. Erhard, E. Grosse[1], A. Hartmann, A.R. Junghans, C. Nair, K.D. Schilling, W. Schulze, R. Schwengner, A. Wagner

The accomplishment of a photoactivation experiment consists of two steps: first, the activation itself, when bremsstrahlung is produced and a target is irradiated, and second, the measurement of γ quanta from the decay of the activated nuclei in a well-shielded setup [1].

In 2004, the first activation runs were performed at the existing nuclear-resonance-fluorescence (NRF) setup at ELBE. We used high-purity germanium (HPGe) detectors to measure the photon flux and the shape of the bremsstrahlung spectrum with the six strongest transitions in an NRF target of boron acid ($H_3{}^{11}BO_3$) containing 97.3 % enriched ^{11}B. The photon flux density amounts to $\approx 10^8/(\mathrm{s}\cdot\mathrm{cm}^2\cdot\mathrm{MeV})$ at half of the endpoint energy. In order to increase the intensity significantly, we placed the activation targets inside the electron-beam dump behind the vacuum steel vessel. A cylindrical Al tube was inserted, and a target holder consisting of an Al rod with a clamping bolt was mounted.

In order to determine the photon flux for photoactivation experiments, samples consisting of natural Au at two experimental sites were used as normalisation standards. The photon flux at the NRF site was measured utilising photon scattering from the boron target together with a gold activation target. Another Au disk sandwiched with the Mo target under investigation was placed behind the electron beam dump. The resulting activation yield ratio displayed in Fig. 1 increases linearly with the energy caused by the higher photon-flux at the beam dump site.

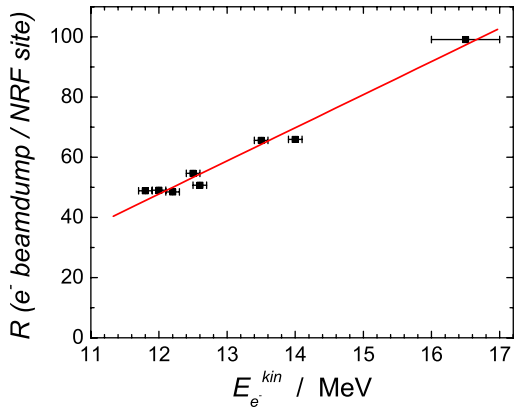

Fig. 1 *Activation yield ratio of the Au targets, activated in the electron-beam dump and at the NRF site simultaneously. The decay of ^{196}Au ($T_{1/2} = 6.2$ d) was measured with a 100 %-HPGe detector (356 keV transition in ^{196}Pt, $\sigma_R < 0.4$ %).*

The targets were prepared as circular discs with a diameter of 2 cm while their thickness was chosen according to the expected photodisintegration cross section with a maximum irradiation period of ≈ 16 h and $\approx 500\,\mu$A electron-beam current. Depending on energy and duration of the irradiation, we used Mo targets consisting of several 0.2 to 0.3 mm thick slices corresponding to masses of 0.63 g up to 0.98 g.

The activity of the Mo targets 20 min after shutdown of the electron beam was 5.2 kBq/g in the run with the highest energy (16.5 MeV), irradiated for 7 h, and the total target dose rate was measured to be 2.4 μSv/h.

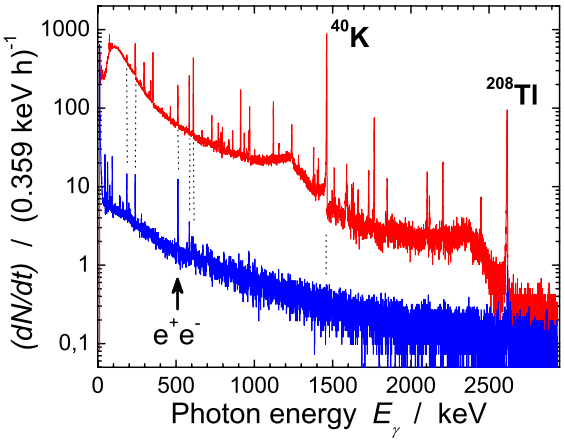

Fig. 2 *Background of an HPGe det. (60 % rel. eff.) outside (upper curve, 12 h meas. time, overall count rate: $127\,s^{-1}$) and inside the lead castle (lower curve, 41 h, $2.9\,s^{-1}$). Background suppression is better than 1400× for ^{40}K.*

For the measurement of very low activities, the reduction of radiation from surrounding materials is needed [2]. Fig. 2 shows the background suppression measured with a 60 %-HPGe coaxial detector (n-type) inside and outside the lead castle shown in Fig. 3.

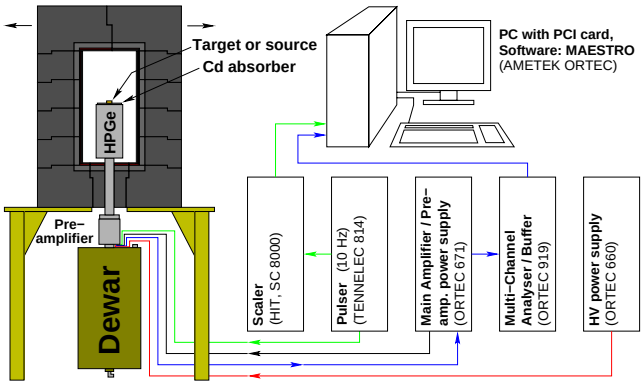

Fig. 3 *Low-level counting setup at ELBE with lead castle, HPGe detector and data acquisition system.*

The preamplifier-output signals are amplified and then processed by a multi-channel analyser. Deadtime and coincidence-summing corrections [3] were done by applying a 10 Hz pulser signal to the preamplifier test input.

[1] M. Erhard, A. Wagner et al., Wiss.-Techn. Berichte FZR-401 (2004) 13

[2] P. Theodórsson, Measurement of Weak Radioactivity, World Scientific Publishing Co. Pte. Ltd., 1996

[3] C. Nair, A.R. Junghans et al., this report, p. 18

[1] *also Technische Universität Dresden*

Improvements of the Bremsstrahlung Facility at ELBE

K.D. Schilling, M. Döring, M. Erhard, E. Grosse,[1] A. Hartmann, A.R. Junghans, K. Kosev, R. Matjeschk, T. Riedel,[2] G. Rusev, W. Schulze, R. Schwengner, W. Seidel, J. Steiner, A. Wagner

In continuation of the status report presented in [1] and based on the methodical experiences gathered during extensive beam time periods with the bremsstrahlung facility at ELBE, further improvements have been realized. They are displayed in Fig. 1 and will be described in the following:

• The Al window mentioned in [2] that separates the ultra-high vacuum in the accelerator (electron) beam tube from the vacuum system of the bremsstrahlung beam line was exchanged for a quartz window of 3.3 mm thickness and 35.6 mm effective diameter. In this way, a system for the laser alignment of the beam tube between the last bending magnet on the left of the steering magnets (not shown in Fig. 1) and the γ beam dump including the bremsstrahlung collimator [3] has been realized. Thus, the collinearity of the collimated bremsstrahlung beam with the incident electron beam can be achieved.

• The polarization monitor [4,1], which houses the target of deuterated polyethylene (CD_2) of about 50 μm thickness, was moved upstream to a position in front of the third Pb wall (in beam direction) in the experimental cave (Fig. 1). This led to a considerable γ-background reduction observed in the HPGe (+ BGO) detector array as a result of the essential shielding effect of the third Pb wall.

• A EUROBALL cluster detector [5] consisting of 7 individual hexagonal shaped HPGe crystals has been installed at an average angle of $\Theta = 140°$ relative to the photon beam direction in order to detect γ radiation emitted to the backward hemisphere.

• A photon-beam position monitor [6] consisting of four segmented scintillation detectors has been constructed and installed at the entrance of the γ beam dump. It serves to monitor the position and the intensity of the bremsstrahlung photon beam.

• An essential new ingredient of the bremsstrahlung facility consists in the installation of a photoactivation setup [7]. It enables measurements of activation yields, e.g., of p-nuclei in order to determine photodisintegration cross sections of astrophysical interest [8.]. The new setup is positioned inside of the iron casing of the electron beam dump (Fig. 1) downstream of the graphite cylinder utilizing a high bremsstrahlung intensity for activation purposes. A cylindrical Al tube contains an Al rod with a clamp-type target holder. The setup will be upgraded by a pneumatic-tube delivery system in near future. See also [7] for more details.

• An automatic N_2-filling system for the HPGe detectors has been installed that gives a permanent information about the status via TV camera and sends an SMS in case of an alert signal.

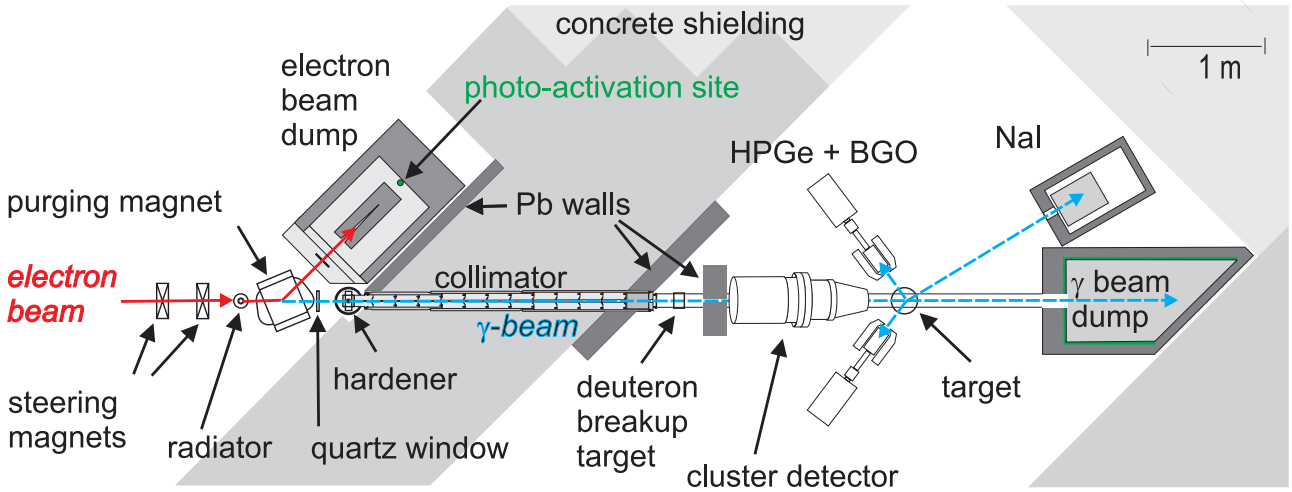

Fig. 1 *Current layout of the bremsstrahlung facility for nuclear-physics and astrophysics experiments at ELBE.*

[1] K.D. Schilling, F. Dönau et al., Wiss.-Techn. Ber. FZR-401 (2004) 5
[2] K.D. Schilling, A. Wagner et al., Wiss.-Techn. Ber. FZR-341 (2002) 41
[3] K.D. Schilling, R. Schwengner et al., Wiss.-Techn. Ber. FZR-341 (2002) 37
[4] R. Schwengner, H. Sharma, A. Wagner, Wiss.-Techn. Ber. FZR-341 (2002) 39
[5] J. Eberth, H.G. Thomas et al., Progr. Part. Nucl. Phys. 38C (1997) 29
[6] M. Döring, R. Matjeschk et al., this report p. 23
[7] M. Erhard, E. Grosse et al., this report p. 14
[8] M. Erhard, E. Grosse et al., this report p. 13

[1] *also Technische Universität Dresden*
[2] *FZ Rossendorf, FWF*

Measurement of the Beam Energy at ELBE via the Photodisintegration of the Deuteron [D]

R. Schwengner, G. Rusev, K. D. Schilling, A. Wagner, E. Grosse[1], A. Hartmann

During photon-scattering and photoactivation measurements it is important to monitor the electron energy, which defines the maximum energy of the bremsstrahlung spectrum. This monitoring can be done via the photodisintegration of the deuteron. The maximum energy of the incident photons can be deduced directly from the measured proton spectrum.

For the detection of the protons following the disintegration of deuterons we use a set-up of four silicon detectors placed perpendicular to the photon beam at azimuthal angles of 0°, 90°, 180° and 270° [1]. The detectors have sensitive areas of 600 mm^2 and thicknesses of 300 μm. They are mounted in a cylindrical reaction chamber at a distance of 6 cm from the beam axis. A polyethylene film, in which hydrogen is substituted by deuterium (CD2), is used as a target [2]. The CD2 film has a thickness of 40 μm and is positioned parallel to the incident beam such that it is observed by all four detectors under 45°.

The spectrum of the incident photons times the cross section for the disintegration of the deuteron can be obtained by rescaling the measured proton spectrum according to $N_\gamma(E_\mathrm{p} + E_\mathrm{n} + E_\mathrm{B}) \sim N_\mathrm{p}(E_\mathrm{p})$. Here, N_γ and N_p denote the photon and proton intensities at the given energies, respectively, $E_\mathrm{p} \approx E_\mathrm{n}$ are the energies of the proton and neutron, respectively, and $E_\mathrm{B} = 2225$ keV is the binding energy of the deuteron. The photon spectrum is obtained by dividing by the disintegration cross section, σ_dis, for which the expression given in Ref. [3] was used.

The spectrum of incident photons obtained by rescaling a proton spectrum measured at $E_\mathrm{e}^\mathrm{kin} = 13.2$ MeV is shown in Fig. 1. This spectrum may be compared with spectra calculated (i) by using the formula given by Schiff [4], (ii) by using the programme GEANT4 [5], which applies a parametrisation of the data given by Seltzer and Berger [6], and (iii) by using the formula given by Bethe and Heitler (BH) [7], respectively. The increase of the experimental spectrum towards energies below 6 MeV is due to scattered photons hitting the silicon detectors. The calculations based on the Schiff formula and on GEANT4 do not reproduce the spectrum at the edge close to the maximum energy. The calculations according to Bethe and Heitler apparently reproduce the experimental spectrum fairly well and may thus be used to describe the photon flux.

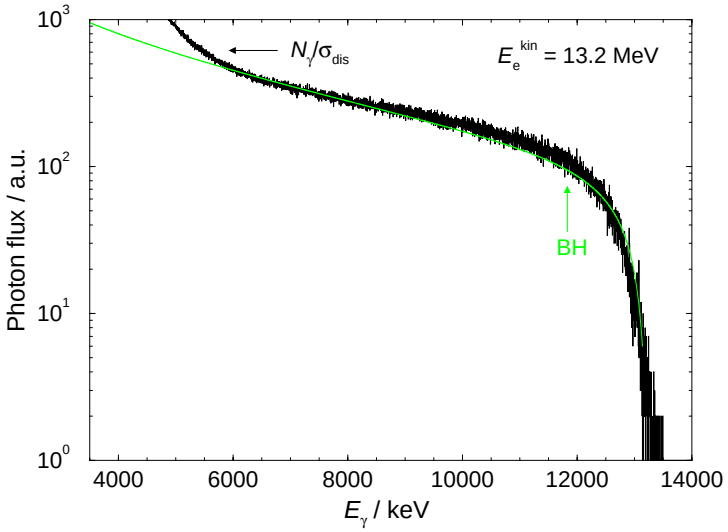

Fig. 1 *Spectrum of incident photons recalculated from the proton spectrum over the cross section for the photodisintegration of the deuteron σ_dis. The experimental spectrum is compared with a spectrum calculated according to Ref. [7] (see text).*

[1] R. Schwengner, H. Sharma, A. Wagner, Wiss.-Tech. Berichte FZR-341 (2002) 39
[2] By courtesy of D. K. Geiger, SUNY Geneseo, NY 14454, USA
[3] H. Bethe, C. Longmire, Phys. Rev. 77 (1950) 647
[4] L.I. Schiff, Phys. Rev. 83 (1951) 252
[5] S. Agostinelli, J. Allison et al., Nucl. Instrum. Meth. A 506 (2003) 250
[6] S.M. Seltzer, J. Berger, Nucl. Instrum. Meth. B 12 (1985) 95; Nucl. Data At. Data Tables 35 (1986) 345
[7] W. Heitler, The quantum theory of radiation, Dover publications, New York 1984, p. 242

[1] *also Technische Universität Dresden*

Photodisintegration of the Deuteron [D]

R. Beyer, E. Grosse [1], A.R. Junghans, G. Rusev, K.D. Schilling, R. Schwengner, A. Wagner

Experimental investigations of the deuteron-photodisintegration [1] have mainly been performed at energies near and above 100 MeV, where inelastic channels like nucleon resonances and meson production open up and where many partial waves contribute. At photon energies below 10 MeV the situation seems much simpler with only two channels (photon scattering and $d\gamma \rightarrow pn$) and only $l=0$ and $l=1$ beeing of importance. Nevertheless an exact knowledge of the cross section near the disintegration threshold is of great importance in the field of nuclear astrophysics, as it - together with the inverse reaction $pn \rightarrow d\gamma$, related to it by detailed balance - determines [2, 3] the reaction rate of the first step in the big bang nucleosynthesis (BBN).

A detailed quantitative understanding of BBN allows to calculate the primordial abundance ratio of the lightest elements and their isotopes as a function of the photon-to-baryon ratio. From now available observations of abundances in distant and thus young stars a big bang photon-to-baryon ratio can be determined to be compared to the value obtained for the later photon decoupling phase of the universe. This value was determined with high accuracy from the inhomogenity of the cosmic microwave background radiation (CMB) [4].

Most previous photodisintegration experiments at near threshold energies were performed with monochromatic photons, delivered either by radioactive decay or by Compton backscattering of a laser beam. In both cases the low photon intensity and systematic errors in determining it accurately have limited the quality of the results. Especially in the region below the maximum cross-section data have been published which are inconsistent within their error bars. One experiment has been reported from a conventional bremsstrahlung facility [5]; there the actual center-of-momentum (CM) energy was determined by a measurement of the outgoing proton energy within the range of 7 - 20 MeV.

As already pointed out in early theoretical work by Bethe et al. [6], the $l=0$ (M1) disintegration predominant at energies below 100 keV above threshold can be predicted from the nucleon magnetic moments by an extrapolation from the thermal n-capture on H, which was rather well determined at 295 K. Similarly, the $l=1$ (E1) disintegration, determinin the cross section above 500 keV, can be connected to the processes thoroughly investigated in the multi MeV range. Proton-neutron potentials (of type Argonne-Urbana, Bonn etc.) [7] as well as effective field theories [8] have made different predictions for the energy range around 100 keV. This range has been shown to be of special importance for the nucleosynthesis at 10^9 K. Here the cross section is governed by the competition between M1 and E1 [1].

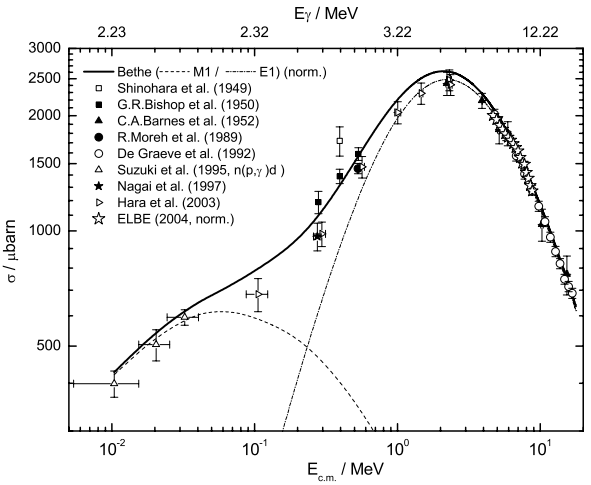

Fig. 1 *Cross section for the Photodisintegration of the deuteron vs. photon energy (top scale) resp. c. m. energy above threshold (bottom scale).*

First studies have been undertaken at the IKH to find out if the electron beam parameters at ELBE - repetition rate in the MHz range and sub-nanosecond pulse width - allow us to improve the data base and thus the comparison to the CMB results. For an extraction of the CM-energy from the nucleon velocities the good time resolution allows a rather short flight path and consequently large solid angle. In an preparative experiment we could show that the low emittance of the electron beam together with the complex photon collimation system allows a proton energy measurement over an extended range (cf. Fig. 1). The energy dependence of these data from ELBE agrees very well to an extended study of the same process at the Ghent linac [5]; obviously the determination of the c. m. energy via the measurement of only one dissociation product delivers consistent results. In future runs at ELBE a normalization to the energy dependent-photon flux can be attained by a simultaneous measurement of photon scattering from added target nuclei with previously determined resonance widths. This method was already successfully applied for the nuclear resonance fluorescence experiments at ELBE.

[1] H. Arenhövel & M. Sanzone, Few Body Systems, Suppl. 3 (1991)

[2] R. H. Cyburt, Phys. Rev. D 70 (2004) 023505

[3] K. M. Nollet & S. Burtes, Phys. Rev. D 61 (2000) 123505

[4] WMAP Coll., Astroph. I., Suppl. Ser. 148 (2003) 1 & 175

[5] A. DeGraeve et. al., Nucl. Phys. A 530 (1991) 420 and Phys. Rev. C 45 (1992) 860

[6] H. A. Bethe & G. E. Brown et. al., Nucl. Phys. A 324 (1979)

[7] I.E. Marcucci, Nucl. Phys. A, in press

[8] G. Rupak, Nucl. Phys. A 678 (2000) 405

[1] *also Technische Universität Dresden*

Coincidence Summing Corrections and Peak Fit Functions for γ- Spectra

C. Nair, A.R. Junghans, A. Wagner, M. Erhard, E. Grosse[1]

Coincidence summing is a process in which the emission of γ-rays in cascade from the decay of a single radionuclide occurs within the resolving time of the detector and ends up being recorded together as a single event. This causes counts to be lost from the full-energy peaks and calls for a correction of the peak areas. The magnitude of the corrections depends on the sample-to-detector geometry and the decay scheme of the nuclides.

For a complex decay scheme when more than two photons are emitted in cascade, like the ones with ^{133}Ba, the effect of absorbers becomes significant. With the insertion of Cadmium absorbers between the source and the detector which effectively blocks the X-rays summing with the γ-rays, considerable modification in the spectra is observed (see Fig. 1). In our measurements the sample is put directly on top of high purity germanium (HPGe) capsule to maximise the absolute efficiency of the detector.

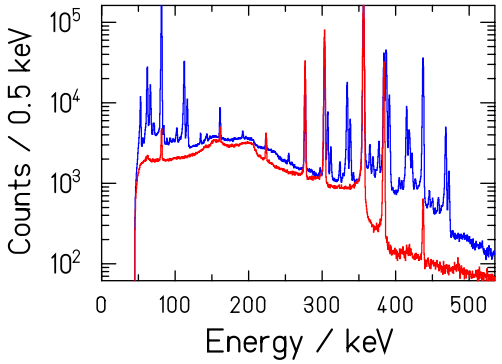

Fig. 1 *HPGe spectrum of ^{133}Ba - upper spectrum is without absorber and lower one is with a 2.1 mm thick Cd absorber.*

While analysing γ-ray lines from the spectra, precision is generally limited by the ability to define and compute consistent peak areas [1]. Simple methods with Gaussian functions are adequate for single, well-resolved peaks. But for a complex peak shape with considerable spectral background and low-energy tailing, an adapted fit routine is necessary.

The extraction of relevant peak parameters from the measured spectrum is done with a fit routine similar to the one in Radware package, see [2] also. Components in their functional form reads

1) a Gaussian

$$y_g = \frac{h \cdot R}{100} \exp\left(-\frac{(x-x_0)^2}{2\sigma^2}\right)$$

2) a skewed Gaussian,

$$y_s = h \cdot \left(1 - \frac{R}{100}\right) \exp\left(\frac{x-x_0}{\beta}\right) \operatorname{erfc}\left(\frac{x-x_0}{\sqrt{2}\sigma} + \frac{\sigma}{\sqrt{2}\beta}\right)$$

3) and a smoothed step function to increase the background on the low-energy side of the peak.

$$y_b = \frac{h \cdot S}{100} \operatorname{erfc}\left(\frac{x-x_0}{\sqrt{2}\sigma}\right) + A + B(x-x_0)$$

[1] *also Technische Universität Dresden*

Components (2) or (3) can easily be set to zero if not required.

The Gaussian is the main component of the peak which arises from the complete charge collection of an event inside the detector. The skewed Gaussian represents incomplete charge collection due to impurities inside the detector material resulting in an exponential tail on the low-energy side with β as the decay constant. The different constant background below and above the full efficiency peak stems from multiple interactions (multi-compton scattering, cf.) of one γ-ray inside the crystal where the full energy is not deposited. Fig. 2 illustrates how the components go together to make up the total peak shape.

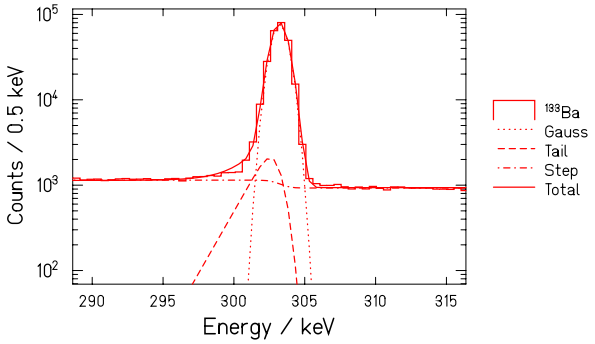

Fig. 2 *Peak fit for one of the strongest decay lines of ^{133}Ba - Fit parameters chosen for display are $R = 97.3$, $\beta = 3$ chs and with a step $S = 0.24$.*

To study the effect of crystal geometry on the distance dependence of absolute efficiency we simulated the detector setup using GEANT3 [3]. From the simulations we see that we can account for this geometrical effect reasonably well.

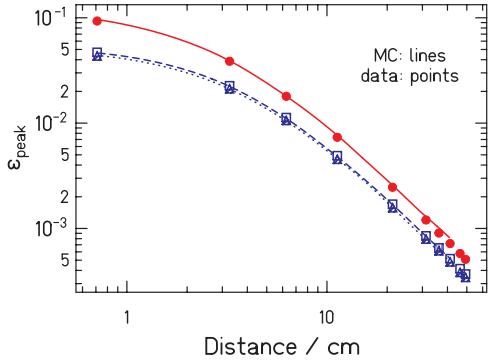

Fig. 3 *GEANT simulations showing the effect of crystal geometry on photopeak efficiencies - upper line is for ^{137}Cs and lower ones are for ^{60}Co.*

[1] T. Kishikawa, C. Yonezawa et al., Nucl. Instrum. Meth. A 369 (1996) 689

[2] K. Debertin, R.G. Helmer, γ and X-ray Spectrometry with Semiconductor Detectors, Elsevier Science Publ. (2001)

[3] CERN program Library Long Writeup Q121, CERN, Geneva (CH), 1994

Development of the Neutron Time-of-Flight Source at ELBE

E. Altstadt[2], C. Beckert[2], R. Beyer, H. Freiesleben[1], V. Galindo[2], M. Greschner[1], E. Grosse [also 1], A.R. Junghans, J. Klug, B. Naumann[3], S. Schneider[4], K. Seidel[1], A. Wagner, F.-P. Weiss[2]

The ELBE electron beam of up to 40 MeV can be used to produce intense neutron beams in a liquid lead radiator. The short beam pulses (5 ps) provide the basis for an excellent time resolution of neutron time of flight experiments. Due to the very short neutron pulses, an energy resolution of about 1 % can be reached after a ToF distance of only 3.6 m. The usable energies range from 200 keV up to 10 MeV with an electron beam repetition rate of 1.6 MHz. This is an interesting energy interval to measure neutron cross sections needed e.g. in the context of minor actinide transmutation. Lower neutron energies from 30-100 keV are accessible with a reduced intensity for possible nuclear astrophysics experiments. The long-term needs for nuclear data have been formulated e.g. in Ref. [1].

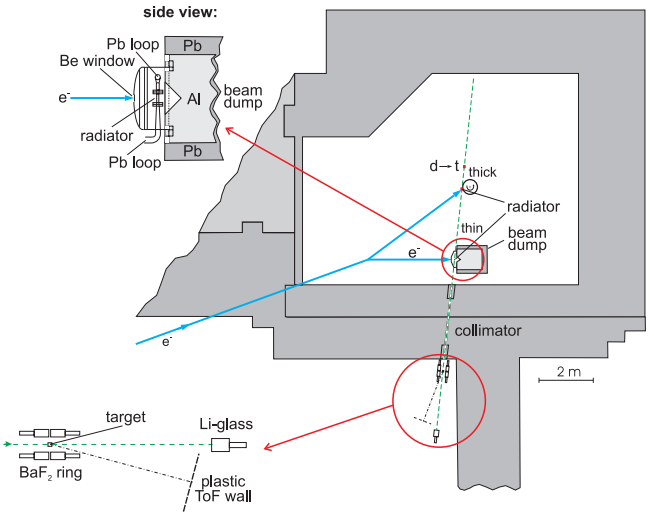

Fig. 1 *Floorplan of the ELBE-nToF setup in the neutron cave. Insets show a side view of the neutron radiator and the planned experimental site.*

Fig. 1 shows the floorplan of the ELBE nToF facility. The set up essentially consists of a liquid lead radiator confined by a molybdenum channel inside a vacuum chamber, the beam dump absorbing the unused radiation (electrons, photons, neutrons), the collimator, and the ToF detectors. The liquid lead target (through a heat exchanger) and the beam dump need to be cooled by a water circuit. The electron beam hits the radiator, producing bremsstrahlung photons and subsequently neutrons are emitted by (γ, n) reactions. The source strength can be as high as $2.7{\cdot}10^{13}\,\mathrm{s}^{-1}$ for an electron energy of 40 MeV and an average current of 1 mA. After a flight path of only 3.6 m the neutron flux on target is about $1.7{\cdot}10^{6}(\mathrm{cm}^{2}\mathrm{s})^{-1}$ with a beam repetition rate of 1.6 MHz. A comparison of the parameters of operational and planned neutron time of flight facilities can be found in Ref. [2].

The construction of the single components has started as well as the assembly of the main mechanical parts. A spindle lifter was constructed to lift the whole production target 3 m up from its rest position inside a lead shield to the level of the electron beam line. The design of the instrumentation and control system including the interfaces with the ELBE LINAC has been finished. Thermal hydraulic and structural mechanic calculations were necessary to improve the design of the lead/water heat exchanger in order to allow for a faster response to changing heat deposition in the lead target and to exclude freezing or overheating of the lead throughout the circuit. A hot lead test experiment (400-500°C) runs in a dedicated loop to gather long term experience on the behaviour of components and materials which are in permanent contact with the liquid lead.

Monte Carlo calculations were performed with MCNP to optimise the collimator with respect to lowering the background of inelastically scattered neutrons and of photons at the experiment site. It was found that collimator insertions made from borated PE together with Pb to absorb the photon flash coming from the radiator represent the best solution, see Fig. 2. Due to the scattering of photons off the edges of the lead, an additional lead absorber should be used to shield γ sensitive detectors, e.g. the BaF_2 detector array to be used for (n, γ) and $(n, n'\gamma)$ reaction studies.

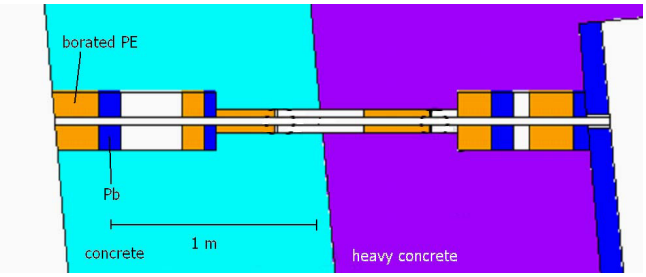

Fig. 2 *Cross section of the optimized collimator. The neutron production radiator is located on the left side.*

The correlation between neutron energy and time of flight is shown in the MCNP spectrum, see Fig. 3. The main ridge in the spectrum is from neutrons with a correct energy to time-of-flight correlation. Neutrons that have lost their undisturbed correlation between energy and time-of-flight form a tail to the main ridge. They are supressed by two to three orders of magnitude, and constitute only 4 % of all events. The low intensity ridge approx. 20 ns above the distribution of unscattered neutrons is due to scattering off the stainless steel windows

[1] *Institut für Kern- und Teilchenphysik, TU Dresden*
[2] *FZ Rossendorf, FWS*
[3] *FZ Rossendorf, FKT*
[4] *FZ Rossendorf, FWF*

of the vacuum housing surrounding the Mo-radiator, and contains only a fraction of $6 \cdot 10^{-4}$ of all neutrons.

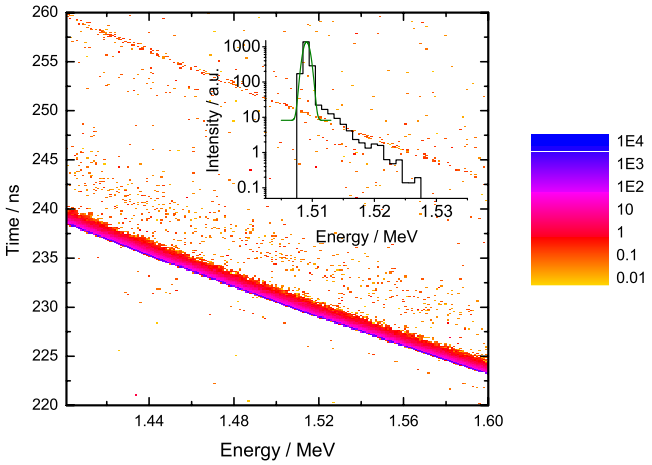

Fig. 3 *Time of flight vs. energy correlation calculated with MCNP 4C2. The plot only shows a part of the neutron spectrum between 1.4 to 1.6 MeV. The calculation was done with a realistic geometry using a nominal flight path of 3.90 m. Note the logarithmic scale of the cluster plot. The inset shows a horizontal cut of the tof-energy correlation at a time-of-flight of 230 ns.*

The energy width (FWHM) of the peak for neutrons with a time of flight of 230 ns is 1.2 keV. This corresponds to an energy resolution of 0.1 % at a neutron energy of 1.51 MeV.

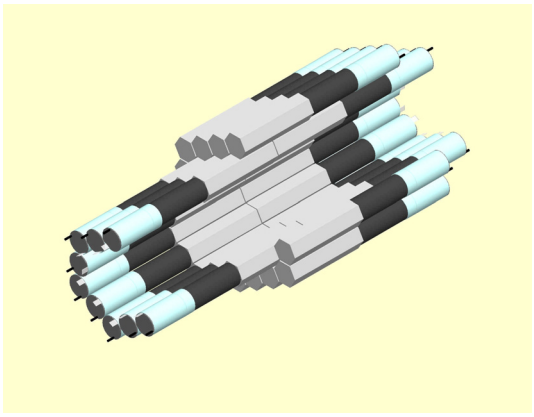

Fig. 4 *BaF_2 scintillation detector array. The target position is in the center of the cylindrical ring of hexagonal BaF_2 crystals.*

For measurements of neutron-induced reactions, different detector types are being developed. For neutron-capture γ rays, a BaF_2 scintillation detector array of up to 60 crystals is being built, see Fig. 4. The crystals have a length of 19 cm and a hexagonal cross section with an inner diameter of 53 mm. They are read out by fast Hamamatsu PMTs R2059, which are UV sensitive to be able to measure both the slow and the shorter wave-length fast component of the BaF_2 scintillation light. This allows to use pulse shape discrimination (PSD) to separate photon signals from intrinsic α-particle background. The time resolution reached with a ^{60}Co γ source is typically 650 ps (FWHM).

The read out will be performed with dedicated ADC/TAC modules [3] that allows simultaneous measurement of timing and energy signals including PSD in VMEbus standard. The system will be controlled by a RIO3 real-time unix computer.

For neutron detection Li-glass scintillators and a plastic scintillator wall is being built. The plastic scintillator wall will allow detection of fast neutrons from approx. 500 keV kinetic energy through proton recoil in the scintillation material. The wall will cover an active area of approx. 1 m^2 consisting of 10 scintillation panels (100 x 12 x 1 cm^3) read out on both ends.

For neutron energies below 500 keV Li-glass scintillators are used. They are enriched with ^{6}Li up to 18 % and allow detection of low-energy neutrons mainly through the reaction ^{6}Li(n,t)^{4}He.

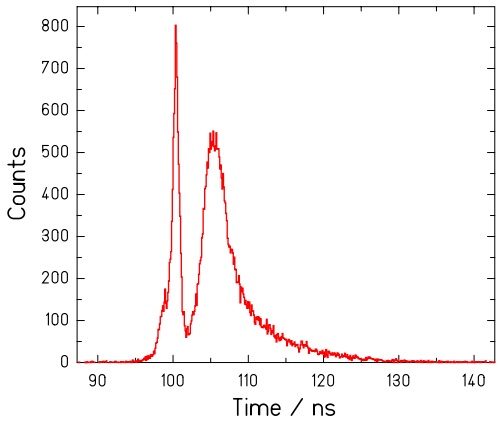

Fig. 5 *Time of flight spectrum of a ^{252}Cf neutron source measured with a plastic scintillator panel of 1 m length at 10 cm distance. The left peak is from photons, while the right peak is due to fission neutrons, with an average energy of 2.35 MeV.*

With a ^{252}Cf neutron source time-of-flight measurements have been made with one prototype panel of a plastic scintillator read out on both ends by PMTs. The fission was triggered by the γ rays detected with a BaF_2 detector close by the ^{252}Cf. With a flight path of approx. 10 cm, fission neutrons can be clearly separated from fission photons, see Fig. 5 The time resolution of the plastic scintillator from the photon peak is approx. 900 ps (FWHM).

[1] Long Term Needs for Nuclear Data Development, comp. M.Herman, INDC(NDS)-428, IAEA Nuclear Data section, Vienna Austria (2001)

[2] A.R. Junghans et al., Wiss.-Techn. Berichte, FZR-401 (2004) 15; E. Altstadt et al., Wiss.-Techn. Berichte FZR-426 (2005)

[3] C.P. Drexler, U. Thöring, et al. IEEE Trans. Nucl. Sci 50 (2003) 969

A DAQ Scheme for BaF_2 Detectors

R. Beyer, M. Erhard, A. R. Junghans, A. Wagner

The detector development for the ELBE nToF project involves a BaF_2-detector array for efficient detection of neutron-capture reactions [1]. BaF_2 is one of the fastest known scintillation materials. It has the special property of having two scintillation-light components with very different decay times ($\tau_{fast} = 0.6\,\mathrm{ns}$, $\tau_{slow} = 0.6\,\mu\mathrm{s}$). The relative intensity of the two components depends on the incoming particle. Thus pulse-shape discrimination (PSD) can be employed to distinguish e.g. photon events from intrinsic detector background due to α decay of ^{226}Ra. We have developed a read-out system that in principle allows PSD measurements for all our BaF_2 detectors [2]. The read-out electronics is sketched in Fig. 1. It is based on multi-channel VMEbus modules manufactured by CAEN. The PMT (THORN EMI 9954QB) signals are integrated by two CAEN V792 QDCs [3], one set to a short gate length (72 ns), the other set to 2.98 μs by a CAEN V486 gate generator [3].

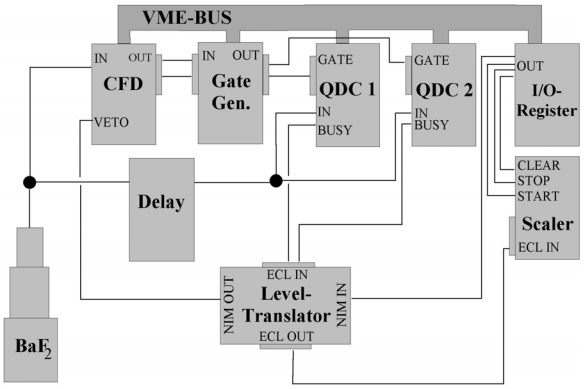

Fig. 3 *Diagram of the read-out electronics set-up for pulse-shape discrimination of a BaF_2 detector.*

The VME crate is controlled by a PC running the graphical programming language LABVIEW via a Wiener PCI-VME bus master [4]. A LABVIEW programm performs the synchronized read out of the two QDCs and produces listmode data as well as a two dimensional histogram of the BaF_2-detector signals. The QDCs are vetoed whenever one of them is not ready to accept data, because of dead time of the QDC or the read-out program.

Fig. 2 shows a background spectrum measured with a BaF_2 detector and the set up described above. The four peaks are from different α-decay energies in the ^{226}Ra-decay chain. Radium is chemically similar to Barium and is an impurity in the crystal. The count rate of α decays in a BaF_2 crystal depends on the detector and is in the range from 10 - 100 s^{-1}. In addition, the γ-emission rate of a BaF_2 crystal was measured with a well shielded HPGe detector and characteristic lines from the ^{226}Ra-decay chain were found.

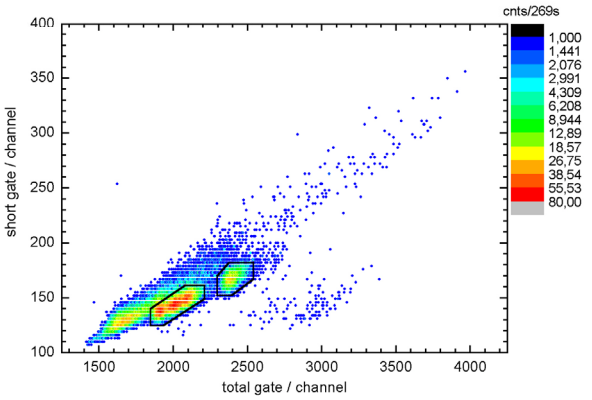

Fig. 2 *Background spectrum of the BaF_2 detector. The area surrounded by the black lines marks events due to α decay from ^{226}Ra impurities. The background from natural γ-emitters has been shielded with a lead housing of 5 cm thickness.*

The PSD is illustrated in Fig. 3, where the detector was not shielded against background in the laboratory. The α-decay events are lying systematically lower than the γ induced signals. The discrimination is not as good as expected. A potential source for this is that the short gate was approx. 70 ns long. A length of only 40 ns would have allowed for a better separation of the fast and slow components. Unfortunately, the gate generators used were not capable of delivering a shorter gate.

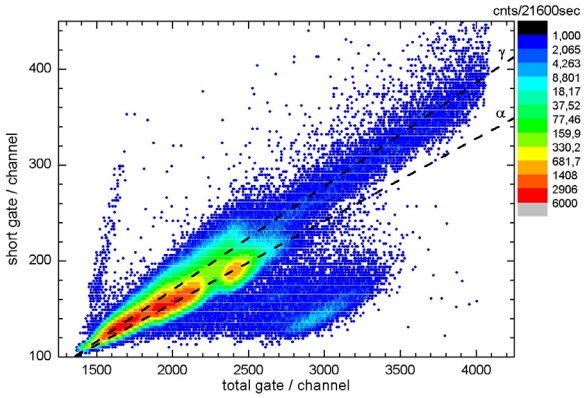

Fig. 3 *Discrimination of intrinsic detector background stemming from α decay of ^{226}Ra impurities. Here, the detector has not been shielded with a lead housing. The lines mark the regions where events due to α decays in the crystal and γ ray signals are located.*

The read-out system developed allows to test fast scintillators comfortably in the laboratory in general, and also has demonstrated the ability of PSD in BaF_2 at low energies.

[1] A. R. Junghans et al., this report, p. 19
[2] R. Beyer, Supplement Lab report, Institut für Kern- und Hadronenphysik, 2004, unpublished
[3] CAEN S.p.A., http://www.caen.it
[4] Wiener, Plein & Baus GmbH, http://www.wiener-d.com

Time- and Energy-Resolution of BaF_2 detectors

J. Brabandt, R. Beyer, A.R. Junghans, A. Wagner

For efficient detection of neutron-capture reactions in the framework of the ELBE nToF project a BaF_2 detector array is being developed [1]. The BaF_2 crystals have a length of 19 cm and a hexagonal cross section with an inner diameter of 53 mm. To optimize the time resolution new Photomultipliers (Hamamatsu R2059) with an active high voltage base [2] have been connected to the existing BaF_2 crystals and compared with the PMTs used before (THORN EMI 9954 QB). The active bases allow to control the high voltage bias (up to 3 kV) of the PMT remotely with a PC through a CAN bus connection. As the high voltage is produced directly in the active base, no high voltage cables are required. The heat dissipation of the base is reduced significantly compared to a regular stabilized base. A sub-ns time resolution in the measurement of the capture γ rays is required to achieve a an energy resolution better than 1% for neutrons of 1 MeV kinetic energy and a flight path of approx. 4 m.
Fig. 1 shows the signal shape of a BaF_2 detector signal from a detector with the new PMT/base assembly. One can clearly recognize the fast and slow scintillation light components. The fall time of the signal is 1.8 ns.

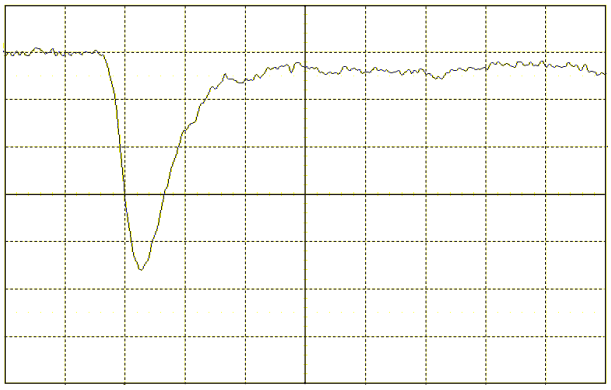

Fig. 1 *Measured pulse shape of a BaF_2 detector with PMT Hamamatsu R2059 and ISEG base PHQ2059. The gain was set to 200 mV/div. The timebase is 5 ns/div.*

Energy spectra of a ^{60}Co source where taken using a peak sensing ADC and a spectroscopic amplifier with a shaping time of 0.5 μs. The energy resolution is typically $\Delta E/E \simeq 12\,\%$. The peak-valley ratio defined as the ratio of the peak height of the 1332 keV γ-line to the valley between the 1173 keV and 1332 keV line is shown in Fig. 2. This quantity is a measure for the energy resolution of the different detector modules. A value of 1 corresponds to the case where there is no visible valley and both gamma lines merge into a single peak. The new PMTs are not expected to cause a large improvement of the detector energy resolution.
The time-resolution was measured in comparison with a reference detector module. The two γ rays from ^{60}Co are emitted in coincidence within the precision of these measurements. The source was placed in close geometry between two BaF_2 detectors. The TAC dispersion was 2.55 ps/channel. The choice of the constant fraction discriminators (CFDs) is crucial to obtain the optimum time resolution. We used Phillips Scientific Model 6915 CFDs. The CFD developed in-house [3] delivered equally good results. We plan to use it for the full setup.

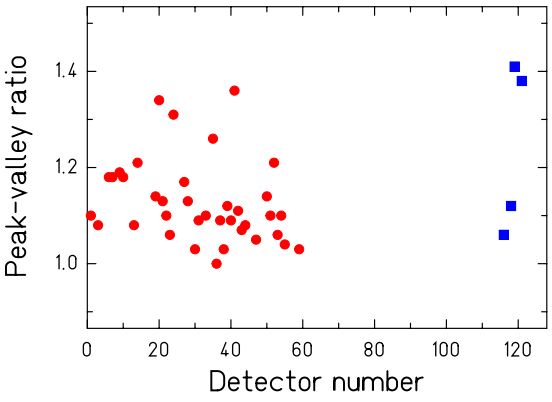

Fig. 2 *Peak-Valley ratio of BaF_2 detector modules for a ^{60}Co source. The circles show detectors with THORN EMI PMTs, while the squares show detectors with Hamamatsu PMTs.*

Fig. 3 shows the time resolution for each one detector module. The average time resolution (FWHM) for detectors read out by the EMI PMTs is 830 $\pm$ 10 ps. With the new Hamamatsu PMTs we obtain a time resolution of approx. 640 ps.

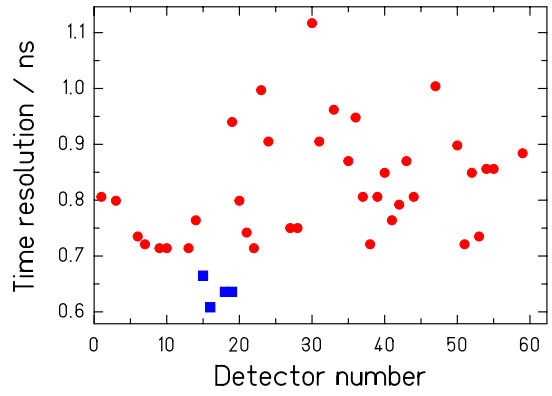

Fig. 3 *Time resolution (FWHM) measured with a ^{60}Co source with respect to a reference detector. The circles show data from detectors with EMI PMTs, while the squares show data from detectors with Hamamatsu PMTs.*

The time resolution was tested in high-count rate background (up to 160 kHz singles rate) of an additional ^{137}Cs source set up close to the BaF_2 detectors and increased only by 5 %.

[1] A.R. Junghans et al., this report, p. 19
[2] ISEG Spezialelektronik GmbH, Dresden, active base PHQ2059
[3] K. Heidel, Institut für Kern- und Hadronenphysik, Constant Fraction Discriminator

A Beam Position Monitor for Bremsstrahlung Photons at ELBE

M. Döring[1], R. Matjeschk[2], A. Hartmann, K.D. Schilling, W. Schulze, A. Wagner

In order to monitor the position and intensity of the photon beam at the bremsstahlung facility at ELBE we constructed and tested a segmented scintillation detector. The detector should determine both misalignements of the photon beam inside the experimental area as well as intensity asymmetries caused by a non-centered electron beam spot at the bremsstrahlung radiator where photons are produced. The mechanical setup consists of four identical plastic scintillators, lightguides, and photomultiplier tubes. The four plastic scintillators of size $35 \times 35 \times 4\,\mathrm{mm}^3$ made of NE104 [1] are arranged symmetrically around the center of the photon beam. Scintillation light of each scintillator is registered by an individual $3/4''$ photomultiplier tube of type R3478 [2]. The mechanical setup of the detector is shown in Fig. 1.

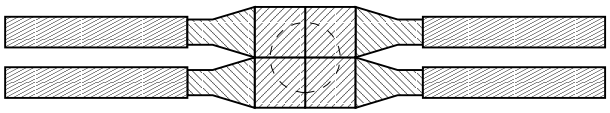

Fig. 1 *Mechanical setup of the photon beam monitor. Each scintillator bar is read out by a separate photomultiplier tube via an attached lightguide. The projected photon beam distribution is indicated by a circle.*

In order to calibrate the light output we irradiated each detector with a ^{60}Co γ-source and determined the location of the Compton-scattering edge. Varying the high voltage bias setting for each detector individually we adjusted all four detectors to give the same energy signal. Results are shown in the following table.

Detector No.	Serial No.	$U_{Compton}$	U_{Rate}
1	KA 1651	-1535 V	-1614 V
2	KA 1753	-1525 V	-1570 V
3	KA 1692	-1580 V	-1600 V
4	KA 1751	-1800 V	-1725 V

Table 1 *High voltage bias settings $U_{Compton}$ for each tube resulting at the same signal amplitude for the Compton-edge using a ^{137}Cs-source. U_{Rate} is the value for equal count rates obtained for a discriminator threshold setting of -52 mV.*

With the aim of increasing the flux of ionizing particles inside the scintillator we wrapped them with several layers of thin aluminium foil working as converters of photons into electrons by Compton scattering. We found that for thicknesses between 0 and 500 μm there was no increase in count rate using a rather low-energy photon source of 667 keV (^{137}Cs). Moreover, the aluminium foil proved to be an absorber decreasing the detection efficiency by up to 20 %.

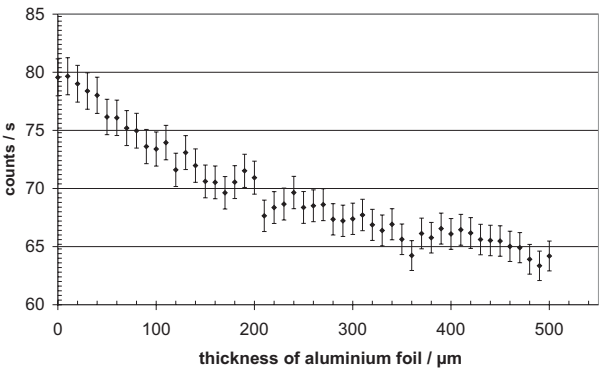

Fig. 2 *Count rate variation of the scintillating detector for different thicknesses of aluminium foil wrapped around.*

The position sensitivity has been determined by scanning the detector surface with a collimated photon beam. We used two linear stepper motor drives and we scanned across the detection area determining the count rate for each scintillation detector individually. The expected count rate variation has been calculated by folding the source's circular aperture of 10 mm diameter with the rectangular shape of the scintillator bar. The results are shown in Fig. 3 for a scan in one direction. The overall agreement between the measured and expected count rates is quite convincing. It enables us to use the device as a position-sensitive photon detector at the bremsstrahlung facility at ELBE.

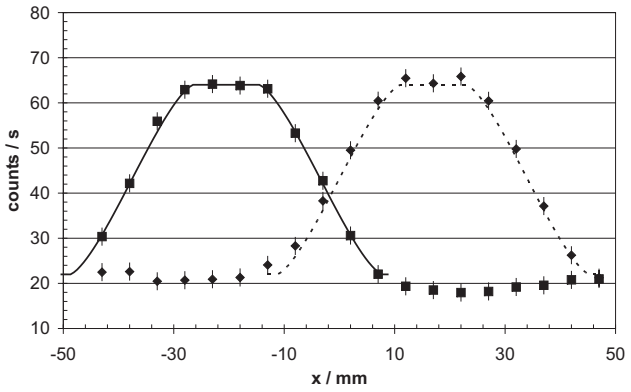

Fig. 3 *Count rate variations for scans over the detection area of two of the scintillators (filled squares and diamonds) using a collimated photon source. Lines indicate the expected distribution by folding the circular aperture with the geometrical size of the detector.*

The detector is now installed inside the photon beam dump of the bremsstrahlung facility at ELBE.

[1] Saint-Gobain Crystals & Detectors, Paris, France
[2] Hamamatsu Photonics, Hamamatsu City, 430-8587, Japan

[1] *Technische Universität Chemnitz*
[2] *Technische Universität Dresden*

Position Resolution of a TOF Spectrometer for Photo-Fission Fragments and Beams of Exotic Nuclei

K. Kosev, N. Nankov, A. Wagner, E. Grosse[1], A. Hartmann, A.R. Junghans, K.D. Schilling, M. Sobiella

A double time-of-flight spectrometer is being developed in order to detect fission fragments produced by the high-intensity photon beam from bremsstrahlung at ELBE. In this spectrometer, position sensitive detectors play a key role. Extensive experimental investigations and data analysis have been conducted to study the performance of these detectors in combination with an electrostatic mirror. This turns out to be an important issue for the TOF spectrometer [1].

A detector setup with an electrostatic acceleration grid and electrostatic mirror has been built as shown in Fig. 1. An alpha source was used to test the position resolution of the setup. Only those particles which passed through the holes of a mask in front of the detector could drive electrons out from a metallized 5 μm thin polyethylene foil. The foil thickness was selected to meet the requirements of low background generation and reduced small angle scattering. The electrons were then accelerated by an electrostatic field of 10 kV/cm and afterwards deflected by 90 degrees by an electrostatic mirror before hitting a stack of micro-channel plate detectors (MCP) with a 2D position sensitive delay line anode. The signal arrival time difference at both ends of each pair of delay-lines enabled us to derive the position of each dimension independently. The alpha particles were detected in a Si-detector in coincidence with the signals from the MCP stack. The detector setup was operated inside a vacuum chamber at a pressure of about 4×10^{-7} mbar.

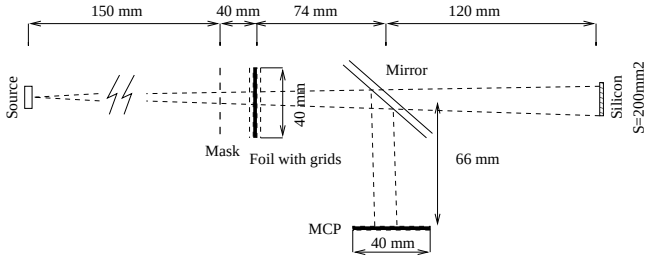

Fig. 1 *Experimental setup of the test setup.*

A dedicated electronics setup was implemented for these measurements. To process the signals from the MCP, we used the DLA-TR6 block from the company "RoentDek", which combined up to six differential amplifiers and CFD connected to their outputs [2]. The time sequence of the signals was measured by a CAEN V775 TDC VME module and recorded by MBS DAQ [3]. For time reference both MCP back and front signals were taken. As one could expect, the projected mask image onto the the 2D anode was dependent upon the solid angle determined by the detector-source distance as well as by the detector surface (see Fig. 2).

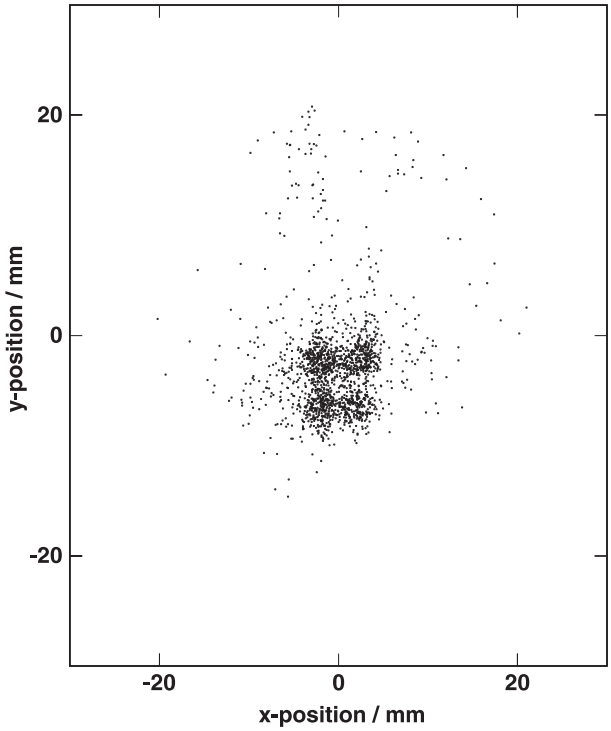

Fig. 2 *The 2D image shows projection of two adjacent apertures with diameters of 2 mm and separated by 4 mm onto the delay-line anode.* Fig. 3 demonstrates that the position resolution of such a device is limited by the spread of the emitted electron's velocity vectors to several mm. Work is in progress to improve the position resolution by means of electrostatic lenses.

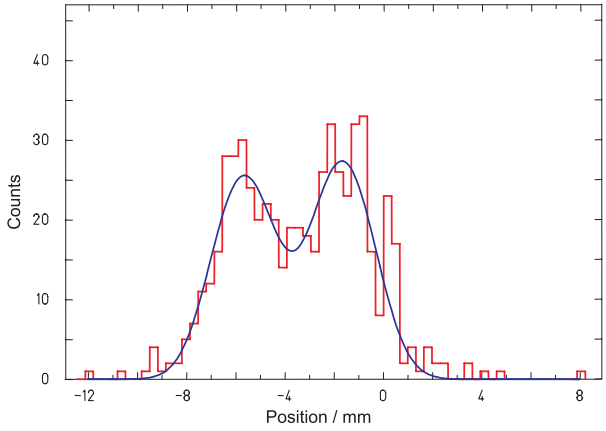

Fig. 3 *Projection of events onto the y axis showing that the position resolution determined from a fit with Gaussian convoluted with a box is approximately 2 ± 0.3 mm (FWHM).*

[1] H. Sharma, A. Wagner, E. Grosse, Wiss.-Techn. Berichte FZR-372 (2003) 36
[2] RoentDek GmbH:http://www.roentek.com
[3] MBS DAQ:http://www-w2k.gsi.de/daq

[1] *also Technische Universität Dresden*

Calculations for the Optimization of the Time and Space Resolution of an Electrostatic Mirror [G]

N. Nankov[1], K. Kosev, A. Wagner, K.D. Schilling, A. Hartmann, A.R. Junghans, M. Sobiella

For the experimental studies of exotic neutron-rich nuclei, produced via bremsstrahlung induced photofission, two-dimensional, a position-sensitive time-of-flight (TOF) spectrometer is under development [1]. The essential part in this device is an electrostatic mirror. Its primary purpose is to deflect the accelerated secondary electrons (SE), knocked out from a thin foil by the heavy fission fragments, towards the micro-channel-plate (MCP) detector (see Fig. 1). In order to achieve higher time and space resolution for a given geometry, careful calculations of the mirror potentials are required. In first order of approximation one can consider the electrostatic field inside the mirror as homogeneous. In this case exact calculations of the TOF of the SE are possible. In order to perform the calculations, the whole system, consisting of the foil, the mirror and the MCP detector is subdivided into three regions (see Fig. 1). The first one extends from the foil to the mirror front side. One assumes it is field free. The second one is between the mirror surfaces, where we assume a homogeneous electric field. The third region is between the mirror front side and the MCP. It is assumed to be field free too. Three particles, starting from the same point and in the same direction but with different energies are traced inside the system. The exact solution of the equations of motion in these three regions gives the following result for the TOF of the probe particles:

$$T = T_0 + \left(\mp \frac{L_1 + L_2 - d\sqrt{2}\Delta V_f/\Delta V}{v_0} \pm \frac{2 m_e v_0 d \sin\theta}{e\Delta V} \right) \delta, \tag{1}$$

where T_0 is the mean TOF, L_1 and L_2 are the distances between the mirror and the foil and between the mirror and the MCP respectively, d is the mirror height, ΔV_f and ΔV are the foil acceleration potential and the mirror deflection potential, v_0 and δ are the mean velocity of the secondary electrons and its spread, θ is the angle between the flight direction and the mirror plane and m_e is the electron mass (see Fig. 1). In order to make the TOF of the secondary electrons independent of their initial velocity spread, the factor before δ in Eq. (1) must vanish. This leads to the following condition for the isochronous transport of the secondary electrons, assuming that $\theta = 45°$:

$$d/(L_1 + L_2) = 0.236\,(\Delta V/\Delta V_f)\,, \tag{2}$$

where the parameters have the same meaning like in Eq. (1). In our present setup no optimizations are made to fulfill the isochronous condition given by Eq. (2). This could play an important role in experiments with heavy fragments, where the energy spread of the secondary electrons is expected to be very large [2].

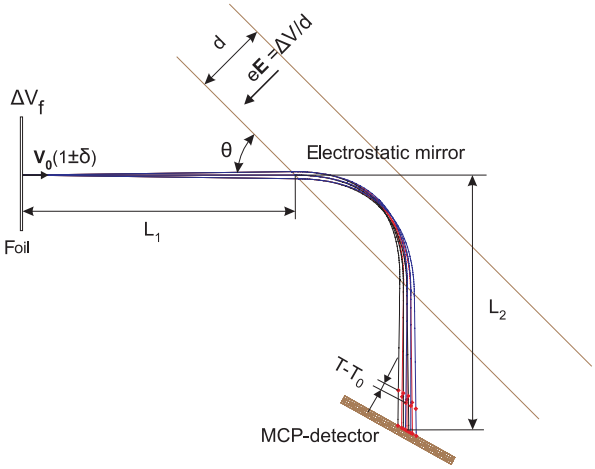

Fig. 1 *Time spread due to the initial energy spread of the SE.*

Preliminary calculations have been done to optimize the space focussing properties of the electrostatic mirror. For this purpose an einzel lens has been simulated in front of the mirror (see Fig. 2). The results show that an improved position resolution could be achieved. However the lens aberrations are still large, so further optimizations are required before experimental tests can be made.

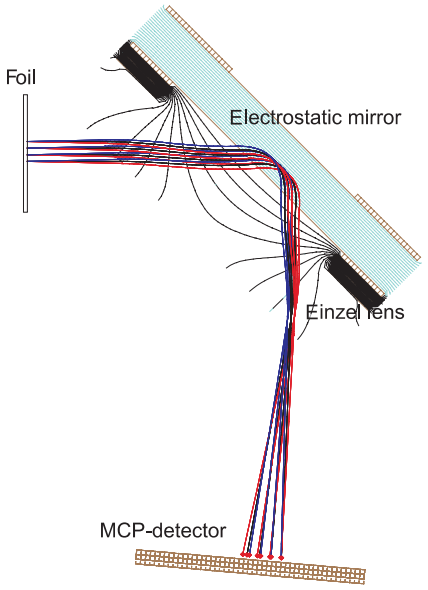

Fig. 2 *Simulated electron trajectories, deflected by the electrostatic mirror with an einzel lens in front of it.*

[1] H. Sharma, K. Kosev et al., Wiss.-Techn. Berichte FZR-372 (2002) 38
[2] Š. Šaro, R. Janik et al., Nucl. Instrum. Meth. A 381 (1996) 520

[1] *also INRNE, Sofia, Bulgaria*

Efficiency of the Time-of-Flight Detector for Photo-Fission Fragments [G]

N. Nankov[1], K. Kosev, A. Wagner, K.D. Schilling, A. Hartmann, A.R. Junghans, M. Sobiella

At ELBE the high-intensity photon-beam will be used to induce photo-fission in heavy nuclei like uranium. The neutron-rich fragments will be then identified via precise mass and charge determination, using a high resolution double-arm time-of-flight (TOF) spectrometer (see Ref. [1]).

The method is based on the detection of the secondary electrons, emitted from a 5 μm thin foil, the heavy particles are passing through. The foil is made of polyethylene, coated with aluminum. The secondary electrons (SE) are then accelerated and deflected by an electrostatic mirror (see Ref. [2]) toward the position-sensitive multi-channel-plate detector (MCP) (see Ref. [3]). One of the important characteristics of the TOF-detector is its secondary electrons detection efficiency. For the efficiency measurement we have used α-particles with energies from 4.72 MeV up to 7.88 MeV. The experimental setup consists of the TOF-detector and a silicon detector, working in coincidence with discrimination levels set as low as possible. The efficiency is taken to be the ratio of the electron counts of the MCP-detector over the silicon detector energy peak counts. Efficiency measurements for the forward, as well as for the backward emitted secondary electrons were made. The results are shown in Fig. 1.

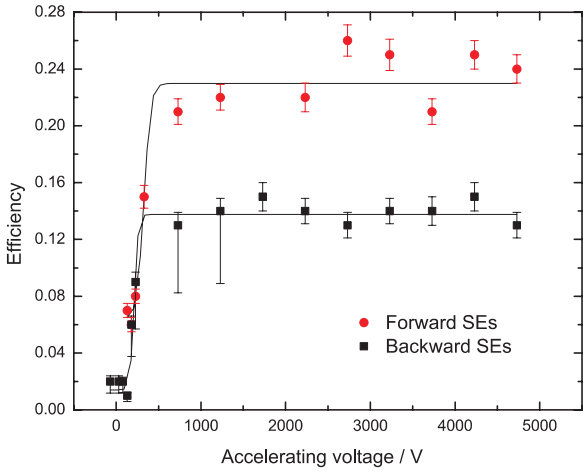

Fig. 1 *Detection efficiency for forward and backward emitted SE as a function of the accelerating potential.*

A stable detection efficiency has been reached at an accelerating potential of about 1 kV, which is in a good agreement with other similar experiments (see Ref. [4]). The ratio between the forward and backward efficiency, taken in the saturation area is 1.92, which agrees well with the results, presented in Ref. [5]. The larger error bars in the efficiency curve for the backward emitted electrons result from the fact, that for this measurement the MCP-detector was moved 10 mm closer to the electrostatic mirror, increasing in such a way the solid angle. This has an impact on the efficiency at small accelerating potentials, where the energy and the angular spread of the secondary electrons become obvious (see Fig. 2). The value, obtained for the efficiency is about 3 times smaller, then one, reported in Ref. [4] in similar experimental conditions. This can be explained by the fact, that in that experiment one used a carbon foil, which was also 50 times thinner, then in our case. The detection efficiency of the silicon detector was assumed to be 100 %.

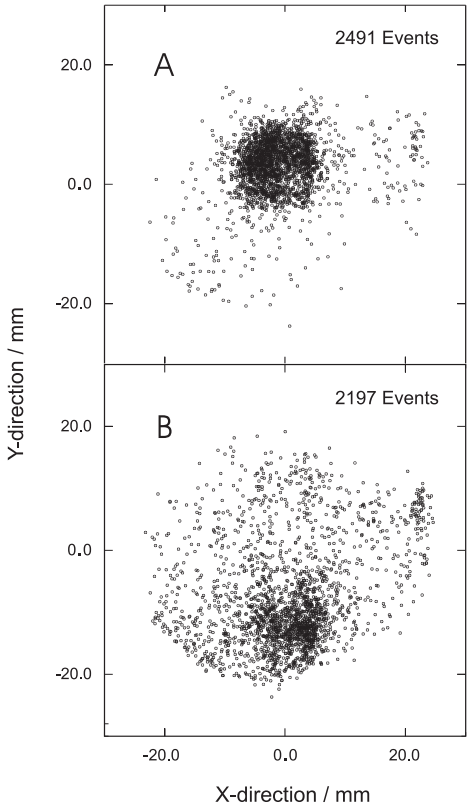

Fig. 2 *Two-dimensional image of the silicon detector, obtained with backward emitted SE, accelerated to 3230 keV (A) and 430 eV (B).*

[1] H. Sharma, A. Wagner, E. Grosse, Wiss.-Techn. Berichte FZR-372 (2002) 36
[2] H. Sharma, K. Kosev et al., Wiss.-Techn. Berichte FZR-372 (2002) 38
[3] RoentDek GmbH: http://www.roentdek.com
[4] G. Dérasmo, V. Paticcio, Nucl. Instrum. Meth. A 234 (1985) 91
[5] K.E. Pferdekämper, H.-G. Clerc, Z. Physik A 280 (1977) 155

[1] *also INRNE, Sofia, Bulgaria*

An Interface for Online Beam Parameters at ELBE

A. Wagner, P. Evtushenko[1], F. Herbrand[2], R. Jainsch[2], K. Leege[2]

Modern experiments at accelerators like ELBE quite often need online control and monitoring of accelerator parameters. For the electronic data acquisition system for nuclear physics experiments we developed a software scheme which enables to include various parameters into the online data stream of the experiment. The system uses a TCP/IP data communication stack on a dedicated Windows-based server machine which can be accessed from different data acquisition front-ends simultaneously. The server machine communicates exclusively with the accelerator control system which is based on a SIMATIC S7 [1]system and an interface on basis of WINCC [2] which prevents the accelerator control from getting locked by hanging processes or communications problems. The server is connected to the accelerator control system via Profibus [3] hardware and OPC [4] SimaticNET software.

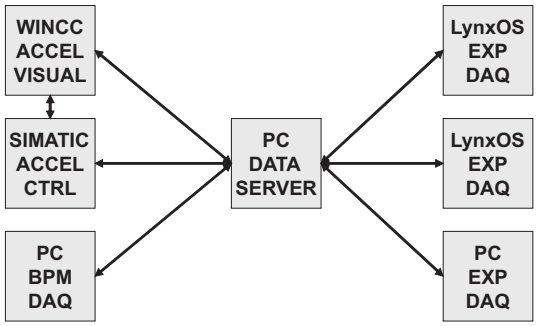

Fig. 1 *Data flow of online accelerator control information, beam position monitor (BPM) data into the data stream of the experiment data acquisition systems (EXP DAQ).*

The communication procedures are implemented in standard C-code using a standardized TCP/IP communication stack. The use of standardized libraries allows for easy integration into different data acquisition front ends. Data are being send by the data server on request from the front end. Each parameter from a predefined list can be accessed independently in either *read only* or *read write* mode. The binary readout data format consists of one 32 bit wide long word (LW) indicating the data quality followed by a LW for the parameter data value and two LW for the time stamp of the last parameter value update.

Right now, the predefined list of parameters is shown in Tab. 1 which can be extended on request by the experimenters.

Data Source	Parameter
AC	acceleration field strengths
AC	injector current
AC	macro-pulse settings
AC	beam position monitor data
AC	NP beam line radiator setting
AC	NP beam shutter setting
AC	NP steerer magnet settings
AC	RP interlock status
AC	RP radiation monitors
NP	online detector count rates

Tab. 1 *Available parameters for front end data acquisition systems (AC stands for accelerator control, NP stands for nuclear physics, RP stands for radiation physics).*

The system has been used in various experiments. The average readout time for about 10 parameters delivered to the nuclear physics data acquisition system [5] is about 15 $\pm$ 2 ms. This system uses the real-time Unix operating system LYNX-OS [6] on several VME-based Power-PC processors [7].

[1] SIMATIC, Process automation systems, Siemens AG, Munich, http://www.automation.siemens.com/simatic

[2] SIMATIC WinCC. Process visualization, Siemens AG, Munich, http://www.automation.siemens.com/wincc

[3] PROFIBUS SIMATIC NET. S7/PC hardware interface, Siemens AG, Munich, http://www.automation.siemens.com/net

[4] Open Connectivity data exchange standard, http://www.opcfoundation.org

[5] H.G. Essel, N. Kurz: The General Purpose Data Acquisition System MBS, IEEE Trans. NS 47,2 (2000) 337 and http://daq.gsi.de

[6] Lynx-OS hard real-time operating system. LynuxWorks Inc., http://www.lynuxworks.com

[7] Creative Electronic Systems, S.A., http://www.ces.ch

[1] *FZ Rossendorf, FWL*
[2] *FZ Rossendorf, FWF*

The Central Depression in the Nuclear Density and its Consequences for the Shell Structure of Superheavy Nuclei

A.A. Afanasjev,[1] S. Frauendorf[2]

Certain self-consistent microscopic calculations find a central depression in the nuclear density distribution, which generates a wine-bottle shaped nucleonic potential. Such potentials give different magic numbers than the phenomenological flat-bottom potentials. We have studied the influence of this depression on the shell structure of spherical superheavy nuclei [1].

As a theoretical tool we used the RMF theory for spherical nuclei without pairing [2]. The calculated density profiles are shown in Fig. 1.

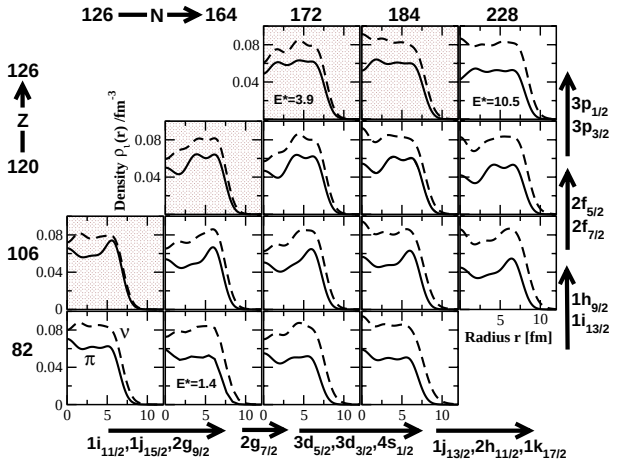

Fig. 1 *The evolution of proton and neutron densities with the changes of proton and neutron numbers. Arrows indicate the group of single-particle subshells which become occupied with the change of the nucleon number. The figure is based on the results of spherical RMF calculations without pairing employing the NL3 parametrization. The shaded background is used for nuclei located beyond the proton-drip line. If the indicated configuration is not lowest in energy, its excitation energy (in MeV) is given by E*.*

The appearance of a central depression is caused by the occupation of high-j orbitals, which are located in the nuclear surface. The occupation of low-j orbitals, which are located in the nuclear center, lifts the central depression.

In order to study the influence of the central depression on the shell closures, we compared ground state configurations that shows a central depression with excited configurations that have a flat-bottom density profile. Fig. 2 shows an example. In the ground state, all subshells below $Z = 120$ and $N = 184$ are fully occupied. In the excited configuration, 12 particles are excited from the subshell $\nu 1j_{15/2}$ into low-j orbitals. The magic numbers for superheavy nuclei are $Z = 120$ and $N = 172$ for the wine-bottle potentials and 126 and 184 for the flat-bottom potentials.

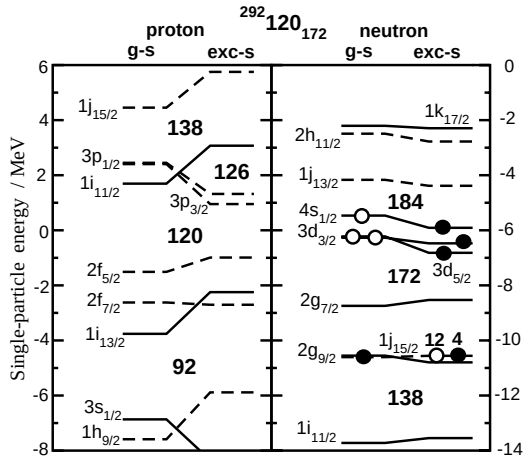

Fig. 2 *Single-particle spectra of the ground state (indicated as 'g-s') and the excited (indicated as 'exc-s') configurations in the $^{292}120_{172}$ system obtained in the RMF calculations with the NL3 interaction. Solid and dashed lines are used for positive and negative parity, respectively. Solid and open circles indicate the occupied and empty orbitals, respectively.*

The self-consistent microscopic calculations found in literature differ in predicting Z and N for the super-heavy elements. The main reason seems the strength of the central depression. Energy density functionals leading to a small effective mass give a strong depression, whereas the functionals leading to an effective mass close to one give a small depression. In the surface region, the ratio m^*/m changes from a low value (< 1) in the interior to one in the exterior. Classically, nucleons with given kinetic energy are more likely to be found in regions with high effective mass than in the regions with low one because they travel with lower speed. The increase of the effective mass in the surface region favors the transfer of mass from the center there, which makes the above discussed polarization mechanism of the high-j orbitals more effective for functionals with low effective mass.
The predicted shell gaps at $Z = 120, 126$ and $N = 172, 184$ seem to be most likely. Their combination depends on the magnitude of the central depression. The RMF theory gives a pronounced double shell closure at $Z = 120, N = 172$. The non-relativistic theories (Gogny [3], Skyrme [4, 5]) give a large shell gap at $N = 184$ and less pronounced gaps at $Z = 120$ and 126, the size of which strongly depends on neutron number.

[1] A.A. Afanasjev, S. Frauendorf, Phys. Rev. C 71 (2005) 024308
[2] P. Ring, Prog. Part. Nucl. Phys. 37 (1996) 193
[3] J.-F. Berger, L. Bitaud et al., Nucl. Phys. A 685 (2001) 1c
[4] K. Rutz, M. Bender et al., Phys. Rev. C 56 (1997) 238
[5] A.T. Kruppa, M. Bender et al., Phys. Rev. C 61 (2000) 034313

[1] *Department of Physics, University of Notre Dame, Notre Dame, Indiana 46556, USA*
[2] *also Department of Physics, University of Notre Dame, Notre Dame, Indiana 46556, USA*

Triaxiality of Neutron-Rich Nuclei around Mass 110

V. Dimitrov[1], S. Frauendorf[2]

The structure of the nuclides with $Z = 42 - 46$ and $A = 105 - 116$ is not yet well explored. Gamma spectroscopy of light fission fragments is a tool for studying these neutron-rich nuclei. Spectroscopy of the fragments from spontaneous fission of ^{252}Cf by means of GAMMASHPERE provides detailed information about the excitation spectra of these nuclei [1, 2, 3, 4]. The investigation of the structure of nuclei in this region by means of γ-induced fission is planned for the ELBE facility. The knowledge of how the nuclear structure develops with increasing neutron number will be useful for a better understanding of the more neutron-rich nuclides encountered in the stellar r-process.

Mean-field calculations consistently predict that these nuclei should be soft with respect to triaxial deformations or even take a stable triaxial shape (gamma-soft or gamma-deformed). There is experimental evidence for the lighter isotopes that they are gamma-soft, as indicated by the observation of the two-phonon gamma band in ^{106}Mo [5]. The heavier isotope even seem to attain a more stable gamma deformation, as e.g. indicated by the observation of a very low-lying second 2^+ state in ^{110}Ru [3].

The appearance of chiral sister bands is a clear evidence of triaxial deformation [6]. The first example in this mass region of such a pair of $\Delta I = 1$ - bands of the same parity and nearly the same energy has been reported for the odd-odd nucleus ^{104}Rh [7]. The chiral configuration consists of a $g_{9/2}$ proton hole and a $h_{11/2}$ neutron particle. We have studied the neighbor ^{105}Rh. One pair of sister bands has the configuration $[\pi g_{9/2}^{-1}, \nu h_{11/2}(g_{7/2}d_{5/2})]$. The band is similar to the chiral pair in ^{104}Rh. The positive parity neutron plays the role of a spectator [8]. The other pair has the structure $[\pi g_{9/2}^{-1}, \nu h_{11/2}^2]$ [9]. We carried out tilted axis cranking (TAC) calculations, which indeed gave chiral solutions for both configurations. The composite chiral configuration $[\pi g_{9/2}^{-1}, \nu h_{11/2}^2]$ seems to be the best example of a chiral doublet found so far. The lower parts of the bands corresond soft chiral vibrations, with a frequency equal to the band separation. At the highest spins the chiral configuration becomes stable and the energy splitting becomes the smallest known. This means the left-right tunneling is weaker than in other cases. There, the moment of inertia (slope of spin vs. rotational frequency ω) increases, as expected for the onset of stable chirality. For the first time evidence for stable chirality also comes from the transition probabilities. The summed strengths of the in-band and cross-band transitions seem to become equal for the states, which belong to the chiral regime according to their energies.

Pairs of $\Delta I = 1$ - bands of the same parity with less than 200 keV separation have been observed in ^{110}Rh [3], ^{106}Mo [2], and ^{100}Zr[4]. The pairs may represent soft chiral vibrations. This is consistent with our TAC calculations and the nearly spin independent energy separation. However, there is an alternative interpretation as pseudo spin doublets. The decay out from the band heads indicates stable or dynamical triaxiality (no K-selection rule, strong decay into the gamma bands).

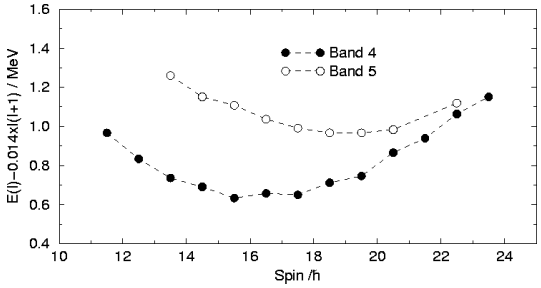

Fig. 1 *Energy splitting of the two chiral sister bands in ^{105}Rh. From [9].*

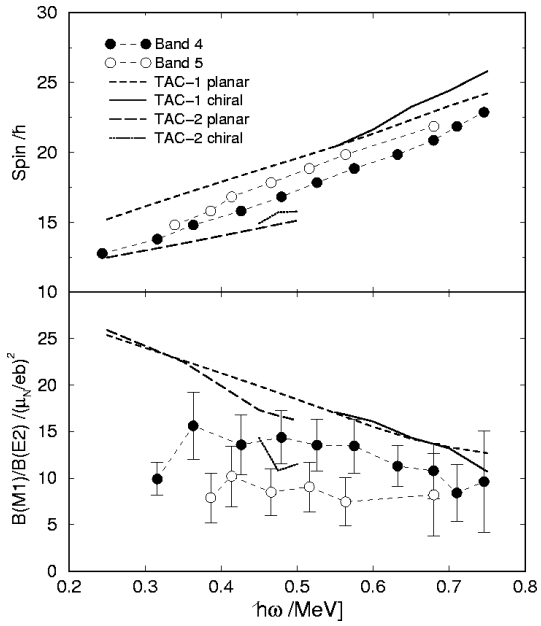

Fig. 2 *Experimental and calculated total spin (top panel) and summed $B(M1; I \to I-1)/B(E2; I \to I-2)$ strengths (bottom panel), for the chiral sister bands. TAC-1 and TAC-2 correspond to calculations without neutron pairing and with neutron pairing, respectively. From [9].*

[1] J.H. Hamilton, S.J. Zhu et al. Nucl. Phys. A 734 (2004) 257
[2] Z.J. Zhu, J.H. Hamilton et al. Phys. Lett. B, submitted
[3] S.J. Zhu, Y.X. Luo et al., to be published
[4] J.K. Hwang, A.V. Ramayya et al., to be published
[5] A. Guessous, N. Schulz et al., Phys. Rev. Lett. 75 (1995) 2280
[6] S. Frauendorf, Rev. Mod. Phys. 73 (2001) 463
[7] C. Vaman et. al., Phys. Rev. Lett. 92 (2004) 032501
[8] J.A. Alcantara-Nunez, J.B.R. Oliviera et al., Phys. Rev. C 69 (2004) 024317
[9] J. Timar, P. Joshi et al., Phys. Lett. B 589 (2004) 178

[1] *IAC, Idaho State University Pocatello, Idaho 83209, USA*
[2] *also Department of Physics, University of Notre Dame, Notre Dame, Indiana 46556, USA*

Quadrupole Moments of High-Spin Isomers in ^{193}Pb

M. Ionescu-Bujor[1], A. Iordachescu[1] D.L. Balabanski[2,3], S. Chmel[4], G. Neyens[2], G. Baldsiefen[4], D. Bazzacco[5], F. Brandolini[5], D. Bucurescu[1], M. Danchev[3], M. De Poli[6], G. Georgiev[7], A. Görgen[4], H. Haas[8], H. Hübel[4], G. Ilie[1,9], N. Marginean[1,6], R. Menegazzo[5], P. Pavan[5], G. Rainovski[3,10], R.V. Ribas[11], C. Rossi Alvarez[5], C.A. Ur[1,5], K. Vyvey[2] and S. Frauendorf[12]

Understanding the structure and the γ-decay of isomeric states is important for the description of stellar burning and explosive scenarios, because trapping in isomers may change the reaction rates considerably. Since many of the relevant nuclei will not be experimentally accessible in near future, one has to rely on mean-field calculations for medium and heavy nuclei. Usually, these give a good description of the energy and spin of the isomers. However, their reliability is much less tested for non-energetic properties, because of the lack of sufficiently accurate data. We measured g-factors and the spectroscopic quadrupole moments Q_s of the $13/2^+$, $21/2^-$, and $33/2^+$ isomers in ^{193}Pb [1] and Q_s of the $29/2^-$ isomer [2] by means of time-differential perturbed γ-ray angular distribution method.

As the mean-field theory we used the pairing plus quadrupole tilted axis cranking (PQTAC) model [6]. Fig. 1 and Tab. 1 demonstrate that PQTAC reproduces the data very well. The different values of Q_s can be explained in terms of pair correlations and a slight quadrupole deformation induced by the excited quasiparticles. The N-dependence of Q_s of the neutron configurations reflects the filling of the $i_{13/2}$ shell. In the middle of the shell ($N \approx 106$) the quadrupole moment of the quasiparticles is zero. It grows with N but remains small in the considered intervall. The Q_s of the $29/2^-$ isomer is much larger because the proton system is unpaired. The non-attenuated quadrupole moments of the proton particles and holes drive the nucleus to a larger deformation. The $29/2^-$ state is the head of a magnetic dipole band. The value of Q_s is the first accurate measurement of the small deformation of magnetic rotors, which was predicted by the PQTAC calculations [6].

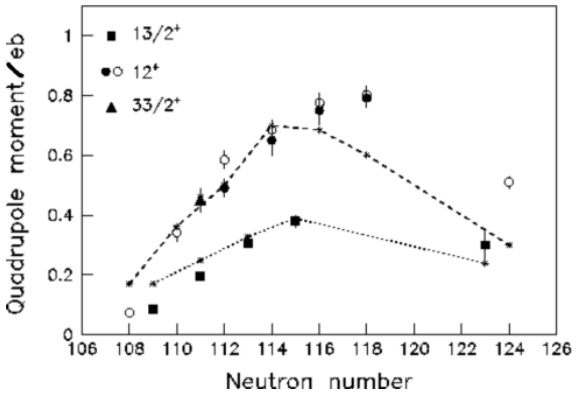

Fig. 1 *Experimental spectroscopic quadrupole moments in light lead nuclei for the $13/2^+$, 12^+ and $33/2^+$ states (from [3] and present work) compared to PQTAC calculations (small star symbol). Dotted and dashed lines connect the values calculated for $13/2^+$ and 12^+ states, respectively. The configurations are $i^n_{13/2}$, $n = 1, 2, 3$, respectively. For the 12^+ states quadrupole moments obtained in static moment measurements (full symbol) and derived from $B(E2)$ (open symbol) are shown.*

[1] M. Ionescu-Bujor, A. Iordachescu et al., Phys. Rev. C 70 (2004) 034305
[2] D.L. Balabanski, M. Ionescu-Bujor et al. Eur. Phys. J. A 20 (2004) 191
[3] *Table of Isotopes*, 8th ed. edited by R.B. Firestone and V.S. Shirley (Wiley, New York, 1996)
[4] S. Chmel, F. Brandolini et al. Phys. Rev. Lett. 79 (1997) 2002
[5] S.B. Dutta, R. Kirchner et al., Z. Phys. A 341 (1991) 39
[6] S. Frauendorf, Rev. Mod. Phys. 73 (2001) 463, Nucl. Phys. A 677 (2000) 115

Tab. 1 *Experimental electromagnetic moments for neutron isomeric states in ^{193}Pb compared with the PQTAC calculations. The data [a] is from [4] and data [b] from [5].*

J^π	Configuration	g_{exp}	$g_{\rm PQTAC}$	$\lvert Q_{exp}\rvert$ (eb)	$Q_{\rm PQTAC}$ (eb)
$13/2^+$	$\nu 1i_{13/2}$	–0.177(1)[b]	–0.172	+0.195(10)[b]	+0.25
$33/2^+$	$\nu(1i_{13/2})^3$	–0.171(9)	–0.174	0.45(4)	+0.46
$21/2^-$	$\nu(1i_{13/2})^2_{12^+} \otimes 3p_{3/2}$	–0.059(11)	–0.108	0.22(2)	+0.26
$29/2^-$	$\nu 1i_{13/2}\pi(1h_{11/2})^2(4s_{1/2})^{-2}$	0.68(3) [a]	0.67	2.84(26)	-2.85

[1] *National Institute for Physics and Nuclear Engineering, Bucharest, Romania*
[2] *IKS, Katholieke Universiteit Leuven, Celestijnenlaan 200 D, B-3001 Leuven, Belgium*
[3] *Faculty of Physics, St. Kliment Ohridski University of Sofia, BG-1164 Sofia, Bulgaria*
[4] *Helmholtz-Institute für Strahlen- und Kernphysik, Universität Bonn, Germany*
[5] *Dipartimento di Fisica dell' Universitá and INFN, Sezione di Padova, Padova, Italy*
[6] *INFN, Laboratori Nazionali di Legnaro, Legnaro, Italy*
[7] *Grand Accélérateur National d'Ions Lourds, F-14076 Caen Cedex 5, France*
[8] *Hahn-Meitner Institut, Bereich Festkörperphysik, D-14109 Berlin, Germany*
[9] *Faculty of Physics, University of Bucharest, Romania*
[10] *Department of Physics, University of Liverpool, Liverpool L69 7ZE, UK*
[11] *Instituto de Fisica, Universidade de Sao Paulo, Sao Paulo, Brasil*
[12] *also Department of Physics, University of Notre Dame, Notre Dame, Indiana 46556, USA*

New Measurements with HADES [B,G]

F. Dohrmann, E. Grosse[1], B. Kämpfer, K. Kanaki, R. Kotte, L. Naumann, A. Sadovsky,
and the HADES collaboration

In 2004 the HADES collaboration concentrated on completing the first experimental proposal S262 focused on dielectron production in nucleus-nucleus and nucleon-nucleon collisions. Two dedicated production runs using carbon and proton beams were successfully conducted. In the runs in August and December 2004, dielectron production was measured in C + C collisions at 1 AGeV. In this measurement, we took data for a system in which a noticeable excess of electron pairs above the pion Dalitz region was found by the DLS collaboration [1]. The analysis of these data will permit a substantial assessment of the results published by the DLS collaboration. The experimental set-up with full coverage in the outer MDC III and four chambers in the MDC IV layers were achieved as compared to the previous 2 AGeV run. Using the same trigger setting as for the previous run $9 \cdot 10^7$ second level trigger (LVL2) events, corresponding to almost $2 \cdot 10^9$ first level trigger (LVL1) events, were accumulated. An online, and hence very preliminary, dielectron analysis was performed in parallel to the data taking using online detector calibration. Fig. 1 shows the invariant mass distributions of unlike-sign, combinatorial background and signal pairs normalized to the number of LVL1 triggers. A statistics equivalent to 5400 signal pairs was obtained from the analysis of 75 % of the collected statistics. It is expected that better detector calibration and analysis of all available data will further improve the pair statistics. Nevertheless, one can already conclude that the data quality is sufficient to arrive at a final conclusions about the enhancement observed by the DLS collaboration, at the BEVELAC [1, 2]. Data analysis is in progress.

First physics results from HADES from previous experiments concern dielectron production in C + C collisions at 2 AGeV. The analysis procedure is described in [3, 4]. All six sectors were fully equipped with ring imaging Cherenkov (RICH), inner tracking chambers (MDC I II) and time-of-flight/PreShower (META) detectors. In two sectors two outer tracking planes (MDC III and MDC IV) were installed; for two additional sectors the third tracking plane was equipped. The first data analysis concentrated on a symmetric six sector configuration not making use of detector information provided by the outer drift chambers. The two sectors with complete tracking system were utilized for tracking studies focusing on the purity and efficiency of track reconstruction. This allowed to better estimate tracking errors of the low-resolution configuration. In the C + C experiments data acquisition is triggered by a LVL1 trigger based on the hit multiplicity in the time-of-flight wall with a condition requiring 4 or more charged particles in the acceptance. In the production run in 2002 the LVL2 trigger was successfully used for the first time. It on-line selects events with at least one electron candidate inside the HADES acceptance by means of conditions on a correlated electron hit in the RICH and META detectors within a coarse azimuthal correlation. With this trigger setting a pair efficiency of 92 % was realized reducing at the same time the accepted event rate by a factor of 12. The LVL2 trigger bias was studied carefully by examination of electron distributions in events taken with and without positive LVL2 trigger. The later events were recorded applying a proper scale down to LVL1 triggered events. Besides overall scaling no significant effect was found [5]. For the analysis a total statistics of $6 \cdot 10^7$ LVL2, corresponding to more than $6 \cdot 10^8$ LVL1 events, was used. In the first stage of the analysis single electron tracks were reconstructed requiring charged tracks matched to a ring in the RICH detector as well as to a hit in the META detectors.

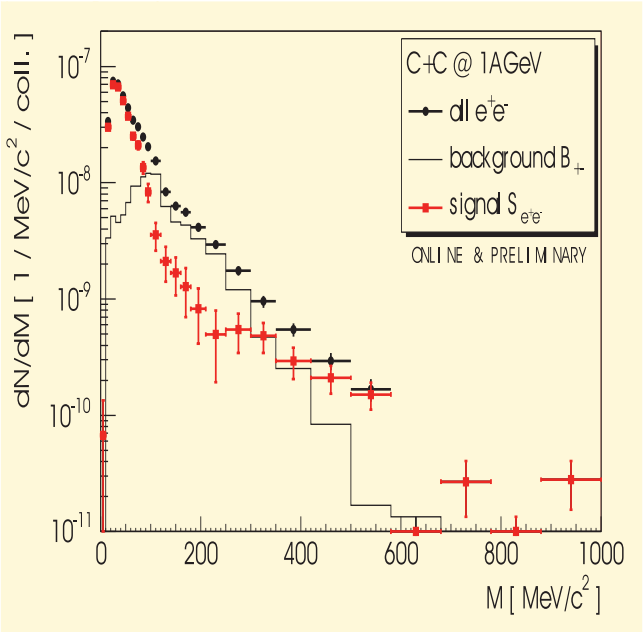

Fig. 1 *Preliminary invariant-mass distributions of unlike-sign pairs (black symbols), combinatorial background (solid histogram) and signal pairs (grey symbols) from C + C collisions at 1 AGeV.*

Fig. 2 shows a comparison of the reconstructed dielectron invariant-mass distribution with simulations. In the simulation we used 10^8 events obtained from the ultra relativistic quantum molecular dynamics (UrQMD) transport model (Version 1.3) which were filtered through the spectrometer using GEANT and digitized applying realistic detector response functions. The data obtained in that way was processed through exactly the same analysis procedure as it was used for the experimental data. Finally, the simulation events were normalized to the number of UrQMD events passing the LVL1 trigger condition used for the real data. We like to point out

[1] *also Technische Universität Dresden*

that the simulated spectra essentially represents contributions from π^0 and η decays. It can be seen that in the low-mass region (dominated by π^0 Dalitz pairs) the simulation overestimates the data but in the higher-mass region the simulation and data agree rather well. The systematic errors of the comparison were studied in details and are shown in Fig. 2 by two shaded bands. The extended shaded area shows the variation of the experimental dielectron signal due to the action of various selection criteria imposed on pair tracks. It was obtained by switching off one cut in the experimental data analysis but keeping the others active. As it can be seen, variations of the signal yield are rather small. However, a systematic difference between the simulation and the experimental data was found in the reaction of the pair yields to the analysis cuts at low invariant masses. Its magnitude (upper shaded area below 250 MeV) was obtained by comparing the relative reduction of the unlike sign and like sign pair yields due to the action of all cuts in the data and the simulation. In a perfect case these reductions should be identical. However, we observe a systematic difference (bias) which leads to smaller reduction of unlike sign and larger reduction for like sign pairs, and as a consequence larger signal yield, in the simulation. The reason for this difference is presently under investigation.

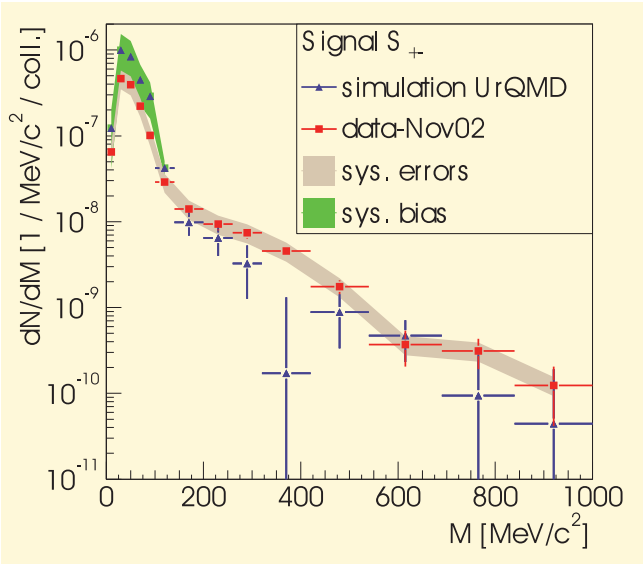

Fig. 2 *Preliminary invariant-mass distributions of signal pairs (squares) after combinatorial background subtraction normalized to the number of LVL1 events from $C + C$ collisions at 2 AGeV. The shaded area displays variations due to pair cuts used in the analysis and systematic bias (see text for more details). Triangles represent a simulated signal based on events from the UrQMD transport code analyzed and normalized as the experimental data.*

The main scientific goal of the $p + p$ run at 2.2 GeV in January 2004 is to exclusively reconstruct η production in both a hadronic channel and a leptonic decay channel using missing mass technique. With this measurement, the efficiency for reconstruction of dielectron decay of the η meson can be determined experimentally. Detailed information on the reconstruction efficiency for electron and positron tracks, an important ingredient in the analysis of dielectron production in heavy ion collisions, can be deduced. The reaction channels with a single meson were selected as a means to verify the dielectron reconstruction efficiency needed for an absolute normalization of the nucleus-nucleus data. A proton beam with an intensity of $2 \cdot 10^7$ protons/s and a 5 cm long liquid hydrogen target were used in this experiment. Typical ratios of trigger rates for the full and empty target of 10/1 were achieved during data taking. We collected around $4 \cdot 10^8$ events with two main LVL1 trigger settings: (1) charged particle multiplicity MUL ≥ 2 in opposite META sectors for pp elastic scattering and (2) MUL ≥ 4 in the META for exclusive meson identification. In the latter case we also used a LVL2 trigger setting as for C + C collisions to enhance events with electron pairs. The prerequisite for the identification of a reaction channel with a single neutral meson is missing mass resolution. In order to achieve it, precise MDC calibration and detector alignment is mandatory. For this purpose several alignment procedures are being pursued. One is based on straight track reconstruction from runs without magnetic field and the second one uses the advantage of the pp elastic scattering kinematics. The mass resolution amounts to $m/\Delta m = 25$ and is still a factor 2 lower than the one expected assuming ideal detector calibration and geometry. Nevertheless, it is already sufficient for a single neutral meson channel identification and therefore processing of all collected data has been started.

In the meantime, the construction of the last two drift chambers of plane MDC IV is continuing in IPN Orsay. Moreover, substantial progress was achieved in the design of the new inner time-of-flight system, which is based on single cell RPC detector elements. This system will replace the preliminary TOFINO detector which does not provide sufficient granularity and time resolution for performing studies with heaviest nuclei.

[1] R.J. Porter et al., Phys. Rev. Lett. 79 (1997) 1229

[2] W.K. Wilson et al., Phys. Rev. C 57 (1998) 1865

[3] P. Tlusty, J. Otwinowski (for the HADES collaboration), Proceedings of XLII International Meeting on Nuclear Physics, Bormio 2004, Vol. 120, p. 171

[4] P. Salabura et al., Nucl. Phys. A 749 (2005) 150c

[5] A. Toaia, PhD thesis, University of Giessen, 2005

Identification of K^+ Mesons with HADES Using Runge-Kutta Tracking [B, G]

A. Sadovsky, R. Kotte, F. Dohrmann, E. Grosse [1], B. Kämpfer, K. Kanaki, L. Naumann
for the HADES collaboration

The investigation of K^+ meson production in heavy-ion collisions has a comparatively long history, with most of the experiments having a small acceptance usually around midrapidity and performed near the threshold [1, 2, 3]. The FOPI experiment [4] covers a wide acceptance and detects both positively and negatively charged particles within one set-up. The HADES spectrometer is also a wide acceptance detector. This makes it convenient to study the $K^\pm$ production as well.

Therefore, the HADES experiment of C + C at 2 AGeV beam energy is expected to obtain in a single measurement the K^+ spectrum within a wide phase space region, comparable to that accessible by the KaoS experiment [3] where measurements at different polar angles are merged. This serves as additional test of the HADES performance.

The analysis of HADES data requires precise alignment of the tracking detectors and high resolution tracking. The identification of rare probes allows to understand analysis problems and improves signal-to-background ratio.

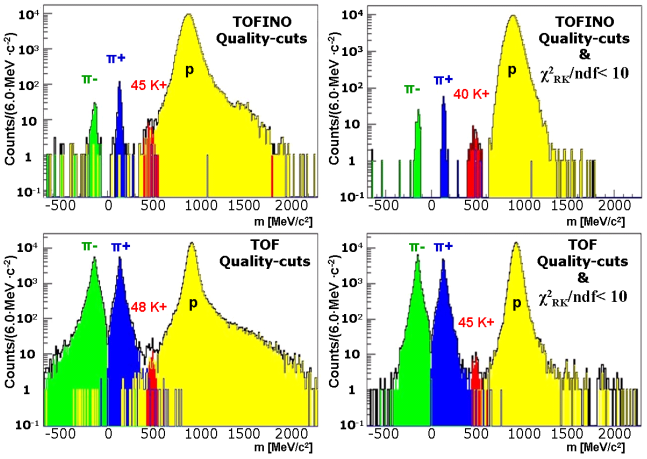

Fig. 1 *Demonstration of background suppression due to a quality cut $\chi^2_{RK}/ndf < 10$ with simulation data of $3.2 \cdot 10^6$ events. Upper panels: mass reconstruction of positively charged particles in TOFINO ($18° < \theta < 44°$) acceptance. Lower panels: the same in TOF ($44° < \theta < 88°$) acceptance. The plots on the left side show the results of K^+ selection cuts i) to vi). The plots on the right side include the additional $\chi^2_{RK}/ndf < 10$ cut.*

Data of the C + C run were analyzed to identify K^+ mesons. A set of tracking methods was tested on sectors fully equipped with four Multiwire Drift Chambers (MDC) enabling for high-momentum resolution (i.e. better than 6 % for protons with momentum larger then 400 MeV/c). We selected the Runge-Kutta tracking/fitting algorithm which provides a specific additional quality parameter, i.e. the track propagation quality χ^2_{RK}. This parameter is used for additional selection of good track candidates. The effect of cutting on this parameter per degree of freedom $\chi^2_{RK}/ndf < 10$, when applied to simulated data is shown in Fig. 1. The K^+ peak becomes clearly visible.

The situation with experimental data was not as good as with simulation, but it is expected to improve after better alignment of the tracking detectors. Using Runge-Kutta tracking with selected π^+ and π^- tracks taken with magnetic field a dedicated one-sector alignment was performed by adjusting 24 parameters defining the geometrical positions of 4 MDCs in one sector. The typical time scale for this kind of alignment is about one man month work. The agreement between data and simulation has improved considerably in this sector.

After applying strong selection cuts, i.e. *i*) tracks coming from the target, *ii*) MDC tracking has a good quality, *iii*) tracks in MDC do match well with hits in time-of-flight detectors (TOF/TOFINO), *iv*) tracks of positively charged particles, *v*) particle energy loss in the plastic rods of TOF/TOFINO in agreement with charge 1, *vi*) cut on particle velocity (slow kaons decay; resolution decreases at high velocities), and *vii*) track reconstruction quality $\chi^2_{RK}/ndf < 10$, we are able to establish a meaningful K^+ identification in experimental data in the TOF region for polar angles $44° < \theta < 88°$ within a velocity range of $0.35 < \beta < 1.0$ and in the TOFINO region for $18° < \theta < 44°$ within $0.4 < \beta < 0.76$.

Among $2.9 \cdot 10^7$ events about 430 K^+ tracks (adding both θ-regions of one of the six MDC sectors) were identified, see Fig. 2. Also, the number of π^+ tracks in the full HADES acceptance $18° < \theta < 88°$ was estimated to be about $4 \cdot 10^5$. When normalizing the K^+ and π^+ yields to 4π it leads to a very preliminary estimate of the K^+/π^+ ratio on the level of 10^{-3} (no corrections for tracking and cut efficiencies were taken into account).

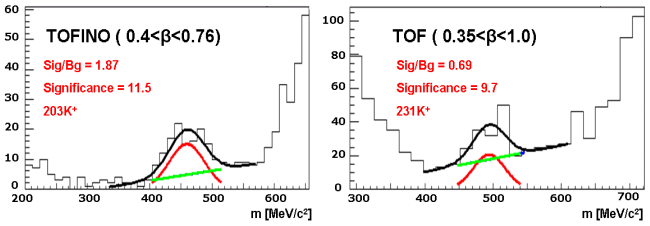

Fig. 2 *Results of experimental data. The mass distribution for reconstructed tracks in TOFINO (left panel) and in TOF (right panel) acceptance. Smooth curves indicate a fit around the K^+ mass region, with the assumption of a Gaussian signal plus linear background.*

[1] S. Schnetzer, M.-C. Lemaire et al., Phys. Rev. Lett. 49 (1982) 989

[2] A.B. Kurepin, V.S. Pantuev, S.N. Filippov, JETP Lett. 47 (1988) 17; V.S. Pantuev, S.N. Filippov, A.B. Kurepin, Nucl. Phys. A 585 (1995) 13c

[3] F. Laue, C. Sturm et al., Phys. Rev. Lett. 82 (1999) 1640; F. Laue, I. Boettcher et al., Eur. Phys. J. A 9 (2000) 397

[4] D. Best and the FOPI Collab., Nucl. Phys. A 625 (1997) 307

[1] *also Technische Universität Dresden*

Search for Strange Baryons with the HADES Spectrometer [B,G]

K. Kanaki, F. Dohrmann, E. Grosse [1], B. Kämpfer, R. Kotte, L. Naumann, A. Sadovsky
for the HADES collaboration

The study of strangeness production in heavy ion collisions provides valuable information about nuclear matter with consequences for the equation of state and in-medium properties of hadrons. Many experiments have provided data covering the range from elementary $p+p$ reactions up to heavy ion collisions and for a wide range of incident beam energies [1-4]. The aim of our current analysis is the study of strange baryons in $C+C$ reactions at incident beam energies of 2 AGeV, as there are no available data for this particular system at the given energy.

Due to its large phase space coverage and high resolution tracking abilities, the HADES spectrometer at the heavy ion synchrotron SIS of GSI/Darmstadt offers the possibility to investigate also hyperons. Our interest is focused on the reconstruction of Λ hyperons. This investigation leads to a possible extension of the HADES physics program towards detecting heavier resonances, such as Σ^+ which is an interesting accompanying channel for Θ^+ excitations in elementary $p+p$ collisions.

Lambda hyperons are neutral and thus cannot be directly identified. They can be reconstructed via their delayed decay $\Lambda \rightarrow p\pi^-$ (64 % branching ratio, $c\tau = 7.89\,\mathrm{cm}$). The competing decay mechanism $\Lambda \rightarrow n\pi^0$ (36 % branching ratio) leads to neutral products. The analysis steps needed for the Λ reconstruction impose track quality criteria for the single particles of the decay, as well as for the reconstructed momentum vector that corresponds to the parent particle. These criteria are determined by detailed GEANT simulations.

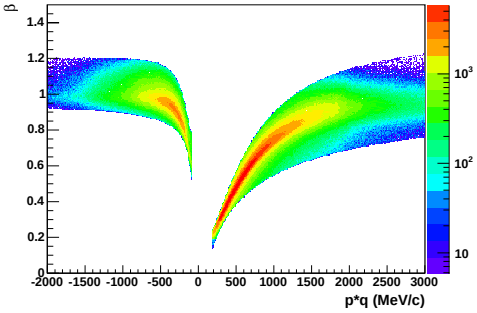

Fig. 1 *Velocity (β) distribution for protons (right) and negative pions (left) as a function of momentum (p) multiplied by particle charge (q). Displayed are the results of an UrQMD simulation of C(2 AGeV) + C reaction after the full GEANT simulation and the filter of HADES analysis software.*

For a given set of data the particle identification for protons and pions is done via graphical cuts from the beta vs. momentum distribution plot (see Fig. 1). The entries of the plot are for two out of the six sectors of the spectrometer, as these were the only ones performing high resolution tracking at the time the experiment was performed. Having these particles at hand it is now possible to reconstruct the invariant mass of the $p\pi^-$ pairs from

$$m_{inv} = \sqrt{(E_p + E_{\pi^-})^2 - (\vec{p}_p + \vec{p}_{\pi^-})^2}. \qquad (1)$$

The obtained distribution is depicted in Fig. 2.

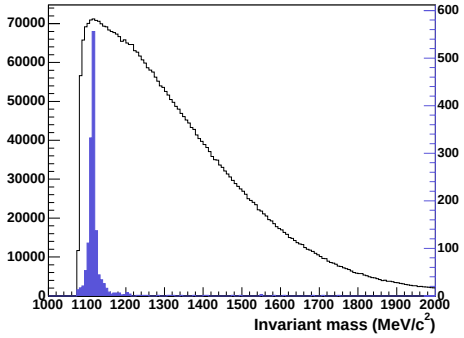

Fig. 2 *Invariant mass distribution of $p\pi^-$ pairs from simulation. The contribution of Λ decays is depicted as a filled histogram with its corresponding axis on the right side.*

In order to reduce the background contribution, cuts on proper quantities are needed, such as the opening angle distribution, the distance between a proton and a π^- track within the same event or the distance between the secondary and the primary vertex. A typical opening angle distribution for the $p\pi^-$ pairs is shown in Fig. 3.

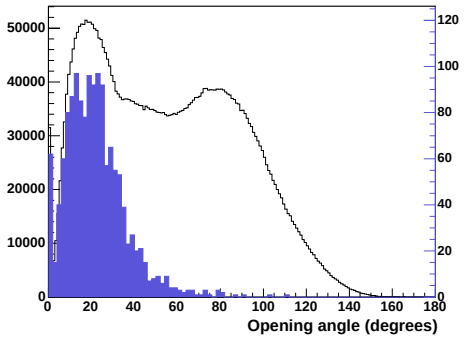

Fig. 3 *Opening angle distribution of $p\pi^-$ pairs from simulation. The meaning of the curves is as in Fig. 2. The left maximum of the distribution comes from p and π^- that hit the same sector and the second one from those which hit the two opposite sectors.*

The geometrical acceptance of this data set leads to a characteristic opening angle distribution of the Λ decay. An upper limit of 40° can throw away pairs that do not come from interesting decays. By applying similar cuts to the experimental data which are under consideration, a successful reconstruction of the Λ hyperons is expected.

[1] P. Kowina, M. Wolke et al., Eur. Phys. J. A 22 (2004) 293
[2] P. Chung, J.M. Alexander et al, J. Phys. G 25 (1999) 255
[3] X. Lopez, Prog. Part. Nucl. Phys. 53 (2004) 149
[4] D.A. Armutlijski et al., JINR-P1-83-354 (1983)

[1] *also Technische Universität Dresden*

Feasibility Study of Exotic Pentaquark Analyses in Elementary pp Collisions for the HADES Spectrometer

R. Kotte and J. Mayer

Recently Diakonov, Petrov and Polyakov predicted the existence of an anti-decuplett of exotic pentaquark baryons [1]. Though there is an impressive number of experiments supporting the first observation [2] of the Θ^+ baryon (with typical significances of about 3 to 5) there are still others who did not find the corresponding signal [3]. (For an overview of both lists of positive and negative results we refer to ref. [3].)

In a recent letter of intent [4] it was proposed to search for the exotic Θ^+ (there called Z^+) baryon with the HADES spectrometer [5] in the reaction

$$p+p \rightarrow \Theta^+ + \Sigma^+ \rightarrow p + K^0_S + \Sigma^+ \rightarrow p + \pi^+ + \pi^- + p + \pi^0 \quad (1)$$

at beam momentum of 3.5 GeV/c. Note that only the charged particles can be measured with HADES. In the present feasibility study we estimate the limiting momentum resolution allowing a successful analysis of such an experiment. Using both stand alone Monte Carlo (MC) programs incorporating the CERN N-body phase-space generator GENBOD [6] and the HADES MC tool Pluto^{++}v.358 [7] we simulated the reaction of interest (1) and the relevant background reactions

$$p + p \rightarrow p + K^0_S + \Sigma^+ \rightarrow p + \pi^+ + \pi^- + p + \pi^0, \quad (2)$$

$$p + p \rightarrow p + \pi^+ + \pi^- + p + \pi^0. \quad (3)$$

The cross section of channel (1) of 0.5 μb has been taken from a recent COSY-TOF paper [8], while for the background channels tabulated data of Landolt-Börnstein [9] have been interpolated. Thus, 650 μb have been deduced for channel (3) while the 25 μb found for $pp \rightarrow pK^0\Sigma^+$ have to be multiplied by the branching ratios of 50 %, 68.9 % and 51.6 % for the decays $K^0 \rightarrow K^0_S$, $K^0_S \rightarrow \pi^+ + \pi^-$ and $\Sigma^+ \rightarrow p\pi^0$, respectively. Channel (3) is suppressed drastically by setting narrow windows 2σ around the K^0_S invariant mass and the Σ^+ missing mass. A similar 2σ cut around the π^0 missing mass reduces the contribution from the reaction with four particles in the exit channel, $p + p \rightarrow p + p + \pi^+ + \pi^-$, which cannot be discriminated experimentally.

Typically, 10^7 events have been generated for each reaction and parameter set. The resonance masses are chosen 1530 MeV/c^2, 1189 MeV/c^2 and 498 MeV/c^2 for the exotic Θ^+ baryon, the Σ^+ hyperon and the K^0_S meson, respectively. Since all intrinsic widths are set to zero, the observed widths reflect the assumed experimental resolutions. While the beam-momentum resolution was kept fixed to 0.5 %, the momentum resolution of the measured charged particles in the exit channel varied from 1 % to 4 %. Finally, the experimental filter demands all four charged particles of the exit channel to be within the HADES polar angle limits $18^o < \theta < 85^o$.

The resulting $p\pi^+\pi^-$ invariant mass distributions are displayed in Fig. 1. Clearly, a peak is visible at the nominal Θ^+ mass position which systematically vanishes behind a broad background when decreasing the momentum resolution. Note that even channel (1) contributes to the background since in an experimental-like analysis it is unknown which of both protons in the exit channel is the Θ^+ daughter. Without applying additional cuts, the Θ^+ yield after background subtraction would be $4.7 \cdot 10^{-5}$ per ($pp\pi^+\pi^-$) event.

Summarizing, the overall momentum resolution of the HADES spectrometer should be better than 3 % in order to allow for reliable studies of the exotic Θ^+ baryon - a value achievable after precise software alignment of the subdetectors.

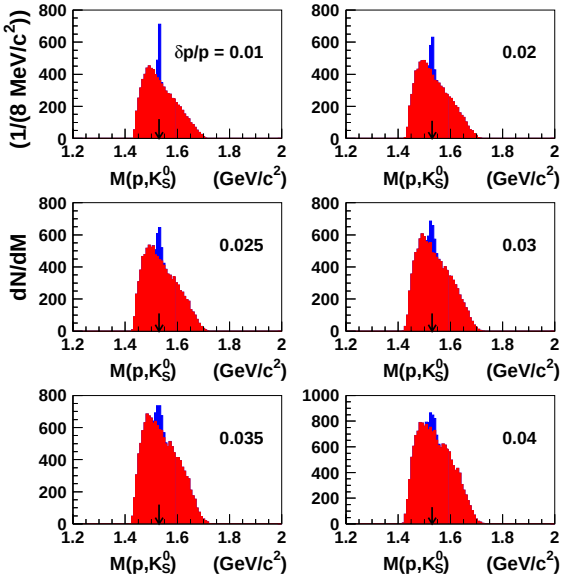

Fig. 1 *The distribution of the $p\pi^+\pi^-$ invariant mass from $pp \rightarrow pp\pi^+\pi^-(\pi^0)$ reactions at 3.5 GeV/c in dependence on the momentum resolution of the charged particles as indicated. The arrows indicate the nominal Θ^+ mass.*

[1] D. Diakonov, V. Petrov and M.V. Polyakov, Z. Phys. A 359 (1997) 305

[2] T. Nakano et al. (LEPS collaboration), Phys. Rev. Lett. 91 (2003) 012002

[3] Yu.M. Antipov et al. (SPHINX collaboration), Eur. Phys. J. A 21 (2004) 455

[4] N.V. Rabin and V.T. Smolyankin, Letter of Intent: The study of exotic pentaquark bayon Z^+ with HADES setup, http://www.gsi.de/documents/DOC-2003-Aug-1-1.ps

[5] J. Friese (for the HADES collaboration), Prog. Part. Nucl. Phys. 42 (1999) 235; http://www-hades.gsi.de/

[6] W515: N-Body Monte-Carlo Event Generator, http://wwwasd.web.cern.ch/wwwasd/cernlib/mc/genbod.html

[7] M. A. Kargalis, Pluto^{++}. A Monte Carlo simulation tool for hadronic physics, GSI Report 2000-03 (2000)

[8] M. Abdel-Bary et al. (COSY-TOF collaboration), Phys. Lett. B 595 (2004) 127

[9] A. Baldini, V. Vlaminio, W.G. Moorhead, D.R.O. Morrison, Landolt-Börnstein. Numerical Data and Functional Relationships in Science and Technology, Vol. 12

Inclusive $K^{\pm}$ Production in Proton-Nucleus Collisions near Threshold [B]

F. Dohrmann, E. Grosse[1], L. Naumann, W. Scheinast, H.W. Barz, B. Kämpfer and the KaoS Collaboration

The $p\mathrm{A} \to K^{\pm}X$ reaction has been measured by the KaoS collaboration [1, 2] to provide a competitive data base which fills the gap of $K^{\pm}$ production between pp and AA collisions. A systematic description of the data has been obtained by using a Jüttner type function

$$E\frac{d^3\sigma}{dp^3} = \sigma^{\mathrm{fit}}\frac{\hat{E}}{4\pi m_K^2 K_2(m_K/T)}\exp\left(-\frac{\hat{E}}{T}\right) \qquad (1)$$

with the parameters σ^{fit}, v, and T; $\hat{E} = (E - vp\cos\Theta)/\sqrt{1-v^2}$ and $E = \sqrt{m_K^2 + p^2}$. Here σ^{fit} is the fittet total cross section, v is the velocity of the kaon emitting source, T is the slope parameter. E, p and θ are the corresponding energy, momentum and azimuthal angle of $K^{\pm}$ in the laboratory system, as discussed in [2]. Eq. (1) provides an estimate of the total cross section by the parameter σ_{fit}. In Fig. 1 we demonstrate the influence of the nuclear medium on the $K^{\pm}$ production by converting the fitted total cross section, σ^{fit}, into multiplicities by $M_K = \sigma^{\mathrm{fit}}/\sigma_R$, σ_R the geometrical cross section, using $R = 0.6\,\mathrm{fm} + 1.2A^{1/3}\,\mathrm{fm}$ (proton radius 0.6 fm), $\sigma_R = 0.35$ b for pC and $\sigma_R = 1.8$ b for pAu. The multiplicities for $K^{\pm}$ in proton-nucleus collisions systematically exceed the proton-proton data, represented by dashed lines. Whereas an enhancement by factors of 1.5 - 4 can be attributed to the difference in the number of participants for pp, pC and pAu collisions, resp., at beam energies close to threshold the pp data steeply drop such that the proton-nucleus data exceeds the pp data by more than an order of magnitude. An even more pronounced effect was found for K^- multiplicities in nucleus-nucleus collisions. Microscopic transport models interpret these effects by including strangeness exchange reactions, i.e. the conversion of a hyperon into a non-strange baryon and a K^- meson in the medium, as well as an attractive optical potential for the K^- mesons [3].

A subset of the data [1] has been analysed within a transport code of BUU type [3]. These calculations reveal the necessity of a weakly repulsive K^+N optical potential ($V_{K^+N} = +25\,\mathrm{MeV}$) and an attractive K^-N optical potential, ($V_{K^-N} = -80\,\mathrm{MeV}$). In addition, the strangeness exchange channel $NY \to K^-NN$ is found to be very important, but not sufficient to explain the data without in medium $K^{\pm}$ optical potentials. In Fig. 2 the ratios of partially integrated cross sections are displayed. Some parts of the systematic errors are expected to cancel out. The figure clearly demonstrates the need for an improved theoretical description of the data.

[1] W. Scheinast et al. (KaoS Collaboration), Prepared for Meson 2002: 7th International Workshop on Meson Production, Properties and Interaction, Cracow, Poland, 24-28 May 2002

[2] W. Scheinast, Dissertation, TU Dresden (2004)

[3] H.W. Barz, L. Naumann, Phys. Rev. C 68 (2003) 041901

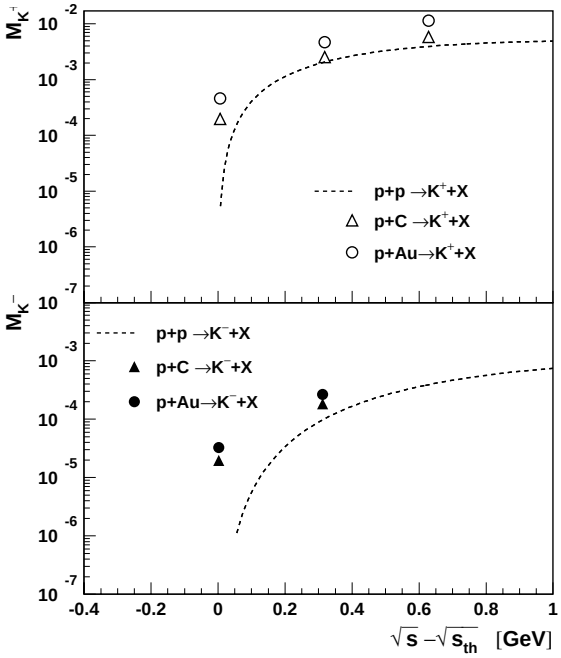

Fig. 1 *Multiplicity of K^+-mesons (upper panel) and K^--mesons (lower panel) for $p + C$ (triangles) and $p + Au$ collisions (stars) as function of the available energy in the NN cm system. The lines correspond to parameterizations of the $p + p$ data.*

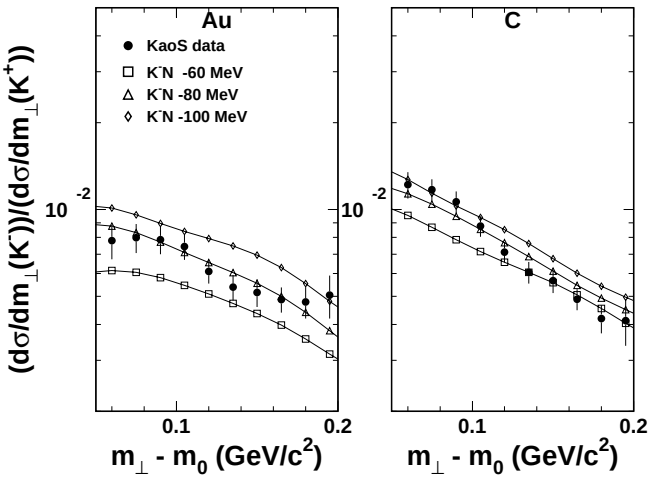

Fig. 2 *Ratio of the invariant production cross sections of K^- mesons for inclusive $p + Au$ (left panel) and $p + C$ collisions (right panel) as function of transverse mass. The data (filled circles) were taken at a beam energy of 2.5 GeV and were integrated over laboratory angles between $\theta = 40^\circ$ and 56°. The open symbols, connected by lines, denote results of BUU transport model calculations including strangeness exchange reaction as well as a K^+N optical potential of +25 MeV and three different depths for the K^-N optical potential as indicated.*

[1] *also Technische Universität Dresden*

Electroproduction of Strangeness on ^{3,4}He

F. Dohrmann for the Jefferson Lab E91016 Collaboration

The electroproduction of strangeness is a complementary approach to experiments on strangeness production induced by pion and kaon beams [1]. Jefferson Lab experiment E91016 measured $^{3,4}\mathrm{He}(e,e'K^+)$, using high intensity continuous wave (CW) electron beams. Hypernuclear bound states have been observed for the first time in kaon electroproduction on ^{3,4}He targets. The production cross sections have been determined at $Q^2 = 0.35$ GeV^2 and $W = 1.91$ GeV (cf. [2] for these kinematical quantities). For either hypernucleus the nuclear form factor is determined by comparing the angular distribution of the $^{3,4}\mathrm{He}(e,e'K^+)^{3,4}_{\Lambda}\mathrm{H}$ processes to the elementary cross section $^1\mathrm{H}(e,e'K^+)\Lambda$ on the free proton, measured during the same experiment.

Three angle settings between the virtual photon γ^* and the ejected kaon were studied, $\theta^{\mathrm{lab}}_{\gamma^*K} \simeq 1.7^{\mathrm{o}}$, $\simeq 6^{\mathrm{o}}$, and $\simeq 12^{\mathrm{o}}$, that correspond to increasing the momentum transfer to the hypernucleus ($\mid t \mid \simeq (0.12,\ 0.14,\ 0.23)$ GeV^2). The central spectrometer momenta were 1.29 GeV/c for the kaon arm and 1.58 GeV/c for the electron arm. Special high density cryogenic targets were used. The background from the aluminum walls of the targets cells was subtracted to obtain charge normalized yields.

The analysis of the data is described in [2]. Fig. 1 shows the resulting cross sections for angular distributions on the reaction $^3\mathrm{He}(e,e'K^+)^3_{\Lambda}\mathrm{H}$, $^4\mathrm{He}(e,e'K^+)^4_{\Lambda}\mathrm{H}$ and for comparison the quasifree production of a Λ hyperon on the proton, $^1\mathrm{H}(e,e'K^+)\Lambda$.

Fig. 2 shows the ratio $R = \sigma_{\mathrm{lab}}(^{3,4}\mathrm{He})/\sigma_{\mathrm{lab}}(^1\mathrm{H})$ of the laboratory cross sections of $^{3,4}\mathrm{He}(e,e'K^+)^{3,4}_{\Lambda}\mathrm{H}$ to the cross section on the free proton. R is related to the nuclear form factor $F(k)$ by $R(k) = S \cdot W_A^2 \cdot F^2(k)$ [3], where k is the three momentum transfer to the hypernucleus, S is a spin factor and W_A combines phase space and flux factors. We calculate $R(k)$ for our kinematics. For ^{3}He the parametrization given in [3] is used, for $^4_{\Lambda}$H an expression of $F(k)$ similar to the $^3_{\Lambda}$H case is derived [4] More details may be found in [2]. At 1.7$^{\mathrm{o}}$ the calculated reduction of the elementary cross section by the form factor is ~ 250 ($^3_{\Lambda}$H) and 100 ($^4_{\Lambda}$H). The shape of the calculated $R(k)$ for both hypernuclei is similar to the shape of the data for 1.7$^{\mathrm{o}}$ and 6$^{\mathrm{o}}$, while it deviates for the 12$^{\mathrm{o}}$ data. The latter may indicate a breakdown of approximating the underlying wave functions by Gaussians. This should be tested by performing more precise calculations using realistic wave functions. These data and future measurements using dedicated spectrometer systems with resolutions below 1 MeV [5] may trigger a renaissance of the spectroscopy of the lightest hypernuclei that have not been studied since the first emulsion experiments many years ago.

The author acknowledges the support by the the A.v.Humboldt Foundation through a Feodor Lynen Research Fellowship and the support by Argonne National Laboratory as the host institution for this research.

[1] J.-M. Laget, Nucl. Phys. A 691 (2001) 11c
[2] F. Dohrmann, A. Ahmidouch et al. Phys. Rev. Lett. 93 (2004) 242501
[3] T. Mart, L. Tiator et al., Nucl. Phys. A 640 (1998) 235
[4] H.W. Barz, private communication (2004)
[5] Y. Fujii, O. Hashimoto et al., Nucl. Phys. A 721 (2003) 1079

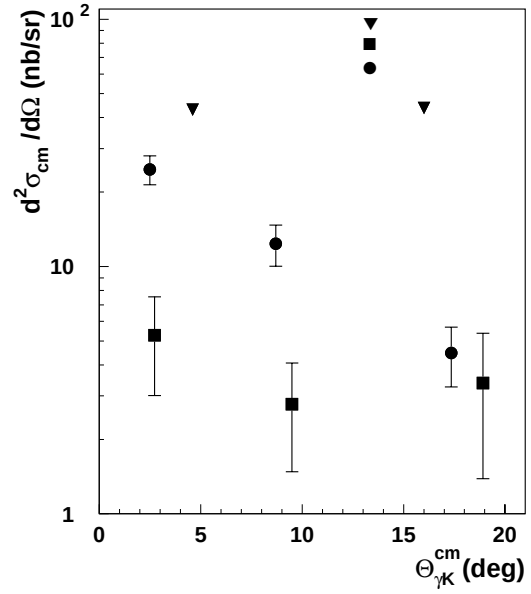

Fig. 1 *Angular distributions of cross sections in the virtual photon-nucleus center of mass for the $^{3,4}He(e,e'K^+)^{3,4}_{\Lambda}H$ and $^1H(e,e'K^+)\Lambda$ (scaled by 0.1) processes, plotted vs. $\Theta^{cm}_{\gamma K}$ (from [2]).*

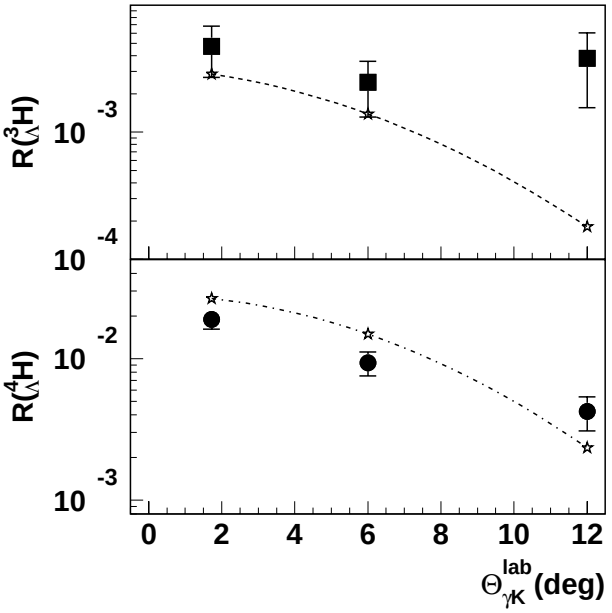

Fig. 2 *$R = \sigma_{lab}(^{3,4}He)/\sigma_{lab}(^1H)$ for $^3_{\Lambda}H$ (upper panel) and $^4_{\Lambda}H$ (lower panel). The dashed and dot-dashed curves are related to the respective nuclear form factors (from [2]).*

Azimuthal Asymmetry for Pentaquark Production in Proton-Proton Collisions [A, B]

H.W. Barz, M. Zétényi[1]

Recently a number of experiments have confirmed the existence of a narrow pentaquark state Θ^+ with a mass of about 1.53 GeV. It decays into the pK^0 or the nK^+ channel with a width of less than about 15 MeV. There is good reason to identify this resonance with the pentaquark state predicted in [1]. According to this approach it belongs to a $J^\pi = 1/2^+$ antidecuplet as an isospin singlet with the five quark configuration $uudd\bar{s}$. Experimentally the spin-parity assignment is still not verified. At the COSY facility this resonance was observed in proton-proton collision $pp \to \Sigma^+ + \Theta^+ \to p\Sigma^+ K^0$ at a center-of-mass energy of 130 MeV above production threshold [2] where the invariant masses of the pK^0 pairs indicate the existence of the Θ^+ resonance. Soon it was realized that at threshold the parity π of the Θ^+ particle determines the spin of the initial protons via $(-1)^S = \pi$. Therefore, a measurement with polarized protons with anti-parallel (parallel) spins gives a remarkable cross section only for positive (negative) parity. Generally one should measure the angular distribution as a function of the azimuthal angle ϕ of the final particle which reads

$$\begin{aligned}\frac{d\sigma}{d\Omega} = \sigma_0[1 \quad &+ \quad A_{yy}\, P_{1\perp} P_{2\perp} \sin(\phi-\alpha_1)\sin(\phi-\alpha_2) \\ &+ \quad A_{xx}\, P_{1\perp} P_{2\perp} \cos(\phi-\alpha_1)\cos(\phi-\alpha_2) \\ &+ \quad A_{zz}\, P_{1z} P_{2z} \\ &+ \quad A_{xz}\, P_{1\perp} P_{2z} \cos(\phi-\alpha_1) \\ &+ \quad A_{zx} P_{1z} P_{2\perp} \cos(\phi-\alpha_2)] \,. \end{aligned} \tag{1}$$

Here the vectors $\mathbf{P}_{1,2}$ describe the polarization of the incoming protons 1,2 with $\alpha_{1,2}$ being their angles in the x-y plane perpendicularly to the z direction of the beam. The spin correlation coefficients A_{ij} depend on the polar angle.

At threshold the coefficients obey the relations $A_{xx} = A_{yy} = A_{zz} = -1$ and $A_{xz} = 0$ for positive parity and the weaker relations $A_{xx} = A_{yy} > 0$ and $A_{zz} = 1 - 2A_{xx}$ for negative parity.

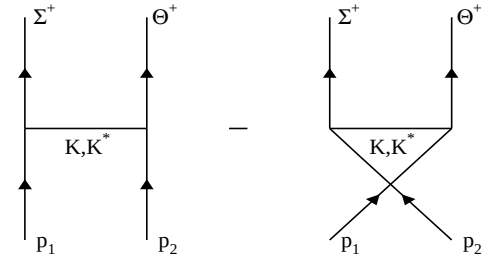

Fig. 1 *Diagrams for Θ^+ production.*

Now we are going to extend the study of proton-proton reactions to larger energies using a model dependent interaction. We describe the interaction by Feynman diagrams (see Fig. 1) with a combination of K and K^* exchanges similarly as in [3]. The coupling parameters of the Lagrangians and the formfactors are constraint by assuming a production cross section of about 0.4 μb and a decay width of 10 MeV for the Θ^+ particle. These values are consistent with the COSY data. The results are shown in Fig. 2 for different assumptions on spin and parities $J = 1/2^\pm, 3/2^\pm$ of the Θ^+. One recognizes that in general the above mentioned threshold behavior survives up to an excess energy of about 50 MeV allowing the determination of the parity. Exceptionally cases as the thick lines for the $3/2^+$ case can be identified by an anomal threshold behavior of the production cross section. However to identify the spin a very careful analysis combining various measured data is needed.

[1] D. Diakonov, V. Petrov, M.V. Polyakov, Z. Phys. A 359 (1997) 305

[2] M. Abdel-Bary et al. (COSY collaboration), Phys. Lett. B 595 (2004) 127

[3] C. Hanhart, J. Haidenbauer et al., Phys. Lett. B 606 (2005) 67

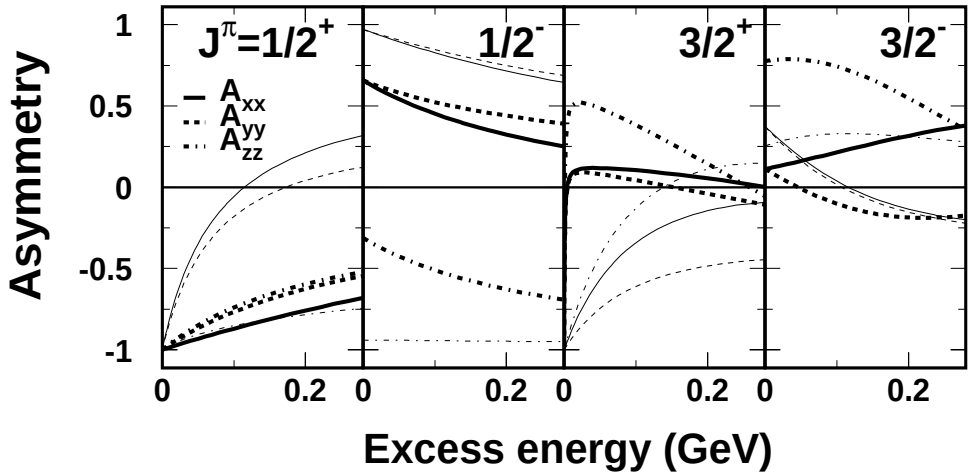

Fig. 2 *Spin correlation parameters at 90 degrees polar angle as a function of the excess energy. The thick (thin) lines present calculations with a positive (negative) ratio of the coupling strengths of K and K^* exchange.*

[1] *KFKI Budapest, Hungary*

Transport Model Calculations of Di-Electron Spectra in Heavy Ion Collisons at SIS18 Energies [B, E]

Gy. Wolf [1], B. Kämpfer

The in-medium behavior of light vector mesons is directly accessible via their di-electron decay channels. Various theoretical approaches predict sizeable modifications of ρ and ω mesons which can be parameterized by mass shifts and width broadening; also more complex modifications like peak splittings are conceivable. There is a tight relation to phenomena governed by chiral symmetry breaking and chiral symmetry restoration. Of particular interest is the dependence of vector meson properties on quark condensates suffering a change in nuclear matter.

With the HADES detector dedicated experiments are performed [1] with the aim to measure di-electron spectra in heavy ion collisions and shed light on the mentioned issues. First results are at our disposal and call for a theoretical interpretation. A suitable tool bases on transport models of Boltzmann-Uehling-Uhlenbeck (BUU) type. The proper implementation of the propagation of finite-width resonances is still a challenge and is differently realized in the various code versions of several groups. The previous simplifications, employed e.g. in [2], need to be improved for a reliable treatment of di-electron sources. Instead of considering reactions of the type $NN \to NN\rho$ with subsequent decay $\rho \to e^+e^-$, we now implemented in our BUU code reactions like $NN \to NR$ (here R stands for baryon resonance) with subsequent decays $R \to N\rho$ and $\rho \to e^+e^-$. This procedure gives fairly different invariant mass distributions. To be more explicit, we adjust first the resonance parameters to reactions $\pi N \to R$ by fitting the decay channels of R (say, $N\pi$, $N\pi\pi$, $N\rho$ etc.) by method resembling the Manley procedure [3], but without quantum interference effects, as the BUU model is semi-classical transport model. Analogously the remaining parameters for reactions of the type $NN \to NR$ are adjusted, where the mass (energy) of the resonances is not fixed but subject to Monte Carlo sampling.

Some results of our calculations are displayed in Figs. 1 and 2. In Fig. 1 the vacuum parameters of the vector mesons are employed as default, while in Fig. 2 we assume in line with various models an in-medium mass shift of the ρ meson and an in-medium broadening of both ρ and ω mesons.

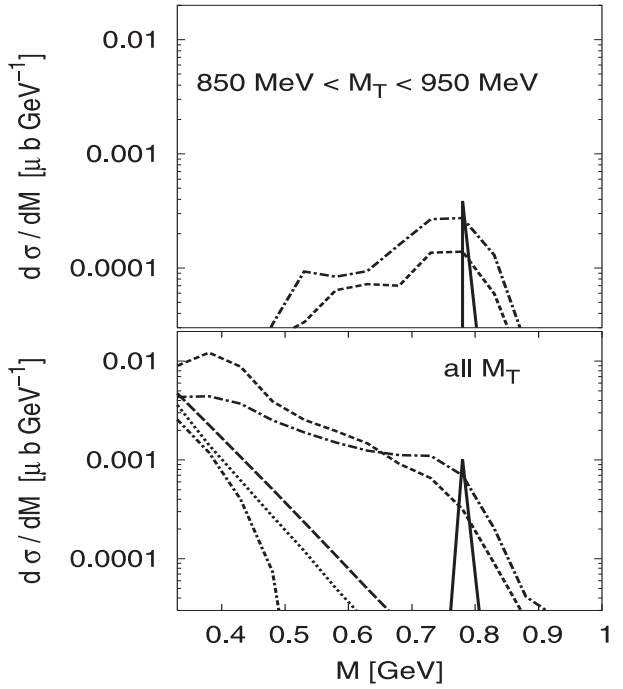

Fig. 1 *Contributions to di-electron spectra as a function of the invariant mass for central collisions of Au on Au at 1 AGeV kinetic beam energy. Upper panel: selecting pairs with transverse masses in the interval 850 ··· 950 MeV, lower panel: for all transverse masses. The line code is as follows: solid – ω decays, dashed – ρ decays (emerging from $R \to N\rho$), long dash-dotted – ρ decays (emerging from $\pi^+\pi^- \to \rho$), dotted – Δ Dalitz decays, dash-dotted – η Dalitz decays, long-dashed – pn bremsstrahlung.*

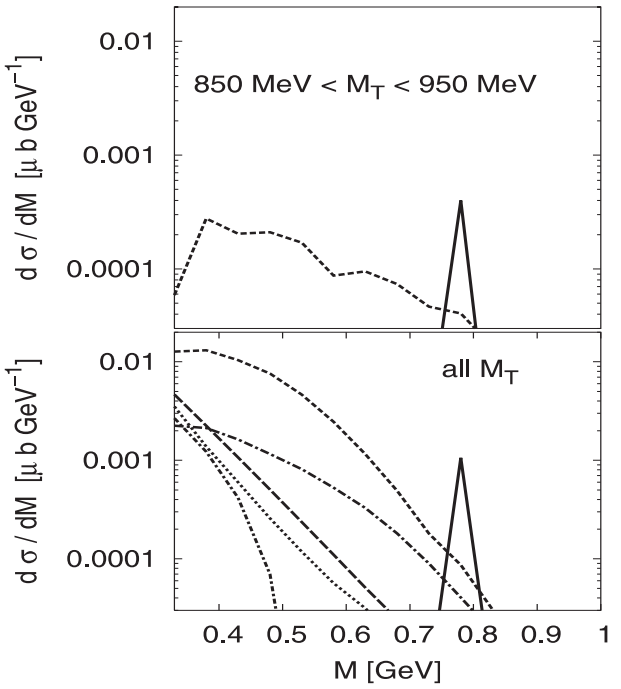

Fig. 2 *As in fig. 1 but with mass shift of the ρ meson by 150 MeV and broadening of the widths of ρ and ω mesons by a factor 3.*

[1] P. Salabura (HADES Collaboration), Nucl. Phys. A 749 (2005) 150
[2] Gy. Wolf, O.P. Pavlenko, B. Kämpfer, nucl-th/0306029
[3] D.M. Manley, E.M. Saleski, Phys. Rev. D 45 (1992) 4002

[1] *RMKI-KFKI Budapest, Hungary*

Electromagnetic Probes in Heavy-Ion Collisions at CERN-SPS Energies [B,E]

K. Gallmeister[1], B. Kämpfer

To lowest order in temperature, the vector and axial vector correlators become degenerate at chiral restoration temperature and the vector-axialvector mixing modifies the dilepton emissivity to a smooth thermal continuum above a certain duality threshold [1]. Extending the duality to soft modes one arrives at the hypothesis that the emissivity of strongly interacting matter can be parameterized by the Born term $q\bar{q}$ annihilation rate, irrespectively whether the matter is in a confined or deconfined state. This ansatz works astonishingly well [2]. Here, we give an update of our parametrization since new CERES data [3] are at our disposal.

In Figs. 1 and 2, both the invariant mass di-electron spectra and the transverse momentum spectra are exhibited. In contrast to the parametrization of previously known data by a single space-time averaged effective radiation temperature $\langle T\rangle = 170$ MeV, the new data within larger phase space coverage enforce the inclusion of a second thermal radiation component with $\langle T\rangle = 120$ MeV which may arise from the enlarged sensitivity to the late stages prior to freeze-out.

The physics motivation behind such a parametrization is the following observation [2]: Integrating the radiation off an expanding fireball with volume $V(t)$ and temperature $T(t)$ for certain evolutionary scenarios results in spectra which can be described by a temperature $\langle T\rangle$ and an effective space-time volume. Enlarging the phase space coverage by lowering the minimum single-electron transverse momentum threshold reveals that the final spectrum appears as superposition of two effective temperatures. The new high-statistics NA60 data will shed further light on this issue.

As consistency check one may try to describe the WA98 photon data by exactly the same source parametrization. Fig. 3 shows that our new parametrization delivers indeed a better description of the data than previous ones.

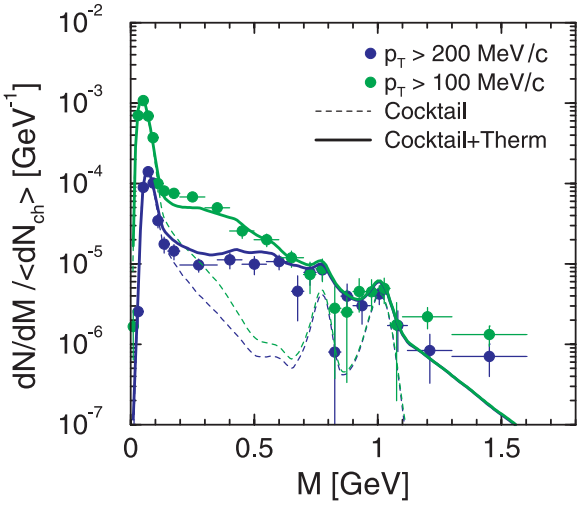

Fig. 1 *Comparison of our parametrization with new CERES data [3] for invariant mass spectra. The minimum single-electron transverse momenta are 200 and 100 MeV/c.*

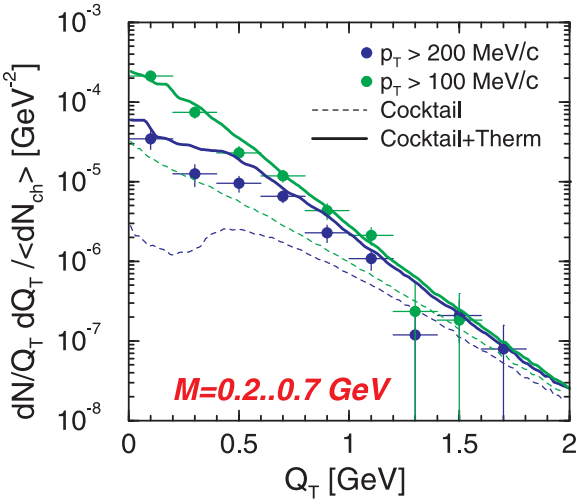

Fig. 2 *As Fig. 1 but for transverse momentum spectra for the mass bin 0.2 ... 0.7 GeV.*

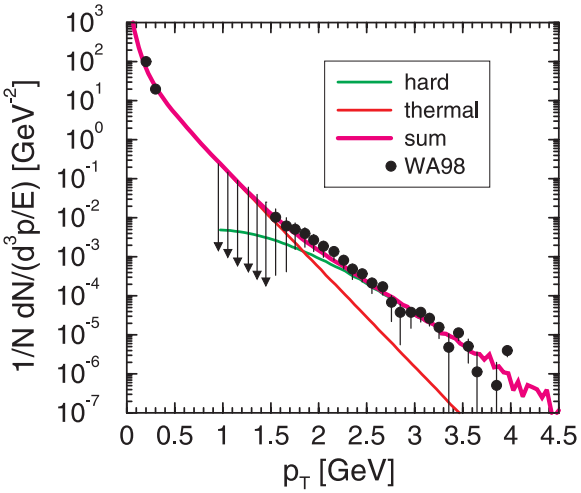

Fig. 3 *Adopting the same source parametrization as in Fig. 1 for describing the WA98 photon data [4]. The thermal component employs in line with [5] the complete lowest order rate with collinear enhancement factor. For the calculation of the hard Drell-Yan like component see [2].*

[1] R. Rapp, J. Wambach, Adv. Nucl. Phys. 25 (2000) 1

[2] K. Gallmeister, B. Kämpfer, O.P. Pavlenko, Nucl. Phys. A 715 (2003) 705; Nucl. Phys. A 698 (2002) 424; Nucl. Phys. A 688 (2001) 939; Phys. Rev. C 62 (2000) 057901; Phys. Lett. B 473 (2000) 20

[3] A. Marin (CERES), J. Phys. G 30 (2004) S209 H. Appelshäuser (CERES), invited talk at Hard Probes, Lisboa, Nov. 4 - 10, 2004

[4] M.M. Aggarwal et al. (WA98), Phys. Rev. Lett. 93 (2004) 022301

[5] P. Arnold, G.D. Moore, L.G. Yaffe, JHEP 0111 (2002) 057

[1] *Institut für Theoretische Physik, Universität Gießen*

Propagation of Broad Resonances within Transport Models [A,B]

H.W. Barz, M. Zétényi[1]

In recent years effort [1,2] was taken to calculate the transport of hadrons in nucleus-nucleus collisions beyond the quasi-particle approximation. As starting point of these approaches serve the Kadanoff-Baym equations which describe the time evolution of the Green functions of the excited nuclear system as a function of the self energy Σ^{ret} of the particle under consideration. The Wigner transformed of the Green function $iS^<(x,y) = < \Phi^+(y)\Phi(x) >$

$$iS^<(x,p) = \sum_i \delta(\mathbf{x}-\mathbf{x}_i)\delta(\mathbf{p}-\mathbf{p}_i)\delta(p^0-\epsilon_i) \qquad (1)$$

can be interpreted as a generalized phase-space density suggesting a test particle ansatz for the numerically solution of the Kadanoff-Baym equations. The phase-space density contains a spectral function $\mathcal{A}(p)$ which describes a mass distribution of the particle with a width proportionally to Im Σ^{ret}. The equations of motions for the three spatial coordinates and the four momentum components of the test particles can be found in [1,2] for the relativistic and the non-relativistic case, respectively.

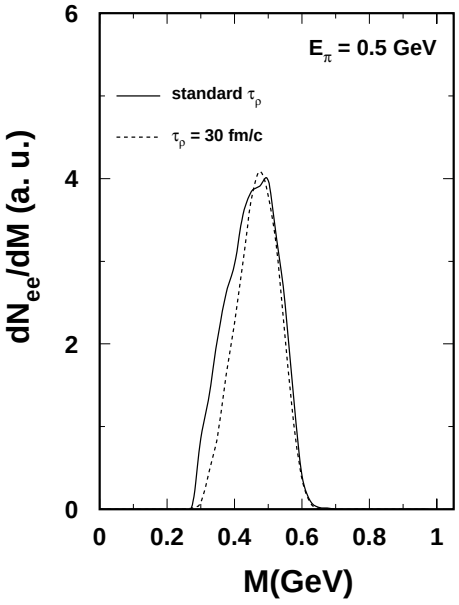

Fig. 1 *The di-electron mass spectrum as a function of the invariant mass M calculated using different lifetimes τ of the ρ meson.*

Now we are going to study the consequences of the equation of motion for the propagation of unstable particles within the transport model. For simplicity reasons we consider a system with a restricted number of degrees of freedom. We allow only two excited states of the nucleons, the $\Delta(1230)$ and the $N(1520)$ resonance, and include the π and the ρ mesons. Only the ρ mesons are treated by the generalized phase-space distribution (1). Its initial mass distribution originates from the decay of the the $N(1520)$ resonances. As an example we simulate the situation of a nucleus bombarded with a pion of an energy of 0.5 GeV and calculate the di-lepton spectrum coming from the ρ^0 decay.

The lifetime of the ρ meson is very short compared to the reaction time. Therefore, the invariant mass of the emitted di-electrons reflects essentially the mass of the ρ meson at the instant of its formation. Thus the time evolution of the mass is important. To illustrate the effect of the dynamical change of the ρ mass we have switched off the absorption of the ρ mesons in the nuclear matter such that the ρ mesons live till the end of the reaction of about 30 fm/c. Then the mass spectrum of the ρ mesons tends to approach the vacuum spectrum. Fig. 1 shows that the shape of the original di-electron spectrum is indeed wider than that of long lived ρ mesons.

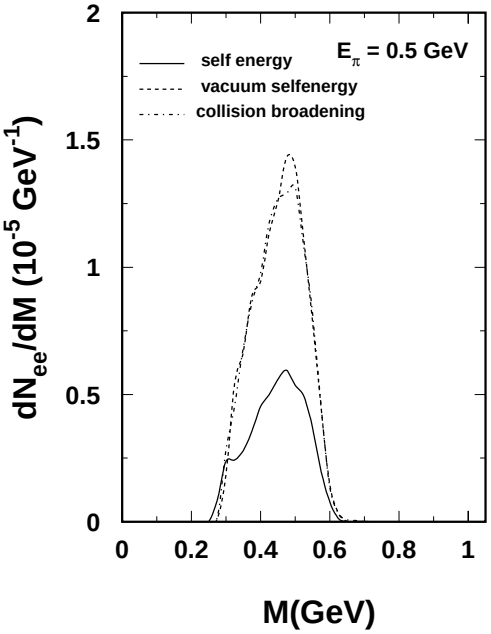

Fig. 2 *Di-electron spectra calculated for a central πCu collision for different assumptions on the spectral function.*

In Fig. 2 we compare the di-electron spectra calculated with the vacuum selfenergy of the ρ meson with that calculated including the collisional broadening of the ρ resonance. The difference is very small due to the small cross section of the ρ meson hitting the nucleon with an energy clearly below the $N(1520)$ resonance energy. Finally, the thick line illustrates the effect of the selfenergy calculated in a many body theory [3]. In this case the di-electron rate is smaller since the lifetime of the ρ meson is shorter than in vacuum.

[1] W. Cassing and S. Juchem, Nucl. Phys. A 672 (2000) 417
[2] S. Leupold, Nucl. Phys. A 672 (2000) 475
[3] Gy. Wolf, private communication

[1] *KFKI Budapest, Hungary*

Deuteron Polarimetry at ANKE [B]

D. Chiladze[1], A. Kacharava[2], F. Rathmann[1], S. Trusov and C. Wilkin[3] for the ANKE Collaboration

The first measurement of the deuteron-induced charge-exchange reaction [1] was carried out at the ANKE spectrometer using a polarized deuteron beam at $p_d = 2400$ MeV/c. The polarized deuterons ($\approx 3 \times 10^9$) stored in the COSY ring impinge on a hydrogen cluster-jet target. Two fast protons, emitted in a narrow forward cone with momenta around half that of the deuteron beam, are detected by the Forward Detector (FD) system of the ANKE set-up. Fig. 1 shows the ANKE experimental acceptance for single charged particles for different reactions as functions of the laboratory production angle and magnetic rigidity, together with loci for the kinematics of different allowed reactions. The $dp \to dp$ reaction has a significant acceptance for $4^\circ < \Theta^d_{lab} < 10^\circ$. The observables A_y, A_{yy}, and A_{xx} of this reaction were studied previously at Argonne [2] and SATURNE [3] for $T_d = 1198$ MeV.

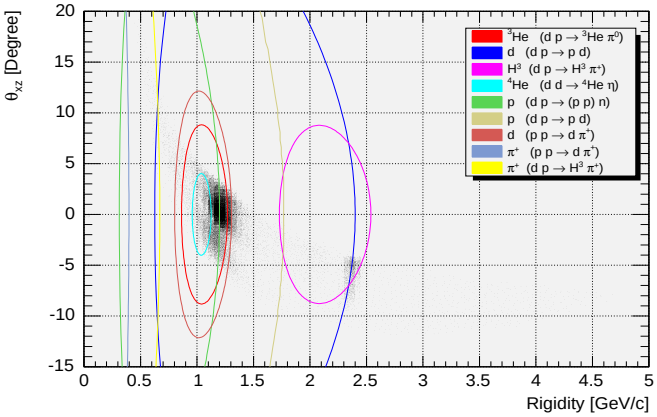

Fig. 1 *ANKE experimental acceptance for different reactions in dp collisions at $T_d = 1170$ MeV.*

The dp elastic peak region in the momentum spectrum of the single track events was fitted by the sum of a Gaussian and linear function, and events selected within 3σ of the mean. The $dp \to {}^3$He π^0 reaction can be studied using just the ^{3}He information. The high momentum branch of ^{3}He particles was isolated well in an line analysis, applying two-dimensional cuts in ΔE versus momentum and Δt versus momentum for individual layers of the forward hodoscope. The quasi-free $np \to d\pi^0$ can be clearly identified by detecting two final charged particles in the $dp \to p_{sp} d\pi^0$ reaction, where p_{sp} is a spectator proton which has essentially half the beam momentum. The differential cross section should be half of that for $pp \to d\pi^+$, whereas all the analysing powers should be equal. The charge-exchange process was identified from the missing-mass (see Fig. 2) with respect to the observed proton pairs and time difference information. The spectra for all spin modes reveal a well defined peak at M_{miss} equal to the neutron mass to within 1%; the mean value for the reconstructed neutron mass is $M_n = 940.4 \pm 0.2$ MeV/c^2. The background was less than 2% and stable, so that the charge-exchange process could be reliably identified.

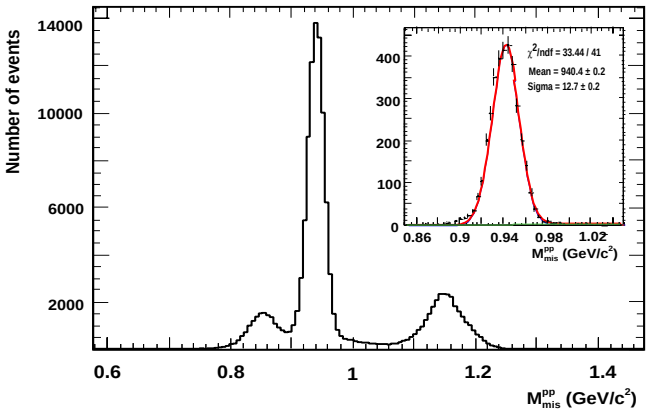

Fig. 2 *Missing mass distribution of all observed proton pairs. The inset shows the distribution near the neutron mass for the pairs selected by the TOF.*

Using the $\vec{d}p \to dp$, $\vec{d}p \to (2p)n$, $\vec{n}p \to d\pi^0$, and $\vec{d}p \to {}^3$He π^0 reactions, which all have large and well known analyzing powers, a simultaneous calibration of the vector and tensor components of the polarized deuteron beam at COSY becomes possible for the first time. The results are summarized in Table 1.

Reaction	Facility	α_z	α_{zz}
$\vec{d}p \to dp$	EDDA	0.74 ± 0.02	0.59 ± 0.05
$\vec{d}p \to dp$	ANKE	0.73 ± 0.02	0.49 ± 0.02
$\vec{n}p \to d\pi^0$	ANKE	0.73 ± 0.02	-
$\vec{d}p \to {}^3 He\pi^0$	ANKE	-	0.58 ± 0.05
$\vec{d}p \to (pp)n$	ANKE	-	0.48 ± 0.05

Tab. 1 *Table 1: Values of vector and tensor polarization parameters. Only statistical errors are given.*

The average of the ANKE measurements is $\alpha_z^{ANKE} = 0.72 \pm 0.02$ and $\alpha_{zz}^{ANKE} = 0.52 \pm 0.03$, which is compatible with EDDA results [4] measured prior to the ANKE run but at lower beam energy and intensity.

[1] A. Kacharava et al., ANKE Proposal #125 (2003)
[2] M. Haji-Said et al., Phys. Rev. C 36 (1987) 2010
[3] J. Arvieux et al., NIM A 273 (1988) 48
[4] B. Lorentz et al., proceedings of 9^{th} EPAC conference, July 5-9, 2004, Lucerne, Switzerland

[1] *FZ Jülich*
[2] *Universität Erlangen*
[3] *University College London, UK*

Virtual Bremsstrahlung in the Reaction $Dp \to e^+e^-p_{\rm spec}pn$ [B,G]

L.P. Kaptari[1], B. Kämpfer

The HADES physics programme addresses the important issue of virtual bremsstrahlung in elementary hadron reactions. The detailed understanding of the elementary cross sections is an important prerequisite for analyzing heavy-ion reactions, but has also its own right in particular with respect to isospin effects. For real bremsstrahlung the cross section for the pp channel is much smaller than for the pn channel. For virtual photons the situation is not so clear. Experimentally the pn channel is accessible in the reaction $Dp \to e^+e^-p_{\rm spec}pn$. The HADES collaboration plans to study this reaction with detection of the fast forward spectator proton $p_{\rm spec}$ under angles smaller than 5^o. In such a way the tagged subreaction $np \to npe^+e^-$ will be separated.

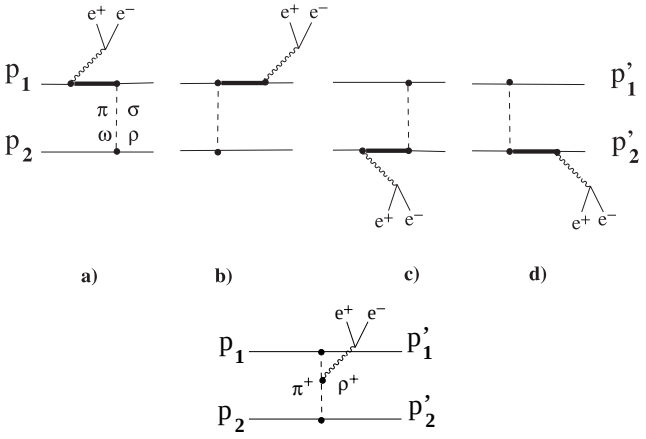

Fig. 1 *Born diagrams for bremsstrahlung. upper line: pure bremsstrahlung diagrams a) - d). The fat line may be a nucleon or a Δ. The lower graph depicts the internal radiation diagram. The dashed line may be a π^+ or ρ^+.*

Within an effective nucleon-meson theory we calculated Born terms for virtual bremsstrahlung in the low-mass region. The processes are depicted in Fig. 1. Theoretical issues concern (i) gauge invariance and Ward-Takahasi identity when using effective vertices and including the internal radiation diagram, (ii) the spin-3/2 propagators when considering the excitation of the intermediate Δ, and (iii) the factorization of the cross section

$$2E_{\rm spec}\frac{d\sigma}{d^3p_{\rm spec}dM^2} = 2m_D\sqrt{\frac{\lambda(s_{NN},m_N^2,m_N^2)}{\lambda(s_{NN},m_N^2,m_D^2)}} \times n_D(p_{\rm spec})\,\frac{d\sigma_{NN\to NNe^+e^-}}{dM^2},$$

where M is the invariant e^+e^- mass and n_D denotes the deuteron momentum distribution. We have extended previous attempts [1] and adjusted our approach in the pp channel to results of [2] which in turn reproduce the Di-Lepton-Spectrometer (DLS) data.

Results of our calculation are displayed in Figs. 2 and 3. They may serve as predictions of the continuum background below the resonance region. Fig. 2 illustrates isospin effects at a given beam energy, and Fig. 3 exhibits the systematics of cross sections for various kinematical settings envisaged at HADES.

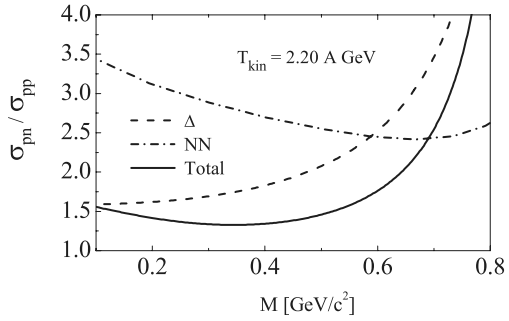

Fig. 2 *Ratio $\sigma_{pn\to pne^+e^-}/\sigma_{pp\to ppe^+e^-}$ as a function of the e^+e^- invariant mass for a beam energy of 2.20 GeV. The dashed curve depicts the pure NN bremsstrahlung part, while the dashed curve exhibits the contribution from Δ excitation. The solid curve is for the total ratio.*

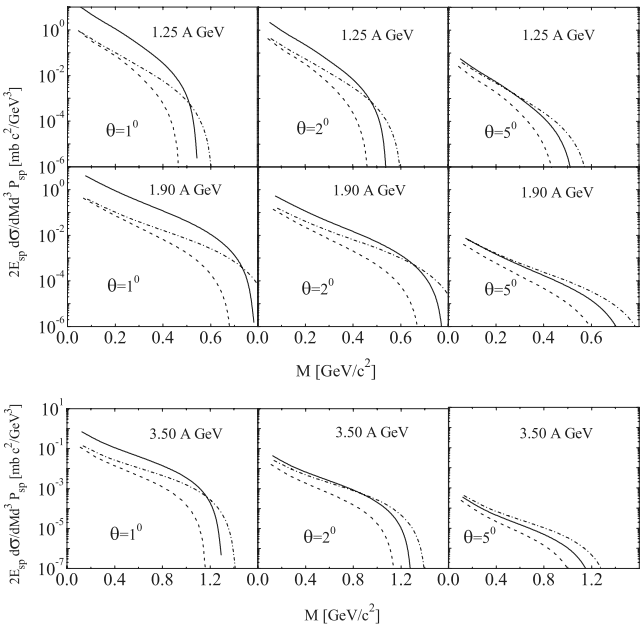

Fig. 3 *Invariant mass distributions in the reaction $Dp \to e^+e^-p_{\rm spec}np$ for the kinetic beam energies T_D = 1.25, 1.90 and 3.50 AGeV for various angles Θ of the detected fast forward proton with the momenta $p_{\rm spec} = 0.45p_D$ (dot-dashed curves), $0.50p_D$ (solid curves) and $0.55p_D$ (dashed curves), respectively.*

[1] A.I. Titov, B. Kämpfer, E.L. Bratkovskaya, Phys. Rev. C 51 (1995) 227

[2] R. Shyam, U. Mosel, Phys. Rev. C 67 (2003) 065202

[1] *Bogolyubov Laboratory of Theoretical Physics, JINR Dubna, 141980, Russia*

The ω Meson in Nuclear Matter and Chiral Symmetry Restoration [B,G]

R. Thomas, S. Zschocke, B. Kämpfer

The CB-TAPS collaboration studied the reaction $\gamma A \to A'\omega(\to \pi^0\gamma)$. Count rates as a function of the invariant mass $m_{\pi^0\gamma}$ have been measured for LH_2 and Nb targets. It is remarkable that for the Nb target the strength is noticeably shifted to smaller values of $m_{\pi^0\gamma}$ for small values of the ω momentum, while for larger ω momenta the difference for both targets diminishes. Even without knowledge of acceptance corrections, phase space factor etc. one may use the count rate as estimator of the ω distribution and deduce a small down shift of m_ω. Supposing (i) the validity of the standard QCD sum rule, and (ii) assuming that the measured decays $\omega \to \pi^0\gamma$ happen to a large extent inside nuclear matter, and (iii) neglecting poorly known higher terms, the unavoidable conclusion is that in-medium 4-quark condensates are reduced at least by 30%. Such a strong density dependence of 4-quark condensates is needed to balance the strong density dependence of the Landau damping which tends to shift the in-medium ω strength to higher energy [1].

Among the problematic issues for the interpretation of the CB-TAPS experiments is the role of the final state interaction of the intermediate π^0, which tends to decrease the invariant mass $m_{\pi^0\gamma}$ thus faking a mass shift. In this respect the reaction $\pi A \to A'\omega(\to e^+e^-)$ to be studied by the HADES collaboration offers a more direct access to the ω properties in the nuclear medium.

The subject is of importance for investigating chiral symmetry restoration. The chiral condensate is an order parameter for the spontaneous breaking of chiral symmetry in the theory of strong interaction. Its role is demonstrated, e.g., by the Gell–Mann-Oaks-Renner relation relation $m_\pi^2 \propto -\langle\bar{q}q\rangle$ for the pion mass. It is experimentally checked that more than 94% of the pion mass stem from the chiral condensate. There is growing evidence that the quark-gluon condensate $\langle\bar{q}\sigma_{\mu\nu}G^{\mu\nu}q\rangle \propto \langle\bar{q}q\rangle$ is another order parameter. The QCD trace anomaly related to scale invariance breaking gives rise to the gluon condensate $\langle(\alpha_s/\pi)G_{\mu\nu}G^{\mu\nu}\rangle$ with $G_{\mu\nu}$ as chromodynamic field strength tensor. There are many other condensates characterizing the complicated structure of the QCD vacuum. In a medium, described by temperature T and baryon density n, these condensates change, i.e., the vacuum state is rearranged. Since hadrons are considered as excitations above the vacuum, a vacuum change should manifest itself as a change of the hadronic excitation spectrum.

To elucidate the role of various condensates for the ω meson we revisited the corresponding QCD sum rule [2]. The results are exhibited in Fig. 1, both for vacuum and nuclear medium. The genuine chiral condensate turns out to be unimportant. Rather, the 4-quark condensates are important for the ω meson. Recent approaches factorized the 4-quark condensates into squared chiral condensate and advocated the chiral symmetry restoration as driving mechanism for in-medium modifications of the ω. In our view, however, the helicity flipping parts of the 4-quark condensates serving as further order parameter cause the in-medium modification.

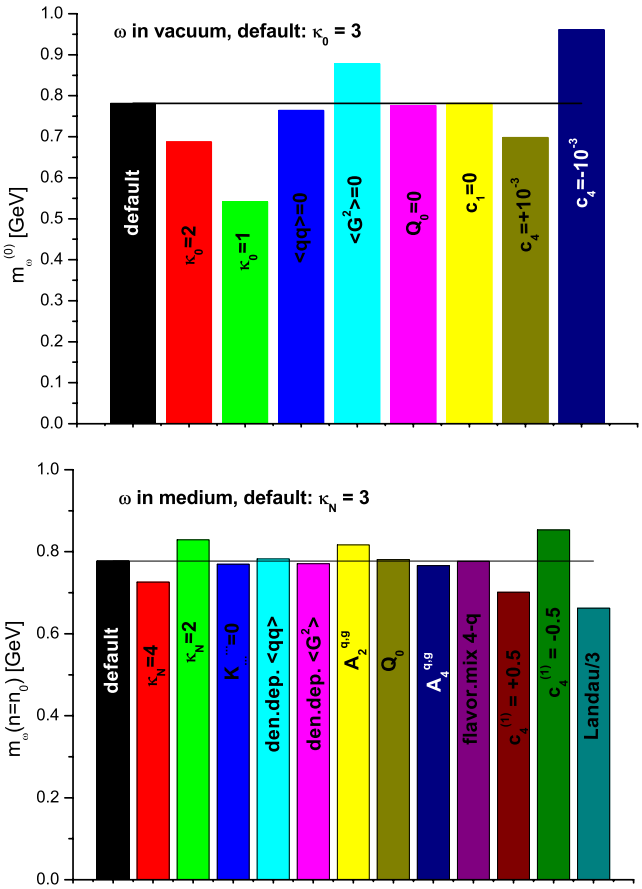

Fig. 1 *Importance of various quantities for the ω mass parameter in the QCD sum rule [2]. Top (bottom) panel: for vacuum (nuclear matter). Default values are $\langle\bar{q}q\rangle = (-0.245\ \mathrm{GeV})^3, \langle(\alpha_s/\pi)G^2\rangle = (0.33\ \mathrm{GeV})^4$. The 4-quark condensates enter in the combination $-\frac{112}{81}\pi\alpha_s\kappa_0\langle\bar{q}q\rangle_0^2[1 + \frac{\kappa_N}{\kappa_0}\frac{\sigma_N}{m_q\langle\bar{q}q\rangle_0}n]$ with $\sigma_N = 45$ MeV and $m_q = 5.5$ MeV. Furthermore, the sum rule contains a term $\propto Q_0^2$ responsible for the $\rho - \omega$ mass splitting in vacuum. $A_{2,4}^{q;g}$ are contributions which can be traced back to moments of the parton distribution in the nucleon. "flavor.mix" and $K_{\dots}^{\dots}$ indicate poorly known terms stemming from flavor mixing condensates. The mass dimension-2 term is determined by $m_{u,d}^2$. The complete mass dimension-8 term c_4 is presently unknown. In the default calculation this term is discarded. To estimate its influence we assume ad hoc $c_4(n) = \pm 10^{-3}\mathrm{GeV}^8(1 + c_4^{(1)}n)$ with $c_4^{(1)} = \pm 0.5/n_0$.*

[1] R. Thomas, K. Gallmeister, S. Zschocke, B. Kämpfer, Acta Phys. Hung. (2005) in print

[2] S. Zschocke, O.P. Pavlenko, B. Kämpfer, Phys. Lett. B 562 (2003) 57; B. Kämpfer, S. Zschocke, Prog. Part. Nucl. Phys. 53 (2004) 317

Splitting and Mixing of ρ and ω Mesons [B, E, G]

S. Zschocke, B. Kämpfer

One of the important topics of nuclear physics is to study how properties of hadrons, like mass and width, change in a dense and hot nuclear environment. Since lepton-hadron interactions are relatively weak, the observation of dileptons is a promising way to probe the conditions in the hot and compressed interaction zone produced in nucleus-nucleus collisions. Accordingly, the light vector mesons become interesting due to their decay mode $V \to \gamma^* \to e^+ e^-$ which allows to explore directly a mass shift and width broadening of the parent vector mesons inside the fireball by measuring the lepton pair. Strong evidences for such in-medium modifications of ρ mesons have already been found in the heavy-ion collision experiments CERES [1] and HELIOS-3 [2]. Very recently, the experiment TAPS [3] has also reported about a noticeable mass shift of the ω meson.

On the theoretical side the mass shift predictions for ρ and ω differ: for instance the Brown-Rho scaling [6] predicts a dropping mass with same strength for ρ and ω, while hadronic models [7] and QCD sum rules [4, 8] (see Fig. 1) predict a non-unique mass parameter shift when taking into account properly the Landau damping term.

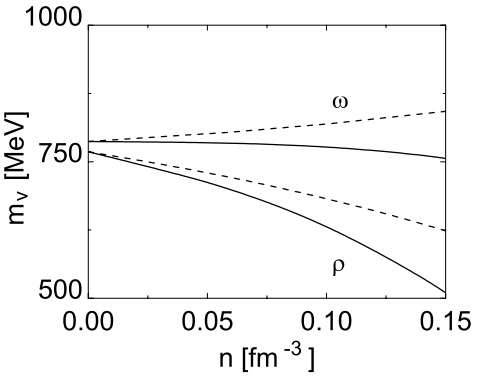

Fig. 1 *The ρ and ω meson mass splitting as a function of the density [4]. The parameter κ_N (dashed line: $\kappa_N = 2$, solid line: $\kappa_N = 3$) governs the strength of the density dependence of the poorly known scalar flavour-unmixed four-quark condensate.*

An experimental investigation of the mixing effect between ρ and ω, governed by the mixing parameter ϵ via

$$\begin{pmatrix} \rho \\ \omega \end{pmatrix} = \begin{pmatrix} 1 & -\epsilon \\ \epsilon & 1 \end{pmatrix} \begin{pmatrix} \rho^I \\ \omega^I \end{pmatrix} , \qquad (1)$$

would enable to distinguish between these different mass shift scenarios. Starting with an evaluation of the mixing effect in vacuum (see Fig. 2) we have, by means of the QCD sum rule approach, investigated how the mixing angle ϵ changes with baryon density (see Fig. 3). We have found that the mixing effect, while significantly pronounced for the Brown-Rho scaling scenario, is strongly suppressed when taking into account the individual mass shift of ρ and ω.

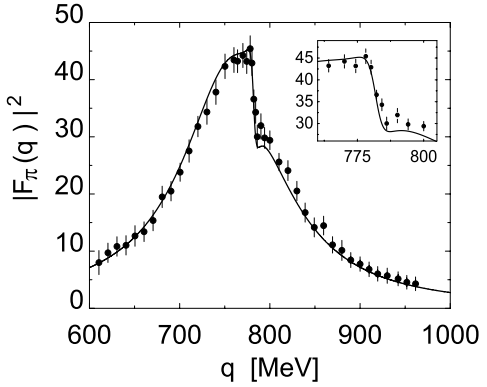

Fig. 2 *Pion formfactor in vacuum as a function of pion momentum. Our results (solid line) [4] in comparision with CMD-2 experiment (solid circles) [5].*

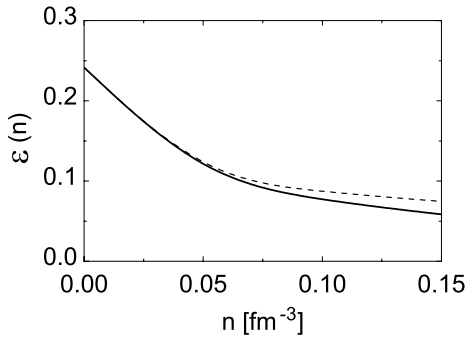

Fig. 3 *Mixing angle ϵ as a function of baryon density (dashed line $\kappa_N = 2$, solid line $\kappa_N = 3$). The decrease of ϵ with increasing density is mainly caused by the strong mass splitting between ρ and ω seen in Fig. 1.*

In summary, we have explored how the mixing effect allows to distinguish between two different mass shift scenarios of the light vector mesons ρ and ω. It is supposed that future experiments with HADES [9, 10] might be able to pin down such an effect.

[1] G. Agakichiev et al. (CERES Collaboration), Phys. Rev. Lett. 75 (1995) 1272;
D. Adamova et al. (CERES Collaboration), Nucl. Phys. A 698 (2002) 253
[2] M. Masera et al. (HELIOS-3 Collaboration), Nucl. Phys. A 590 (1995) 93c
[3] D. Trnka et al. (CB-TAPS Collaboration), to be published in Acta Phys. Hung. A 19/1 (2005)
[4] S. Zschocke, B. Kämpfer, Phys. Rev. C 70 (2004) 035207
[5] R. R. Akhmetshin et al. (CMD-2 collaboration), Phys. Lett. B 527 (2002) 161
[6] G.E. Brown, M. Rho, Phys. Rev. Lett. 66 (1991) 2720.
[7] F. Klingl, N. Kaiser, W. Weise, Nucl. Phys. A 624 (1997) 527
[8] A.K. Dutt-Mazumder, R. Hofmann, M. Pospelov, Phys. Rev. C 63 (2001) 015204
[9] P. Salabura et al. (HADES Collaboration), Nucl. Phys. A 749 (2005) 150c
[10] http://www-hades.gsi.de, 07.01.2005

Combined Analysis of Near-Threshold Production of ω and ϕ Mesons in Nucleon-Nucleon Collisions [B,G]

L.P. Kaptari,[1] B. Kämpfer

The study of near-threshold vector meson production is a substantial part of the experimental programme at ANKE-COSY. Due to the strong coupling of vector mesons to di-electrons, the corresponding results are of importance for HADES. Furthermore, a combined analysis of the production of ω and ϕ mesons in nucleon-nucleon collisions is interesting with respect to OZI rule violations. OZI rule violations can give hints to a significant $s\bar{s}$ admixture in the proton.

We have studied the production of ω and ϕ in NN collisions within an effective meson-nucleon theory [1]. A few results are reported here.

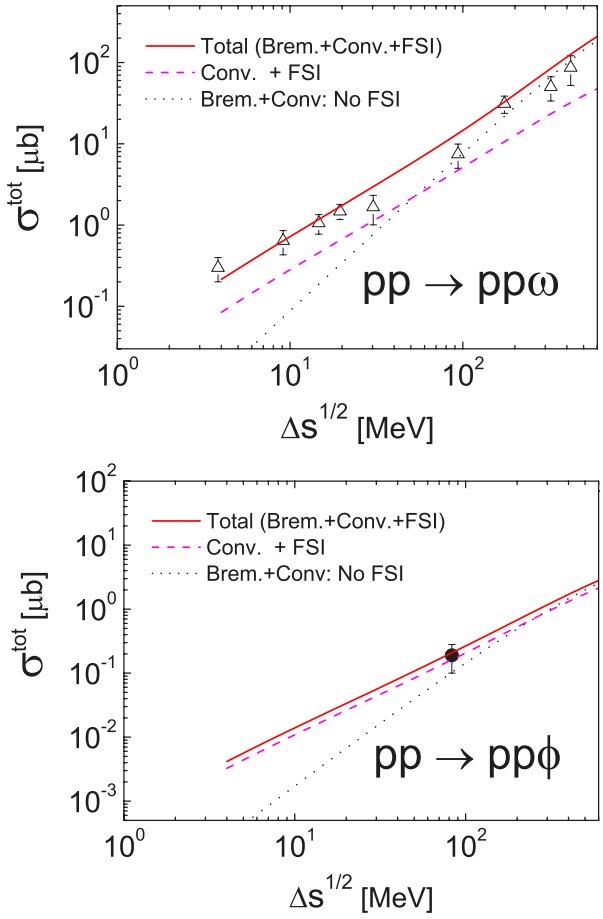

Fig. 1 *Total cross sections of near-threshold production of ω (upper panel) and ϕ (lower panel) mesons in pp reactions as a function of the energy excess $\Delta s^{\frac{1}{2}} = \sqrt{s} - 2m_p - m_{\omega,\phi}$. Dashed lines correspond to contributions of conversion currents solely, dotted and solid lines represent results with including bremsstrahlung and conversion diagrams (without and with final state interaction (FSI) effects taken into account), respectively. Experimental data are from SATURNE, COSY-TOF and DISTO (cf. [1] for references).*

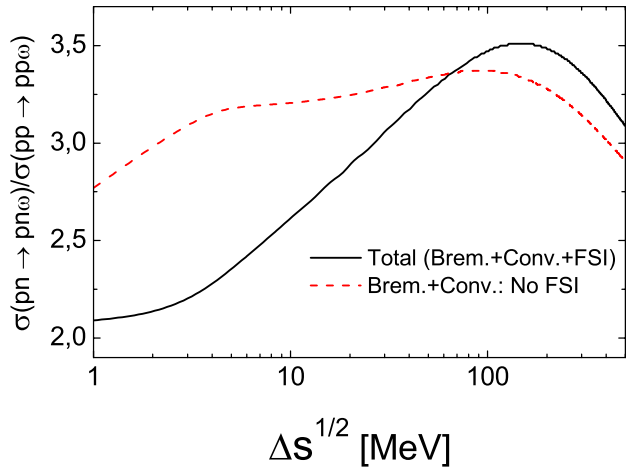

Fig. 2 *Ratios of the total cross sections of ω meson production in pp and pn channels as a function of excess energy. Dashed line denotes the ratio of cross sections without FSI; solid line reflects the ratio of total cross sections with FSI taken into account.*

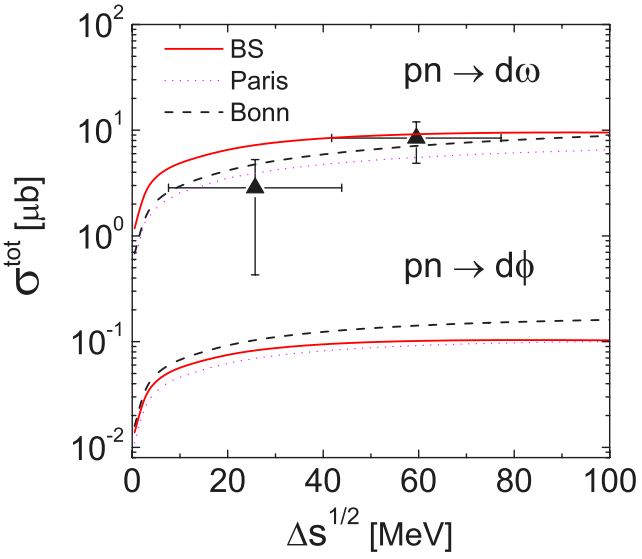

Fig. 3 *Total cross sections for ω and ϕ mesons for $pn \to dV$ reactions as a function the excess energy $\Delta s^{\frac{1}{2}} = \sqrt{s} - M_d - m_{\omega,\phi}$. Solid lines: results of calculations with the deuteron wave function obtained within the Bethe-Salpeter formalism; dashed (dotted) lines: using the non-relativistic deuteron wave function with the Bonn (Paris) potential. The experimental data are from COSY-ANKE (cf. [1] for references).*

[1] L.P. Kaptari, B. Kämpfer, Eur. Phys. J. A 23 (2005) 291

[1] *Bogolyubov Laboratory of Theoretical Physics, JINR Dubna, 141980, Russia*

Two-Proton Intensity Interferometry in Central Heavy-Ion Collisions [B,G]

R. Kotte for the FOPI collaboration

Previous studies of two-proton intensity interferometry have been completed aiming at systematic investigations of the *pp* correlation function in central heavy-ion collisions at SIS energies. The results of this system-size and beam-energy dependent study have been published recently [1]. Here, we shortly report on the system-size dependence of such small-angle correlations measured in central reactions at 400 *A*MeV beam energy. The data are taken with the FOPI detector system at the heavy-ion synchrotron SIS at GSI Darmstadt.

Let $Y_{12}(\mathbf{p}_1, \mathbf{p}_2)$ be the coincidence yield of pairs of particles having momenta $\mathbf{p}_1$ and $\mathbf{p}_2$. Then the two-particle correlation function is defined as

$$1 + \mathrm{R}(\mathbf{p}_1, \mathbf{p}_2) = \mathcal{N} \frac{\sum_{events,pairs} Y_{12}(\mathbf{p}_1, \mathbf{p}_2)}{\sum_{events,pairs} Y_{12,mix}(\mathbf{p}_1, \mathbf{p}_2)}. \quad (1)$$

The sum runs over all events fulfilling cuts on high charged-particle multiplicities, hence allowing for the selection of the most central 10 % - 15 % events, and over all pairs satisfying certain conditions. Event mixing, denoted by the subscript "mix", means to take particle 1 and particle 2 from different events. $\mathcal{N}$ is a normalization factor fixed by the requirement to have the same number of true and mixed pairs. Artificial correlations arising from the mixing of differently azimuthally oriented events are strongly reduced by rotating all events into a unique reaction plane. The correlation function (1) is then projected onto the relative momentum

$$q = |\mathbf{q}| = \frac{1}{2} |\mathbf{p}_1^{cm} - \mathbf{p}_2^{cm}|. \quad (2)$$

Here, $\mathbf{p}_i^{cm}$ are the particle momenta calculated in the c.m. system of the colliding nuclei.

Figure 1 shows the experimental results (symbols) of pp-correlation functions at small relative momenta for central ^{40}Ca + ^{40}Ca, ^{96}Ru + ^{96}Ru and ^{197}Au + ^{197}Au reactions at a beam energy of 400 *A*MeV. At $q \simeq 20$ MeV/c a strong peak is visible. This "^{2}He"-resonance is the result of the common action of the enhancement due to the attractive nucleonic potential and the suppression due to both the mutual Coulomb repulsion and the antisymmetrization of the *pp* wave function. The data are confronted to simulations performed with a final-state-interaction (FSI) model [2] for zero lifetime but varying the Gaussian radius parameter R_0^* in order to reproduce the shape of the correlation peak. Clearly, the peak decreases, i.e. the apparent source radius increases, with increasing system size. This system-size dependence is expected from the larger volume due to a larger number of participants in the central source.

For both the small and the medium-size systems, our results can be compared directly with existing data: Gaussian radii were derived from pp correlations measured with the "Plastic Ball" at BEVALAC for the reactions Ca + Ca and Nb + Nb, both at 400 MeV per nucleon, as function of proton multiplicity [3]. Taking into account the different radius definitions [1], the apparent source radii for central collisions agree perfectly.

The data are also compared to another version of the final-state interaction model which does not utilize static Gaussian sources but proton one-body phase-space distributions provided by a Boltzmann-Uehling-Uhlenbreck (BUU) transport approach. Here, the *pp* correlation function is found rather insensitive to the stiffness of the equation of state entering the transport model calculations [1].

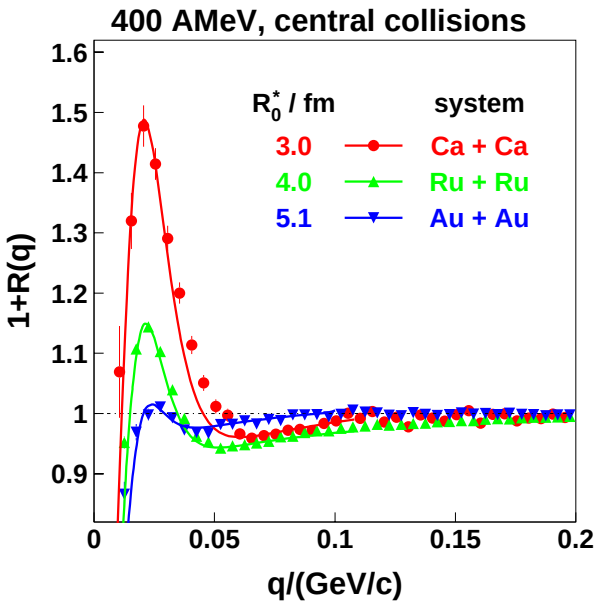

Fig. 1 *The two-proton correlation function at small relative momenta in central collisions of Ca + Ca, Ru + Ru and Au + Au at 400 AMeV. Symbols: experimental data, full lines: FSI-model simulations for zero lifetime and different values of the Gaussian radius parameter R_0^* as indicated. The simulated correlation functions are folded with the experimental q resolution of 4 MeV/c.*

[1] R. Kotte, J.P. Alard et al. (FOPI collaboration), Eur. Phys. J. A 23 (2005) 271

[2] R. Kotte, H.W. Barz et al. (FOPI collaboration), Eur. Phys. J. A 6 (1999) 185

[3] H.A. Gustafson, H.H. Gutbrod et al., Phys. Rev. Lett. 53 (1984) 544

QCD Sum Rules for the Nucleon: Where is its Mass coming from? [B, E, G]

R. Thomas, S. Zschocke, B. Kämpfer

The nucleon is the hard core of the visible matter in the universe. With the mass of 939 MeV it determines by far the weight of bodies. One possibility to explain the value of the nucleon mass is offered by QCD sum rules. There, various quantities, like vacuum mass or scalar and vector in-medium self-energies, are related to expectation values of products of quark and gluon operators, the so-called condensates, and moments of the parton distribution. Since these latter objects determine properties of other hadrons too, one might expect to describe a wealth of hadron characteristics by an optimized set of condensates.

Since previous approaches [1] employed the factorization hypothesis for higher-order condensates, especially for the condensates including four quark operators, it is tempting to spell out the complete Borel sum rule up to a given mass dimension and to study the influence of the relevant quantities for the nucleon mass, both in vacuum and in nuclear medium. The results of our investigations are exhibited in Fig. 1. In contrast to the QCD sum rule for the ω meson [2], the chiral condensate is the dominating quantity determining to a large extent the nucleon mass. In line with the often quoted Ioffe formula we find a linear dependence $M_{\rm N} \propto -\langle\bar{q}q\rangle$ when keeping other parameters fixed. On dimensional grounds the chiral condensate enters in case of the ω meson only via the renormalization invariant combination $m_q\langle\bar{q}q\rangle$ which suppresses numerically this condensate. On the other hand, the decomposition of Dirac structures in the nucleon case leads to a set of sum rules which allows for the occurence of even and odd operator dimensions. Other quantities, like the gluon condensate, the nucleon interpolating field mixing or 4-quark condensates are of subleading order for the vacuum mass. The deviation from the factorization of the 4-quark condensates is parameterized by $\kappa_{\rm N}^{\rm vac}$.

The in-medium changes of the chiral condensate cause substantial changes of the scalar nucleon self-energy at saturation density, see lower panel of Fig. 1. Furthermore, the density dependence of the 4-quark condensates, parameterized by a strength factor $\kappa_{\rm N}^{\rm med}$, becomes important in the nuclear medium. As noticed in [1], the known phenomenology of the in-medium nucleon is obtained only by assuming a weak density dependence of the 4-quark condensates. This looks like a contradiction to results for the ω meson [2], where a strong density dependence of the 4-quark condensates is assumed. It must be noted, however, that the nucleon sum rule is entered by many more 4-quark condensates. These differ in colour and Dirac structures from those entering the ω meson sum rule. It is conceivable that the net effect of the 4-quark condensates leads to some cancellation for the nucleon, while the ω meson sum rule is sensitive to the few entering 4-quark condensates.

The study of the density dependence of linear combinations of 4-quark condensates in other hadrons as well as di-electron measurements at HADES can provide further constraints on these parameters and can thus offer further insight into the origin of the mass of visible matter in the universe.

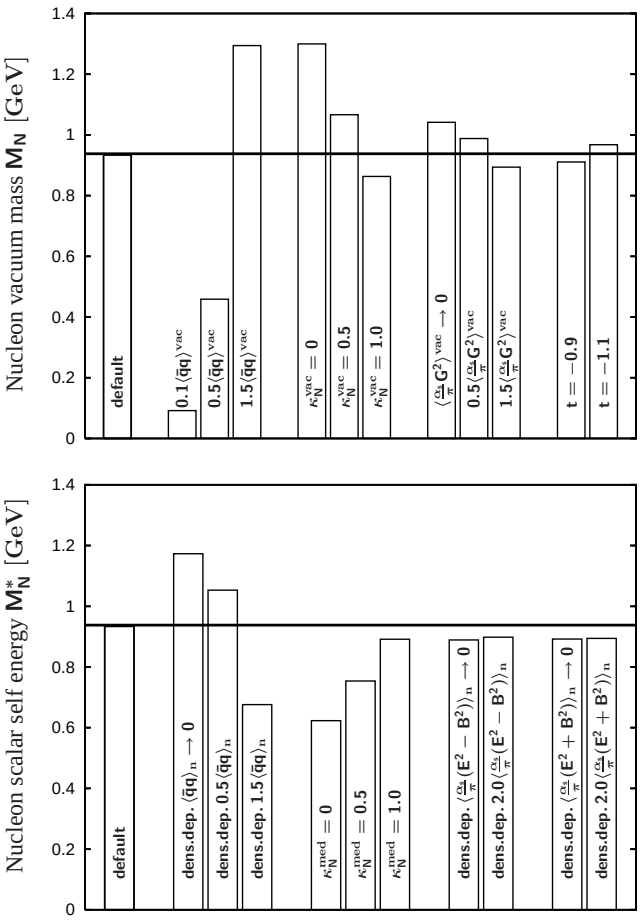

Fig. 1 *Importance of various contributions to the nucleon mass. Default values are* $\langle\bar{q}q\rangle^{\rm vac} = (-0.245\,{\rm GeV})^3$ *and* $\langle(\alpha_s/\pi)G^2\rangle^{\rm vac} = (0.33\,{\rm GeV})^4$. *The general interpolating fields have a default mixing angle of* $t = -1$, *which corresponds to the Ioffe field. The factorized and summed up 4-quark condensates are fine-tuned with a factor* $\kappa_N^{vac} = 0.8$ *to the vacuum nucleon mass. Upper panel: Nucleon in vacuum. Lower panel: Nucleon in medium at saturation density. The linear density dependence of in-medium 4-quark condensates is regulated by the factor* $\kappa_N^{\rm med}$. *The variations of the gluon condensate, whose density dependence is written here in terms of the color-electromagnetic fields E and B, cause minor effects.*

[1] T.D. Cohen, R.J. Furnstahl, D.K. Kriegel, X.M. Jin, Prog. Part. Nucl. Phys. 35 (1995) 221

[2] R. Thomas, K. Gallmeister, S. Zschocke, B. Kämpfer, hep-ph/0501202

Strangeness Saturation in Relativistic Heavy Ion Collisions [B]

J. Cleymans,[1] B. Kämpfer, M. Kaneta,[2] S. Wheaton,[1] N. Xu[3]

Whether chemical equilibrium is reached in heavy-ion reactions is a longstanding and controversially debated question. Despite of a lacking rigorous proof the thermostatistical models are successful in describing a wealth of data by a few parameters. Among them are temperature, baryo-chemical potential and strangeness chemical potential characterizing the chemical freeze-out. At low energies often a strangeness saturation factor needs to be introduced. This strangeness factor is shown to increase with centrality in heavy-ion collisions at CERN-SPS energies [1].

We extended our analysis of strangeness saturation at RHIC energies and report here on collisons Au + Au at $\sqrt{s_{NN}} = 130$ GeV. Data at midrapidity are at our disposal from various collaborations. We use as input the following ratios: $\pi^-_{(2)}$ / $\pi^+_{(2)}$, $\pi^-_{(1)}$ / $\pi^+_{(1)}$, $K^+_{(2)}$ / $K^-_{(2)}$, $\bar{K}^{*0}$ / K^{*0}, $\bar{p}_{(1)}$ / $p_{(1)}$, $\bar{p}_{(2)}$ / $p_{(2)}$, $\bar{\Lambda}_{(1)}$ / $\Lambda_{(1)}$, $\bar{\Lambda}_{(2)}$ / $\Lambda_{(2)}$, $\bar{\Xi}^+_{(1)}$ / $\Xi^-_{(1)}$, $\bar{\Omega}^+$ / Ω^-, $K^-_{(2)}$ / $\pi^-_{(2)}$, $K^-_{(2)}$ / $\pi^-_{(1)}$, K^0_s / $\pi^-_{(1)}$, $\bar{p}_{(1)}$ / $\pi^-_{(2)}$, $\bar{p}_{(2)}$ / $\pi^-_{(1)}$, $\Lambda_{(1)}$ / $\pi^-_{(1)}$, $\Lambda_{(2)}$ / $\pi^-_{(2)}$, $\langle K^*0\rangle$ / $\pi^-_{(1)}$, ϕ / $\pi^-_{(1)}$, $\Xi^-_{(1)}$ / $\pi^-_{(1)}$, $(\Omega^- + \bar{\Omega}^+)$ / $\pi^-_{(1)}$, where the subscript "(1)" indicates yields corrected for weak decay feed-down, while yields labelled by "(2)" include a contribution from weak decays. The results are exhibited in Fig. 1. Most interesting is the rise of strangeness saturation towards unity with centrality. If one considers the strangeness saturation factor as indicator of a possible departure from equilibrium than one can conclude that for central collisions an equilibrium description is adequate.

In addition, freeze-out parameters allow a valuable orientation in the temperature-density phase diagram of strongly interacting matter.

[1] J. Cleymans, B. Kämpfer, S. Wheaton, Phys. Rev. C 65 (2002) 027901, Nucl. Phys. A 715 (2003) 553c

[2] J. Cleymans, B. Kämpfer et al., Phys. Rev. C (2005) in print

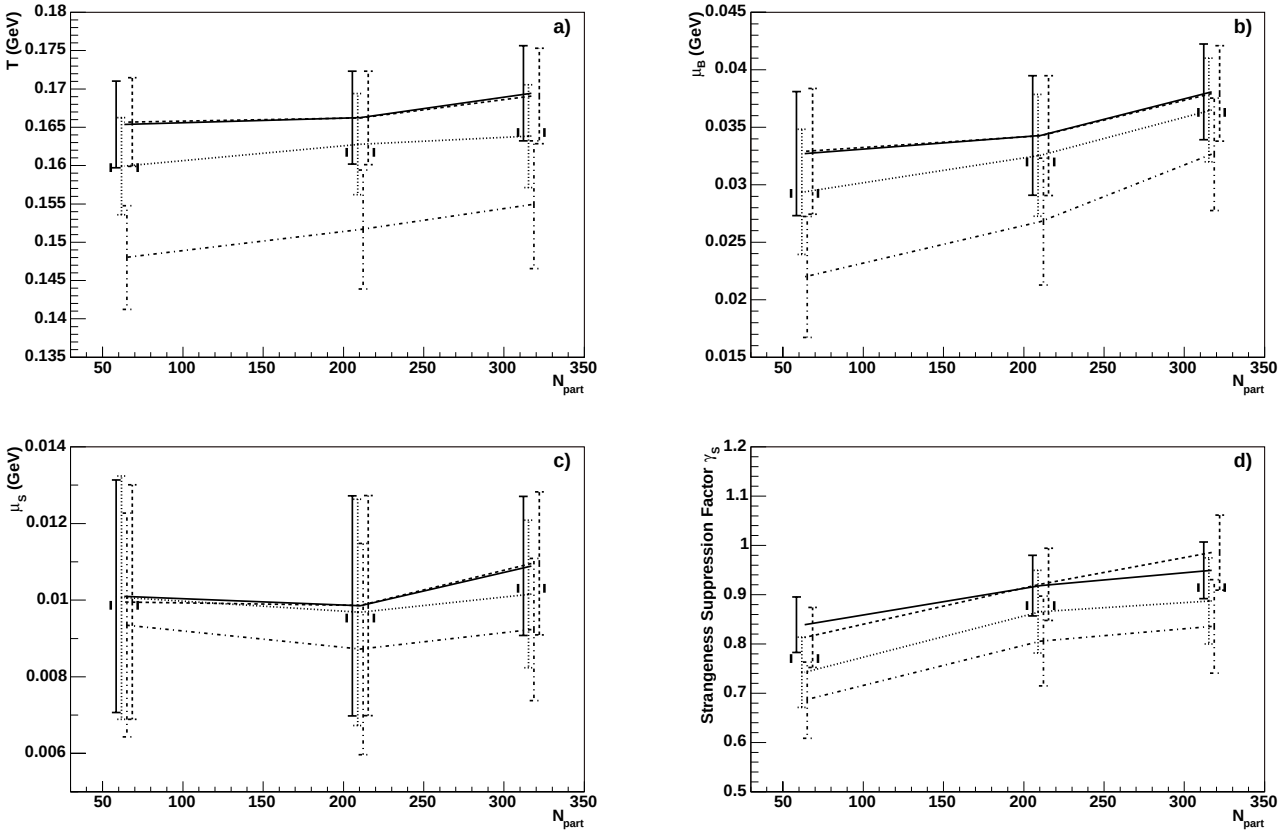

Fig. 1 *Results of the fit procedure of 21 hadron ratios for three centrality classes determined by the participant number $N_{\rm part}$. a): temperature T, b): baryo-chemical potential μ_B, c): strangeness chemical potential μ_S, d): strangeness saturation factor γ_S. For each centrality class, four fits were performed: Fit I: all available ratios listed in text included; Fit II: only ratios of π, K, p, Λ and Ξ included; Fit III: only ratios of π, K, p and Λ included; Fit IV: only ratios of π, K and p included. In this way, the effect of the various multiplicities on the thermal parameters is investigated. For details see [2].*

[1] *UCT-CERN Research Centre, Dep. of Physics, University of Cape Town, Rondebosch 7701, Cape Town, South Africa*

[2] *RIKEN BNL Research Center, Brookhaven National Laboratory, Upton, New York 11973, USA*

[3] *Lawrence Berkeley National Laboratory, Berkeley, California 94720,USA*

Equation of State of Strongly Interacting Matter [B,G]

M. Bluhm, B. Kämpfer, G. Soff[1]

The Compressed Baryon Matter (CBM) project at the future Facility for Anti-Proton and Ion Research (Darmstadt) envisages a systematic investigation of heavy-ion reactions in an energy range where maximum baryon densities can be achieved. In such a way the equation of state in a certain region of temperature T and density n will be probed. Particularly interesting is the region around the phase boundary from confined to deconfined matter and the tri-critical end point.

Valuable information on the equation of state is delivered by lattice QCD where this information is derived from first principles. The present lattice QCD evaluations are still restricted to small baryon densities. In addition, the employed quark masses are unphysically large, resulting in an excessive pion mass. In this situation effective models are useful which allow both a chiral extrapolation and the extrapolation to large baryon density. The second goal can be accomplished by our quasi-particle model [1]. The chiral extrapolation, however, requires knowledge on the equation of state for various quark masses which is not yet at our disposal.

Our quasi-particle model [1, 2] receives some support from Φ derivable functionals. It can be directly related to the equation of state from lattice QCD [3]. There, the pressure is determined on the lattice in the form

$$p(T,\mu) = c_0(T) + c_2(T)(\mu/T)^2 + c_4(T)(\mu/T)^4 + c_6(T)(\mu/T)^6 + \cdots , \quad (1)$$

where μ is the quark-chemical potential. Our model in turn bases on a compact expression for the pressure $p(T,\mu)$ and a thermodynamic consistency condition. By straightforward but cumbersome differentation, the coefficients $c_{2,4,6}$ can be derived as $c_i = \frac{T^{i-4}}{i!}\frac{\partial^i p}{\partial \mu^i}|_{\mu=0}$. All expansion coefficients are related to one effective coupling $G^2(T)$ and its derivatives. Therefore, comparison with lattice data for c_j serves as sensitive test of the model.

In Fig. 1 the model's results are compared with the available lattice data. One observes a good agreement, even if c_4 seems slightly to be under-estimated. Nonetheless, the direct comparison of the pressure looks very promising, see Fig. 2. Encouraged by this agreement one can continue the equation of state into the region of large baryon density without introducing additional assumptions or parameters. Various flow patterns in heavy-ion collisions can be modelled within a hydrodynamical approach. We are preparing a study of the azimuthal anisotropy v_2 at large baryon density as relevant for CBM.

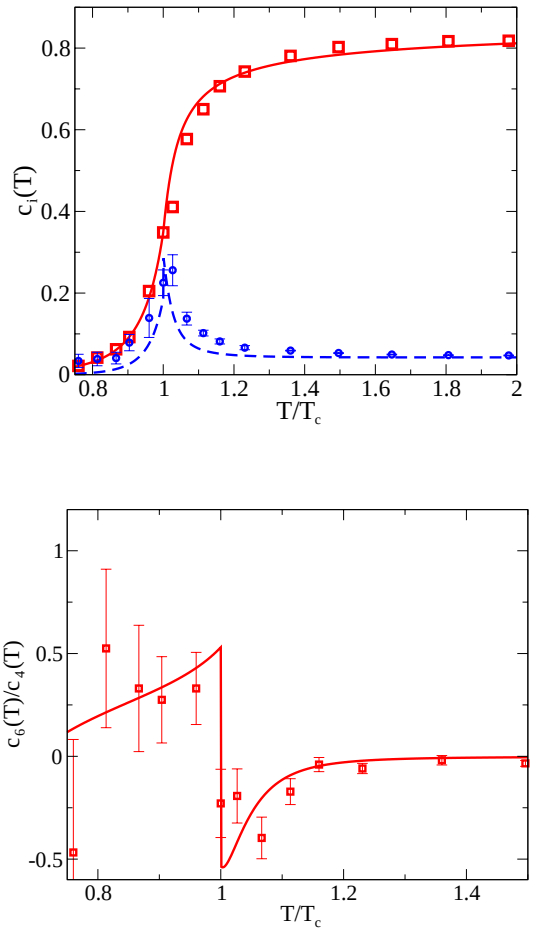

Fig. 1 *Comparison of lattice QCD data [3] for the coefficients $c_{2,4}$ (upper panel, squares: c_2, dots: c_4) and c_6/c_4 (lower panel) with our quasi-particle model.*

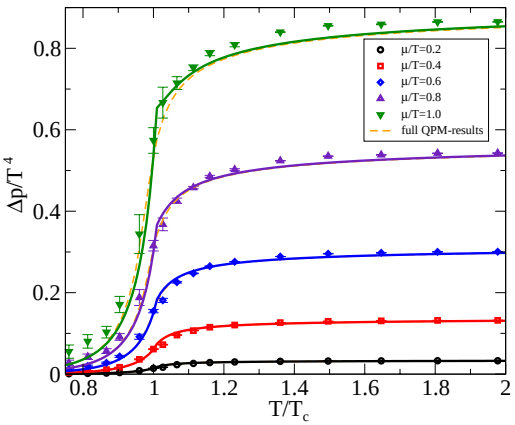

Fig. 2 *Comparison of lattice QCD data [3] for the excess pressure $p(T,\mu) - c_0(T)$ with our quasi-particle model.*

[1] A. Peshier, B. Kämpfer, G. Soff, Phys. Rev. D 66 (2002) 094003
[2] M. Bluhm, B. Kämpfer, G. Soff, J. Phys. G 31 (2005) in print
[3] C.R. Allton, S. Ejiri et al., Phys. Rev. D 68 (2003) 014507; S. Ejiri, C.R. Allton et al., hep-lat/0409033

[1] *Technische Universität Dresden*

Cosmic Confinement Dynamics [B, E]

M. Bluhm, B. Kämpfer

During the cosmic confinement transition freely roaming quarks and gluons were converted into hadrons. Since the order of the transition is still matter of debate, many speculations on possible imprints on the subsequent evolution have been put forward (for a survey see [1]). Among the dramatic traces of confinement could be a modified (inhomogeneous) nucleosynthesis and strangelets. Both speculations base on the assumption of a first-order confinement transition with strong super-cooling. By now, however, the improved evaluations of the equation of state of strongly interacting matter within lattice QCD point to a smooth transition which looks like a cross-over. The resulting equation of state [2] can be parameterized with our quasi-particle model [3]. Supplemented by the lepton and photon background contributions we have studied the dynamics of the cosmic confinement transition by solving numerically the corresponding Friedmann equations. With the equation of state the temperature evolution in the universe becomes smooth, as exhibited in Fig. 1. We contrast the new evolutionary scenario with the one obtained by employing the bag model. The large latent heat causes a long period of constant temperature. Another extreme scenario bases on the assumption of deep super-cooling. The resulting differences in the time evolution of the cosmic scale factor ("world radius") are tiny, see Fig. 2. Even the possible mini-inflationary epoch with accelerated expansion driven by the vacuum energy [4] has minor differences to the smooth confinement dynamics.

In a first-order phase transition with growing bubbles of hadron matter, a distinct baryon contrast develops. It was argued that the remaining islands of deconfined matter transform into quark droplets (strangelets). As evidenced in Fig. 3, the lattice QCD supported equation of state points to a smoothly interpolating baryon density from the high-temperature deconfinement to the low-temperature confinement phase.

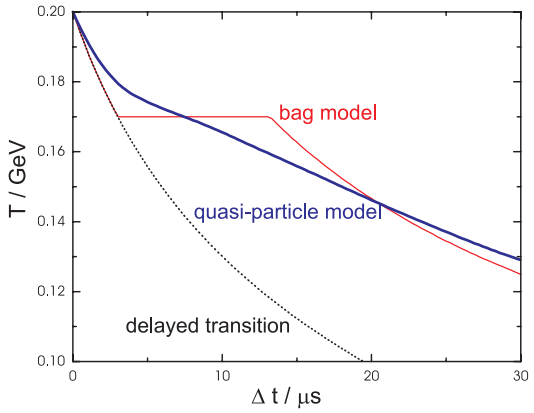

Fig. 1 *Temperature T as a function of time. The quasi-particle model results are compared with previous estimates basing on the bag model. The case of a strongly delayed confinement transition is exhibited too.*

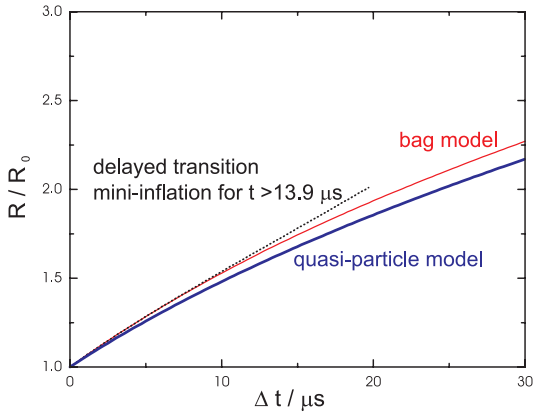

Fig. 2 *Time evolution of the scaled world radius R/R_0 for the scenarios in Fig. 1.*

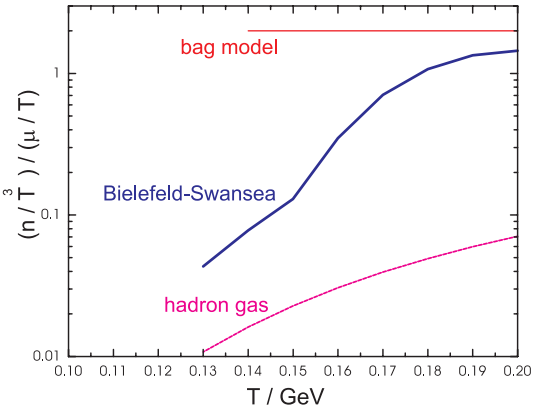

Fig. 3 *Appropriately scaled net baryon density n as a function of temperature. (here, μ is the chemical potential). The curves labelled by "bag model" and "hadron gas" depict the density in the deconfined and confined phases within the bag model approach. The curve labelled by "Bielefeld-Swansea" is for the lattice QCD results parameterized by our quasi-particle model.*

[1] B. Kämpfer, B. Lukacs, Gy. Paal, Cosmic Phase Transitions, Teubner-Verlag, Stuttgart 1994; B. Kämpfer, Ann. Phys. 9 (2000) 605

[2] F. Karsch, E. Laermann and A. Peikert, Phys. Lett. B 478 (2000) 447; Eur. Phys. J. C 29 (2003) 549

[3] B. Kämpfer, M. Bluhm, G. Soff, hep-ph/0402252

[4] L.L. Jenkowski, B. Kämpfer, V.M. Sysoev, Z. Phys. C 48 (1990) 147

Hadro-Chemistry in the Strange Early Universe [B,G]

M. Bluhm, B. Kämpfer

The evolution of the hadron content of the universe from confinement till the onset of primordial nucleosynthesis can be described by means of quantum statistics. A sizeable part of the strong interaction among the thermally excited hadrons is absorbed in resonances according to the Dashen-Ma-Bernstein theorem [1]. Moreover, the equation of state formulated within the resonance gas model agrees quantitatively with results of lattice QCD calculations once the same approximations are applied[2]. This framework can be exploited to follow the fate of individual hadron species.

Using adiabaticity and baryon number conservation and the presently observed photon-to-baryon ratio of $\eta = \mathcal{O}(10^{10})$ as constraints [3, 4], one obtains the evolution of selected hadrons as exhibited in Fig. 1. Remarkably, a pronounced splitting of nucleon and anti-nucleon number densities at a temperature between 30 and 40 MeV is seen. It should be noted that, just below 30 MeV, the nucleon–anti-nucleon annihilation rate becomes too small to maintain hadro-chemical equilibrium. Given the observed tiny asymmetry of baryons to anti-baryons, the increase of the chemical potential (see Fig. 2) happens before this decoupling, ensuring that the anti-baryons have sufficiently annihilated to prevent a noticeable anti-matter component in the universe.

The early universe was quite strange. Shortly after the cosmic confinement the strange baryons (mainly Λ's) contribute up to 30 % to the total baryon number (see Fig. 3). Also the kaon number amounts to such a fraction of the hadron number. However, with elapsing time (see Fig. 4) these contributions annihilate or decay without recreation.

Finally, we emphasize the strong and unexpectedly long-lasting dominance of pions which ceases just prior to nucleosynthesis, as seen in Fig. 1.

[1] R. Dashen, S.H. Ma, H.J. Bernstein, Phys. Rev. 187 (1969) 345

[2] F. Karsch, K. Redlich, A. Tawfik, Phys. Lett. B 571 (2003) 67

[3] M.J. Fromerth, J. Rafelski, astro-ph/0211346

[4] B. Kämpfer, M. Bluhm, J. Phys. G 31 (2005) in print

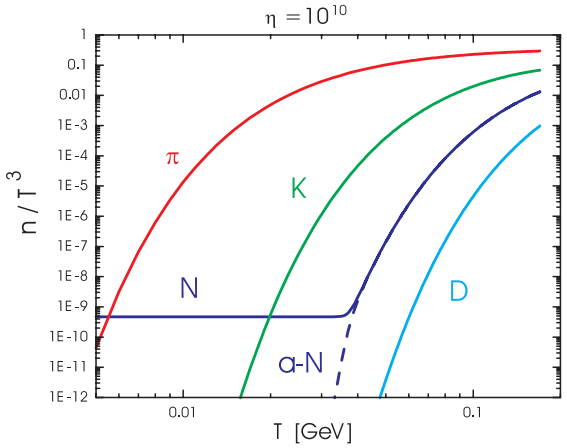

Fig. 1 *Hadron densities (π: pions, K: kaons, N: nucleons, $a-N$: anti-nucleons, D: D mesons) as a function of temperature.*

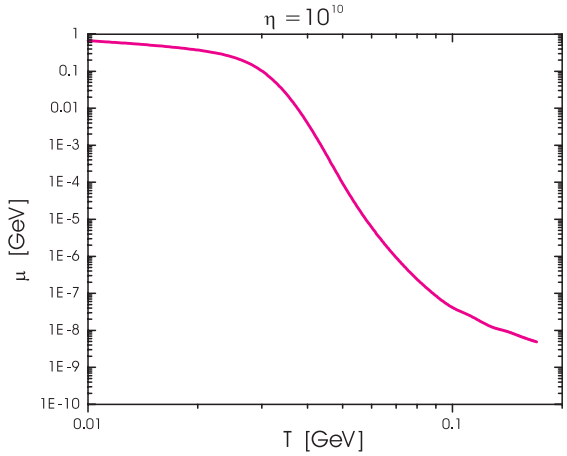

Fig. 2 *Chemical potential as a function of temperature.*

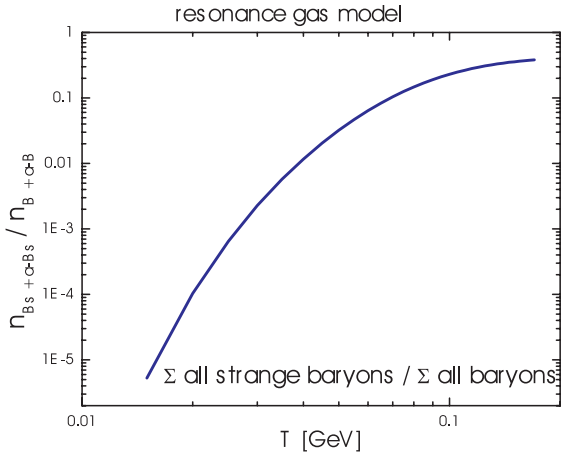

Fig. 3 *Ratio of baryons with strangeness to total baryon number as a function of temperature.*

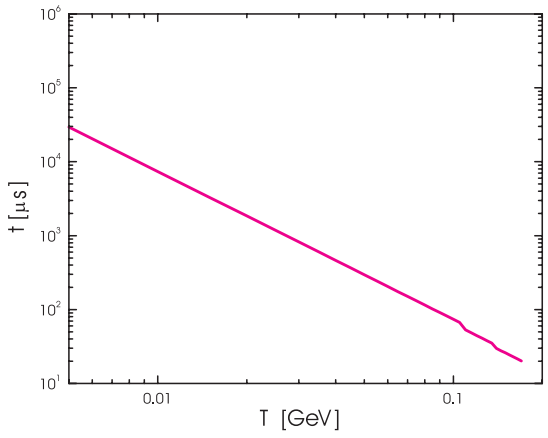

Fig. 4 *Elapsed time as a function of temperature.*

Testing Novel TOF Detectors for CBM at ELBE [E, G]

F. Dohrmann, R. Kotte, L. Naumann, B. Kämpfer, E. Grosse

Testing of detectors often involves minimum ionizing particles (mips). Usually the intrinsic time resolution of the desired beam is quite broad such that additional reference counters are needed. For testing resistive plate chambers (RPC), which have a wide spectrum of application in particle physics and beyond [1, 2, 3], such reference counters need to have a time resolution comparable or better to that of an RPC detector. The time resolution of the RPC detector has to be corrected for contributions by electronics as well as reference counters and moreover the pulse height dependence (walk) of the reference counter has to be taken into account. If however the test beam itself has a very good time resolution, one may avoid these problems by referencing the test detector against the beam structure. The Rossendorf electron accelerator ELBE provides up to 40 MeV electrons. The beam packets with time spread of better than 10 ps are well suited for testing time resolutions. Moreover, electrons with energies of a few 10 MeV have very similar specific energy losses as minimal ionizing hadrons and thus may simulate the behavior with respect to pulse height, time resolution and detection efficiency.

The focus of the RPC detector tests at ELBE will be time resolution. The challenge of this elegant method is to provide rather low intensity electron beams. E.g. the CBM experiment at the future FAIR facility at GSI considers hit densities between 20 kHz/cm^2 (near beam) and 1 kHz/cm^2 for acceptable time resolution as well as efficiency. Currently, beam diagnostics at ELBE require a minimal beam intensity of $\sim 1\,\mu$A. Beam experiments have been achieved with three orders of magnitude lower intensities, i.e. ~ 1 nA or $\sim 1 \times 10^{10}$ Hz , but this rate is still too high for detector tests even when distributed over a sufficiently large area. It is conceivable that in the future even lower beam intensities are available. Currently a reliable solution is to reduce beam intensities by a scatterer if necessary.

First parasitic beam tests were performed at the radiation facility cave at ELBE. A 15 MeV electron beam was scattered off a thin Al foil. Electrons were detected under 45 degrees scattering angle. Fig. 1 shows the testing telescope. The background distribution was scanned with respect to the main scattering direction, as shown in Fig. 2. A second test in preparation will use scintillators with very good time resolution as have been used for testing RPC in other laboratories.

We have contacted RPC developing groups within our JRA 12 for preparations on RPC tests and prepared the installation of a gas supply facility for gases required for RPC tests. This allows mixing and using these gases at the accelerator as well as in the laboratory. Moreover, cabling, acquisition of hardware and electronics has been completed and first test of an RPC prototype in the laboratory with ^{90}Sr source have been performed.

The test facility is set up for RPC tests. In addition we will set up a second experimental facility which will enable us to perform detector tests completely independent of the radiation facility cave. This second cave should be available for more intensive tests.

This project is supported in part by the EU FP6 I3HP, proposal 506078, JRA12.

[1] http://www.gsi.de/zukunftsprojekt/forschung_e.html

[2] M. Petrovici, K.D. Hildenbrand et al., Nucl. Instr. Meth. A 508 (2003) 75

[3] A. Blanco, R. Ferreira-Marques et al., Nucl. Instr. Meth. A 508 (2003) 70

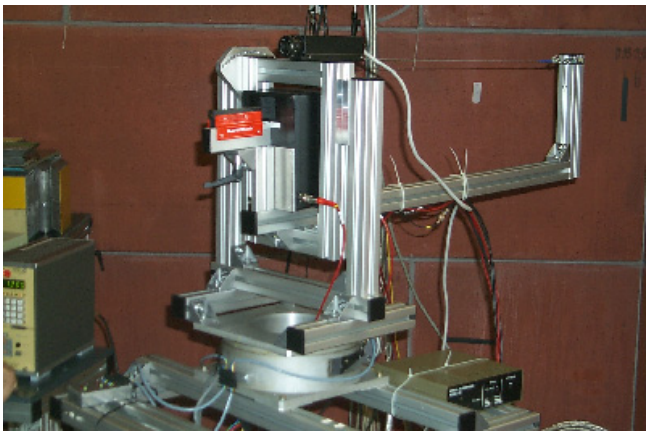

Fig. 1 *The testing telescope for background studies. Two thin scintillators are fixed on a rotating step motor. A laser is used for position calibration.*

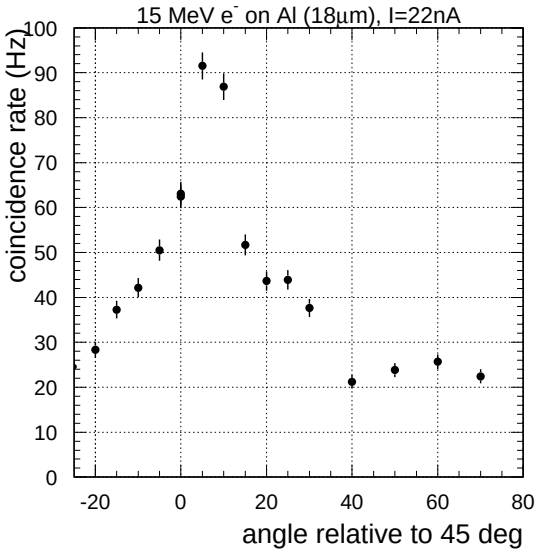

Fig. 2 *Distribution of background relative to 45 degrees. The main peak corresponds to elastically scattered electrons observed under 45 degrees with respect to the beam direction.*

Life Sciences:

Biostructures and Radiation

Biomedical research in the Institut of Nuclear and Hadron Physics focusses onto three main topics
(i) Studies on the structural dynamics of biomolecules by means of infrared light,
(ii) Radiation biology with soft, quasi-monochromatic X-rays,
(iii) In-beam positron emission tomography (PET) for quality assurance of charged hadron therapy.

Structural dynamics of biomolecules: The diverse functions of biomolecules are determined by their structure. We are particularly interested in the detection of structural alterations in proteins and DNA. Our research exploits IR-radiation from different sources to induce and monitor structural changes in two protein classes, G protein-coupled receptors (GPCRs) and bacterial surface layers. The former are the main drug targets involved in biological signalling, whereas the latter are of biotechnological interest due to their binding of heavy metals.
We have established several new general approaches to study conformational changes in biomolecules. For example, by 2D cross-correlation spectroscopy from combined infrared and fluorescence data, we investigate the steric coupling between distant protein domains. Additionally, using IR-pulses, conformational transitions can be induced in biomolecules. We are particularly exploring the combination of IR-pulse and optical probe techniques, that provide high sensitivity and spatial resolution. Here, refractive index-based methods such as transient grating and Brewster microscopy have been set up and tested. With the first lasing of the FEL, preliminary results have thus been obtained, showing that IR-induced superstructural changes in plasmid DNA can be followed by reflection / diffraction of visible laser light.

Cell radiobiology: Photon radiation in the energy range from 10 to 100 keV is widely used in diagnostic and therapeutic radiology. Therefore, a precise determination of the relative biological effectiveness (RBE) of such X-rays and moreover of the RBE dependence on photon energy for different cell types and biological endpoints is highly desirable. The necessary intensive quasi-monochromatic X-ray beam of variable energy can be produced at the ELBE superconducting electron accelerator by channeling of the relativistic electrons in single crystals. In a series of experiments channeling radiation (CR) has been produced in diamond crystals at low beam intensity which allowed to measure the X-ray energy distribution. The energy, energy width and yield of the channeling X-rays in dependence on the energy of the electron beam and on the thickness of the diamond crystal have been investigated. Furthermore, the spatial and spectral distribution of the background radiation at the irradiation site has been measured proving that the quasi-monochromatic channeling X-rays can be separated from the unavoidable polychromatic bremsstrahlung background by Bragg reflection in polycrystalline graphite. The encouraging results initiated the next step, which will be the increase of the CR intensity by enhancement of the corresponding electron beam intensity in order to meet the photon flux requirements of cell irradiations. In parallel with the CR experiments at ELBE, extensive cell irradiation studies at conventional low-energy X-ray tubes have been performed which will result in RBE values for chromosomal aberrations in a mammary epithelial cell line. In addition to the Giemsa staining, the technique of fluorescence in-situ hybridisation (FISH) was established and will allow to extend the studies on the investigation of aberrations for specific chromosomes. The coupling of photon and electron transport in the Monte Carlo program AMOS allows now the simulation of both primary and secondary radiation down to cellular dimensions.

In-beam PET for quality assurance of charged hadron therapy: During the three therapy beam times of the year 2004 another 40 cancer patients have bean treated with ^{12}C beams at the Ger-

man heavy ion therapy facility at GSI Darmstadt. For quality assurance all fractionated patient irradiations have been controlled by means of in-beam PET. Successively significant numbers of patients with a sufficiently long follow up time become available and first conclusions on the clinical benefit of carbon ion therapy can be drawn: The analysis of 44 patients with extracranial chordomas revealed after 4 years a local tumour control rate of 74 % for carbon ions compared to 60 % for patients treated by means of modern fractionated stereotactic photon therapy. Obviously carbon ions offer advantages in the treatment of these tumours. Besides the clinical activities, extensive work on the further development of the in-beam PET method for therapy monitoring has been performed, comprising 3 topics: (i) In the course of generalisation of in-beam PET from ^{12}C-beams to all therapeutically relevant ions with atomic numbers between 1 and 8 the results of a comprehensive experimental study for proton beams have been published, experiments with ^{3}He beams have been carried out and advanced methods for predicting the β^{+}-activity from the treatment plan are being developed. (ii) The experimental proof of principle for an in-beam dedicated data acquisition scheme suppressing efficiently the beam induced random coincidences and allows the counting statistics in the in-beam PET images to be increased by nearly a factor of 2. (iii) Investigation on the feasibility of real time reconstruction of in-beam PET data has been initiated. A successful solution of this problem would allow the dose delivery process to be immediately observed.

The collaboration with various groups from outside the Institute is gracefully acknowledged.

Structural Dynamics of Biomolecules

- *Rockefeller University, New York*
- *Universität Orenburg*
- *Universität Erlangen-Nürnberg*
- *MPI für Zellbiologie und Genetik, Dresden*
- *ISAS, Berlin*
- *ENEA, Frascati (Italien)*
- *CLIO, Paris (Frankreich)*

Cell radiobiology

- *Institut für Bioanorganische und Radiopharmazeutische Chemie (FZ Rossendorf)*
- *Klinik für Strahlentherapie und Radioonkologie, TU Dresden*
- *Institut für Kern- und Teilchenphysik, TU Dresden*
- *GSI Darmstadt*
- *Medizinische Fakultät, Universität Göttingen*

In-beam PET for quality assurance of charged hadron therapy

- *DKFZ Heidelberg*
- *Universität Heidelberg*
- *GSI Darmstadt*
- *Soltan Institute for Nuclear Studies, Otwock Swierk, Poland*
- *MedAustron, Wiener Neustadt, Österreich*
- *Atominstitut der Österreichischen Universitäten an der TU Wien, Österreich*
- *Universite Claude Bernard Lyon 1, Frankreich*
- *CERN, Genf, Schweiz*
- *Harvard Medical School, Boston, USA*

Secondary Structure of the Refolded Extracellular Domains of the Human Glycine Receptor α_1-Subunit

U. Breitinger[1], H.-G. Breitinger[1], F. Bauer[1], D. Glockenhammer[1], C.-M. Becker[1], K. Fahmy

The strychnine-sensitive glycine receptor is a ligand-gated chloride channel composed of ligand-binding α- and gephyrin-anchoring β-subunits. No crystal structure is available and a low total α-helical content of only $\approx 15\,\%$ is predicted. As transmembrane segments are prime candidates for helical structure, little helical structure would be expected in extracellular domains. Vice versa, detection of helical extracellular domains would imply that alternative transmembrane structures may be present. We have assessed by infrared spectroscopy the secondary structure of the extracellular N-terminal domain (aa 1 - 219) and of the TM3-4 loop (aa 309 - 392) of the human GlyR-α_1 subunit expressed in *E. coli* [1]. The amide I (C = O stretching) absorption in the 1620 - 1690 cm^{-1} range is characteristic of the type of secondary structure. Frequencies in the 1620 - 1640 cm^{-1} and 1652 - 1660 cm^{-1} range are typically associated with β-sheet and α-helical structures, respectively, whereas random structures mainly absorb between 1640 and 1650 cm^{-1}. Here, we follow established assignments [2, 3, 4].

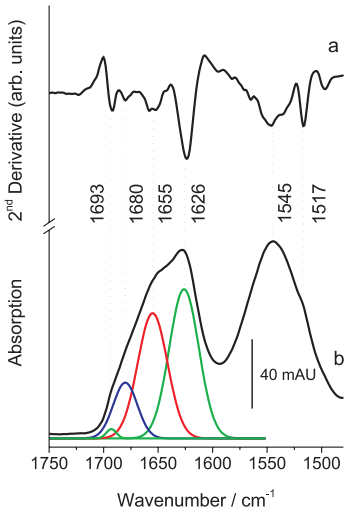

Fig. 1 *FTIR-based secondary structure analysis of the N-terminal extracellular domain of the glycine receptor measured in 10 mM sodium phosphate buffer pH 7.4. a) Second derivative of the IR-absorption spectrum in the amide I and II frequency range. b) Gaussian bands obtained from a fit of the amide I and II absorption. For clarity, only the four bands in the amide I range are shown.*

Fig. 1 (b) shows the amide I and II absorption bands of the N-terminal extracellular domain at pH 7.4. The minima in the second derivative of the absorption spectrum (Fig. 1 (a)) indicate the presence of amide I modes near 1626, 1655, 1680, and 1692 cm^{-1} which give rise to the shoulders in the amide I contour of the expressed receptor domain. In agreement with this unbiased identification of underlying components, the fit of the amide I band resulted in four components with centre frequencies within less than 2 cm^{-1} deviation from the second derivative minima. The reproduction of the measured band by the sum of the fitted Gaussian bands is a strong indication for the presence of α-helical (1655 cm^{-1} component) as well as β-sheet (1626 cm^{-1} component) structural elements. The band at higher frequencies, particularly at 1692 cm^{-1}, is typically associated with antiparallel β-sheets. The 1680 cm^{-1} component may additionally indicate the presence of β-turns. Based on the band integrals, the analysis of the FTIR-spectra suggests a secondary structure composition of 48 % β-sheets, 25 % α-helices.

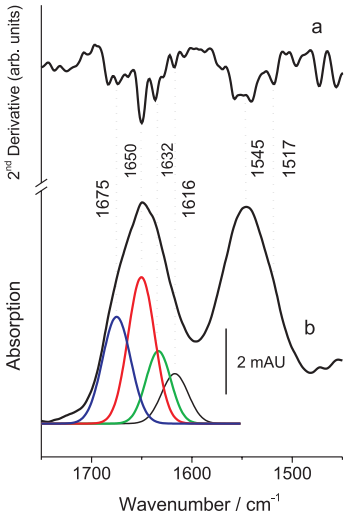

Fig. 2 *FTIR-based secondary structure analysis of the TM3-4 loop of the glycine receptor measured in 10 mM sodium phosphate buffer pH 7.4. a) Second derivative of the IR-absorption spectrum in the amide I and II frequency range. b) Gaussian bands obtained from a fit of the amide I and II absorption.*

Fig. 2 shows the analogous investigation of the secondary structure of the TM3-4 loop. Again, Gaussian bands could be fitted that agree well with the positions identified by the second derivative spectrum. The prominent Gaussian component is centred at 1650 cm^{-1}, a frequency that is difficult to assign because it falls between the typical frequencies of absorption by α-helices above 1650 cm^{-1} and of "random coils" below 1650 cm^{-1}. The second largest band is located at 1675 cm^{-1}, indicative of β-turns. The band at 1632 cm^{-1} agrees with β-sheet structure, whereas the lowest frequency band at 1616 cm^{-1} cannot be assigned to a classical secondary structure. In summary, the TM3-4 loop peptide appears to contain roughly 20 % β-sheet structure and 30 % β-turns but is probably less ordered than the N-terminal extracellular domain and has less if any α-helical content. The $\approx 25\,\%$ α-helical content in the N-terminal domain accounts for 12 % of the total of 15 % predicted α-helical structure. Another 5 % would be contributed by TM2 [5]. Provided, the prediction models are correct, our results suggest that the segments TM1, 3, and 4 may not be classical transmembrane helices.

[1] U. Breitinger, H.-G. Breitinger et al., J. Biol. Chem. 279 (2004) 1627
[2] A. Dong, P. Huang, W.S. Caughy, Biochemistry 29 (1990) 3303
[3] S. Krimm, J. Bandekar, Adv. Prot. Chem. 38 (1986) 181
[4] J. Bandekar, Biochimica et Biophysica Acta 1120 (1992) 123
[5] N. Unwin, Nature 373 (1995) 37

[1] *Biochemistry Dept., University Erlangen*

Coupling of Cytosolic Domain Movements and Transmembrane Structure in Rhodopsin studied by 2D-IR-Fluorescence Correlation Spectroscopy

N. Lehmann, U. Alexiev[1], K. Fahmy

Activation of G-protein-coupled receptors (GPCRs) requires the transmittance of a ligand-induced structural change at the extracellular ligand-binding site to the cytosolic face where G-proteins become activated. The bovine photoreceptor (rhodopsin) is a prototypical GPCR acting as a molecular switch in visual signal transduction. We have investigated the steric coupling between distinct functional sites in rhodopsin. In the past, light-induced secondary structural changes have been recorded by FTIR-difference spectroscopy, but site-specific structural changes have been assigned only to a few side chains mainly in the transmembrane part [1, 2]. These assignments do not allow to draw conclusions on the movement of a larger protein domain, as the latter may not alter its secondary structure and is thus IR-spectroscopically silent. Therefore, cytosolic domains have been addressed mainly biochemically and by fluorescence and spin-labelling [3, 4, 5, 6]. We have established a new approach by combining FTIR-difference spectroscopy with site-directed fluorescence labeling. FTIR difference spectra of the formation and decay of metarhodopsin II in Cys^{316}-fluoresceine-labeled rhodopsin were recorded. By ATR-spectroscopy [7, 8] changes in fluorescence could be detected simultaneously with the recording of IR-absorption changes using branched light guides for fluoresceine excitation (475 nm laser diode) and emission (photomultiplier tube, 530 Schott filter). Thus, a precise time-correlation between secondary structural changes and the alteration of the local environment of Cys^{316} in helix 8 of rhodopsin could be achieved. We have shown that the extreme C-terminus of rhodopsin is crucial for the stability of the MII state by coupling structural changes around Asp^{83} to the cytosolic receptor surface (see Annual Report 2003). Here, we have addressed the question whether it acts as a link between helix 8 and other cytosolic sites. In this case, the kinetics of the identified C-terminally coupled conformational changes should be highly correlated with the kinetics of helix 8 movement monitored by the fluorescence label. This correlation was evaluated by 2D-cross correlation. The IR-difference bands measured at 5° C in 18 time slices (covering a total of 15 min) were correlated with the averaged fluorescence observed after MII formation in the same time slices. The resulting synchronous and the disrelation spectrum are shown in Fig. 1. They represent the averaged amplitudes of the Fourier components of the time evolution at a given wavenumber that are in phase and out of phase with the corresponding Fourier component in the fluorescence signal, respectively. For comparison, the initial IR-difference spectrum is also shown. The insert displays the typical fluorescence decay after MII formation caused by repositioning of helix 8 during MII decay. IR bands highly correlated with helix 8 movement are characterized by a peak in the synchronous

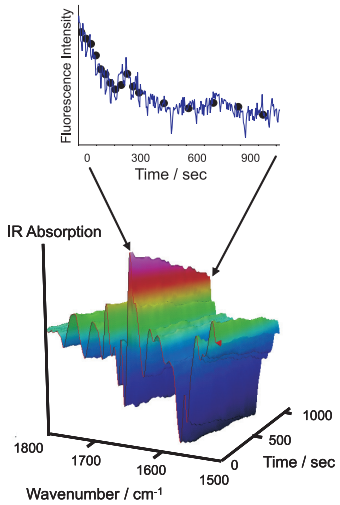

Fig. 1 *Top: Change of fluorescence intensity after MII formation measured at pH 5 at 5° C in Cys^{316}-fluoresceine-labeled rhodopsin; bottom: time-dependent FTIR-difference spectra of MII-decay of the identical sample.*

spectrum and the absence of a corresponding peak in the disrelation spectrum. Amplitudes in the correlation spectra in Fig. 2 where squared (resulting in positive peaks only) and scaled such that $2R^{0.5}$ is the % difference of a hypothetical first order rate constant of an IR-decay relative to the rate of the fluorescence change (R: ratio of intensities asynchronous / synchronous). The C = O stretch of Asp^{83} and the 1643 cm^{-1} absorption correlate strongly with the fluorescence, whereas the C = O stretching bond of glu^{122} evolves highly asynchronously with alterations around the label in helix 8. The data provide a strong indication that the Schiff base environment, rather than the β-ionone ring, couples to the surface conformation around helix 8 and that the latter may partially unwind in the MII state.

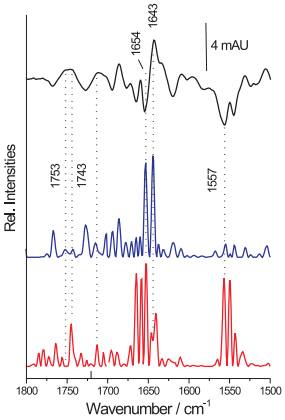

Fig. 2 *Top to bottom: MII difference spectrum after 15 sec of photoactivation, synchronous cross-correlation of temporal IR-spectral changes with fluorescence intensity, asynchronous cross-correlation of temporal IR-spectral changes with fluorescence intensity. Amplitudes of correlation spectra are squared.*

[1] K. Fahmy, Curr. Org. Chem. 6 (2002) 1259
[2] K. Fahmy, T.P. Sakmar, F. Siebert, Biochemistry 39 (2000) 10607
[3] B.W. Bailey, B. Mumey et al., Protein Sci. 12 (2003), 2453
[4] U. Alexiev, I. Rimke, T. Pöhlmann, J. Mol. Biol. 328 (2003) 705
[5] J.M. Janz and D.L. Farrens, J. Biol. Chem. (2004)
[6] C. Altenbach, J. Klein-Seetharaman et al., Biochemistry 38 (1999) 7945
[7] K. Fahmy, Recent Res. Devel. Biophys. Chem. 2 (2001) 1
[8] J. Heberle and C. Zscherp, Appl. Spectrosc. 50 (1996) 588

[1] *Institute of Physics, FU-Berlin*

IR-Induced Diffraction Holograms in Organic Liquid Layers

H. Közle, Yu. Lantukh, O. Savchuk, W. Seidel, K. Fahmy

Holography has been originally developed for the display of three-dimensional (3D) images on photosensitive plates. Since then, it has been adapted to various scientific fields such as the investigation of photochemical and thermo-physical properties of atomic and molecular systems related to sensors and transient information storage[1, 2]. Dynamic holography uses a transiently laser-induced grating from which diffraction can be detected with high time-resolution. In principle an interference pattern is formed at the intersection of two coherent optical beams in a planar sample that responds to the incident radiation leading to transient periodical distribution of altered optical sample properties (absorption, refractive index or thickness). During the life time of the grating, the intensity of a HeNe beam diffracted at the grating is measured. Since no light is observed in the absence of a hologram, the lack of background light (in contrast to transmission geometry) allows extremely high sensitivity. Formation of amplitude or phase holograms depends on the nature of the processes induced by the absorbed radiation. The hologram grating period Λ depends on the incident cross-section angle Θ of the two writing beams and on their wavelength $\lambda(\Lambda = \lambda/2\sin(\Theta/2))$. If $d > \Lambda$ (where d and Λ are the thickness and period of the hologram, respectively), the formation of a 3D (volume) hologram occurs, while under the opposite condition $d < \Lambda$ a flat 2D hologram is generated. Refractive index changes resulting from local heating or radiation-induced dispersion changes cause phase gratings. Among other parameters, the decay rate of the grating depends on Λ as temperature equilibration and mass transport follow the steepness of the generated periodic profile. To provide new information on the properties of molecular systems, we have studied the applicability of dynamic holography in the IR. We were able to generate thermal relief-phase holograms in thin water layers using a CO_2 laser tuned to the absorption of the DNA-phosphate backbone (Fig. 1b). We have observed the expected dependence of the grating lifetime on its period which evidences the feasibility of IR-holography. As an example, we have detected the diffusion process of DNA from the maximal heated to the less heated areas of a thermal grating in a thin layer ($d < \Lambda$) of DNA in aqueous solution. A delayed increase in grating efficiency (Fig. 1a) after an initial fast response is observed only in the presence of DNA, whereas the fast component can be ascribed to an IR-induced thermal grating on water which is seen also in the absence of DNA (Fig. 1b).

We are particularly interested in investigating the potential of IR-transient grating for the study of biopolymer structural dynamics. As a model system we have used hydrated polyvinyl alcohol (PVA) films. As seen in Fig. 2, an IR-pulse of 100, 200 ms induces a stable relief-phase grating which can be destroyed by a second pulse. These data suggest that transitions between different conformations of macromolecules can be induced by IR-light and their reaction kinetics detected with high sensitivity by diffraction of visible light.

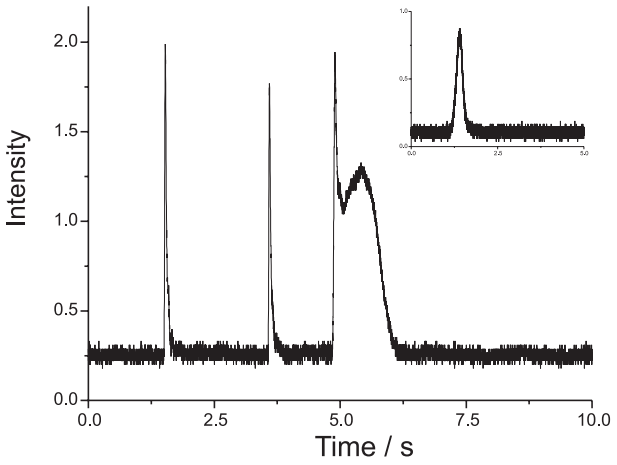

Fig. 1 *Time dependence of the first order diffraction efficiency of a HeNe laser read-out beam that passed a 2D thermal grating generated by recombination of coherent CO_2-Laser beams (1050 cm^{-1}: a) Time-course of the relief-phase hologram recorded in a thin layer of an aqueous DNA solution (0.1 nM). b) Same experiment in the absence of DNA (excitation at 1034 cm^{-1}).*

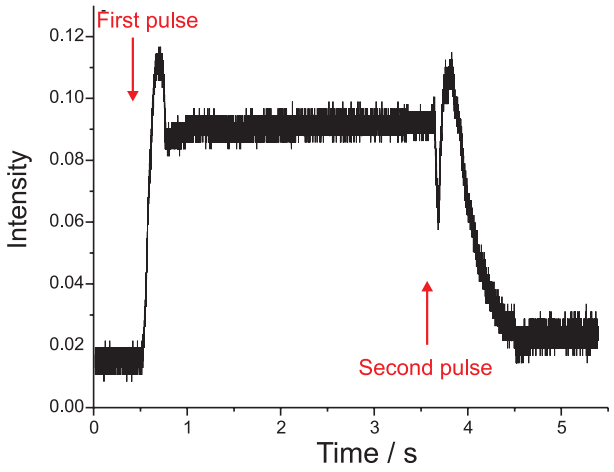

Fig. 2 *Recording and destruction kinetic of relief-phase grating on moistened surface of PVA layer containing Acridine Orange.*

[1] H.A. Ketsle, Yu.D. Lantukh et al., In SPIE's Milestone Series: Photopolymers. Physics, Chemistry and Applications. Vol. MS 114 (1995) 408

[2] Yu.D Lantukh, H.A. Ketsle et al., Patent RU #2182719 (2002)

Resonator Commissioning for First Lasing at ELBE and Characterization of the IR Radiation

W. Seidel for the ELBE-project group

First lasing of the mid-infrared free-electron laser U27 [1] at ELBE was achieved on May 7, 2004. At a wavelength of 19.8 μm an optical power of 3 W was outcoupled in a macro pulse of 0.4 ms duration using an electron beam energy of 16.1 MeV and an energy spread of less than 100 keV. The electron bunch charge was 50 pC.

Trimming the alignment and length of the resonator is an essential prerequisite for the satisfactory work of the laser. The optical cavity of the laser is nearly concentric, with a length of 11.53 m corresponding to 77 ns round trip time. To ensure the stability of the resonator at wavelengths down to 3 μm we require the mirror angular adjustment to have a resolution and stability in the order of 6 μrad [2]. For the initial alignment of the mirror angles an accuracy in the order of 20 μrad is required. To achieve this accuracy we built an alignment system consisting of two collinear He- Ne lasers using insertable adjustment apertures (aligned by optical method) inside the cavity.

The general idea for the first FEL turn-on was to observe the spontaneous undulator radiation and to maximize it by systematic adjustment of the optical cavity and the electron beam parameters. First, the spontaneous radiation was observed downstream the undulator so that the optical cavity was not incorporated in the measurements. For that purpose a mirror was inserted behind the last dipole magnet. The radiation was outcoupled through a KRS-5 window and focused by a parabolic mirror on a liquid nitrogen cooled MCT detector. The first observation of the spontaneous radiation at the diagnostic table [3] was an important step for the commissioning. Having observed the spontaneous radiation, we could optimize the machine using it as a tuning signal.

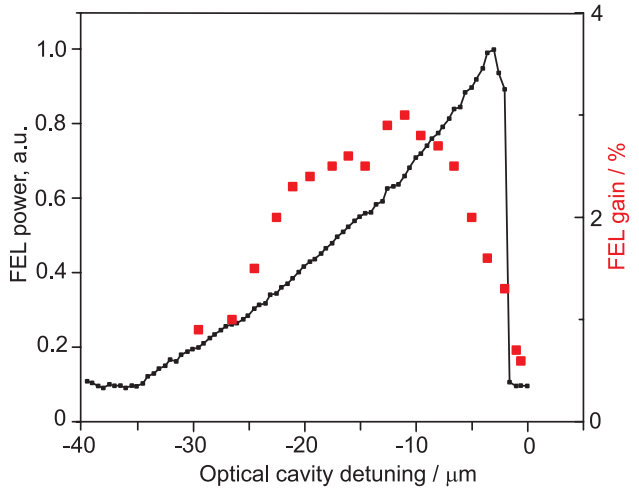

Fig. 1 *The saturation power (line) and the FEL net gain (dots) vs. optical cavity detuning.*

The adjustment of the cavity length is an important prerequisite for lasing. It has been performed by means of an external frequency stabilized fs mode-locked Ti:sapphire laser (Femtolasers, Austria) [4]. The fs laser runs at 78.0 MHz, i.e. the 6^{th} harmonic of the FEL. A 390 MHz reference signal is derived from the RF electronics of the gun, which is used for stabilizing the repetition rate of the fs laser with a phase-lock loop at its 5^{th} harmonic. This synchronization scheme reduces the time jitter of the fs laser to 500 fs [7]. The pulse train of the fs laser operating at 800 nm with 15 fs pulse duration is directed through the outcoupling hole into the FEL cavity. The light re-emitted through the outcoupling hole is detected via beam splitter by a fast photodiode. When perfect synchronism of the fs laser and the FEL cavity is achieved, the detected optical pulse is enhanced due to constructive superposition of pulses circulating in the cavity. This results in an increase of the detected pulse intensity by a factor of five. The correct cavity length is determined by this method with an accuracy of some μm, i.e. a relative accuracy of 10^{-7}. Since the expected FEL operation covers a cavity detuning range of several 10 μm, this accuracy was sufficient to start lasing at the preset cavity length.

A Hewlett-Packard interferometer system is used to monitor and stabilize the resonator length [8]. Its time constant is one Hz and hence fast in comparision to the thermal time constant of the resonator.

We operate the FEL in a pulsed mode using an MCT detector to measure the FEL power as a function of time. In that mode, the small-signal gain is measured by fitting an exponential function to the rising slope of the MCT signal at its very beginning. The amplitude of the MCT detector close to the macropulse end is associated with the saturated power. The saturation power as well as the small-signal gain are measured as a function of the optical cavity detuning. Typical results of such measurements are shown in Fig. 1. It is clearly observed that the detuning which optimizes the FEL gain differs from the detuning that optimizes the saturated power. The curves appear in correspondence with the shape predicted by theory [5].

The peak power is deduced from the average power measurement (a broadband power meter 13PEM001/J with a thermopile detector, both from Melles Griot), by taking into account the time structure of the laser. These values have been measured at the diagnostic table, placed at about 10.5 m from the outcoupling hole. To avoid absorption losses we have purged the optical beam line and the diagnostic station with dry nitrogen. The average power depends on the repetition rate of the FEL. A maximum value of 7 mW has been obtained in the diagnostic room at 17.2 μm with a repetition rate of 5 Hz and 300 μs macro pulse duration. With an optical pulse length of 2 ps we get a peak power of about 0.2 MW or an optical pulse energy of 0.36 μJ.

The FEL spectra were measured with a Czerny-Turner type spectrometer (SpectraPro-300i from ARC) which contains a turret with three different gratings

(75 lines/mm, blazed at 8 μm; m; 60 lines/mm, blazed at 15 μm; 30 llines/mm, blazed at 30 μm). For these measurements we used the side exit slit equipped with a single MCT detector.

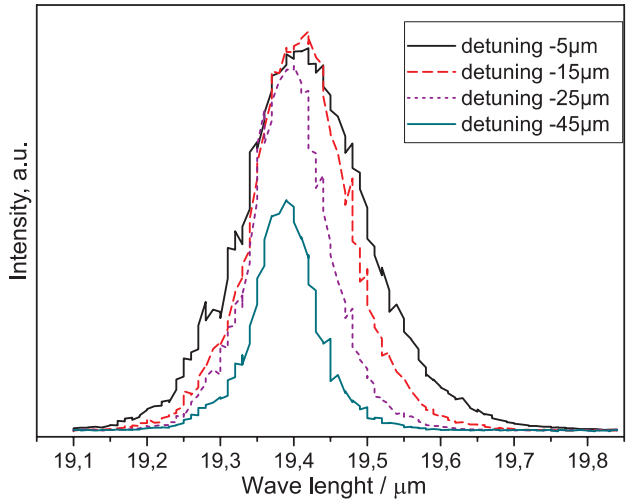

Fig. 2 *FEL spectra measured at different optical cavity detuning.*

Fig. 2 shows how the spectral width decreases with the detuning of the cavity length. By changing the undulator gap from 13 8 mm (minimum) up to 20.5 mm we achieved lasing in the wavelength region from 14.8 μm to 22 μm in the electron energy range from 15.0 MeV to 16.1 MeV, respectively.

The undulator U27 is composed of two identical units, each less than 1 m long, independently adjustable [1]. We have tried to lase with one unit only. Due to the large optical losses in the narrow vacuum tube and the low gain around 15 μm lasing has not been achieved.

To characterize the ultrashort pulses generated by the FEL we built a non-collinear background-free autocorrelator system. We use a CdTe crystal [6] as SHG medium, since it is transparent for a wide wavelength range in the FIR. We measured the autocorrelation function at maximum power of the detuning curve at a wavelength of 17.25 μm. We deduce a pulse duration of 2.1 ps, assuming a Gaussian temporal pulse shape. The corresponding FWHM of the spectrum is approx. 220 nm. The calculated time-bandwidth product is 0.46 which indicates Fourier-transform limited operation.

The optical cavity losses can be measured similar to the small signal gain. At the end of the macropulse, the electron beam is turned off instantaneously. Then, the characteristic decay time of the MCT signal carries the information about the cavity losses, which includes diffraction losses at the undulator vacuum chamber as well as the losses at the mirrors including the outcoupled fraction. The total cavity losses have been measured as a function of the FEL wavelength. The losses have been also calculated using the numerical code GLAD, where the vacuum tube has been replaced by a series of rectangular apertures. The measurements are in good agreement with the calculations. However, one has to note that the calculations are also limited in accuracy, probably of the same order of magnitude as the measurement accuracy. Measurement and the calculation are shown in Fig. 3.

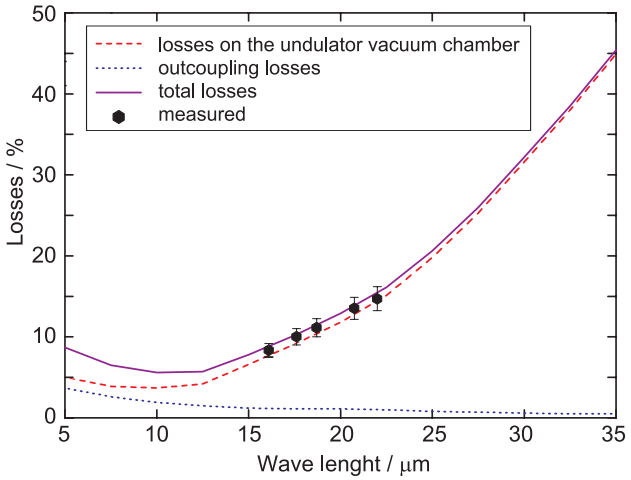

Fig. 3 *Optical cavity losses.*

[1] P. Gippner et al., Wiss.-Techn. Berichte FZR-319 (2001) 24-26, and http://www.fz-rossendorf.de/ELBE

[2] W. Seidel et al., Wiss.-Techn. Berichte FZR-401 (2004) 51

[3] W. Seidel E. Grosse, D. Wohlfarth, Wiss.-Techn. Berichte FZR-341 (2002) 34

[4] K.W. Berryman, P. Haar, B.A. Richman, Nucl. Inst. Meth. A 358 (1995) 260

[5] G. Dattoli et al., IEEE Journal of Quantum Electronics 34 (1998) 1782

[6] J. Xu, G.M.H. Knippels, D. Oepts, A.F.G. van der Meer, Opt. Comm. 197 (2001) 379

[7] T. Dekorsy et al., Wiss.-Techn. Berichte FZR-375 (2003) 40

[8] W. Seidel et al., Proc. of the 25th Int. FEL Conference, Tsukuba, Japan, September 8-12, 2003, in Nucl. Instrum. Meth. A 528 (2004) II-27

Enhancement of Spatial Resolution of the Photothermal Beam Deflection Technique towards the Low Micrometer Range

H. Foerstendorf[1], W. Seidel, F. Glotin[2], R. Prazeres[2], J.M. Ortega[2]

The photothermal beam deflection (PTBD) technique is based on the theory of photothermal spectroscopy which describes the conversion of absorbed energy of a light beam incident on a sample into heat by nonradiative deexcitation processes [1]. In typical PTBD experiments a solid sample is irradiated by a modulated beam of monochromatic light produced by a tunable infrared laser and a probe beam (*e.g.* a HeNe laser) which is reflected from the sample. Depending on the modulated intensity of the pump beam, the probe beam is deflected due to the photoinduced displacement which can be observed by a position detector [2]. PTBD spectroscopy provides spatial information about surfaces of samples. In PTBD, generating and detection of the thermal waves occur generally in the sub-millimeter length scale. With a sufficient small laser probe it should, therefore, be possible to obtain a spatial resolution of a few micrometers. In our PTBD experiment using the free electron laser CLIO/Orsay as an infrared pump source we investigated a distinct pattern of O^+-implanted and untreated regions of germanium (Ge) substrates serving as complex model surface. The pattern was created by a special stainless steal mask in front of the substrate during the implantation process. The areas of the O^+-doped regions can be distinguished from areas of pure germanium by increased optical absorption (*i.e.* the amplitude of the deflection signal) at $\lambda_{FEL} = 11.6\,\mu$m of the Ge-oxide produced during the implantation process (Fig. 1).

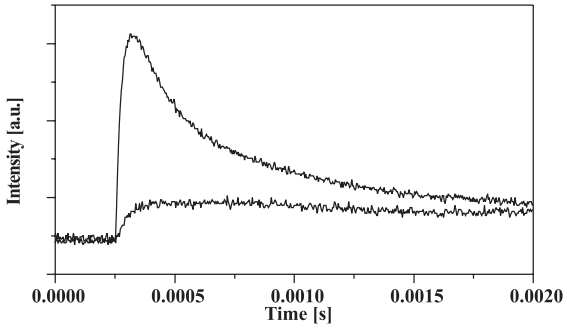

Fig. 1 *Time-resolved beam deflection signals of a strong absorbing (upper case) and a nearly transparent sample (lower case).*

The dimensions of the mask are given in Fig. 2A and as gray stripes throughout Figs. 2B-D. The diameter of the probe beam at the sample surface was ∼15 μm which was verified by pinholes.

The acquisition of deflection signals at distinct positions of the sample permits the calculation of absorption profiles as shown in Fig. 2B-D. The profile presented in Fig. 2B clearly reproduces the structure of the implanted regions generated by the mask.

In Fig. 2C an enlarged range of five thin implanted regions were detected at high resolution of positioning (step width: 2 μm). Again, the recovery of the pattern of implantation (dimensions of 30 μm) is of excellent quality. A high spatial resolution ($< 20\,\mu$m) was obtained which is near the diffraction limit of the pump beam. For demonstration that the deflection signal is solely caused by optical absorption the same sample area was recorded at a wavelength of 7.7 μm where no absorption occurs (Fig. 2D). It is noteworthy, that all profiles shown in this work were obtained with only one FEL macropulse for each sample position. In the future, a better focusing of the probe beam by using an objective lens and averaging of several FEL pulses is expected to enhance the quality of the microspectrometric PTBD-FEL measurements.

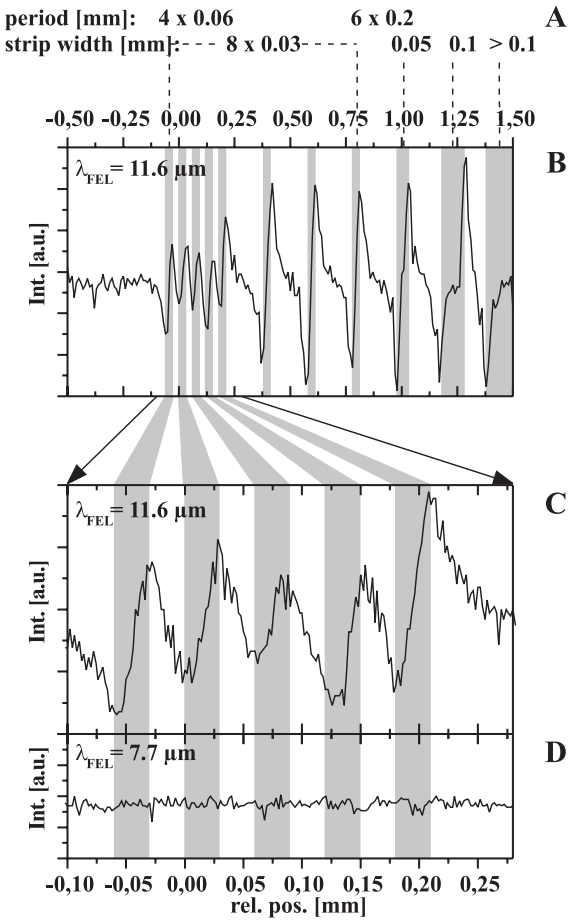

Fig. 2 *Dimensions of the implantation pattern for the preparation of the Ge-substrate with O^+-ions (A). Extracted absorption profiles from the maximum of the deflection curves (B-D): Profile (step width: 10 μm) of the whole implanted structure (B). Profiles (step width: 2 μm) of five thin lines at different FEL wavelengths (C-D) with max. absorption (C) and no absorption (D).*

[1] A. Rosencwaig, A. Gersho, J. Appl. Phys. 47 (1976) 64
[2] W. Seidel, H. Foerstendorf et al., Eur. Phys. J. Appl. Phys. 25 (2004) 39

[1] *Institute of Radiochemistry, FZR, Dresden, Germany*
[2] *LURE, Université de Paris-Sud, Orsay, France*

FEL-Light Induced Changes in Thin Organic Films observed by Dynamic Brewster Angle Microscopy

M. Sczepan, G. Furlinski, D. Wohlfarth, W. Seidel, K. Fahmy

Brewster angle microscopy is a proven technique for the evaluation of thin organic films [1], especially for the observation of phase transitions in monolayers [2]. If a sample is observed under Brewster angle conditions, small changes in the refractive index of the surface can be observed and thus thin layers on the surface can be made visible. Coupling a Brewster angle microscope with a powerful light source like the FEL allows investigation of the IR induced changes in thin organic films. Using the temporal characteristics of the pump light, fast processes (down to 20 μs using an electronic delay system for the camera shutter or even down to some nanoseconds using a synchronized pulsed illumination source and an optical delay line) can be tracked.

The microscope setup (Fig. 1) consists of an illumination system, an imaging system and a pump beam delivery system. The angle of the illumination and imaging systems can be adjusted to work with substrates with different refractive indices and Brewster angles.

The Brewster angle illumination system uses a HeNe-cw-laser as a light source. An additional optical delay line can be used for work with a pulsed illumination source. The light is focussed onto the sample using a 250 mm focal length off-axis paraboloid mirror. A thin film polarizer allows only p-polarized light to illuminate the sample.

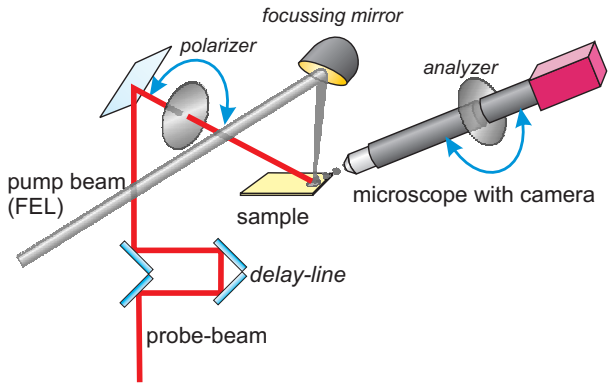

Fig. 1 *Schematic view of the Brewster angle microscope setup. The sample is illuminated by a polarized HeNe laser beam and observed using a home built 20-fold magnification microscope. The FEL pump-light is focussed onto the observed spot using a short focal length off axis parabolic mirror.*

The sample is mounted on a 3-axis translation stage for easier alignment. It is observed using a microscope constructed from a 10 × microscope lens (Zeiss A-Plan), a 200 mm focal length tube lens and a 25 mm focal length projection lens. An internal analyzer eliminates scattered and thus depolarized light emerging from the sample. The image (field of vision is about 300 μm wide) is captured by a 780 x 582 pixel monochrome CCD camera (AVT Marlin 046B). An electronic delay system allows to synchronize the camera with the FEL macropulse structure. The microscope tube can be adjusted in object distance, angle and x and y directions.

The sample is irradiated with the FEL light using an off axis parabolic mirror (focal length 37 mm). With an initial beam diameter of 15 mm the pump beam can be focused down to a spot size of about 100 μm. For easier alignment a HeNe-Laser based co-alignment system has been set up.

We are interested in the study of IR-pulse induced structural changes in biopolymers. A large number of superstructures is particulary important for DNA function. Our experiments aim at the induction and kinetic analysis of the IR-induced transitions between such states.

First tests of the systems have been performed using thin layers of DNA. A small drop (20 μl) of DNA solution (concentration 1 mg/ml) was applied on a zinc selenide substrate. After drying a thin layer (some micrometers) was formed. This sample was irradiated with infrared light from the FEL (17.0 μm wavelength, 400 μs macro bunch length, 2 Hz repetition rate, single pulse energy 100 nJ). A change in reflectivity in the irradiated spot of the layer following the temporal modulation of the FEL light could be observed (Fig. 2). This reflectivity change is probably the result of changes in the refractive index of the DNA film but changes in the thickness of the layer and effects of higher order harmonic wavelengths, which sometimes can be present in the FEL generated light, cannot be excluded at this early stage of the experiments.

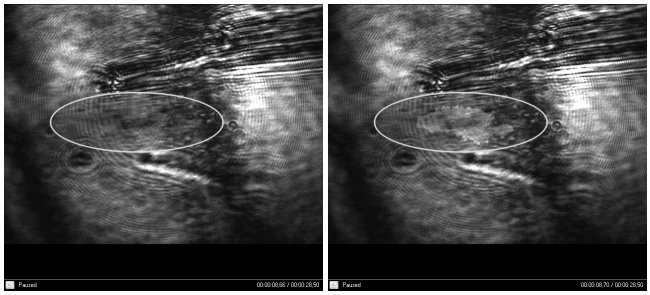

Fig. 2 *Microscopic image of the sample surface without and with FEL illumination. At the irradiated spot a change in reflectivity during illumination (picture right) can be observed.*

However, the preliminary experiments demonstrate the feasibility of high signal/noise detection of IR-pulse induced processes in biofilms.

[1] S. Hénon, J. Meunier, Rev. Sci. Instr. 62 (1991) 936
[2] S. Riviére, S. Hénon et al., J. Chem. Phys. 101(11) (1994) 10045

Radiation Sensor System for the Undulator U27 Using Optical Fiber

W. Seidel, J. Kuhnhenn[1], U. Weinand[1] A. Schamlott[2],

Permanent magnets as components of a Free-Electron Laser (FEL) undulator are irradiated with high-energy electrons and bremsstrahlung X-rays, especially in the initial beam conditioning and in the beam positioning with screen monitors. Several authors have reported radiation damage of permanent magnet materials used in undulators at synchrotron radiation facilities [1, 2]. Because extremely high accuracy of the strength of magnetic fields on the path of an electron beam in the undulator is required, a modification of the field strength would be a serious problem for the lasing process. It is of even more importance in high-duty cycle machines using superconducting accelerators such as the ELBE facility with the high average current. Over the past 25 years, there were numerous publications on magnetization damage induced by radiation in magnets by different kinds [3, 4, 5, 6].

An undulator such as the U27 at ELBE, with NdFeB permanent magnet material can show some degradation in field quality with as little as 10^5 Gy and a dose of 10^6 Gy probably leads to unacceptable undulator performance [2]. This is the reason why we have to be very careful with beam loss around the magnet material. The radiation exposure was continuously monitored in the initial commissioning phase of the FEL by TLD-100-type thermoluminescense dosimeters, placed in between the poles directly at the magnets. Due to the limited linear range of the TLD's (10 Gy) we had to replace the dosimeters every shift. Such a procedure is not feasible in the routine operation of the FEL. Furthermore, we noticed a possible missteering or runs with high dark current levels not until the analysis of the TLD's. To overcome this, an integrating radiation detector placed near to or in the undulator will monitore the dose online. If the dose approaches a predefined threshold, the beam loss must be reduced.

We have installed a system based on the radiation-induced attenuation in optical fibers. Using radiation sensitive P-doped optical graded-index fibers the ionizing radiation leads to a local increase of the attenuation which is measured with a commercial Optical-Time-Domain-Reflectometer (OTDR). In contrast to other optical fibers, P-doped fibers have several advantages for dosimetry purposes. Their radiation-induced attenuation increases linearly with dose before it saturates for doses higher than 1000 Gy. Additional, they do not show a fast fading of the induced attenuation, so they integrate the dose over beam interuptions. Also the induced loss is independent of the dose rate. Since the linear correlation coefficient between dose and attenuation depends on many production parameters of the specific fiber one has to determine this for each fiber separately. At the Co-60 sources of the INT this coefficient was measured for the used fiber. The radiation-sensitive fiber was wound to spools around an Al-plate which fits between the beam pipe and the undulator magnets without restriction of gap tunability. The sensor spools were spliced to radiation hard fiber leads which connected the spools to each other and finally to the OTDR which was located in a neighboring room. To calculate the dose it is necessary to know the exposed length of the fiber. Since the radiation generated at the undulators is not specifically located the exposed length of the fiber has to be determined. This could be done, e.g. with several TLDs which are located perpendicular to the beam axis. This has not been possible so far, thus the exact length of the exposed fiber is not known. Therefore, the doses in Fig. 1 are given in arbitrary units. Further details on the experimental details and data analysis can be found in [7].

The first measured doses for 3 positions in the undulator are shown in Fig. 1. The measurements were performed during the commissioning of the accelerator. Although the absolute doses are unknown, the relative scale is correct. One can clearly identify three major dose depositions: at around 15:30, at 18:30 and at 21:00. This also corresponds to conventional dose-rate measurements which were done using ionization chambers near the entrances of both undulator units (in 5 cm distance from the beam pipe). Both results can be correlated with the operation conditions of the electron beam.

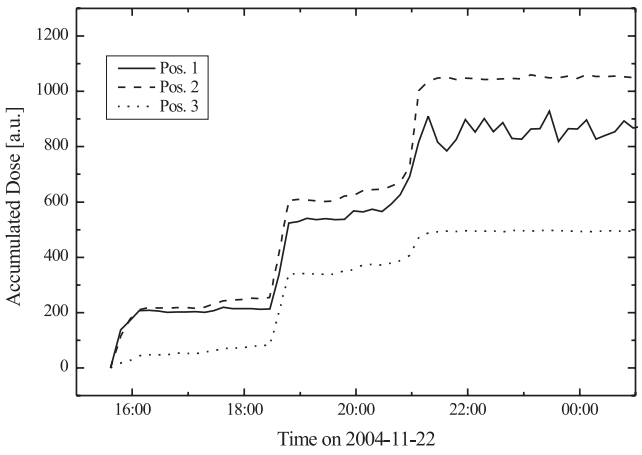

Fig. 1 *Accumulated dose during accelerator commissioning measured by a fiber optic dosimetry system at 3 positions in the undulator at November 22, 2004.*

[1] J. Chavanne et al., ESRF Machine Technical Note 1-1996/ID (1996)
[2] M. Petra et al., Nucl. Instr. Meth. A 507 (2003) 422
[3] K. Boockman et al., J. Magn. Mater. 101 (1991) 345
[4] H. Luna et al., Nucl. Instr. Meth. A 285 (1989) 349
[5] P. Colomp et al., Technical Report ESRF, MARCH-ID, 93-09 (1993)
[6] T. Ikeda and S. Okuda, Nucl. Instr. Meth. A 407 (1998) 439
[7] H. Henschel et. al., Nucl. Instr. Meth. A 526 (2004) 537

[1] *Fraunhofer INT, 53879 Euskirchen, Germany*
[2] *Department Radiation Source ELBE, FZR, Dresden, Germany*

A New Undulator (U100) for the Far Infrared at ELBE

Th. Dekorsy, K. Fahmy, E. Grosse[1], P. Michel, W. Seidel, A. Wolf, R. Wünsch

Starting from May 2004 the U27 undulator at the radiation source ELBE has produced IR light between 16 and 22 μm at electron energies around 16 MeV. Now a second accelerator unit is being installed. The higher electron energy (up to 40 MeV) extends the range down to 3 μm. To enlarge the range to the far infrared ($\lambda \lesssim 150\,\mu$m) another undulator with a larger period will be installed. In the far infrared a FEL constitutes a unique radiation source. Radiation quanta with this energy (10 - 100 meV, 2 - 20 THz) are appropriate for the spectroscopy of low-energy elementary and collective excitations. Such excitations are observed in solid-state quantum-structures and in complex biomolecules as well. Their study establishes the basis for understanding complex phenomena in solids and liquids and for elucidating processes in biological material. Technological and medical innovations are the long-term output of such investigation.

To produce radiation in the THz region by means of the ELBE beam an undulator with a period λ_u of several centimeters is needed. To avoid the use of electron energies below 20 MeV, where the energy spread is larger than 0.3%, we use an undulator with the period of λ_u= 10 cm. To get a sufficiently high single-pass gain 38 undulator periods are envisaged resulting in a total undulator length of approximately 4 m. The design of the electron beam line requires an asymmetric installation of this long undulator. Its middle is located 85 cm downstream from the resonator center. The maximum parameter $K_{\rm rms}$ of this hybrid Sm/Co undulator is about 2.5.

Fig. 1 shows the wavelength range covered by this undulator at the beam of ELBE. It slightly overlaps the range of the U27 undulator and allows to produce light up to

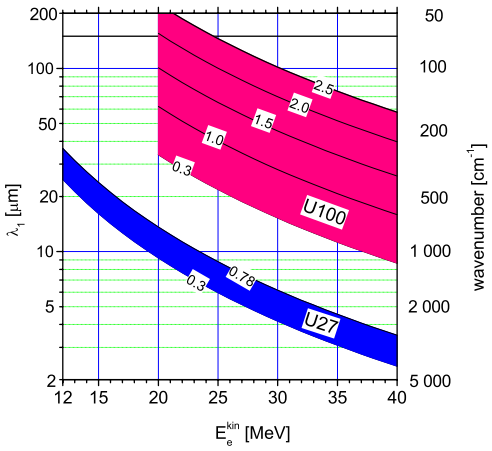

Fig. 1 *Wavelength ranges (first harmonic) λ_1 of the existing U27 and the planned U100 undulator of ELBE as a function of the kinetic electron energy E_e^{kin} calculated for the indicated values of the undulator parameter $K_{\rm rms}$. Note that above roughly 22 μm the diffraction of the optical beam in the vacuum chamber exceeds the gain.*

[1] *also Technische Universität Dresden*

200 μm. Above 150 μm the diffraction losses in the presently designed IR beam line diminishes the power available in the user laboratories considerably.

Above roughly 50 μm the diffraction of the IR beam has seriously to be taken into account. It increases the beam size and reduces the coupling with the electron beam in the undulator (filling factor). Big resonator mirrors, large diffraction losses and a small laser gain are the result. Therefore, a vertical beam compression by means of a rectangular waveguide (10 mm high) spanning from the undulator entrance to the downstream resonator mirror will be applied (see Fig. 2). To avoid ohmic losses in the side walls the waveguide has to be broad enough (5 cm in the undulator and 10 cm at the mirror) to allow a free beam propagation in the horizontal direction [1]. The free propagation on the upstream side of the resonator simplifies the passage through the dipole and quadrupole magnets and provides an approximately round beam profile at the out-coupling mirror (M1). To optimize the coupling between the waveguide and the free optical mode a bifocal mirror with appropriate radii of curvature has to be used (see ref. [2].) The downstream mirror (M2) is a cylindrical one. The proposed setup is similar to that used at the FELIX facility [3].

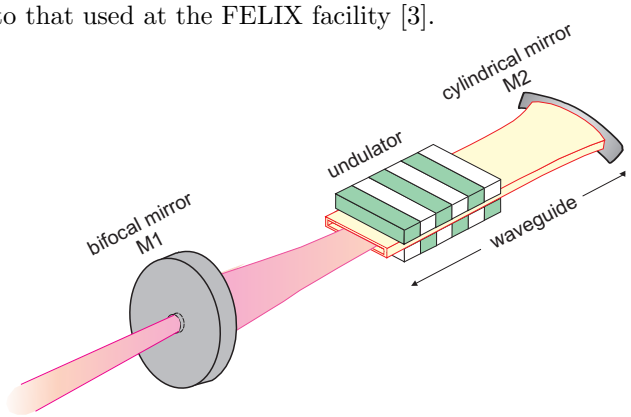

Fig. 2 *Optical mode compression by means of a resonator with partial waveguide.*

To minimize the optical beam cross section in the undulator we shall use an asymmetric resonator with the horizontal beam waist located in the undulator center and a Rayleigh length of 180 cm. The height of the waveguide and the resulting minimal pole gap are large enough for the electron beam and guarantee a sufficiently large magnetic field on the axis.

The undulator will be available at the beginning of the year 2006. Waveguide and resonator should be installed one year later.

[1] L.R. Elias, J. Gallardo, Appl. Phys. B 31 (1983) 229
[2] R. Wünsch, this report, p. 66
[3] http://www.rijnh.nl

The Resonator of the Long-Wavelength FEL (U100) at ELBE

R. Wünsch

The U100 undulator is designed for wavelengths between 15 and 150 μm. At wavelengths above about 50 μm the use of an open resonator becomes inefficient. The optical beam is too thick and does not allow a small undulator gap and an effective interaction with the electron beam. A waveguide is necessary to compress the beam. It can be restricted to the undulator or stretch across the whole resonator from one mirror to the other. We propose a 1 cm high partial waveguide ranging from the undulator entrance to the downstream mirror (see Fig. 2 of Ref. [1]. To minimize ohmic losses in the walls, we use a metallic parallel-plate waveguide which compresses the beam in vertical direction [2]. Adding side walls to the waveguide, they should be sufficiently far away from the beam not to disturb the free propagation in horizontal direction. In our case, the waveguide must be 5 cm wide within the undulator and 10 cm at the upstream mirror. The E^{π}_{mn} eigenmodes of such a resonator are described by Gaussian-Hermite functions of order m in the horizontal direction and sine functions with node number n in vertical direction. They are characterized by negligible losses in the far-infrared region. Up to $n = 20$ the ohmic losses do not exceed 5%/m in the given wavelength range. The fundamental mode ($n = 1$) is attenuated by less than 0.01% per meter.

The absence of waveguide walls on the upstream side of the resonator, which are only 10 mm away from each other, allows the adequate formation of the electron beam by means of the quadrupoles. Moreover, the optical beam gets a more spherical shape when freely propagating to the upstream mirror. On the other hand, the mode conversion at the waveguide exit implies conversion losses and enhances the dispersion of the beam in the far field. That is why the height of the upstream mirror should be larger than twice its width at 150 μm. Since the beam propagates freely in horizontal direction the corresponding radii of curvature of the resonator mirrors are determined by the desired Rayleigh range of 180 cm and the waist position in the middle of the undulator 85 cm downstream the resonator center. Since the waveguide ranges to the downstream mirror it has to be a cylindrical one.

The vertical curvature of the upstream mirror determines the profile of the reflected beam at the waveguide entrance and defines the coupling between the free and the waveguide mode. We have used the code GLAD [3] to study the mode coupling losses. In a first step we took into account a single waveguide mode (n = 0) only. Higher modes will be considered later. The calculations have shown that a single radius of curvature, which corresponds to the distance between resonator mirror and the waveguide entrance, can be used to optimize the coupling losses in the hole wavelength region. Fig. 2 shows the calculated losses of a n = 1 waveguide mode propagating to mirror M1 with the parameters of table 1 then back to the waveguide entrance and converting into the same waveguide mode. Clipping losses caused by the finite cross sections of mirror and waveguide, and outcoupling losses by a hole with diameter D_{h} are included.

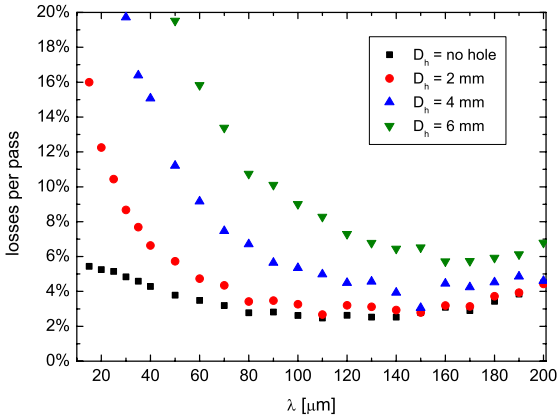

Fig. 1 *Round trip losses as a function of the wavelength λ calculated for the resonator with the parameters of table 1 and various hole diameters D_{h} in the upstream resonator mirror.*

The calculation reveals a twofold effect of the outcoupling hole. The sum of the losses calculated without outcoupling and the outcoupled fraction is remarkably smaller than the losses calculated for the total propagation to the mirror and back. Besides outcoupling, the hole diffracts the reflected beam. This diffraction leads to additional losses which are in the size the outcoupling. The parameters of the resonator proposed for the U100 undulator and used in the calculation are summarize in the table below.

Resonator length		1153 cm
Rayleigh length		
	horizontal	180 cm
Mirror radii of curvature		
	horizontal	M1: 710.5 cm,
		M2: 557.4 cm
	vertical	M1: 447 cm,
		M2: ∞
Mirror size		
	width	M1: 10 cm
		M2: 9 cm
	height	M1: 23 cm
		M2: 1 cm
Waveguide size		
	width	5. . . 10 cm
	height	1 cm
	length	706 cm

Table 1 *Parameters of the optical resonator. M1: upstream mirror, M2: downstream mirror.*

[1] Th. Dekorsy, K. Fahmy et al., this report, p. 65
[2] L.R. Elias, J. Gallardo, Appl. Phys. B 31 (1983) 229
[3] GLAD, Applied Optics Research, Woodland, WA 98674, USA

Gain and Power of the Far Infrared FEL (U100) at ELBE

R. Wünsch

To ensure a satisfactory work in the envisaged wavelength region ($15\,\mu\mathrm{m} \lesssim \lambda \lesssim 150\mu\mathrm{m}$) we have estimated the single-pass gain and the outcoupled optical power of the U100 undulator at the ELBE beam. The calculation is based on a scheme developed by S. Benson [1] for the Jefferson Laboratory. Electron beam, undulator and resonator parameter are the input. Beam and undulator parameters are summarized in Tab. 1. The resonator is considered in Ref. [2].

Electron beam	
Kinetic energy	20-40 MeV
Pulse charge	70 pC
Energy spread	60 keV
Norm. transv. emittance	13 mm mrad
Undulator	
Undulator period	10 cm
Number of periods	38
Magnetic field amplitude on axis	$\lesssim 0.4$ T
Undulator parameter (K_{rms})	$\lesssim 2.5$
Minimum pole gap	20 mm

Tab. 1 *Parameters of the ELBE beam and of the U100 undulator*

The single-pass laser gain depends strongly on the length of the electron pulse. We assumed a longitudinal Gaussian charge distribution and calculated the gain for 3 values of the rms pulse length.

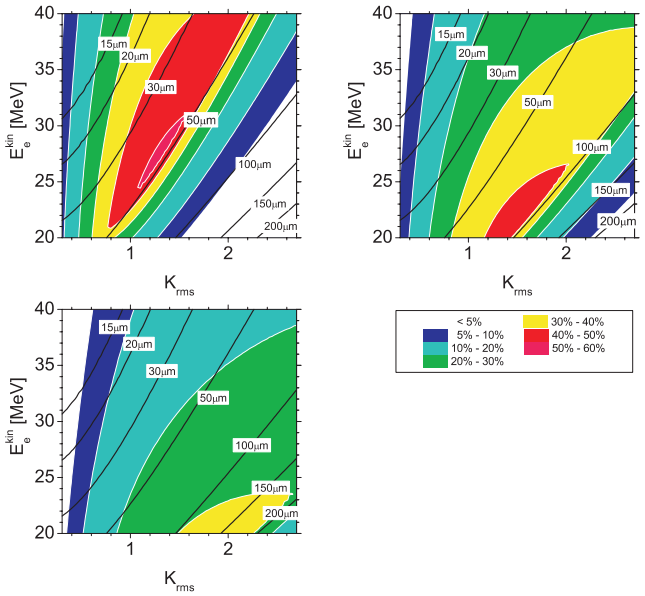

Fig. 1 *Small-signal single-pass gain calculated for the U100 undulator at the ELBE beam for 3 values of the rms electron pulse length τ as a function of the undulator parameter K_{rms} and the kinetic electron energy $E_{\mathrm{e}}^{\mathrm{kin}}$. The figure displays the maximum gain with respect to resonator desynchronization. Upper left panel: τ=1 ps; Upper right panel: τ=2 ps; Lower left panel: τ=4 ps;*

Fig. 1 shows that the gain is larger than the optical losses considered in Ref. [2] in the whole wavelength range. Choosing the appropriate electron pulse length the gain is ever larger than 30 %. The larger the wavelength the longer the electron pulse should be.

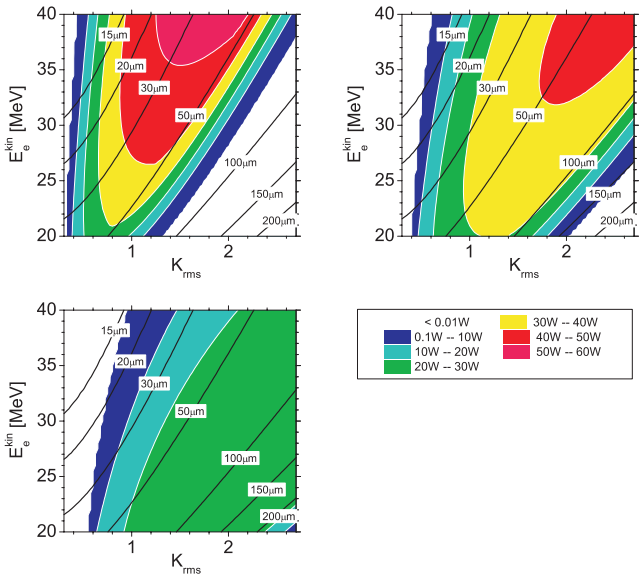

Fig. 2 *Outcoupled average laser power as a function of the undulator parameter K_{rms} and the kinetic electron energy $E_{\mathrm{e}}^{\mathrm{kin}}$ The 3 panels correspond to the same pulse lengths as in Fig. 2.*

Outcoupling and resonator desynchronization have been assumed to be optimal. To realize this outcoupling the radius of the outcoupling hole has to be varied from 1.5 mm around 15 μm up to 6 mm around 150 μm. For a fixed outcoupling hole the power is smaller in general. To cover the whole wavelength region 3 different outcoupling holes are necessary at least.

According to the results of Ref. [2] we assumed resonator losses fixed to 8%. They include mode-coupling, absorption and dispersion losses. The outcoupling was considered separately according to the size of the hole. Around 30 μm the average outcoupled power may achieve 50 Watts. At wavelength around 150 μm the predicted power is still 25 W.

Fig. 2 shows the maximum gain with respect to the resonator desynchronization. This desynchronization is significantly smaller than the desynchronization resulting to the maximum gain, which is displayed in Fig. 1.

[1] S.V. Benson, CEBAF TN#94-065
[2] R. Wünsch, this report, p. 66

Comparison of Electron Channeling Radiation Energies to Calculations

B. Azadegan, L.Sh. Grigoryan[1], J. Pawelke, W. Wagner

Channeling radiation (CR) spectra of diamond have been measured at electron energies of 14.6 and 17 MeV at ELBE. The calculation of CR transition energies represents a many-beam problem [1].

In the case of planar CR the transition energies are computed by solving the one dimensional Schrödinger equation

$$-\frac{\hbar^2}{2m\gamma}\frac{d^2\psi(x)}{d^2x} + V(x)\psi(x) = E\psi(x) \qquad (1)$$

where the potential and the eigenfunctions read as [2]

$$V(x) = \sum_n v_n e^{ingx} \quad , \quad \psi(x) = e^{ikx}\sum_n c_n e^{ingx}$$
$$(n = ..., -1, 0, 1, 2...) \qquad (2)$$

and v_n denotes the Fourier coefficients of the periodic potential. Using the Doyle-Turner approach [3] for the electron-atom interaction they can be written as

$$v_n = \frac{-2\pi}{V_c} a_0^2 \cdot (e^2/a_0) \sum_j e^{-M_j(\mathbf{g})}$$
$$\times e^{(-i\mathbf{g}\cdot\mathbf{r}_j)} \sum_{i=1}^{4} a_i e^{(-\frac{1}{4}(\frac{b_i}{4\pi^2})(ng)^2)} \qquad (3)$$

where V_c is the volume of unit cell, a_0 is the Bohr radius, a_i and b_i are tabulated coefficients [3], $\mathbf{r}_j$ are the coordinates of the atoms in the unit cell, $\mathbf{g}$ is the reciprocal lattice vector of the plane and $M_j(\mathbf{g}) = \frac{1}{2}g^2 < u_j^2 >$ denotes the Debye-Waller factor which describes the thermal vibrations of the j$^{\text{th}}$ atom.

The crystal structure of diamond may be represented by an fcc lattice with a 2-atom basis or, equivalently, by a cubic lattice with an 8-atom basis. In the first sum of Eq. (3) the 8-atom basis is applied.

By substituting of the expressions given above into Eq. (1) the problem reduces to the finding of the eigenvalues of a matrix A which in the planar case consists of the components

$$A_{nm} = v_{n-m} \quad (for\ n \neq m)$$
$$A_{nn} = \frac{\hbar^2}{2m\gamma}(k + ng)^2 + v_0. \qquad (4)$$

The computation of the eigenvalues and eigenfunctions for different planes of diamond has been performed with the help of the software package Mathematica 4.1. Since the potential as well as the eigenvalues converge very fast one can restrict to 21 Bloch functions what leads to a 21×21 matrix. For illustration, the potential of the (111) plane of diamond together with the eigenvalues calculated for the electron energy of 14.6 MeV is shown in Fig. 1.

In the measurements a 42.5 μm thick diamond type-IIa crystal was used. The CR spectra as well as random bremstrahlung spectra have been corrected for detector efficiency and absorption in the crystal and in other window materials. After subtraction of the bremstrahlung background suitable functions have been fitted to the CR lines as shown in Fig. 2.

The CR energies calculated for the lowest transitions are compared with the measured ones for the planes (100), (110) and (111) in Tab. 1. Since the uncertainty of the beam energy (200 keV) governs the maximum error of the measured CR energies (0.4 keV), the many-beam calculations predict the measured CR energies rather well. Principally, some deviation of the measured values from the calculated ones is expected only towards lower energy.

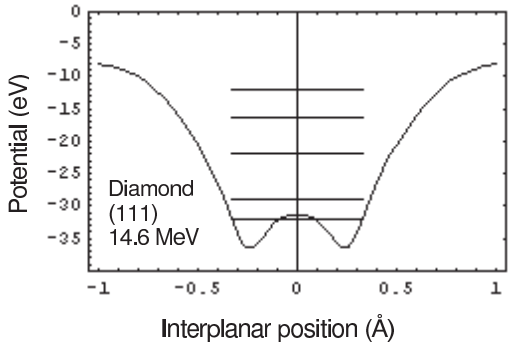

Fig. 1 *The potential of the (111) plane and calculated eigenvalues for 14.6 MeV electron energy.*

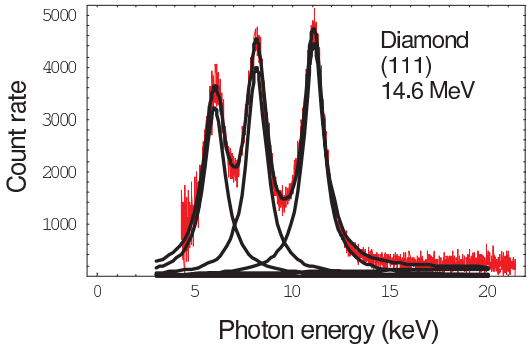

Fig. 2 *Result of the fitting procedure for the CR spectrum of the (111) plane.*

Tab. 1 *Planar CR energies for 14.6 MeV electrons.*

Plane	CR Transition	Measured energy/keV	Calculated energy/keV
(100)	1-0	9.38±0.04	9.87
(110)	1-0	16.54±0.05	17.10
	2-1	7.89±0.04	7.16
(111)	1-0	6.05±0.05	4.93
	2-1	11.07±0.04	11.69
	3-2	8.14±0.03	9.26

[1] J.U. Andersen et al., Physica Scripta 28 (1983) 308
[2] R.K. Klein et al., Phys. Rev. B 31 (1985) 68
[3] P.A. Doyle et al., Acta Crystallogr. A 24 (1968) 390

[1] *IAPP NAS, Yerevan, Armenia*

Yield Dependence of Electron Channeling Radiation on the Crystal Thickness

W. Wagner, B. Azadegan, J. Pawelke, W. Enghardt

The dependence of the yield of channeling radiation (CR) on the thickness (d) of the diamond crystal has been investigated at ELBE.

In earlier works [1,2] one applied the dissipative ansatz for the population of bound states $P_n(z)$ and defined an energy dependent occupation length l_{occ} from the integral

$$N_{ch} \propto \int_0^d P_n(z)dz = 1 - e^{-z/l_{occ}}, \qquad (1)$$

because the intensity of a CR line N_{ch} is given by the product of the thin-target transition probability and the occupation probability of a channeling state (Eq. 1).

First systematic investigations on diamond at low electron energies (5 - 10 MeV) have been extended to a crystal thickness of 200 μm [3]. It has been shown that the population dynamics is governed by multiple scattering of the electrons in the crystal. Especially at larger crystal thickness the intensity rather follows the function

$$N_{ch} \propto \Theta_{MS}(d) \sim \sqrt{d}, \qquad (2)$$

where $\Theta_{MS}(d)$ is the mean angle of multiple scattering. To proof such behaviour a further series of CR measurements has been carried out. The electron beam of ELBE with an energy of 14.6 ± 0.2 MeV was focused at the crystal position into a spot of 1 mm diameter with a divergence of about 0.1 mrad $\langle rms \rangle$. Three perfect diamond crystals, all of type IIa, with the thicknesses 42.5 μm, 102 μm and 168 μm have been used for the measurement of the yield of the 1-0 transition of planar (110) CR.

The CR as well as random bremsstrahlung spectra have been registered by a 300 μm thick Si-pin-diode positioned 3 m away from the target at zero degree with respect to the beam direction inside a thick Pb collimator with an aperture of 1 mm. An auxiliary vacuum line (1.6 mbar) has been installed between the 127.5 μm thick Be-window of the accelerator beamline and the detector to minimize X-ray absorption. The total beam charge was monitored with the help of a secondary electron monitor (SEM) [4] positioned directly behind the crystal to diminish losses due to electron scattering in the target.

The measured spectra were corrected for detector efficiency, self absorption and attenuation in window materials on the path to the detector. After subtraction of the bremsstrahlung background (Fig. 1) an appropriate function has been fitted to the profile of the 1–0 CR line. To calculate the CR yield the number of electrons was obtained by integration of the respective SEM-scaled differential bremsstrahlung flux [5] which was found to increase linearly with target thickness.

The resulting CR yields versus the crystal thickness are shown in Fig. 2 together with the curves obtained in accordance with Eq. (1) (thin line) and Eq. (2) (thick line). It is obvious that the data points approach the Ref. [3]. The effect of multiple scattering also leads to a broadening of the CR line width which amounted to 1.54 keV and 2.5 keV for 42.5 μm and 168 μm, respectively, and a slight shift of the peak centroid (Fig. 1).

When Eq. (1) accounts for the depopulation of channeling states with thickness, multiple scattering seems to come into play at larger crystal thickness (or at lower electron energies) and partly compensates dechanneling leading to a more steep increase of the CR yield with increasing crystal thickness than prescribed by Eq. (1). This is due to contributions from in-plane scattered electrons as well as due to the redistribution of the population of channelling states. If l_{occ} depends linearly on the electron energy, Eq. (1) is able to describe the dependence of the CR yield on the crystal thickness to approximately $2 \times l_{occ}(E)$ only.

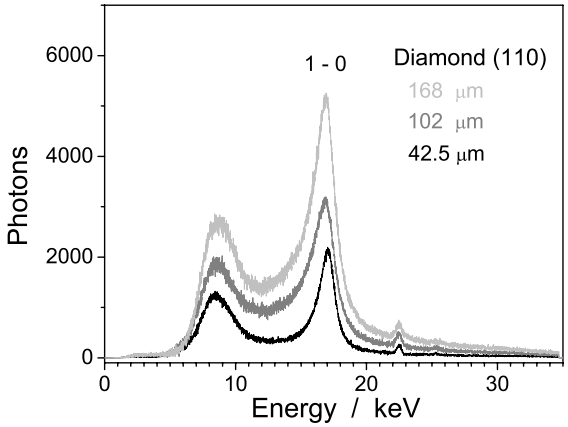

Fig. 1 *CR spectra of (110) diamond at 14.6 MeV.*

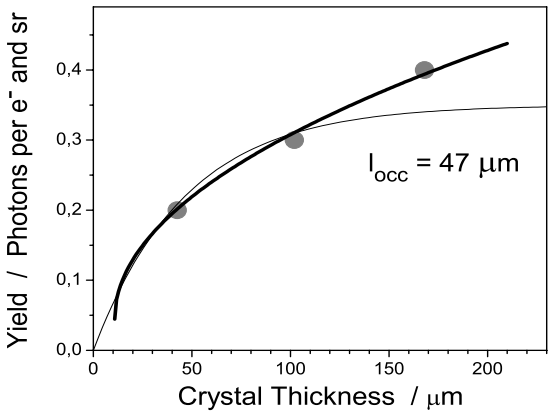

Fig. 2 *CR yield versus crystal thickness.*

[1] J.O. Kephart, R.H. Pantell et al., Phys. Rev. B 40 (1989) 4249
[2] U. Nething, M. Galemann et al., Phys. Rev. Lett. 72 (1994) 2411
[3] I. Reitz, Diplomarbeit, TU Darmstadt (1999)
[4] W. Neubert, K. Heidel et al., this report p. 73
[5] J.D. Jackson, Classical Electrodynamics, Wiley, New York (1975)

Monochromatisation of Channeling X-rays at ELBE Using HOPG Crystals

J. Pawelke, B. Azadegan, W. Wagner, W. Enghardt

The application of channeling radiation (CR) as an unconventional X-ray source to be used for radiobiological research requires the separation of the quasi-monochromatic CR line from the unavoidable polychromatic bremsstrahlung background [1]. Monochromatisation on the base of Bragg reflection in highly oriented pyrolytic graphite (HOPG) mosaic crystals was chosen in order to retain as much as possible of the CR intensity. A first monochromator has been manufactured whose curved surface was designed for optimal separation of the CR peak of 18.4 keV mean energy from the 1-0 transition of the (110) electron planar channeling in diamond [2]. First test measurements at ELBE, however, have been performed with a planar HOPG crystal since the curved monochromator requires a change of the beam line beforehand.

The electron beam of ELBE with an energy of 14.6 ± 0.2 MeV was focussed at the position of the CR crystal into a spot of 1 mm diameter with a divergence of about 0.1 mrad (rms). The CR spectrum has been measured by a Si-PIN photodiode positioned 3.2 m away from the 42.5 μm thick diamond crystal at zero degree with respect to the beam direction (X-axis) inside a thick Pb collimator with an aperture of 1 mm. The energy spectrum of the CR is presented in Fig. 1, showing the CR peak at 16.5 keV with a width of 1.8 keV FWHM.

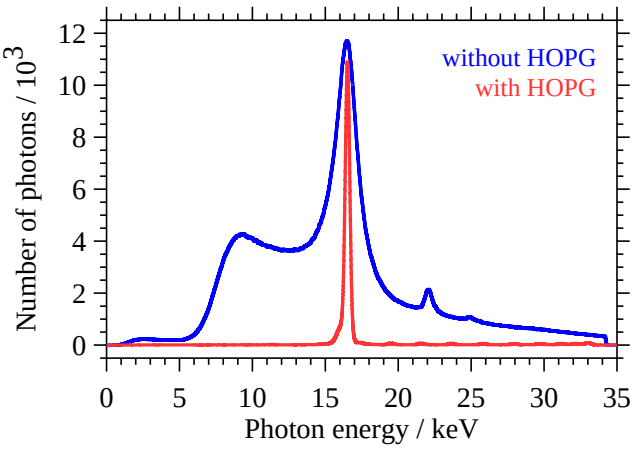

Fig. 1 *Energy distribution of (110) planar CR at zero degree (upper line) and after reflection in the HOPG crystal at 13.1 degree (lower line). Both spectra are scaled for the same electron beam charge, measurement time and detector solid angle.*

Thereafter, a planar HOPG crystal of 10×8 cm^2 size, 1 mm thickness and 0.8 degree mosaicity (Optigraph Ltd., Moscow, Russia) was moved to the centre of the CR cone along the horizontal line (Y-axis) perpendicular to the beam direction by a stepping motor unit. For this purpose, a HOPG crystal from the same batch as used for covering the curved monochromator described in [2] was directly deposited on a 1 cm thick polymethyl methacrylate plate and positioned with its 10 cm side parallel to the horizontal beam direction, the 8 cm side being vertically oriented and the centre of the crystal being at a distance of 1.7 m from the diamond. The stepping motor unit also allowed the rotation of the crystal about its two axes, parallel to the 10 cm ($\theta_{max} = \pm 6\,^\circ$) and the 8 cm ($\phi_{max} = \pm 180\,^\circ$) side, respectively. The energy spectrum after reflection has been measured by a second Si-PIN photodiode positioned 1.7 m away from the centre of the HOPG at $\phi = 13.0 \pm 0.5\,^\circ$ inside a thick Pb collimator with an aperture of 3 mm. With the HOPG crystal at an angle $\phi = 6.5\,^\circ$ the Bragg reflection condition for 16.5 keV photons of the CR peak (cf. Fig. 1) is fulfilled. The spectrum after reflection is shown in Fig. 1 as well, demonstrating a high peak reflectivity of the HOPG crystal. However, the considerably reduced peak width of 0.4 keV FWHM denotes a rather low integral reflectivity and is smaller than the energy spread of about 2.0 keV FWHM expected from the HOPG mosaicity. The reason for that is the small angular acceptance of the HOPG crystal (about 0.15 °) in the CR cone. By moving the HOPG crystal along the Y-axis but keeping the angles constant the peak position and height in the reflected spectrum are changed. In Fig. 2 the peak energy and area of the reflected spectrum are shown for several Y-positions and are compared with the width of the CR peak at zero degree. The width of 1.0 keV FWHM demonstrates the reflection of an HOPG monochromator of optimised geometry with high integral reflectivity which retains the intensity of the rather broad CR peak nearly completely.

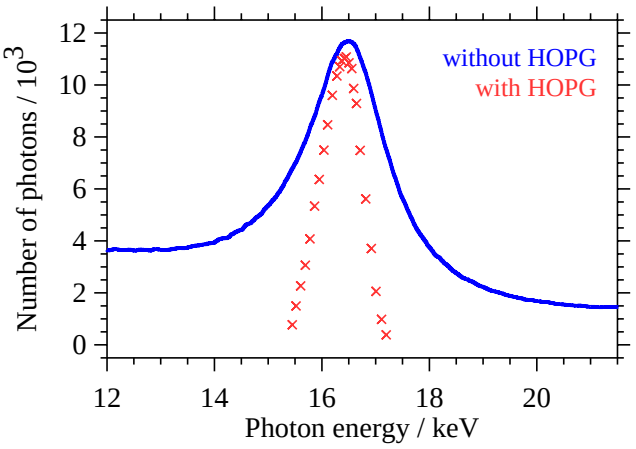

Fig. 2 *Peak-width comparison of (110) planar CR at zero degree (line) with the spectrum obtained by scanning the HOPG crystal 20 mm along the Y-axis (symbols).*

[1] W. Wagner, A. Panteleeva et al., Wiss.-Techn. Berichte FZR-401 (2004) 56
[2] J. Pawelke, A. Heitsch et al., Wiss.-Techn. Berichte FZR-372 (2003) 68

Dose Rate Measurement around the ELBE Channeling X-Ray Beam Line

J. Pawelke, U. Lehnert[1], A. Schamlott[1], W. Wagner, W. Enghardt

A main objective of building up the channeling radiation (CR) source at ELBE is its application for the determination of the RBE of X-rays by cell irradiation. Reliable studies of radiobiological effects on living cells need a maximum irradiation dose rate of about 1 Gy/min where a sufficiently low level of background radiation at the irradiation site is required. However, CR has been produced at ELBE only with low intensity by an electron beam of 1 to 50 nA current so far in order to measure photon energy spectra and to study the dependence of the CR energy and yield on the electron beam energy and on the diamond crystal thickness [1, 2]. The CR yield obtained for the 1-0 transition of (110) planar channeling in a diamond crystal converts into a CR dose rate which meets the required maximum intensity for cell irradiation if one assumes an average electron beam current of 100 μA.

In a first step towards the increase of CR intensity by raising the electron beam current by about four orders of magnitude the photon radiation background (polychromatic bremsstrahlung) at the irradiation site has been measured. Four air filled ionisation chambers (IC), connected to an UNIDOS electrometer (PTW Freiburg) each, were placed around the beam line (Fig. 1). Three Farmer IC (M30001, PTW Freiburg, position I, II and III) and a rigid stem IC (M23332, PTW Freiburg, position IV) have been chosen because of their energy and dose rate range as well as size and handling [3]. In addition, the LB6701 IC (Berthold, Bad Wildbach) was used which is installed at position V and part of the radiation protection interlock system at ELBE.

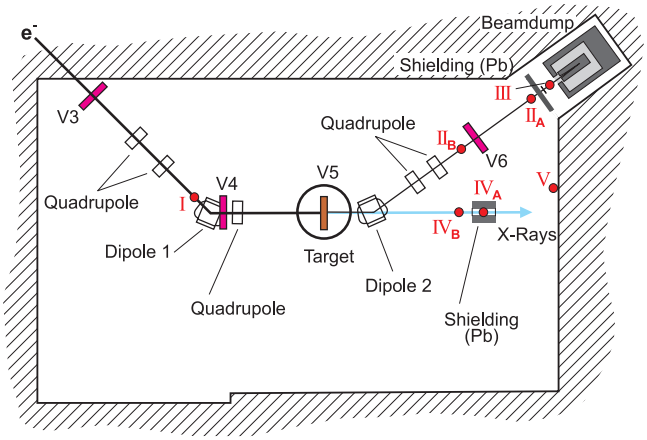

Fig. 1 *Position of the ionisation chambers in the radiation physics cave. The electron beam comes from the accelerator (left) and is stopped in the dump (right).*

After tuning the electron beam of 17.0 ± 0.2 MeV energy and up to 130 μA current, photon dose rates were measured without any target in the beam. The measurement was repeated after an 18 μm thick Al foil was inserted into the beam in order to study the influence of electron scattering in the target on the beam loss, and corresponding generation of background radiation. The Al foil has been chosen for practical reasons since it is used as an optical transition radiation viewer for observation of the electron beam profile and position at the CR target and results in a roughly comparable electron scattering as the thicker diamond crystals used for CR generation. Upon entering the cave and moving IC II and IV from position A to site B the dose rates were measured again for both cases, with and without target in the beam.

Tab. 1 *Comparison of photon dose rates at different positions measured for an electron beam current of 100 μA.*

Position	Exp. no.	Dose rate / (mGy/min)	
		no target	18 μm Al target
I	1	1	1
	2	1	1
II_A	1	286	660
II_B	2	1	814
III	1	829	1042
	2	896	1638
IV_A	1	0	409
IV_B	2	1	450
V	1	74	890
	2	85	1478

Without passing a target the electron beam can be transported to the dump without loss and the corresponding high intensity of bremsstrahlung background at the dump (see Table 1) is considerably attenuated by the 10 cm thick Pb shield in front of the dump and by the concrete wall in which the dump is situated. This results in a very low level of background radiation at the cell irradiation site (position IV_A and IV_B, respectively). In contrast, the electron scattering in the target results in a considerable beam loss and a corresponding overall rise of the background radiation level. However, the high radiation intensity at the cell irradiation site is mainly caused by bremsstrahlung generated in the target and emitted in forward direction of the electron beam. Only a rather small contribution of bremsstrahlung generated at the beam line reaches the irradiation site, as indicated by the about 10 % lower dose rate at position IV_A, i.e. when the IC is shielded by a Pb hollow cylinder against photons arriving from lateral direction, compared to site IV_B. But the about 60 % dose rate variation measured for the target in the beam at position III and V, respectively, also shows the difficulty of reproducible beam tuning behind the second dipole magnet.

[1] W. Wagner, A. Panteleeva et al., Wiss.-Techn. Berichte FZR-401 (2004) 56
[2] W. Wagner, B. Azadegan et al., this report, p. 69
[3] J. Pawelke, T. Mikuletz, A. Panteleeva, Wiss.-Techn. Berichte FZR-401 (2004) 58

[1] *FZR, Department Radiation Source ELBE*

A Goniometer for Channeling Radiation Experiments at ELBE

W. Wagner, F. Müller[1], A. Nowack[2], M. Sobiella, J. Steiner, W. Enghardt

Channeling radiation (CR) is emitted by relativistic electrons travelling through a single crystal along a main lattice plane or axis. For channeling the particles have to be captured by the average planar or axial potential. This happens when their angle of incidence with respect to the plane or axis is smaller than the critical (Lindhard) angle Θ_{cr}.

At ELBE energies $\Theta_{cr} \approx 2\,\mathrm{mrad}$ can be given as a typical value. Considering a beam of sufficiently small divergence ($\approx 0.1\,\mathrm{mrad}$), the angle of incidence has to be adjusted by means of a goniometer which carries the crystal. The goniometer must have at least two rotational axes oriented perpendicular to each other and allowing for a reproducibility of the angular setting better than Θ_{cr}, i.e. $\leq 0.05^{\circ}$. Since the goniometer operates in line with the superconducting cavities of the ELBE accelerator, it has to meet the rather strong demands for an extremely clean UHV. This concerns the composition of the remaining gas mixture as well as the absence of microparticles.

At commercial UHV goniometers (e.g. AML ZTEC107 [1]) the precise angular setting ($\approx 0.001^{\circ}$) is usually reached by means of worm gears. The mechanisms for translatory movement include spindle drives and roller bearings. It is recommended by the producer that gears and bearings have to be lubricated either with UHV grease or with Molybdenum. A gas analysis made by means of a quadrupole mass spectrometer showed that the remaining atmosphere in an UHV chamber housing such type of goniometer contains plenty of masses larger than 32 amu (O_2^+) originating from radicals of higher hydro-carbons, fluorinated hydrocarbons etc.

Furthermore, a measurement of microparticles produced from dryly operating worm gears resulted in concentrations of 10^3–10^4 cft^{-1}. Such values are to large by several orders of magnitude and could be diminished by the use of lubricants only.

To overcome the difficulties mentioned above we, therefore, decided to construct a goniometer which bases on another principle (Fig. 1). All drives are implemented as linear ones using ball bearing screw thread spindles which are driven by Phytron UHV stepping motors and sway a nut element. The translatory movement of the nut is transformed by a connecting rod to the rotation of a frame which carries the crystal holder. All ball bearings used for the bearing of rotating elements are dryly running miniature ones. Special measures have been taken to avoid the propagation of minimal tilt clearance of the also dryly running spindle-nut drive to the rotary motion of the frame. The screw thread rising of the subtle spindles amounts to only 0.25 mm what theoretically results in an angular resolution of $\Delta\vartheta \leq 0.005^{\circ}$ per motor step (MS) at a maximum nonlinearity of the angular scale of 2.5 %.

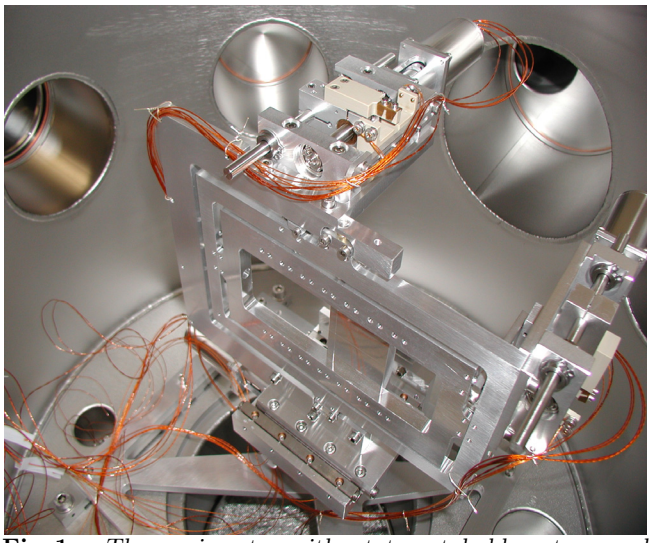

Fig. 1 *The goniometer without target holder at opened UHV chamber.*

Take notice of the relation $\Delta\vartheta \ll \Theta_{cr}$.

The combination of two such nested mechanisms whose axes of rotation are perpendicular to each other allows to simultaneously rotate (ϑ) and tilt (ψ) the crystal around the vertical and the horizontal axis, respectively, up to angles of $\vartheta = \psi = 25^{\circ}$ with respect to the normal of the frames at zero position. The limitation of the available angular ranges is caused by the length of the spindles used but the limitations due to the finite dimensions of the crystal holder take nearly the same values. The special construction of the crystal holder which fixes the crystal to the inner frame of the goniometer, however, guarantees the reproducibility of the angular orientation of the crystal even after multiple changes of the target.

The two rotary mechanisms are mounted onto a sliding carriage which allows shifting (X) of the crystal out of the beam. At a second target position an 18 μm thick Al foil serves as an OTR view screen for the beam setting.

The goniometer is remote-controlled via programmable Phytron OMC/TMC 93-70 MINI step-motor control units. The software allows absolute as well as relative positioning of the goniometer coordinates (X;ϑ,ψ) in units of MS. The once defined zero position serves as a relative reference. The endpoints of the drives cannot be used for that. The practical scales (X/μm, ϑ/degrees and ψ/degrees) have been obtained by a calibration procedure.

The goniometer runs well at pressures down to 10^{-9} mbar. The reproducibility of angular positioning has been checked by measurements of planar CR from diamond. It can be estimated from angular scans to be ≈ 1 mrad (10 MS). This accuracy is enough for CR production experiments.

[1] AML Goniometer Manual, Arun Microelectronics Ltd. Arundel, England, 1994

[1] *FMB GmbH, Berlin, Germany*
[2] *ZFI FZ Rossendorf*

Beam Monitoring at the Radiation Physics Beam Line

W. Neubert, K. Heidel, J. Pawelke, W. Wagner, W. Enghardt

The current monitors installed at the beam line of the electron accelerator ELBE are induction devices suitable for beam intensities $\geq 1\,\mu$A. Experiments to ascertain the conditions for generation of channeling radiation by proper crystals require a precise monitoring of beam intensities from about 1 nA to some hundreds of nA. A commonly used device in the MeV region is the secondary electron monitor (SEM). Such type of monitor constructed in the past and described in [1] was installed at $\simeq 20$ cm behind the the crystal position in the goniometer chamber of the radiation physics beam line. The SEM can be removed from its measuring position by a pneumatic driven UHV bellow without breaking the vacuum.

The SEM must be calibrated by a Faraday cup (FC) positioned as close as possible to the SEM in order to minimize the loss of beam electrons scattered away by the SEM. The installation of such a FC at a distance of $\simeq 20$ cm from the SEM was only possible by the construction of a dedicated adapter flange which substitutes the former one at the exit of the goniometer chamber. The disponable space inside this flange, the required application to beam energies of 20 MeV as well as the realisation of in-beam and out-of-beam positions allowed only a very compact construction. It was realised using ranges in the CSD approximation supported by simulations using the program package GEANT 3.2. The body where the electrons are slowed down consists of a conical cylinder of Al terminated by a Cu disc (see [2]). Although the ratio of backscattered electrons in the energy range from 15 MeV to 20 MeV is about 10^{-3} as a precaution two magnetic pieces of hard sinter ferrits (BaFe/SrFe, type R1212) were inserted into the Al corpus near to the aperture of the FC. They supply a magnetic induction of 5.6 ± 0.2 mT perpendicular to the beam axis which avoids backscattered electrons to escape from the FC. The cylindric body of the FC (diameter = 53 mm, length = 86 mm) is insulated from the outer Al screen by 4 Marcor sticks. It was checked that a negative biased screen is unnecessary due to the implemented ferrits. The FC is held on a Vitronit construction which insulates it from the ground potential of the beam tube.

The beam absorbed in the FC is measured by a current integrator based on the operation amplifier OPA-129 as already described in [1]. The calibration carried out using a precision current generator confirmed a linear response in the dynamical range from zero to 1 μA with an offset of -0.35 mV. The efficiency of the SEM was measured with the same integrator type. Fig. 1 shows that a voltage ≥ 10 V applied to the outer collecting foil electrodes provide for full efficiency. The response of the SEM related to the FC was measured as function of the beam intensity using different pulsing regimes. Fig. 2 demonstrates a linear behaviour in the range of interest.

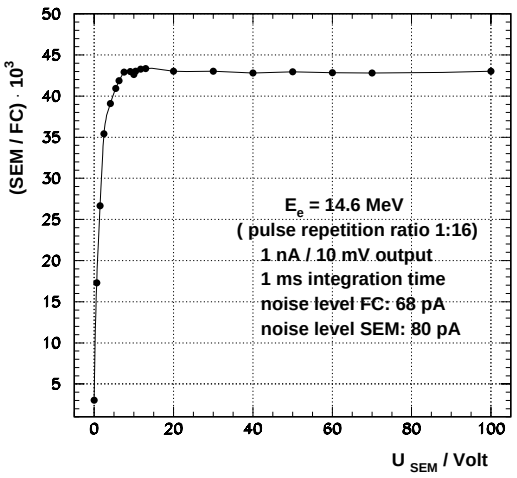

Fig. 1 *Efficiency of the SEM related to the FC as function of the voltage applied to the outer foil electrodes.*

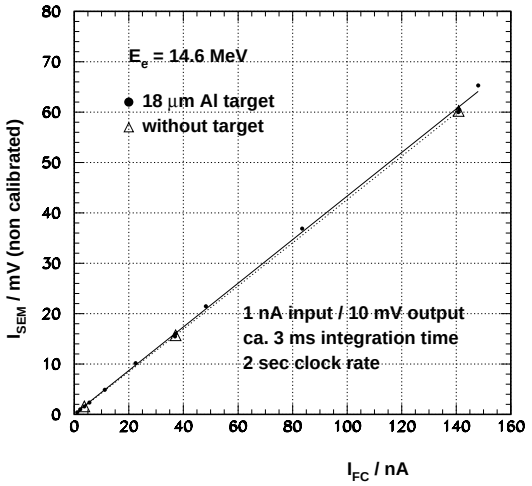

Fig. 2 *Response of the SEM as function of the beam intensity measured with the FC. The solid and dashed lines are fits to the points measured with 18 μm Al and without target, respectively.*

The calibration factor of the SEM obtained with removed target amounts to $R = I(\mathrm{SEM})\,/\,\mathrm{I(FC)} = (4.29 \pm 0.08) \cdot 10^{-2}$ at the incident energy 14.6 ± 0.2 MeV. The accuracy of the current measurement in the FC was estimated to be $\simeq 1\,\%$ as follows from GEANT 3.2 simulations taking into account electron losses caused by scattering in the SEM and electron escape from the FC corpus. Other experimental data cited in ref. [3] obtained with thicker three-Al-foil setups amount to $2.8 \cdot 10^{-2} \leq R \leq 3.4 \cdot 10^{-2}$.

[1] W. Neubert et al., Wiss.-Techn. Berichte FZR-341 (2002) 16
[2] W. Neubert, J. Pawelke et al., this report, p. 74
[3] V.J. Vanhuyse et al., Nucl. Instrum. Meth. 15 (1962) 63

GEANT Simulations for the Beam Monitors at the Radiation Physics Beam Line

W. Neubert, J. Pawelke, W. Wagner, W. Enghardt

The beam monitors described in the preceding contribution [1] have been used to determine absolute yields of channeling radiation produced by electron impact in diamond and other crystals. Measurements of the relative current obtained by the secondary electron monitor (SEM) compared with the corresponding one from the Faraday cup (FC) were performed in subsequent runs at beam intensities which cover more than 2 orders of magnitude. The obtained ratios are shown in Fig. 1 together with the main setup parameters.

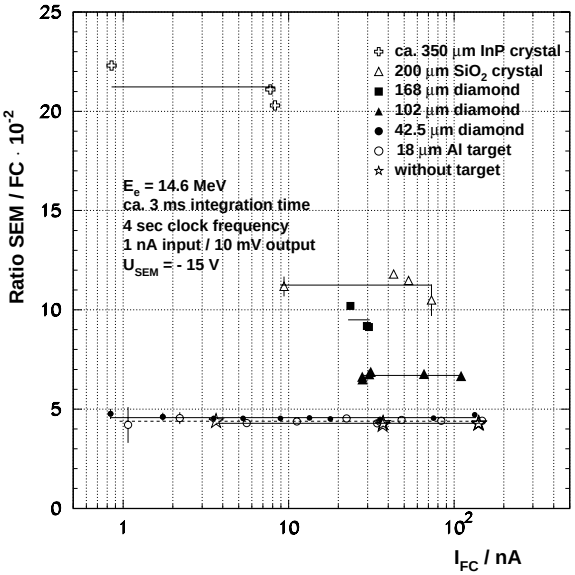

Fig. 1 *Ratios of the beam current measured with the SEM and the Faraday cup as function of the beam intensity.*

The ratio $R = I(\mathrm{SEM})/I(\mathrm{FC})$ was found to be constant for a given target, but the thicker the crystal the larger the measured ratio. Simulations using the program package GEANT 3.2. were performed in order to find out the reason of this behaviour and to quantify the deviations from the calibration ratio $R = 4.29 \pm 0.08$. The beam spot observed at the OTR 18 μm Al screen in target position was imitated by a parallel beam with a Gaussian profile $\sigma_{x,y} = 0.415\,\mathrm{mm}$.

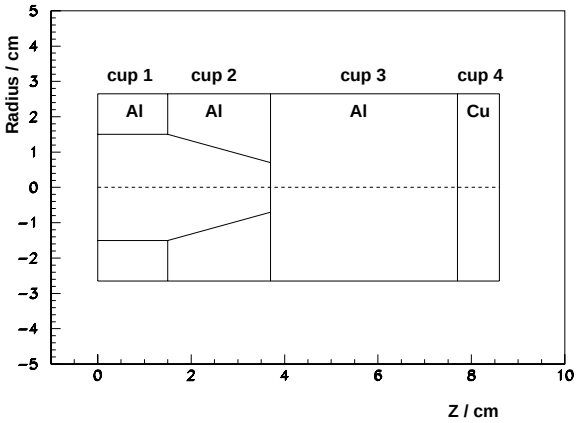

Fig. 2 *Dimensions of the cylindric Faraday cup and its representation as 4 bodies in the simulations.*

The diamond crystal was approximated by amorphous carbon with the average density of diamond $\varrho = 3.516\,\mathrm{g/cm^3}$. The SEM was represented by a compact Mylar disc with the sum thickness of the 3 foil electrodes surrounded by a iron ring corresponding to the construction dimensions of the stainless steel holders. The geometry of the FC is shown in Fig. 2. In the simulations all relevant electron interaction processes were taken into account.

The lateral spread of the electron beam caused by the SEM decreases from $\sigma_{x,y} \simeq 1\,\mathrm{mm}$ at 12 MeV to $\simeq 0.4\,\mathrm{mm}$ at 32 MeV in front of the FC. Thus the main beam intensity fits always into the aperture of the FC. But to a greater extend beam electrons are lost by scattering in the target crystals. The fraction of simulated beam electrons found in the aperture of the SEM and detected in the FC are assembled in Tab. 1. Incoming electrons of $\simeq 15$ MeV are completely stopped in cup 3 of the FC (cf. Fig. 2) but affected by copious electrons mainly produced by inelastic interactions producing δ-rays. In order to avoid double-counting a cut set at 8 MeV allowed to eliminate most of such secondaries. The fraction of electrons assigned to the incoming beam are given in Tab. 1. They allow to correct the measuring data from both the SEM and the FC for electron losses due to scattering mostly in the target. The corrected ratios R_{corr} agree within the estimated errors with the calibration ratio $R = 4.29 \pm 0.08$ measured without target. The multiple scattering in thick targets adulterates mainly the measurement of the beam current in the Faraday cup unlike the SEM, closer located to the crystal. This monitor requires only moderate corrections as seen in Tab. 1. These corrections are nearly independent of the beam profile because dedicated simulations performed with other Gaussian or asymmetric profiles showed that the width of the outcoming beam is almost the same even after passing a moderate thickness. Therefore, the corrections are basically determined by the target thickness.

Tab. 1 *Results of simulations at 14.6 MeV. The fractions of the started beam electrons counted within the aperture of the SEM and detected in the FC are given in columns 2 and 3, respectively. The ratios R_{exp} in column 4 correspond to Fig. 1 whereas column 5 gives these ratios corrected for calculated losses by electron scattering.*

Target	SEM %	FC %	R_{exp} $\cdot 10^{-2}$	R_{corr} $\cdot 10^{-2}$
only SEM	100	99.9	4.29	4.29
18 μm Al	99.0±0.4	93.7	4.36	4.1±0.2
42.5 μm C	98.8±0.8	87.9	4.7	4.2±0.2
102 μm C	95.7±0.8	64.9	6.7	4.6±0.5
168 μm C	90.6±0.6	47.5	9.5	4.8±1.1
200 μm SiO_2	84.0±1.0	36.6	11.24	4.6±1.4

[1] W. Neubert, K. Heidel et al., this report, p. 73

A Cell Irradiation System for the Channeling X-Ray Beam at ELBE

J. Pawelke, A. Panteleeva

One area of research activities at the ELBE facility is devoted to the determination of the relative biological effectiveness (RBE) of X-rays with photon energy in the range 10 to 100 keV for different cell types and biological endpoints. For this purpose, intensive quasi-monochromatic X-rays of variable energy will be produced by channeling of the ELBE electrons in diamond crystals in the radiation physics cave [1] and reference irradiations will be performed at a conventional X-ray tube in a nearby laboratory [2]. For precise RBE measurements, a larger number of cell monolayer probes have to be irradiated and the results from both radiation qualities have to be compared. Here, the irradiation at the ELBE X-ray beam has some peculiarities, coming, on the one hand, from the geometry and spectral characteristics of the source, and on the other hand, from the cell culture conditions [3, 4]. Furthermore, the longer time necessary for switching on and tuning of the ELBE beam and for opening and closing the radiation protection door of the cave requires a steady and consecutive irradiation of several probes controlled from outside the irradiation site. Therefore, an irradiation system which fulfils all these demands and is appropriate for extensive routine use including user-friendly operation has been designed. It was built by IfE-Automatisierung GmbH Dresden and consists of a probe supply unit (Fig. 1), a control unit and a personal computer.

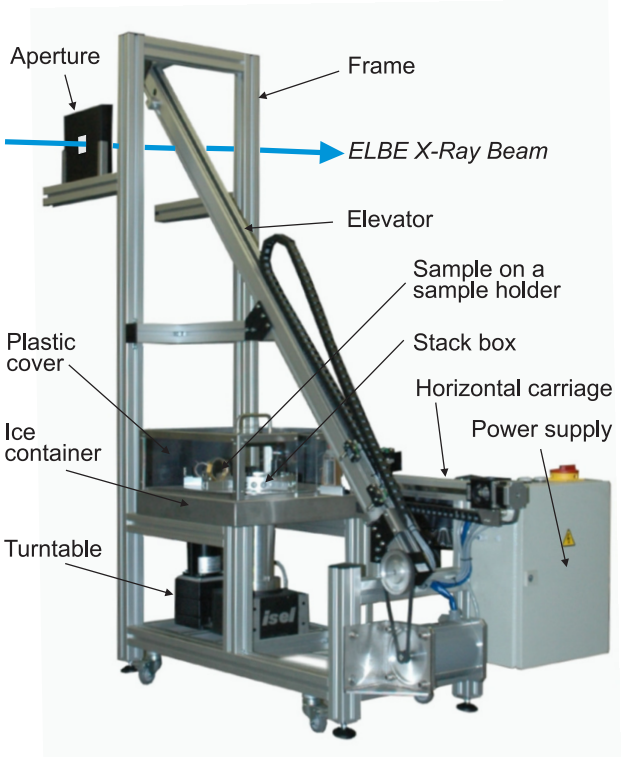

Fig. 1 *View of the cell irradiation system.*

The control unit is placed outside the irradiation site in order to protect the electronics from the radiation background and connected by a 25 m cable to the power supply. From the PC, placed also outside the irradiation site and connected to the control unit, the irradiation procedure is software controlled. In order to provide defined environment conditions before and after irradiation, the probes are placed in a stack box, covered with a plastic lid. In the stack box, a vessel is placed below the probes, which can be filled with ice or water at 37°C, depending on the requirements coming from the studied endpoint. Several irradiation vessel geometries are possible (Fig. 2), all of them being able to be transported and irradiated from the same stack box. The stack box with up to 27 probes is positioned away from the beam and space for additional radiation shielding is provided.

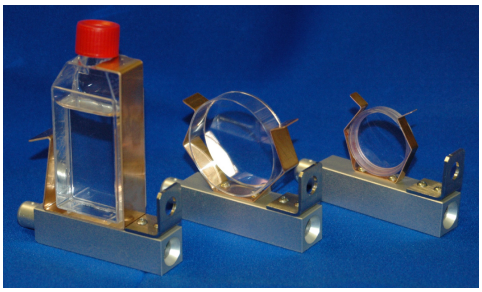

Fig. 2 *Dish holders for different geometries: 25 cm^2 culture flask, 6 cm diameter Petri dish and 3.5 cm diameter Biofolie membrane-based culture dish (from the left).*

The scanning irradiation system fulfils several tasks with different motion and precision. First the desired cell probe has to be brought into starting position, taken out of the stack box and transported to the X-ray beam. Then, homogeneous dose distribution over the sample area is provided by scanning movement of the sample in the plane perpendicular to the beam axis. The movement can be of any composition of a horizontal component and a component along the elevator, both performed by linear guides simultaneously, and depends on the beam characteristics and sample geometry. The changeable beam aperture allows additional flexibility in the irradiation geometry. The dose delivered to the cells follows, on the one hand, from the scan speed, and on the other hand, from the fluctuations in the electron beam intensity, and correspondingly in the X-ray intensity. Therefore, the scan speed is regulated by a feedback signal from an online dose monitoring system. Alternatively a photon flux or electron current monitor can be used, provided that there exist a dependence between the detector signal and the dose rate. Also a non-linear dependence can be online processed by the software. In order to choose the most appropriate solution for the online monitoring system, the dose fluctuation has to be studied and the best practical solution has to be chosen.

[1] W. Wagner, A. Panteleeva et al., Wiss.-Techn. Berichte FZR-401 (2004) 56
[2] J. Pawelke, T. Mikuletz, A. Panteleeva, Wiss.-Techn. Berichte FZR-401 (2004) 58
[3] A. Panteleeva, J. Pawelke, E. Lessmann, Wiss.-Techn. Berichte FZR-341 (2002) 89
[4] A. Panteleeva, E. Lessmann, Wiss.-Techn. Berichte FZR-372 (2003) 65

Design of the Radiation Protection Shielding of the X-Ray Laboratory at ELBE

U. Reichelt, A. Hauptmann[1], B. Naumann[2], J. Pawelke, T. Schönmuth[1], M. Sommer[3]

In preparation of projected experiments with X-rays at the ELBE facility of the FZ Rossendorf [1], it was intended to build up an appropriate laboratory. For dimensioning the radiation shielding, especially at the ceiling, a Monte Carlo transport simulation was done [2]. Now these results were verified comparing them with dose measurements. Furtheron the influence of some changes in the final laboratory construction was investigated.

The floor plan of the laboratory is shown in Fig. 1. Two of its walls consist of heavy concrete. They are at least two meters thick. The other walls are made of 2.8 or 10 cm thick lead panels. The X-ray tube ISOVOLT 320/13 made by Agfa NDT Pantak Seifert is used as source. Its exit window collimates the photons to a cone with 40 degrees opening angle (see Fig. 1). The maximum tube voltage is 320 kV where a maximum anode current of 13 mA is possible [1].

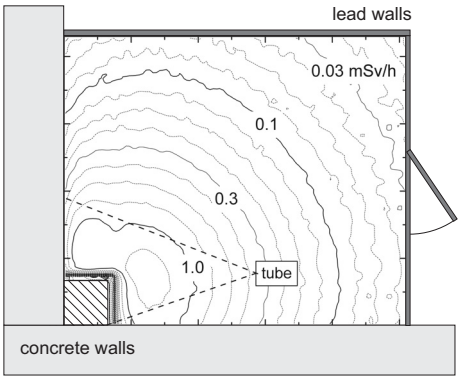

Fig. 1 *Topview of the X-ray laboratory, including tube position and dose rate distribution (320 kV, 1 mA)*

The previously done simulations [2] were adapted to the changed geometry of the laboratory according to its final construction. A main issue was to determine the influence of the concrete cube at the corner where the photons impinge the wall. Furtheron the position of the X-ray source was shifted. The determined dose distribution is plotted in figure 1 and coloured in figure 2. The present changes cause a deformed maximum and a certain decrease of dose rate compared to former results [2]. In order to verify the simulation results, the dose distribution was measured with different thermo luminescence detectors (TLD). The boxed TLD tablets were attached underneath the ceiling on strong steel girders. The exact positions are drawn in figure 2. Different measuring systems were used to reduce systematic errors. The first was provided and analysed by the Fachbereich Sicherheit[1] which was using LiF:Mg,Cu,P detectors. The second one from TU Dresden[3] deployed CaF_2:Cu TLDs. The measurement was done at 3 mA anode current and thirty minutes exposure time. The results are compared to the simulation results in table 1. The ratio varies from 2.0 to 5.7 for TLD 1 and from 1.3 to 2.6 for TLD 2. One reason for the differences is the additional increase of measured doses by back scattered photons from the steel ceiling. At the simulation there was no ceiling material, because this was necessary to estimate the required radiation shielding. For correct experimental results furtheron the energy dependent detector response has to be taken into account. That requires the knowledge of the scattered photon spectra. Also the constructional details like the steel girders were not included into in the geometric model used in the simulation.

Tab. 1 *Comparison of dose in mSv measured by TL detectors and simulated data (320 kV, 3 mA for 0.5 h)*

coord.	TLD 1 (FZR)	TLD 2 (TUD)	simulated
A1	12.0	4.5	2.1
B1	17.0	11.0	4.5
C1	23.0	21.0	8.1
A2	6.5	-	2.6
B2	12.0	-	4.8
C2	22.0	-	8.3
A3	-	3.0	2.2
B3	-	4.5	3.5
A4	6.0	-	1.7
B4	6.7	-	2.4
C4	6.5	-	3.3

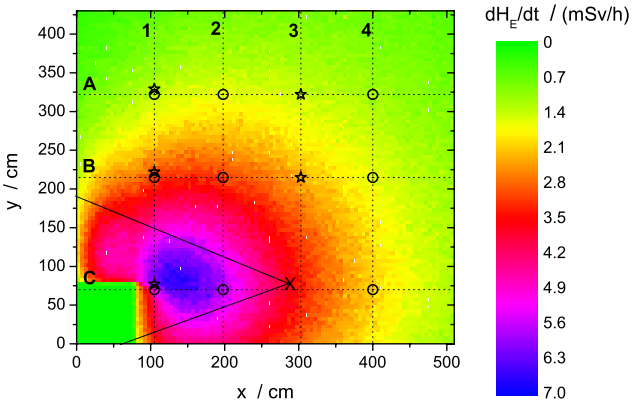

Fig. 2 *Equivalent dose rate determined by simulation (320 kV, 1 mA) and positions of measurements*

Nethertheless with the simulations a time and cost saving solution for dimensioning the radiation protection shielding was found. The comparison to experimental dose values verifies the applicability of AMOS as a useful tool to this field. It had an important part in the permission process by radiation protection ordinance.

[1] J. Pawelke, S. Eckert, W. Enghardt, Wiss.-Techn. Berichte FZR-401 (2004) 57

[2] U. Reichelt, J. Henniger, W. Neubert, J. Pawelke, Wiss.-Techn. Berichte FZR-372 (2003) 71

[1] *Verein für Kernverfahrenstechnik und Analytik Rossendorf e.V. (VKTA), Fachbereich Sicherheit*

[2] *FZ Rossendorf, ZA Technischer Service, Abteilung Sicherheit und Strahlenschutz*

[3] *Technische Universität Dresden, Institute of Nuclear and Particle Physics, Department of Radiation Protection Physics*

Calculation of Secondary Electron Spectra Induced by Photon Irradiation

U. Reichelt, J. Henniger[1], W. Enghardt

In medicine and biology it is common to investigate radiation responses of biological systems with X-rays. The main energy deposition is caused by the produced so called secondary or δ electrons. They are responsible for the main part of ionisations which are the physical endpoint for energy propagation in matter.

Normally the experimental conditions are not fully compatible to the conditions in practice. For instance the surrounding tissue in human body contributes to the radiation field a certain cell is exposed to. If the experimental tissue sample is a single cell layer or significantly different materials are nearby this influence has to be considered.

Hence for reliable results it is necessary to know the electron distribution in the experimental target setup. Therefore, the developed Monte Carlo algorithm AMOS [1,2] is used. It treats the coupled electron and photon transport as well as the production of secondary radiation due to the relaxation of ionised atoms. As target structure a water layer of 250 μm thickness was used. The photons impinge perpendicularly to the layer. The spectral electron flux density φ_E was estimated with 501 plain detectors parallel to the water surface. Their distance is 0.5 μm. The energy axis is diveded into 0.1 keV wide channels. The results are integrated over the infinte extended detector plain. This corresponds to the condition of a small target in a large radiation field.

In the figures the results of depth dependent energy fluence spectra for monoenergetic photon irradiation with 50 keV in figure 1 and 100 keV in figure 2 are presented. They are normalized to the flux density φ_0 of the primary photons. The typical structure in both figures is quite similar. The bar of high intensity at the low energy end of the spectra results from electrons emitted by inelastically scattered photons (Compton electrons). Analytical calculations of the backscattering energy (180 degrees scattering angle) shows possible electron energies up to 8.2 keV for 50 keV and 28.1 keV for 100 keV primary photon energy. This corresponds with the achieved results very well.

The high energy part is produced by absorption of primary photons. Because the absorption cross section is proportional to the atomic number Z to the power of four to five, most of this ionisations take place at oxygen atoms. The energy conservation with the binding energy results in smaller intensities at energies above 49.5 keV and 99.5 keV respectively, because the binding energy of the K shell electrons of oxygen is 537 eV. The flux densities above this limit, visible in figure 1 as a thin light blue stripe, is produced by photoelectrons from higher shells as well as from hydrogen. While at 50 keV the photo effect dominates the secondary electron spectra, at 100 keV the incoherent scattering produces the highest intensities (compare Fig. 1 and Fig. 2).

For experiments it is necessary to determine the depth intervall where the secondary particle equilibrium is fulfilled. Therefore, not a constant depth dose is important but rather a constant electron spectrum is essential. In general this can be a difference for the ionisation of heavier atoms.

Near material boundaries this is not fulfilled. At the incidence surface this region is larger then the one at the backside because of the directional distribution of the produced secondary electrons and scattered photons. While at 50 keV photon irradiation they are about 30 μm and 23 μm thick, 100 keV photons produce varying spectra below 100 and above 185 μm. Hence for biological irradiation experiments with conventional X-ray tubes the thickness of the target should be at least 250 μm. Otherwise additional build-up layers have to be attached in front of as well as behind the target structure.

[1] U. Reichelt, J. Henniger et al., Proc. of 14th Int. Conf. of Solid State Dosimetry, Radiat. Protect. Dosim. (2005) *in press*

[2] U. Reichelt, J. Henniger, Wiss.-Techn. Berichte FZR-401 (2004) 62

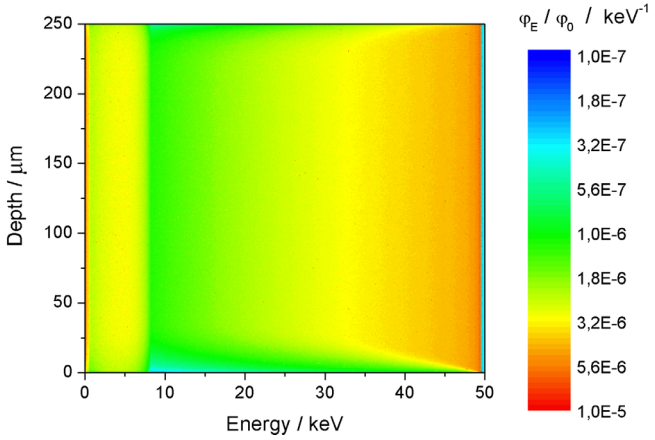

Fig. 1 *Depth dependent secondary electron fluence spectra in a 250 μm water layer for 50 keV photon irradiation*

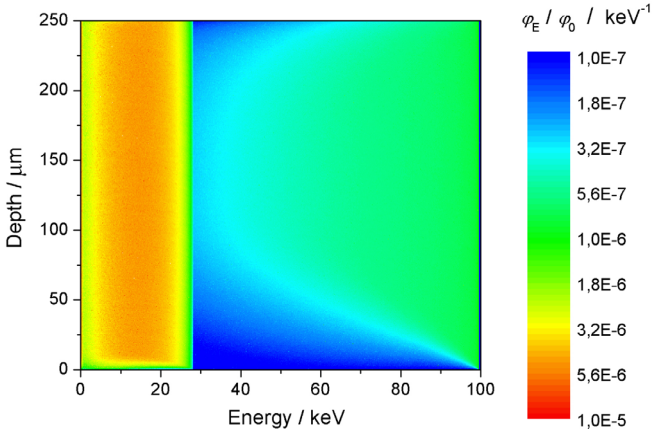

Fig. 2 *Depth dependent secondary electron fluence spectra in a 250 μm water layer for 100 keV photon irradiation*

[1] *Technische Universität Dresden, Institute of Nuclear and Particle Physics, Department of Radiation Protection Physics*

Monte Carlo Simulations of Electron Penetration into Water Layers by means of AMOS

U. Reichelt, J. Henniger[1], W. Enghardt

The accurate description of the propagation of electron radiation in matter is difficult but necessary in various tasks. For instance at radiotherapy with beta or Auger electron emitting isotopes an adequate knowledge about depth dose profiles and the penetration depth of the electrons [1] is required. For this kind of investigations the coupled photon electron transport code AMOS [2] was developed. It treats the electron and photon transport as well as the production of secondary radiation by relaxation processes of ionised atoms.

First simulations of depth dependent electron flux density spectra were simulated. The primary electrons impinge perpendicularly to the surface of a thick water layer. As an example the results for 200 keV monoenergetic electrons are shown in figure 1. Therein it can be seen that low energetic electrons are present at any depth from the surface down to the electron range. Their intensity varies only by about one order of magnitude. There is a kind of upper limit in the energy scale which rapidly decreases with increasing depth. This offers the possibility for the definition of an electron penetration depth from the ratio of the spectral electron flux density and the flux density of the primary electrons. If a value of 10^{-6} for this ratio is assumed, a penetration depth of 480 μm is found for 200 keV electrons in water (Fig. 1).

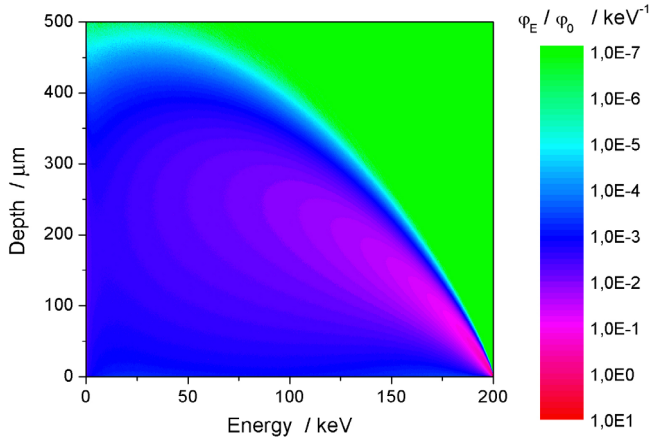

Fig. 1 *Depth dependend normalised electron flux density spectra for 200 keV electron irradiation*

Further simulations were done to investigate the energy deposition and the electron density in irradiated layers. Thereby the energy current I_E, the electron current I and electron flux density φ are determined in certain depths of a 250 μm thick water layer. Therefore, infinite detector planes, which are parallel to the water surface, are used. Hence every particle independent of its lateral displacement crossing this plain contributes to the detector response. This corresponds to two different experimental conditions. Either there is a huge sensitive area with a small irradiated spot or there is a small sensitve volume (e.g. cells) in a large electron radiation field. For 400 keV electron irradiation the parameters normalised to the primary electron flux density φ_0 and current I_0 respectively are shown in figure 2 and their derivatives in figure 3. The differential energy current is equal to the energy deposition. Its maximum at 280 μm correspondes to the highest electron flux in figure 2. This proves that the main damage production is done by δ-electrons, which are mainly represented in the flux density. In contrast to this the electron current is affected by primary and rarely scattered electrons. Their direction is still dominated by the incidence direction. Anyhow the maxima of the differentiated electron current and flux density are at the same depth.

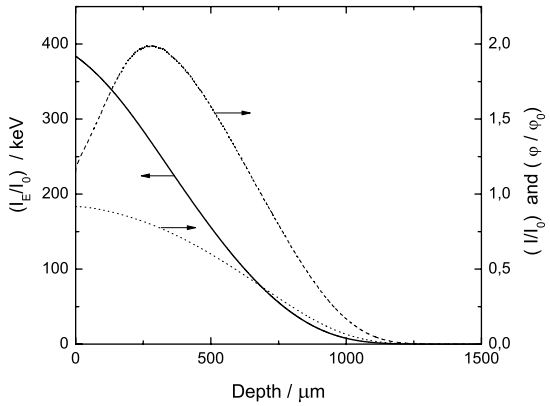

Fig. 2 *Normalised energy current I_E (solid), electron current I (dotted) and flux density φ (dashed) versus depth at 400 keV electron irradiation*

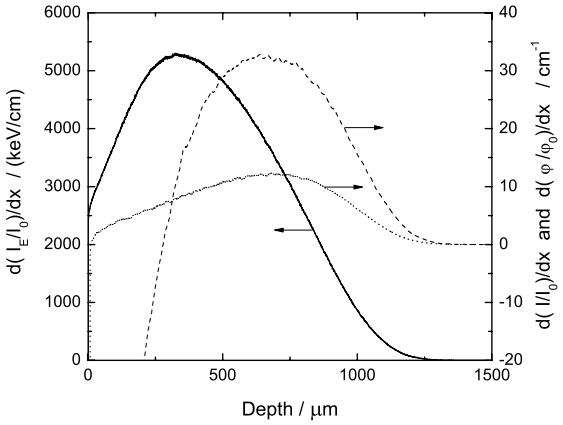

Fig. 3 *Differential normalised energy current I_E (solid), electron current I (dotted) and flux density φ (dashed) versus depth at 400 keV electron irradiation*

By means of AMOS it is possible to determine dose depositions in preparing and analysing biological experiments. Further developments are in process to increase the accuracy of used physical models and to add further physical effects like the Doppler broadening.

[1] H. Krieger, Strahlenphysik, Dosimetrie und Strahlenschutz, B.G. Teubner Stuttgart (2001)

[2] U. Reichelt, J. Henniger, Wiss.-Techn. Berichte FZR-401 (2004) 62

[1] *Technische Universität Dresden, Institute of Nuclear and Particle Physics, Department of Radiation Protection Physics*

Suppression of Random Coincidences during In-Beam PET Measurements [B, G, E]

P. Crespo, T. Barthel[1], H. Frais-Kölbl[2,3], E. Griesmayer[2,3], K. Heidel, K. Parodi, J. Pawelke, W. Enghardt

In-beam positron emission tomography (PET) is currently applied for in-situ monitoring of charged hadron radiotherapy [1]. However, in-beam PET data, measured at beams with a sub-μs-microstructure due to the accelerator radiofrequency (RF), are highly corrupted by random coincidences arising from prompt γ-rays following nuclear reactions as the projectiles penetrating the tissue [2,3]. Since conventional PET random-correction techniques fail, the clinical in-beam PET at the therapy facility at the Gesellschaft für Schwerionenforschung (GSI) Darmstadt merely reconstructs events registered in the pauses ($\sim$ 2 - 4 s) between the beam macropulses ($\leq$ 2 s) [1]. We have successfully tested at GSI two methods for suppressing the micropulse-induced random coincidences during beam extraction. Image statistics increased by about 90 %. Both methods, depicted in Fig. 1 (tested with Lucite phantoms only), synchronize the $\gamma\gamma$-coincidences measured by the positron camera with the time microstructure of the beam, either by using the RF-signal from the accelerator or the signal of a diamond detector placed in the beam path before the target [4].

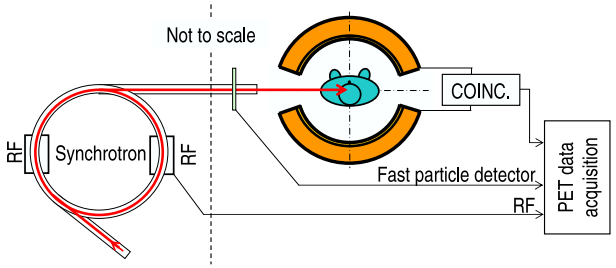

Fig. 1 *Methods proposed for in-beam PET random correction: every detected $\gamma\gamma$-coincidence is correlated with the incoming ion by using either a particle detector or the RF signal from the accelerator.*

The measured correlation between the $\gamma\gamma$ coincidences and the beam microstructure is shown in Fig. 2 for the RF measurements (diamond detector shows similar results). This correlation can first be seen in column 1: the shape of the $\gamma\gamma$ time spectrum is deteriorated by randoms and the $\gamma\gamma$-RF time spectrum shows a peak above a constant plateau, indicating the elevated and expected event flux during the microbunches [3]. After setting an energy window for the photon detectors (column 2), the peak-to-plateau ratio in the $\gamma\gamma$-RF time spectrum decreases more than one order of magnitude and the corresponding $\gamma\gamma$ time distribution presents the same shape and resolution as the spectra aquired during the extraction pauses [5].

Fig. 3 shows the depth profiles obtained by sorting events arriving within the microbunches from those outside it (B_2 and A_2 in Fig. 2, respectively).

In summary, the energy and triple-coincidence time correlated spectra (Fig. 2) and tomographic images of the β^+-activity induced by the beam in a plastic phantom (Fig. 3), first-measured during beam extraction, clearly confirm the feasibility of the proposed random suppression methods [5].

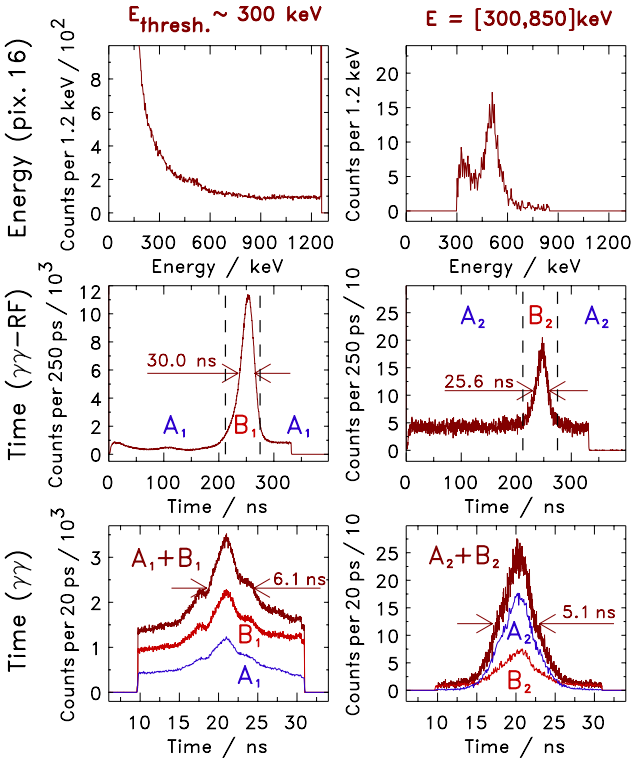

Fig. 2 *Results of $\gamma\gamma$-RF coincidence measurements during beam extraction. The $\gamma\gamma$ coincidence time spectra (bottom) result from different sorting conditions in the γ-ray energy spectra (top) and the $\gamma\gamma$-RF time distributions (middle).*

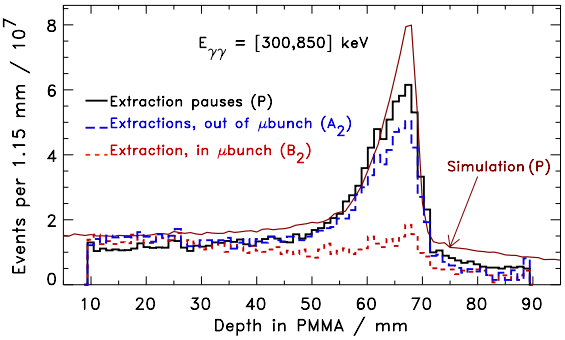

Fig. 3 *Depth profiles obtained with the $\gamma\gamma$-RF method. The simulation regards extraction pauses (P) only.*

[1] W. Enghardt, P. Crespo et al., Nucl. Instrum. Meth. A 525 (2004) 284
[2] J. Pawelke, W. Enghardt et al., IEEE T. Nucl. Sci. 44(4) (1997) 1492
[3] K. Parodi, P. Crespo et al., Nucl. Instrum. Meth. A (2004), accepted
[4] W. Enghardt, P. Crespo et al., Deutschen Patent- und Markenamt München (2004), pending
[5] P. Crespo, T. Barthel et al., IEEE T. Nucl. Sci. (2004), submitted

[1] *was also with Hochschule Mittweida, University of Applied Sciences, 09648 Mittweida, Germany*
[2] *MedAustron, Viktor-Kaplan-Str. 2, 2700 Wiener Neustadt, Austria*
[3] *FOTEC, Viktor-Kaplan-Str. 2, 2700 Wiener Neustadt, Austria*

The Feasibility of In-Beam PET for Therapeutic Beams of ^{3}He [G,E]

F. Fiedler, K. Parodi, W. Enghardt

At the clinical heavy ion treatment facility, which is under construction in Heidelberg, beams of He will also be used for tumour irradiation. These will be monitored by means of in-beam PET for quality assurance. This requires a precise knowledge of the spatial distribution of beam induced positron emitters in the irradiated volume.

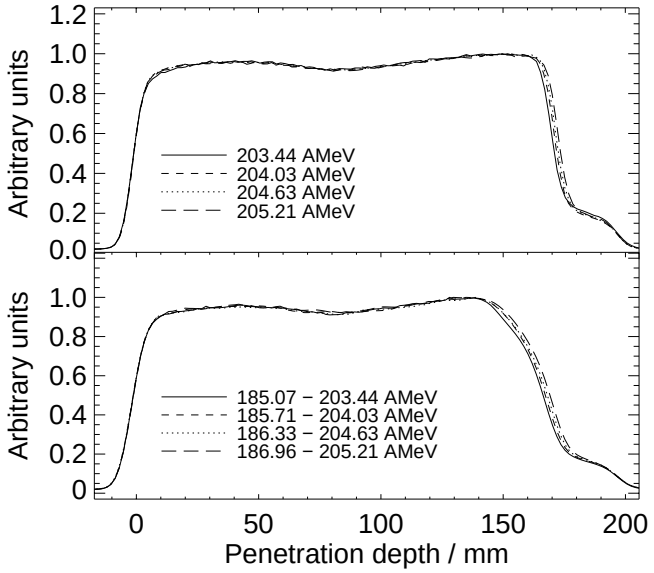

Fig. 1 *Measured depth profile of β^+-activity induced by mono-energetic (top) and SOBP irradiation (bottom), formed by eleven equally spaced energy steps stopped in PMMA.*

For this an experiment at the Gesellschaft für Schwerionenforschung (GSI) with pencil-like ^{3}He-beams of 130.03 AMeV to 207.92 AMeV and mean intensities varying from $2.0 \cdot 10^8$ to $3.5 \cdot 10^8$ ions/s has been carried out. The data were taken in list-mode, the PET-measurement was performed mostly over 10 min of irradiation and 20 min of decay. The beams were stopped in homogeneous thick targets consisting of PMMA, graphite and solid water [1], which were placed in the center of the field of view of the PET-scanner at the experimental carbon ion therapy facility at GSI [2]. The parameters of the irradiation are outlined in Tab. 1. It was shown for a spread-out Bragg peak (SOBP) irradiation of the PMMA phantom as well as for mono-energetic beams that range differences of about 0.9 mm can be resolved (Fig. 1). The lateral profile was found in a reasonable agreement with the calculations from [3] (Fig. 2).

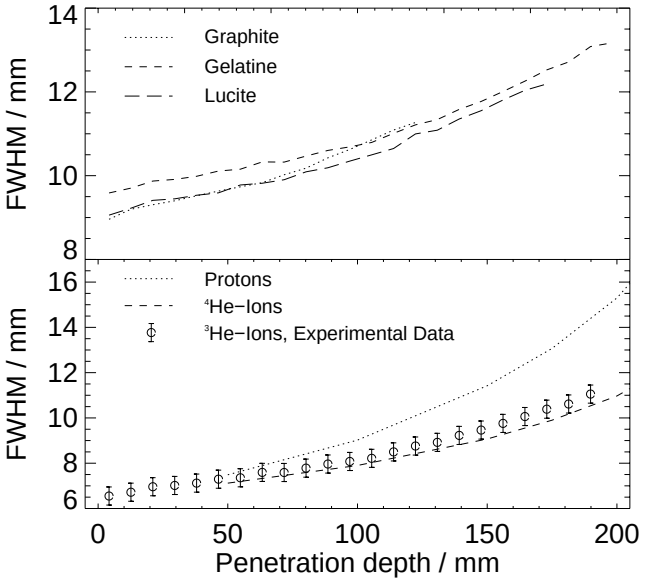

Fig. 2 *Top: Lateral broadening of the measured profiles along the penetration depth for the 3 different targets, irradiations were done by an energy of $E = 207.92$ AMeV. Down: Comparison of the measured beam broadening in the water target with $E = 207.92$ AMeV with the calculations in [3], data are corrected for the system spatial resolution.*

[1] F. Fiedler, K. Parodi, W. Enghardt, this report, p. 82
[2] W. Enghardt, P. Crespo et al., Nucl. Instrum. Meth. A 525 (2004) 284
[3] Th. Haberer, Ph.D. Thesis, GSI Report 94-09 (1994)
[4] K. Parodi, Wiss.-Techn. Berichte FZR-415 (2004)

Target	Energy / AMeV	τ	I_s/ 10^8 spill^{-1}	t_s / s	$N_{\mathrm{ev}}(t_0)$ cps	$P_{^{10}\mathrm{C}}$ / spill	$P_{^{15}\mathrm{O}}$ / spill	$P_{^{13}\mathrm{N}}$ / spill	$P_{^{11}\mathrm{C}}$ / spill	C $\cdot 10^{-3}$	$\mathrm{d}A/\mathrm{d}t$ Bq s^{-1}
PMMA	130.03	120	5.4	1.52 ± 0.02	30972	15197	61935	9106	189832	7.5	667
PMMA	166.05	120	3.6	1.40 ± 0.02	27967	13457	59782	7165	179197	7.1	665
PMMA	207.92	120	2.7	1.37 ± 0.04	26928	12375	58020	7922	175331	6.7	646
Graphite	130.03	120	5.4	1.53 ± 0.04	17536	15810	—	—	247977	6.7	463
Graphite	166.05	120	3.6	1.41 ± 0.06	17284	16034	—	—	232316	6.4	503
Graphite	207.92	120	2.7	1.39 ± 0.06	17834	16743	—	—	236680	6.3	513
Water	130.03	120	5.4	1.54 ± 0.04	57498	10036	215222	23755	90589	9.1	1082
Water	166.05	120	3.6	1.41 ± 0.04	51015	5998	196628	24930	77874	8.7	1002
Water	207.92	99	2.7	1.35 ± 0.02	45110	3858	178386	21882	69643	8.0	900
Water$*$	207.92	720	2.7	1.31 ± 0.04	53250	1485	160456	19670	63269	8.0	783

Tab. 1 *Irradiation parameters for mono-energetic irradiation of the three different targets as well as relative isotope production rates P and relative β^+activity production rate $\mathrm{d}A/\mathrm{d}t$ calculated according to [4]. The number of spills is indicated by τ, t_s gives the average spill duration, C is the correction factor for detection efficiency and γ-ray attenuation and $N_{\mathrm{ev}}(t_0)$ is the count rate at the end of the irradiation. The errors were estimated to be 5% for the correction factor C, 5 % for $P_{^{11}\mathrm{C}}$, 5 % for $P_{^{15}\mathrm{O}}$, 10 % for $P_{^{10}\mathrm{C}}$ and 15 % for $P_{^{13}\mathrm{N}}$ in case of the PMMA-target, whereas for the water target the error for $P_{^{13}\mathrm{N}}$ is 10 %. For the target indicated by $*$ the error of $P_{^{10}\mathrm{C}}$ is calculated to be 35 %.*

The β^+-Activity Production During Therapeutic Irradiation with Beams of Protons, ^{3}He and ^{12}C [G,E]

F. Fiedler, K. Parodi, W. Enghardt

To compare the β^+-activity produced by ^{3}He-beams with that measured earlier for ^{12}C and proton irradiation [1], experiments with PMMA targets have been carried out. The energy was chosen to achieve comparable ranges as in the ^{12}C and proton irradiation. The parameters of the irradiation are outlined in [2]. The spatial distributions obtained by a backprojection with attenuation correction are depicted in Fig. 1, in Fig. 2 the lateral broadening of the ^{3}He-beams for the different energies is displayed.

The estimation of absolute values of positron emitter production during particle extraction (Tab. 1) was done using the approach given in [1]. Ratios r of the β^+-activity production rate P by ^{3}He-beams compared to ^{12}C and proton beams in PMMA at the same physical dose were determined due to formulae (1) and (2), where I is the beam intensity in particles per second, R indicates the range, C gives the correction factor and $\mathrm{d}A/\mathrm{d}t$ is the relative β^+-activity production rate [1, 2]. The factors $\frac{1}{3}$ and 6 compensate for the different stopping power of the projetiles.

$$r_1 = \frac{P(^3\mathrm{He})}{P(^1\mathrm{H})} = \frac{1}{3}\frac{\mathrm{d}A_{^3\mathrm{He}}}{\mathrm{d}t}\left(\frac{dA_p}{\mathrm{d}t}\right)^{-1}\frac{C_p}{C_{^3\mathrm{He}}}\frac{I_p}{I_{^3\mathrm{He}}}\frac{R_p}{R_{^3\mathrm{He}}} \quad (1)$$

$$r_2 = \frac{P(^3\mathrm{He})}{P(^{12}\mathrm{C})} = 6\frac{\mathrm{d}A_{^3\mathrm{He}}}{\mathrm{d}t}\left(\frac{dA_{^{12}\mathrm{C}}}{\mathrm{d}t}\right)^{-1}\frac{C_{^{12}\mathrm{C}}}{C_{^3\mathrm{He}}}\frac{I_{^{12}\mathrm{C}}}{I_{^3\mathrm{He}}}\frac{R_{^{12}\mathrm{C}}}{R_{^3\mathrm{He}}} \quad (2)$$

Energy/ AMeV	IP	$N_{^{11}\mathrm{C}}$ /10^6 IP	$N_{^{15}\mathrm{O}}$ /10^6IP	$N_{^{10}\mathrm{C}}$ /10^6IP	$\sigma^{^{11}\mathrm{C}}$/ mb	$\sigma^{^{15}\mathrm{O}}$/ mb
110	p	23251	7933	586	83	71
110	p	22193	8078	892	79	72
204	^{12}C	98927	19143	7453	367	177
212.12	^{12}C	105052	21167	7932	365	184
212.12	^{12}C	102013	19283	7616	355	168
130.03	^{3}He	46962	15322	3760	119*	136
140	p	33950	12270	1479	79	71
259.5	^{12}C	146461	30798	11470	362	190
166.05	^{3}He	70533	23530	5297	116*	135
175	p	46624	15846	1708	73	62
306	^{12}C	183421	40847	14630	344	192
343.46	^{12}C	198681	50318	15231	309	196
207.92	^{3}He	96413	31905	6805	109*	126

Tab. 1: *Absolute values of positron emitters produced during the irradiation with different incident particles (IP), data from p and carbon are taken from [1], as well as the cross sections σ calculated according to [2].*

* *for calculating the $\sigma^{^{11}\mathrm{C}}_{\mathrm{PMMA}}$ not only the C-atoms but also the O were considered for the atomic density*

Using the data from [1] values for $r_1 = 0.9 \pm 0.2$ and for $r_2 = 3.2 \pm 0.4$ were estimated. If comparing to the same biologically equivalent dose [3], a further increase of the helium induced signal compared to ^{12}C-irradiation up to a maximum of about 3 can be expected because of the higher relative biological effectiveness of carbon ions. A further enhancement can be anticipated from the lower ratio $A_{^{11}\mathrm{C}}/A_{^{15}\mathrm{O}}$ for ^{3}He (3.0 ± 0.1) than for ^{12}C-irradiations (4.8 ± 0.5), because it is expected that the PET-measurement is stopped shortly after the end of the patient irradiation in clinical practise and because of the half lives of ^{11}C ($T_{1/2} = 20.38$ min) and ^{15}O ($T_{1/2} = 2.03$ min) a relatively higher contribution to the signal during or shortly after the end of the irradiation comes from ^{15}O. With respect to the proton case $(A_{^{11}C}/A_{^{15}O} = 2.85 \pm 0.20)$ the ratio is comparable.

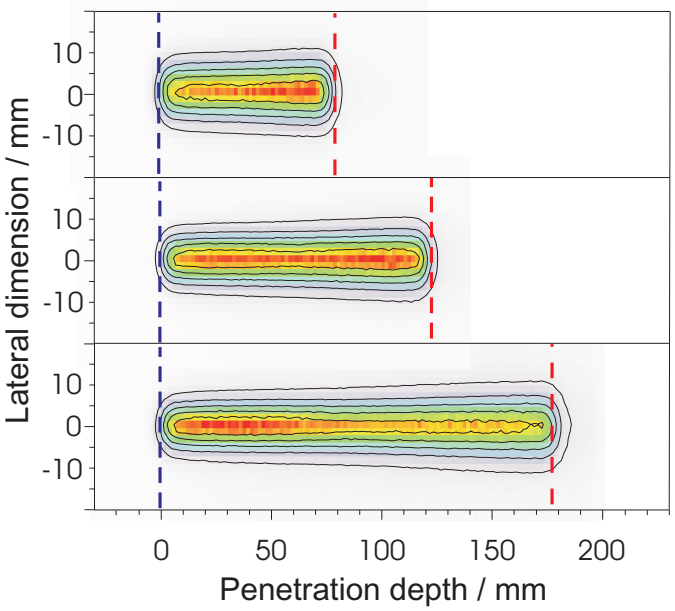

Fig. 1 *Spatial distributions of the β^+-activity induced by ^{3}He-beams at 130.03 AMeV (top), 166.05 AMeV (middle) and 207.92 AMeV (bottom). The blue lines indicate the front face of the PMMA target, the red lines mark the range of the ^{3}He-ions.*

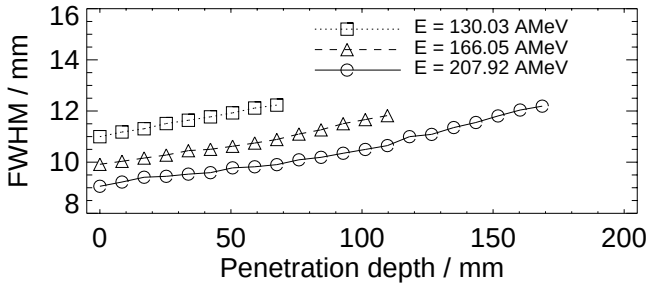

Fig. 2 *Lateral broadening of the measured profiles along the penetration depth for PMMA targets at different energies.*

[1] K. Parodi, Wiss.-Techn. Berichte FZR-415 (2004)
[2] F. Fiedler, K. Parodi, W. Enghardt, this report, p. 82
[3] M. Belli, R. Cherubini et al., Int. J. Radiat. Biol. 76 (2000) 1095

Estimation of Thick Target Cross Sections for ^{3}He Induced Positron Emitter Production [G,E]

F. Fiedler, K. Parodi, W. Enghardt

For PET-monitoring aimed also for ^{3}He-irradiation it is necessary to compare a simulated distribution with the measured one, since the β^+-activity distribution cannot be deduced directly from the dose. Therefore information about the reaction rates is required. Because of a lack of data for partial reaction cross sections, experiments with different targets were performed [1]. The most abundant elements in tissue are carbon, hydrogen and oxygen. Thus reaction rates for ^{12}C(^{3}He, ^{3}He+n)^{11}C and ^{16}O(^{3}He, ^{3}He+n)^{15}O have to be considered. To avoid superimpositions between different positron emitters, pure targets were used, graphite ($9 \times 9 \times 15$ cm^3, $\rho = 1.795$ g cm^{-3}), PMMA ($9 \times 9 \times 20$ cm^3, $C_5H_8O_2$, $\rho = 1.18$ g cm^{-3}) as tissue-equivalent material and a solid water target. In order to avoid the deterioration of the β^+-emitters by convection in liquid water, gelatine has been added, resulting in targets of a stoichiometric composition of $H_{66.2}O_{33.1}C_{0.7}$ with the dimensions of about $9 \times 9 \times 20(30)$ cm^3 and $\rho = 1.0$ g cm^{-3}.

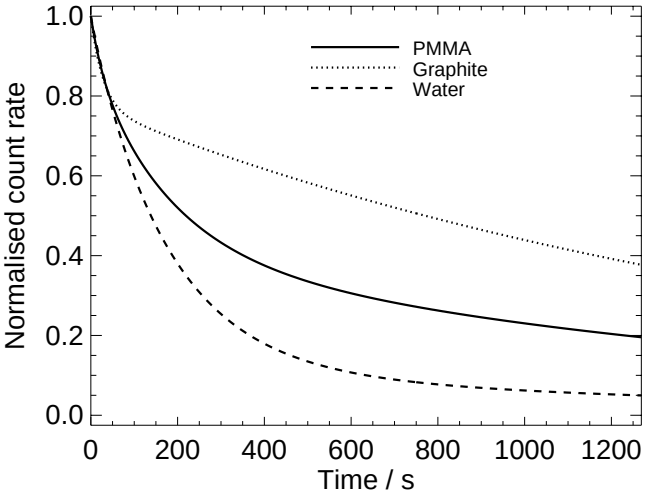

Fig. 1 *Decay measurements for the different targets after irradiation with ^{3}He-beams of $E = 207.92$ AMeV.*

The parameters of the irradiation for the three different targets are outlined in [1]. Following the approach given in [2] the absolute values of produced positron emitters N were estimated from the decay curves (Fig. 1, Tab. 1). By the formula

$$\sigma(E) = \frac{N(E)}{R(E)\ n\ I(E)} \qquad (1)$$

energy dependent cross sections for the formation of a specified isotope for thick targets of the given dimensions have been calculated, where σ is the cross section, R is the range, n gives the atomic density and I is the number of particles. Since there are remarkable contributions coming from ^{11}C observed during the decay measurement with the water target, it can be assumed that the $\sigma^{^{11}\mathrm{C}}_{\mathrm{PMMA}}$ is a mixture between the ^{11}C produced during reactions with the carbon and oxygen atoms of PMMA, therefore n_{PMMA} was calculated as $n^{\mathrm{C}}_{\mathrm{PMMA}} + n^{\mathrm{O}}_{\mathrm{PMMA}}$. From the cross sections $\sigma^{^{11}\mathrm{C}}_{\mathrm{graphite}}$ and $\sigma^{^{11}\mathrm{C}}_{\mathrm{water}}$, respectively, the contributions of the ^{12}C(^{3}He,^{3}He+n) and ^{16}O(^{3}He, $4p + 4n$) reactions to the ^{11}C production can be separated (Tab. 2).

Energy / AMeV	130.03	166.05	207.92
$N^{^{11}\mathrm{C}}_{exp_{graphite}}$	37723	55471	75196
$N^{^{11}\mathrm{C}}_{exp_{water}}$	6649	9010	11480
$N^{^{11}\mathrm{C}}_{exp_{tot}}$	44372	64481	86676

Tab. 2 *Total expected production rate of ^{11}C in PMMA ($N^{^{11}\mathrm{C}}_{exp_{tot}}$) deduced from the separate contributions due to $\sigma^{^{11}\mathrm{C}}_{graphite}$ ($N^{^{11}\mathrm{C}}_{exp_{graphite}}$) and $\sigma^{^{11}\mathrm{C}}_{water}$ ($N^{^{11}\mathrm{C}}_{exp_{water}}$).*

The sum of both reaction channels is for all three energies within ±10% of the value determined by the analysis of the decay combined with information about the PET-camera parameters [1].

[1] F. Fiedler, K. Parodi, W. Enghardt, this report, p. 80
[2] K. Parodi, W. Enghardt et al., Phys. Med. Biol. 47 (2002) 21

Target	Energy / AMeV	$N^{^{10}\mathrm{C}}$ /10^6 IP	$N^{^{15}\mathrm{O}}$ /10^6 IP	$N^{^{13}\mathrm{N}}$ /10^6 IP	$N^{^{11}\mathrm{C}}$ /10^6 IP	$n^{\mathrm{C}} \cdot 10^{22}$ / cm$^-$3	$n^{\mathrm{O}} \cdot 10^{22}$ / cm$^-$3	$\sigma^{^{11}\mathrm{C}}$/ mb	$\sigma^{^{15}\mathrm{O}}$/ mb	$\sigma^{^{13}\mathrm{N}}$/ mb	$\sigma^{^{10}\mathrm{C}}$/ mb
PMMA	130.03	3760	15322	2253	46962	3.55	1.42	119	136	20	—
PMMA	166.05	5297	23530	2820	70533	3.55	1.42	116	135	16	—
PMMA	207.92	6805	31905	4356	96413	3.55	1.42	109	126	17	—
graphite	130.03	4384	—	—	68762	9.00	—	134	—	—	9
graphite	166.05	6923	—	—	100308	9.00	—	127	—	—	9
graphite	207.92	9808	—	—	138648	9.00	—	119	—	—	8
water	130.03	2053	44027	4859	18532	0.0585	3.45	59	140	15	—
water	166.05	1920	62932	7979	24924	0.0585	3.45	52	130	17	—
water	207.92	1792	82850	10163	32345	0.0585	3.45	45	116	14	—
water∗	207.92	691	74694	9157	29452	0.0585	3.45	41	105	13	—

Tab. 1 *Absolute positron emitter production rates N for the three different targets at various energies as well as cross sections. IP means incident particle. The errors were estimated to be 7 % for $N_{^{11}\mathrm{C}}$ and $N_{^{15}\mathrm{O}}$, 12 % for $N_{^{10}\mathrm{C}}$ and 16 % for $N_{^{13}\mathrm{N}}$ in case of the PMMA-target, whereas for the water target the error for $P_{^{13}\mathrm{N}}$ is 12 %. For the target indicated by ∗ the error of $N_{^{10}\mathrm{C}}$ is assumend to be 36 %. For $\sigma^{^{11}\mathrm{C}}$ and $\sigma^{^{15}\mathrm{O}}$ the error is 10 %, for $\sigma^{^{10}\mathrm{C}}$ it is estimated to be 14 % and for $\sigma^{^{13}\mathrm{N}}$ 18 %.*

Modelling the interaction of therapeutic ion beams with matter by means of FLUKA

F. Sommerer, K. Parodi, K. Poljanc[1], A. Ferrari[2], W. Enghardt, H. Aiginger[1]

The in-beam monitoring technique used at the ^{12}C ion therapy facility at GSI Darmstadt should be extended to other ions of therapeutic interest. Therefore, a general purpose particle transport code for the prediction of the β^+-emitter distribution which additionally enables CT-processing is needed. FLUKA [1, 2] is a good candidate for such a code as has been shown for protons [3]. To use FLUKA for the prediction of the β^+-distribution an evaliation of the fragmentation processes and of the electromagnetic interactions, which are responsible for the particle transport has to be done.

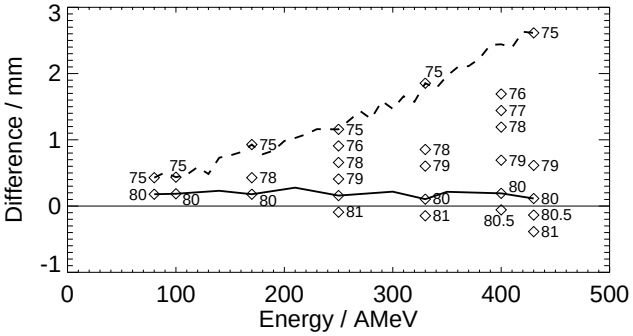

Fig. 1 *Difference of penetration depth between FLUKA and TRiP in dependency on the ionization potential of water (numbers in brackets).*

The validation of the stopping process of ^{12}C projectiles was done by changing the ionization potential I of the target material water to adjust the predicted penetration depth. It could be found that a shift from 75 eV to 80 eV is necessary to reproduce the same particle range as the treatment planning software TRiP within an accuracy of 0.25 mm (Fig. 1).

To evaluate the fragmentation processes for fragments with Z $\leq$ 2 an experiment described in [4] was simulated. A water target was irradiated by ^{12}C ions at 200 AMeV and light fragments escaping the target have been measured. In the simulation corresponding production rates and angular distributions were determined. The promising results of this investigation will be reported in more detail in a forthcoming publication.

Heavier target fragments were studied by simulating experiments done by [5] where a water target of variable thickness has been irradiated by beams of ^{12}C, ^{14}N and ^{16}O at about 670 AMeV. The attenuation of the primary particles could be reproduced with good agreement. The production of projectile fragments with Z $\geq$ 4 is depicted in (Fig. 2).

$Z_P \rightarrow Z_F$	FLUKA	Experiment
8 $\rightarrow$ 7	239 mb	269 mb
8 $\rightarrow$ 6	176 mb	275 mb
8 $\rightarrow$ 5	74 mb	130 mb
7 $\rightarrow$ 6	368 mb	339 mb
7 $\rightarrow$ 5	75 mb	138 mb
6 $\rightarrow$ 5	247 mb	215 mb

Tab. 1 *Partial cross sections calculated of ^{12}C, ^{14}N and ^{16}O projectiles in water targets. Z_P is the nuclear charge of the projectile, Z_F the nuclear charge of the fragment.*

Furthermore, total and partial charge changing cross sections were calculated and compared with measured data. The results for the total charge changing cross sections from the FLUKA simulations are: 1225(1261) mb for ^{12}C projectiles, 1390(1520) mb for ^{14}N and 1423(1549) mb for ^{16}O (values in brackets are the results of [5]). Partial cross sections are shown in Tab. 1.

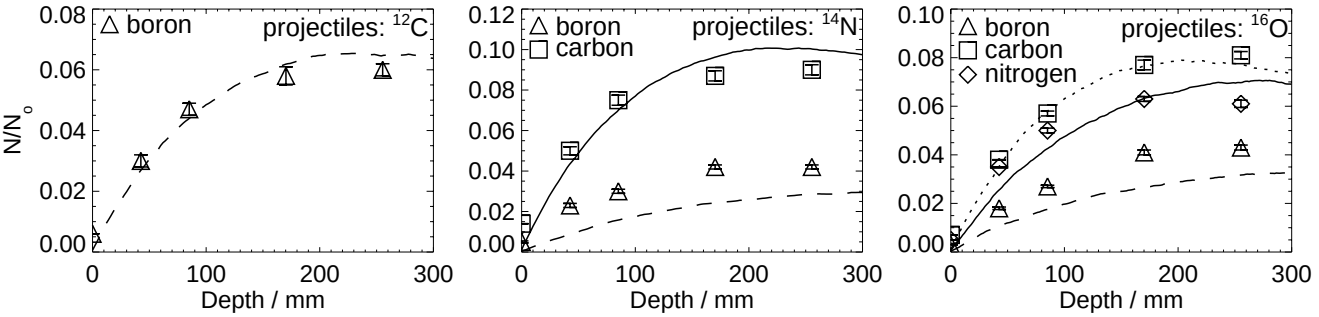

Fig. 1 *Projectile fragments with Z > 4. The symbols show measured data, the lines results of the simulation (broken lines: boron, solid lines: carbon, dotted line: nitrogen).*

[1] A. Fassò et al., Proc. Monte Carlo 2000 Conference, Lisbon, October 23-26 2000 (2001) 159

[2] A. Fassò et al., Proc. Monte Carlo 2000 Conference, Lisbon, October 23-26 2000 (2001) 955

[3] K. Parodi et al., Phys. Med. Biol. 47 (2002) 21

[4] K. Gunzert-Marx, Ph.D. Thesis, GSI Diss. 2004-02 (2004)

[5] I. Schall, Ph.D. Thesis, TU Darmstadt (1996)

[1] *Atomic Institute of the Austrian Universities, Vienna, Austria*
[2] *CERN, Geneva, Switzerland*

The Time Dependent Influence of Tissue Stoichiometry and Reaction Cross Sections on In-Beam PET Imaging of Proton Therapy [G, E]

K. Parodi, W. Enghardt

Following the positive clinical impact for carbon ion therapy [1] and the promising experiments with proton beams [2] at GSI Darmstadt, in-beam positron-emission-tomography (PET) will be used to monitor ion (p, He, C, O) treatment at the future hospital-based facility in Heidelberg. For protons, despite the lack of projectile fragments, millimetre precision for monitoring range and lateral field position was demonstrated in homogenous targets [2]. However, in contrast to heavy ions, the major role of target fragments challenges the accuracy of the modelling for prediction of irradiation-induced activity distributions, which is an essential requirement for therapy monitoring [1]. Although experiments in an inhomogeneous target were also performed, the sensitivity to tissue stoichiometry and reaction cross sections was studied in a more controlled way by time analysis of list mode data acquired during and after irradiation of PMMA ($C_5H_8O_2$) [2]. In this material, the dominant contribution to β^+-activity comes from (p, pn) reactions on C and O nuclei, the main constituents of living tissue. The resulting ^{11}C and ^{15}O isotopes have half-lives $T_{1/2}$ of 20.4 and 2.0 min, respectively. Several subsets of the measured data were reconstructed, corresponding to different ratios of ^{11}C to ^{15}O decays but, where possible, the same number of registered events. The shape of the activity depth profiles and the position $d_{50\%}$ of the 50 % distal fall-off, related to the range, is clearly sensitive to the selected time window (Fig. 1a, b), due to the energy dependence of the cross sections for the involved reaction channels. For comparison, model predictions [2] using different cross sections from the experimental database [3] and the ICRU report [4], largely adopting calculations benchmarked against measurements, were examined. The resulting β^+-emitter profiles clearly differ (Fig. 1c, d). The data from [3] were able to reproduce the trend of the measurement in dependence on the ^{11}C/^{15}O decay ratio. In Fig. 1b, the larger deviation in the fall-off position for low ^{11}C/^{15}O was ascribed to the not negligible contribution of ^{10}C ($T_{1/2} = 19.3$ s) in the first seconds of the irradiation. A correction [2] provided better agreement. In contrast, the data from [4] could not reproduce the experimental trend, even when correcting for ^{10}C. The results point out the high sentivity of in-beam PET monitoring to the time course of irradiation/acquisition as well as tissue stoichiometry and cross section data for protons. Similar considerations apply to light ions up to boron, which produce insignificant amount of β^+-active projectile fragments. In view of applications to therapy, the time integrated ^{11}C/^{15}O decay ratio over a typical 10 min irradiation with the same time structure as for carbon ion therapy at GSI is shown in Fig. 2.

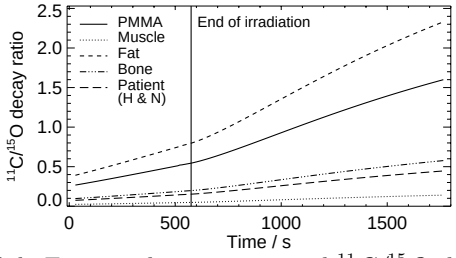

Fig. 2 *Solid: Estimated time-integrated $^{11}C/^{15}O$ decay ratio for 173.13 MeV protons in PMMA. Others: Extension to tissues and a typical head and neck (H&N) patient based on the C/O composition and only (p,pn) reactions [2].*

A rough extrapolation to materials of therapeutic interest is also given, though the corresponding $d_{50\%}$ differs from Fig. 1b, due to different stopping properties. Moreover, isotopes from minor reaction channels (e.g. ^{10}C) have been already shown to have a time dependent, not negligible impact. Hence, in order to achieve the desired accuracy for therapy monitoring, at least in low perfused regions of interest, the time structure of the irradiation and PET acquisition has to be properly chosen to minimise uncertainties from the limited accuracy in the knowledge of tissue stoichiometry and cross sections. For dynamic beam delivery the optimal strategy should be investigated. Decreasing energy steps maximise the ^{11}C/^{15}O decay ratio at the most critical distal edge, minimising $d_{50\%}$ uncertainties, but increase probability of blurring due to perfusion. The stoichiometry problem less affects off-line PET at the expense of lower counting statistics, high sensitivity to perfusion and possible movement of the patient from the treatment position.

[1] W. Enghardt, P. Crespo, et al., Nucl. Instrum. Meth. A, 525 (2004) 284

[2] K. Parodi, Thesis, Wiss.-Techn. Berichte FZR-415 (2004)

[3] Nuclear Reaction Data Center Network, online at http://www.nndc.bnl.gov/exfor (2000)

[4] ICRU Report 63, March 2000

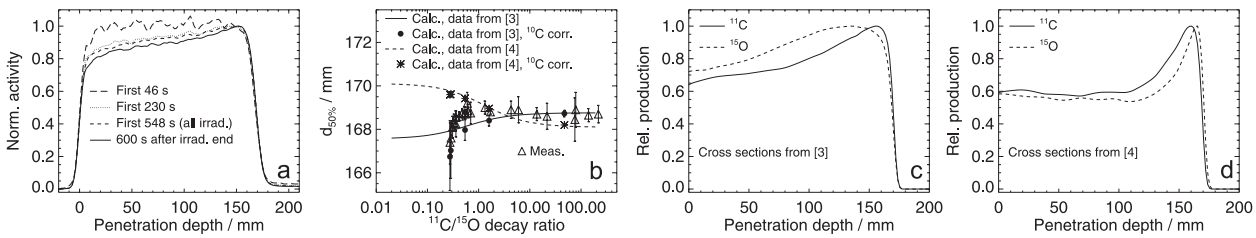

Fig. 1 *Activity profiles from data measured in different time windows at 173.13 MeV energy (a) and $d_{50\%}$ values (b) from more subsets of the same acquisition corresponding to the given $^{11}C/^{15}O$ decay ratio (triangles), compared to calculations based on predicted ^{11}C and ^{15}O profiles (c, d), without (lines) and with (symbols) corrections for ^{10}C (cf. text).*

Real Time Reconstruction of PET Data: First Results

G. Shakirin, W. Enghardt

The in-beam PET scanner for carbon ion therapy monitoring registers annihilation γ-rays following the decay of β^+-radioactive nuclei, which are produced via nuclear reactions between the carbon ions of the therapeutic beam and the atomic nuclei of the irradiated tissue. From a comparison of the reconstructed activity distributions with those predicted from the treatment plan deviations between prescribed and the applied dose distributions can be detected. The results of such an in-beam PET scan become available about 1 hour after finishing a fractionated irradiation. Iterative Maximum Likelihood Estimation Maximization (MLEM) algorithm [1] is used for reconstruction purposes.

It appears to be highly desirable to reconstruct the activity simultaneously with the therapeutic irradiation and the in-beam PET scan. This would provide to the radiotherapist an attractive possibility to observe the process of dose delivery in real time. In that case each event should be proceeded immediately after it has been registered in PET. Result of reconstruction of n events can be used as background for proceeding of n+1-th event. Each event adds new information to the reconstructed image. Time of performing of whole event-by-event reconstruction is equal to time of one iteration of MLEM algorithm.

However, the event-by-event algorithm does not reconstruct activity proportionally to original distribution. Pixels with low and medium levels of activity are hided by pixels having high activity (Fig. 1-c). To avoide this effect it is necessary to have preliminary distribution of activity before starting reconstructing event by event. Such rough activity distribution can be created by backprojecting of some portion of events coming first.

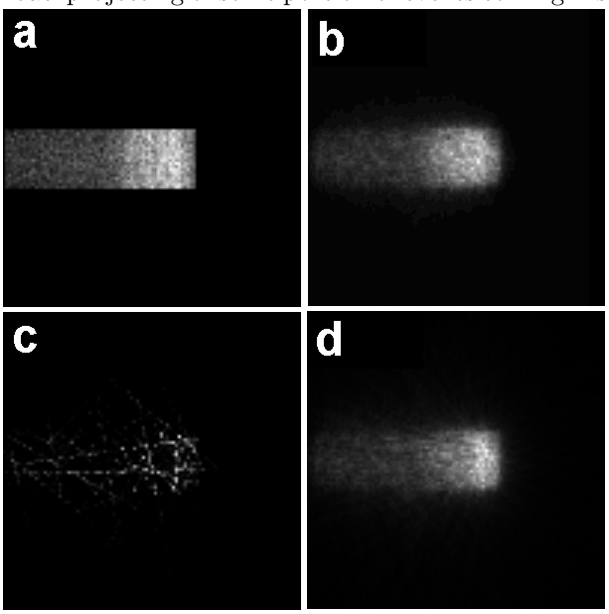

Fig. 1 *Original image (a), reconstruction using MLEM algorithm with 50 iterations (b), event-by-event reconstruction (c), portion-by-event reconstruction with 3000 events in portion (d).*

This procedure can be named as "portion-by-event" reconstruction algorithm. This technique is closely related to Ordered Subsets Expectation Maximization algorithms [2].

On the Fig. 1-a a 2D 100×100 pixels image which emulates the activity distribution is presented. It is result of proceeding of 31527 events. This image is forward-projected and then reconstructed using 50 iterations of MLEM algorithm (Fig. 1-b), event-by-event algorithm (Fig. 1-c) and portion-by-event algorithm (Fig. 1-d). As it is seen from transversal and longitudinal sums of activity distribution (Fig. 2 and Fig. 3 respectfully), portion-by-event reconstruction has some deviations from curve of original image, but taking into account fast perfomance it is reasonable to continue research and improve reconstruction quality of portion-by-event algorithm.

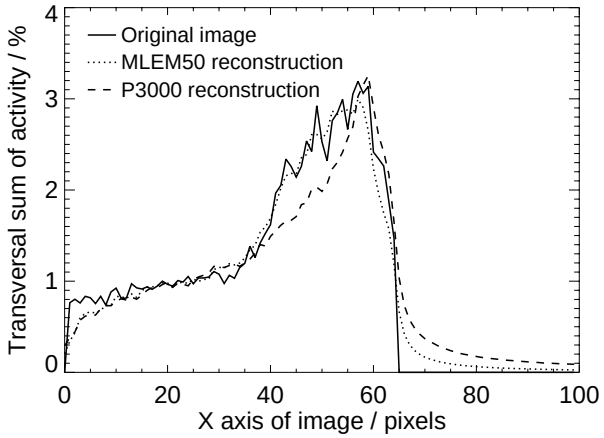

Fig. 2 *Transversal sum of activity distribution.*

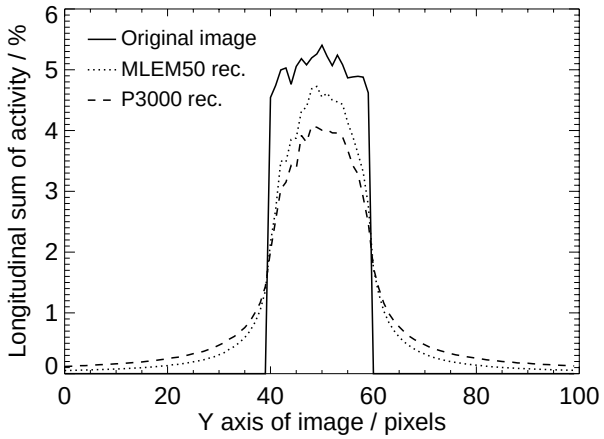

Fig. 3 *Longitudinal sum of activity distribution.*

[1] L.A. Shepp, Y. Vardi IEEE T. Med. Imaging MI-1(2) (1982) 113

[2] M. Hudson, R. Larkin IEEE T. Med. Imaging 13(4) (1994) 601

Index

Publications and Talks

Teaching Activities

Theses

Publications[1]

Neutron-proton pairing in rotating $N \sim Z$ nuclei: dominance of the isovector component

Nucl. Phys. A 746 (2004) 575

Afanasjev, A.V., **S. Frauendorf**

Abstract: Theoretical calculations of rotating $N \approx Z$ nuclei with $A = 58$ - 80 within the cranked Nilsson + Strutinsky approach, cranked relativistic mean field and cranked relativistic Hartree+Bogoliubov theories show good agreement with experiment. They point on the presence of the isovector $t = 1$ np-pairing, but do not show any indications of the isoscalar $t = 0$ np-pairing.

Magnetic dipole and electric quadrupole rotational structures and chirality in ^{105}Rh

Phys. Rev. C 69 (2004) 024317

Alcańtara-Nuńěz, J.A., J.R.B. Oliveira, E.W. Cybulska, N.H. Medina, M.N. Rao, R.V. Ribas, M.A. Rizzutto, W.A. Seale, F. Falla-Sotelo, K.T. Wiedemann, V.I. Dimitrov, **S. Frauendorf**

Abstract: The ^{105}Rh nucleus has been studied with the ^{100}Mo(^{11}B, $\alpha 2n\gamma$) reaction at 43 MeV incident energy. A rich variety of structures was observed at high and low spins, using $\gamma - \gamma - t$ and $\gamma - \gamma - particle$ coincidences and directional correlation ratios. A γ-vibrational band was observed for the first time in this nucleus. A new structure based on the intruder $1/2^+[431]$ proton orbital was identified. Four magnetic dipole bands have also been observed at high spin, three of which have negative parity and have similar characteristics: they are very regular in energy spacing, presenting nearly constant alignments and large values of $B(M1)/B(E2)$ ratios. Two of them are nearly degenerate in excitation energy and could be chiral partners. The $\pi g_{9/2} \otimes \nu h_{11/2}(g_{7/2}, d_{5/2})$ configuration is tentatively assigned for these bands, with the angular momenta of the proton and neutron intruders and the collective angular momentum aligning along the three perpendicular axes of the triaxial core, as predicted by tilted axis cranking calculations.

Chiral bands in ^{105}Rh

Braz. J. Phys. 34 (2004) 999

Alcańtara-Nuńěz, J.A., J.R.B. Oliveira, E.W. Cybulska, N.H. Medina, M.N. Rao, R.V. Ribas, M.A. Rizzutto, W.A. Seale, F. Falla-Sotelo, K.T. Wiedemann, V.I. Dimitrov, **S. Frauendorf**

Abstract: The ^{105}Rh nucleus has been studied by in-beam γ spectroscopy with the heavy-ion fusion-evaporation reaction ^{100}Mo(^{11}B, $\alpha 2n\gamma$) at 43 MeV. A rich variety of structures was observed at high and low spin, using $\gamma - \gamma - t$ and $\gamma - \gamma - particle$ coincidences and directional correlation ratios. Four magnetic dipole bands have also been observed at high spin. Two of them are nearly degenerate in excitation energy and could be chiral partners, as predicted by Tilted Axis Cranking calculations.

Das Projekt MedAustron

Fotec - Forschungs- und Technologietransfer GmbH, Wiener Neustadt, 2004, ISBN 3-200-00141-0

Auberger, Th., M. Benedikt, J. Bogner, J. Bosser, **W. Enghardt**, H. Frais-Kölbl, D. Georg, E. Griesmayer, A. Hofmann, R. Jäger, F. Jenni, R. Meyer, U. Mock, M. Pavlovic, H. Pernegger, W. Pirkl, M. Plesko, K. Poljanc, H. Schönauer, Th. Schreiner, R. Seemann, Th. Seppi, K. Seydl, Th. Strodl, R. Sweeney, P. Torre, M. Vejda, A. Wrulich, N. Zagler

Abstract: Ever since radiation was used for therapeutic applications about one century ago, Radiation-Oncologists were searching for more effective types of radiation. In principle there are two pathways of investigation. The first pathway would seek to make radiations more selective from a geometrical (or ballistic) point of view by increasing the dose to the tumour while sparing normal tissues. The second pathway would aim to select radiation qualities for their better radiobiological selectivity against some types of tumours based on their (biological) characteristics.

[1]From the authors printed in **bold** further information can be obtained

Spectroscopic quadrupole moments of high-spin isomers in ^{193}Pb

Eur. Phys. J. A 20 (2004) 191

Balabanski, D.L., M. Ionescu-Bujor, A. Iordachescu, D. Bazzacco, F. Brandolini, D. Bucurescu, S. Chmel, M. Danchev, M. De Poli, G. Georgiev, H. Haas, H. Hübel, N. Marginean, R. Menegazzo, G. Neyens, P. Pavan, G. Rainovski, C. Rossi Alvarez, C.A. Ur, K. Vyvey, **S. Frauendorf**

Abstract: The quadrupole interaction of high-spin isomers in ^{193}Pb implanted into solid Hg cooled at a temperature T =170 K has been investigated by the time-differential perturbed γ-ray angular-distribution method. Spectroscopic quadrupole moment values of $\mid Q_{\rm s} \mid = 0.22(2)$ eb and 0.45(4) eb have been deduced for the $21/2^-$ and $33/2^+$ three-neutron states, respectively. A much higher value $\mid Q_{\rm s} \mid = 2.84(26)$ eb has been determined for the $29/2^-$ isomer, the band head of a magnetic rotational band.

ϕ meson production in near threshold proton-nucleus collisions

Phys. Rev. C 69 (2004) 024605

Barz, H.-W., M. Zétényi

Abstract: The cross section for production of ϕ mesons in proton-nucleus reactions is calculated as a function of the target mass. The decay width of the ϕ meson is affected by the change of the masses of the $\phi, K^+$and $\rm K^-$ mesons in the medium. A strong attractive K^- potential leads to a measurable change of the behavior of the cross section as a function of the target mass. Comparison between the kaon and electron decay modes are made.

Conserved high-affinity ligand binding and membrane association in the native and refolded extracellular domain of the human glycine receptor alpha 1 subunit

J. Biol. Chem. 279 (2004) 1627

Breitinger, U., H.-G. Breitinger, F. Bauer, **K. Fahmy**, D. Glockenhammer, C.M. Becker

Abstract: The strychnine-sensitive glycine receptor (GlyR) is a ligand-gated chloride channel composed of ligand binding α- and gephyrin anchoring β-subunits. To identify the secondary and quaternary structures of extramembraneous receptor domains, the N-terminal extracellular domain (α1-(1-219)) and the large intracellular TM3-4 loop (α1-(309-392)) of the human GlyR α1-subunit were individually expressed in HEK293 cells and in Escherichia coli. The extracellular domain obtained from *E.coli* expression was purified in its denatured form and refolding conditions were established. Circular dichroism and Fourier-transform-infrared spectroscopy suggested $\sim$25 % α-helix and $\sim$48 % β-sheet for the extracellular domain, while no α-helices were detectable for the TM3-4 loop. Size exclusion chromatography and sucrose density centrifugation indicated that isolated glycine receptor domains assembled into multimers of distinct molecular weight. For the extracellular domain from *E.coli*, we found an apparent molecular weight compatible with a 15mer by gel filtration. The N-terminal domain from HEK293 cells, analyzed by sucrose gradient centrifugation, showed a bimodal distribution, suggesting oligomerization of $\sim$5 and 15 subunits. Likewise, for the intracellular domain from E. coli, a single molecular mass peak of $\sim$49 kDa indicated oligomerization in a defined native structure. As shown by [^{3}H]strychnine binding, expression in HEK293 cells and refolding of the isolated extracellular domain reconstituted high affinity antagonist binding. Cell fractionation, alkaline extraction experiments, and immunocytochemistry showed a tight plasma membrane association of the isolated GlyR N-terminal protein. These findings indicate that distinct functional characteristics of the full-length GlyR are retained in the isolated N-terminal domain.

System-size dependence of strangeness saturation

J. Phys. G: Nucl. Part. Phys. 30 (2004) 595

Cleymans, J., **B. Kämpfer**, P. Steinberg, S. Wheaton

Abstract: The final state in heavy-ion collisions has a higher degree of strangeness saturation than the one produced in collisions between elementary particles such as $p-p$ or $p-\bar{p}$. A systematic analysis of this phenomenon is made for C - C, Si - Si and Pb - Pb collisions at the CERN SPS collider and for Au - Au collisions at RHIC and at AGS energies. Strangeness saturation is shown to increase smoothly with the number of participants at AGS, CERN and RHIC energies.

Evidence for a narrow resonance at 1530 MeV/c^2 in the K^0p-system of the reaction $p\,p \to \Sigma^+ K^0 p$ from the COSY-TOF experiment

Phys. Lett. B 595 (2004) 127

COSY-TOF Collaboration: M. Abdel-Bary, S. Abdel-Samad, K.-Th. Brinkmann, H. Clement, E. Doroshkevich, M. Drochner, S. Dshemuchadse, A. Erhardt, W. Eyrich, D. Filges, A. Filippi, H. Freiesleben, M. Fritscha, J. Georgi, A. Gillitzer, D. Hesselbarth, R. Jäkel, B. Jakob, L. Karsch, K. Kilian, H. Koch, J. Kress, E. Kuhlmann, **L. Naumann**, S. Marcello, S. Marwinski, R. Meier, P. Michel, **K. Möller**, H. Mörtel, H.P. Morsch, N. Paul, L. Pinna, C. Pizzolotto, M. Richter, E. Roderburg, P. Schönmeier, W. Schroeder, M. Schulte-Wissermann, T. Sefzick, F. Stinzing, G.Y. Sun, A. Teufel, A. Ucar, G.J. Wagner, M. Wagner, A. Wilms, P. Wintz, St. Wirth, P. Wüstner

Abstract: The hadronic reaction $pp \to \Sigma^+, K^0 p$ was measured exclusively at a beam momentum of 2.95 GeV/c using the TOF detector at the COSY storage ring. A narrow peak was observed in the invariant mass spectrum of the $K^0 p$ - subsystem at $1530 \pm 5\,\mathrm{MeV}/c^2$ with a significance of 4-6 standard deviations, depending on background assumptions. The upper limit of $18 \pm 4\,\mathrm{MeV}/c^2$ (FWHM) for its width is given by the experimental resolution. The corresponding total cross section is estimated to be about $0.4 \pm 0.1\,(\mathrm{stat}) \pm 0.1\,(\mathrm{syst})\,\mu\mathrm{b}$. Since a resonance in this subsystem must have strangeness $\mathrm{S} = +1$ we claim it to be the Θ^+ state for which very recently evidence was found in various experiments.

First in-beam PET imaging with LSO/APD array detectors

IEEE Trans. Nucl. Sci. 51 (2004) 2654

Crespo, P., M. Kapusta, J. Pawelke, M. Moszynski, **W. Enghardt**

Abstract: The performance and in-beam imaging capabilities of two position-sensitive gamma-ray detectors consisting of Hamamatsu avalanche photodiode arrays (S8550) individually coupled to crystals of cerium-doped lutetium oxyorthosilicate (LSO) are presented. The two detectors were operated in coincidence at the medical beam line of the Gesellschaft für Schwerionenforschung, in Darmstadt, Germany. In a first set of experiments, their imaging performance was tested before, during, and after the irradiation of phantoms of polymethylmethacrylate with carbon ion beams with fluences equivalent to 1000 typical daily therapeutic fractions. Only minor energy, time, and spatial resolution deterioration was observed, with the initial values being recovered after stopping the irradiation. A second set of experiments successfully imaged the depth distribution of positron emitter radionuclides created in a phantom that stopped the high-energy carbon ion beam. The particular details for the in-beam PET acquisition are shortly outlined. The obtained results show that LSO is a suitable material for in-beam PET and that its coupling with avalanche photodiode arrays is feasible for a PET system dedicated to in-beam monitoring of ion therapy.

Gross shell structure at high spin in heavy nuclei

Phys. Rev. C 69 (2004) 044309

Deleplanque, M.A., **S. Frauendorf**, V.V. Pashkevich, S.Y. Chu, A. Unzhakova

Abstract: Experimental nuclear moments of inertia at high spins along the yrast line have been determined for a large number of nuclei. They are found to systematically differ from the rigid-body values. The difference is attributed to shell effects which are well described by a rotating Woods - Saxon potential. The data and quantal calculations are interpreted by means of the semiclassical periodic orbit theory. From this new perspective, features in the moments of inertia as a function of neutron number and spin as well as their relation to the shell energies can be understood. Gross shell effects persist up to the highest angular momenta observed.

Exclusive η production in proton-proton reactions

Phys. Rev. C 69 (2004) 064003

DISTO-Collaboration: F. Balestra, Y. Bedfer, R. Bertini, L.C. Bland, A. Brenschede, F. Brochard, M.P. Bussa, Seonho Choi, M.L. Colantoni, **R. Dressler**, M. Dzemidzic, J.-Cl. Faivre, A. Ferrero, L. Ferrero, J. Foryciarz, I. Fröhlich, V. Frolov, R. Garfagnini, A. Grasso, S. Heinz, W.W. Jacobs, W. Kühn, A. Maggiora, M. Maggiora, A. Manara, D. Panzieri, H.-W. Pfaff, G. Piragino, A. Popov, J. Ritman, P. Salabura, V. Tchalyshev, F. Tosello, S. E. Vigdor, G. Zosi

Abstract: Differential cross sections for the exclusive reaction $\overrightarrow{p}\,p \to p\,p\,\eta$ observed via the $\eta \to \pi^+\,\pi^-\,\pi^0$ decay channel have been measured at $\mathrm{T}_{beam} = 2.15\,\mathrm{GeV}$, 2.50 GeV, and 2.85 GeV (excess energies 324 MeV, 412 MeV, and 554 MeV). The influence of the $N(1535)S_{11}$ resonance is clearly seen in the invariant mass and momentum dependent differential cross sections. The extracted resonance parameters are compatible with existing data. No

significant evidence for further resonance contributions has been found. In addition, angular distributions of the $pp\eta$ final state have been measured. The polar angle distribution of the η shows an anisotropy with respect to the beam axis for the lowest beam energy, which vanishes for the higher energies. The sign of this anisotropy is negative and expected to be sensitive to the dominant production mechanism. In contrast, the proton polar angle in the pp rest frame tends to be more strongly aligned along the beam axis with increasing beam energy. The analyzing power A_y is compatible with zero for all beam energies.

Angular Distributions for ${}^{3,4}_{\Lambda}$H Bound States in the ^{3,4}He$(e,e'K^+)$ Reaction

Phys. Rev. Lett. 93 (2004) 242501

Dohrmann, F., A. Ahmidouch, S. Armstrong, J. Arrington, R. Asaturyan, S. Avery, K. Bailey, H. Bitao, H. Breuer, D.S. Brown, R. Carlini, J. Cha, N. Chant, E. Christy, A. Cochran, L. Cole, J. Crowder, S. Danagoulian, M. Elaasar, R. Ent, H. Fenker, Y. Fujii, L. Gan, K. Garrow, D.F. Geesaman, P. Gueye, K. Hafidi, W. Hinton, H. Juengst, C. Keppel, Y. Liang, J.H. Liu, A. Lung, D. Mack, P. Markowitz, J. Mitchell, T. Miyoshi, H. Mkrtchyan, S.K. Mtingwa, B. Mueller, G. Niculescu, I. Niculescu, D. Potterveld, B.A. Raue, P.E. Reimer, J. Reinhold, J. Roche, M. Sarsour, Y. Sato, R. E. Segel, A. Semenov, S. Stepanyan, V. Tadevosian, S. Tajima, L. Tang, A. Uzzle, S. Wood, H. Yamaguchi, C. Yan, L. Yuan, B. Zeidman, M. Zeier, B. Zihlmann

Abstract: The ${}^{3,4}_{\Lambda}$H and ${}^{4}_{\Lambda}$H hypernuclear bound states have been observed for the first time in kaon electroproduction on ^{3,4}He targets. The production cross sections have been determined at $Q^2 = 0.35\,\mathrm{GeV}^2$ and $\mathrm{W} = 1.91\,\mathrm{GeV}$. For either hypernucleus the nuclear form factor is determined by comparing the angular distribution of the ${}^{3,4}\mathrm{He}(e,e'K^+)^{3,4}_{\Lambda}\mathrm{H}$ processes to the elementary cross section ${}^1H(e,e'K^+)\Lambda$ on the free proton, measured during the same experiment.

Charged hadron tumour therapy monitoring by means of PET

Nucl. Instr. Meth. A 525 (2004) 284

Enghardt, W., P. Crespo, F. Fiedler, R. Hinz, **K. Parodi, J. Pawelke, F. Pönisch**

Abstract: Positron emission tomography (PET) imaging of radioactivity distributions induced by therapeutic irradiation is at present the only feasible method for an in situ and non-invasive monitoring of radiooncology treatments with ion beams. Therefore, at the experimental carbon ion therapy facility at the Gesellschaft für Schwerionenforschung Darmstadt, Germany (GSI) a PET scanner has been integrated into the treatment site for quality assurance monitoring simultaneously to the therapeutic irradiation. Although the device has been assembled from components of positron emission tomographs developed for nuclear medicine applications, substantial modifications had to be made for meeting the requirements of ion therapy monitoring. These changes regard the geometrical detector configuration as well as the data acquisition and processing. Since 1997 this technique has been applied to monitor the fractionated irradiation of more than 180 patients predominantly suffering from tumours in the head and neck region. It could be demonstrated that this new PET technique is capable of assessing parameters being relevant for quality assurance of carbon ion therapy, i.e. the particle range in tissue, the position of the irradiated volume with respect to anatomical landmarks and local deviations between the planned and the applied dose distributions.

Dose quantification from in-beam positron emission tomography

Radiother. and Oncol. 73 (Suppl.2) (2004) 96

Enghardt, W., K. Parodi, P. Crespo, F. Fiedler, J. Pawelke, F. Pönisch

Abstract: Positron emission tomography (PET) imaging of the radioactivity distributions induced by therapeutic irradiation is at present the only feasible method for an in-situ and non-invasive monitoring of radiooncology treatments with ion-beams. The clinical implementation of this imaging technology at the experimental carbon ion therapy facility at the Gesellschaft für Schwerionenforschung (GSI) at Darmstadt, Germany is outlined and an interactive approach for a PET guided quantification of local dose deviations with respect to the treatment plan is presented.

K^+- and K^--production in heavy-ion collisions at SIS energies

J. Phys. G: Nucl. Part. Phys. 30 (2004) 393

Förster, A., (for the KaoS Collaboration: I. Böttcher, A. Förster, **E. Grosse**, P. Koczon, B. Kohlmeyer, S. Lang, F. Laue, M. Menzel, **L. Naumann**, H. Oeschler, M. Ploskon, F. Pühlhofer, **W. Scheinast**, A. Schmah, T.

Schuck, E. Schwab, P. Senger, Y. Shin, H. Ströbele, C. Sturm, F. Uhlig, **A. Wagner**, W. Walus)

Abstract: The production and the propagation of K^+- and of K^--mesons in heavy-ion collisions at beam energies of 1 to 2 AGeV have systematically been investigated with the Kaon Spectrometer (KaoS) at the SIS at the GSI. The ratio of the K^+-production excitation function for Au + Au and for C + C reactions increases with decreasing beam energy, which is expected for a soft nuclear equation-of-state. At 1.5 AGeV a comprehensive study of the K^+- and of the K^--emission as a function of the size of the collision system, of the collision centrality, of the kaon energy, and of the polar emission angle has been performed. The K^-/K^+ ratio is found to be nearly constant as a function of the collision centrality. The spectral slopes and the polar emission patterns are different for K^- and K^+. These observations indicate that K^+-mesons decouple earlier from the reaction zone than K^--mesons.

Shape parameters of the participant source in Ru + Ru collisions at 400 AMeV

Nucl. Phys. A 742 (2004) 29

FOPI Collaboration: N. Bastid, P. Dupieux, A. Bendarag, V. Barret, P. Crochet, X. Lopez, J.P. Alard, A. Andronic, Z. Basrak, M.L. Benabderrahmane, R. Čaplar, E. Cordier, M. Dželalija, Z. Fodor, I. Gašparic, A. Gobbi, Y. Grishkin, O.N. Hartmann, N. Herrmann, K.D. Hildenbrand, B. Hong, J. Kecskemeti, Y.J. Kim, M. Kirejczyk, P. Koczoń, M. Korolija, **R. Kotte**, T. Kress, A. Lebedev, Y. Leifels, A. Mangiarotti, V. Manko, M. Merschmeyer, D. Moisa, **W. Neubert**, D. Pelte, M. Petrovici, F. Rami, W. Reisdorf, B. de Schauenburg, A. Schüttauf, Z. Seres, B. Sikora, K.S. Sim, V. Simion, K. Siwek-Wilczyńska, M.M. Smolarkiewiczk, V. Smolyankin, I.J. Soliwoda, M.R. Stockmeier, G. Stoicea, Z. Tymiński, P. Wagner, K. Wiśniewski, **D. Wohlfarth**, Z. Xiao, I. Yushmanov, A. Zhiling

Abstract: New results on nuclear collective flow are presented for central and semi-central Ru + Ru collisions at 400 AMeV measured with the FOPI detector at GSI-Darmstadt. The source shape parameters, flow angle and aspect ratios, are extracted from Gaussian fits to in-plane and out-of-plane momentum distributions. The orientation and the shape of the source exhibit different trends according to the investigated phase space region. The shape parameters of the participant source are studied as a function of the particle mass and collision centrality. The flow angle is found to be independent of the particle mass. Both the flow angle and the aspect ratios depend sensitively on the impact parameter. Detailed comparisons with the predictions of the isospin quantum molecular dynamics model are performed. It is shown in particular that the source shape parameters permit to extract information on the in-medium nucleon-nucleon cross section.

Droplet formation in expanding nuclear matter: a system-size dependent study

Phys. Lett. B 595 (2004) 118

FOPI Collaboration: W. Reisdorf, F. Rami, B. de Schauenburg, Y. Leifels, J.P. Alard, A. Andronic, V. Barret, Z. Basrak, N. Bastid, M.L. Benabderrahmane, R. Caplar, P. Crochet, P. Dupieux, M. Dzelalija, Z. Fodor, A. Gobbi, Y. Grishkin, O.N. Hartmann, N. Herrmann, K.D. Hildenbrand, B. Hong, J. Kecskemeti, Y.J. Kim, M. Kirejczyk, P. Koczon, M. Korolija, **R. Kotte**, T. Kress, A. Lebedev, X. Lopez, M. Merschmeyer, **J. Mösner**, **W. Neubert**, D. Pelte, M. Petrovici, A. Schüttauf, Z. Seres, B. Sikora, K.S. Sim, V. Simion, K. Siwek-Wilczynska, V. Smolyankin, M.R. Stockmeier, G. Stoicea, Z. Tyminski, P. Wagner, K. Wisniewski, **D. Wohlfarth**, Z.G. Xiao, I. Yushmanov, A. Zhilin

Abstract: Cluster production is investigated in central collisions of Ca + Ca, Ni + Ni, ^{96}Zr + ^{96}Zr, ^{96}Ru + ^{96}Ru, Xe + CsI and Au + Au reactions at 0.4 AGeV incident energy. We find that the multiplicity of clusters with charge $Z \geq 3$ grows quadratically with the system's total charge and is associated with a mid-rapidity source with increasing transverse velocity fluctuations. When reduced to the same number of available charges, an increase of cluster production by about a factor of 5.5 is observed in the mid-rapidity region between the lightest system (Ca + Ca) and the heaviest one (Au + Au). The results, as well as simulations using Quantum Molecular Dynamics, suggest a collision process where droplets, i.e. nucleon clusters, are created in an expanding, gradually cooling, nucleon gas. Within this picture, expansion dynamics, collective radial flow and cluster formation are closely linked as a result of the combined action of nucleon-nucleon scatterings and the mean fields.

Nuclear stopping from 0.09 A GeV to 1.93 A GeV and its correlation to flow

Phys. Rev. Lett. 92 (2004) 232301

FOPI Collaboration: W. Reisdorf, A. Andronic, A. Gobbi, O.N. Hartmann, N. Herrmann, K.D. Hildenbrand, Y.J. Kim, M. Kirejczyk, P. Koczon, T. Kress, Y. Leifels, A. Schüttauf, Z. Tyminski, Z.G. Xiao, J.P. Alard, V. Barret, Z. Basrak, N. Bastid, M.L. Benabderrahmane, R. Caplar, P. Crochet, P. Dupieux, M. Dzelalija, Z. Fodor, Y. Grishkin, B. Hong, J. Kecskemeti, M. Korolija, **R. Kotte**, A. Lebedev, X. Lopez, M. Merschmeyer, **J. Mösner**,

W. Neubert, D. Pelte, M. Petrovici, F. Rami, B. de Schauenburg, Z. Seres, B. Sikora, K.S. Sim, V. Simion, K. Siwek-Wilczynska, S. Smolyankin, M. Stockmeier, G. Stoicea, P. Wagner, K. Wisniewski, **D. Wohlfarth**, I. Yushmanov, A. Zhilin

Abstract: We present a complete systematics (excitation functions and system-size dependences) of global stopping and sideflow for heavy ion reactions in the energy range between 0.09 AGeV and 1.93 AGeV. For the heaviest system, Au + Au, we observe a plateau of maximal stopping extending from about 0.2 to 0.8 AGeV with a fast drop on both sides. The degree of stopping, which is shown to remain significantly below the expectations of a full stopping scenario, is found to be highly correlated to the amount of sideflow.

Azimuthal dependence of collective expansion for symmetric heavy-ion collisions

Phys. Rev. Lett. 92 (2004) 072303

FOPI Collaboration: Stoicea, G., M. Petrovici, A. Andronic, N. Herrmann, J.P. Alard, V. Barret, Z. Basrak, N. Bastid, R. Caplar, P. Crochet, P. Dupieux, M. Dzelalija, Z. Fodor, K.D. Hildenbrand, B. Hong, J. Kecskemeti, Y.J. Kim, M. Kirejczyk, M. Korolija, **R. Kotte**, T. Kress, A. Lebedev, Y. Leifels, X. Lopez, M. Merschmeyer, **W. Neubert**, D. Pelte, F. Rami, W. Reisdorf, D. Schüll, Z. Seres, B. Sikora, K.S. Sim, V. Simion, K. Siwek-Wilczynska, S. Smolyankin, M. Stockmeier, K. Wisniewski, **D. Wohlfarth**, I. Yushmanov, A. Zhilin, P. Danielewicz

Abstract: Detailed studies of the azimuthal dependence of the mean fragment and flow energies in the Au + Au and Xe + CsI systems are reported as a function of incident energy and centrality. Comparisons between data and model calculations show that the flow energy values along different azimuthal directions could be viewed as snapshots of the fireball expansion with different exposure times. For the same number of participating nucleons more transversally elongated participant shapes from the heavier system produce less collective transverse energy. Good agreement with Boltzmann-Uehling-Uhlenbeck calculations is obtained for a soft nuclear equation of state.

Transition strengths between particle hole excitations in ^{95}Ru

Phys. Rev. C 69 (2004) 024304

Galindo, E., M. Hausmann, A. Jungclaus, K.P. Lieb, O. Yordanov, I.P. Johnstone, **R. Schwengner**, A. Dewald, A. Fitzler, O. Möller, G. de Angelis, A. Gadea, T. Martinez, D.R. Napoli, C. Ur

Abstract: High-spin states of ^{95}Ru have been populated using the ^{35}Cl + ^{64}Zn reaction at a beam energy of 135 MeV. In a recoil-distance Doppler-shift experiment, the lifetimes or lifetime limits of 26 high-spin states have been measured, giving information on a total of 49 reduced transition strengths. The results are compared with shell-model calculations with different model spaces and residual interactions. Several families of states with defined proton and neutron seniorities are proposed. The M1 strengths in the negative-parity yrast sequence show a pronounced staggering which is reproduced by the shell-model calculations.

New insights into neutron rich nuclei from fission

Nucl. Phys. A 734 (2004) 257

Hamilton, J.H., S.J. Zhub, A.V. Ramayya, P.M. Gore, J.O. Rasmussen, E.F. Jones, J.K. Hwang, R.Q. Xu, L.Y. Yang, K. Li, Z. Jiang, Z. Zhang, S.D. Ziao, X.Q. Zhang, J. Kormicki, Y.X. Luo, L. Chaturvedi, W.C. Ma, J.D. Cole, M.W. Drigert, I.Y. Lee, P. Fallon, M.A. Stoyer, T.N. Ginter, G.M. Ter-Akopian, A.V. Daniel, Yu.Ts. Oganessian, R. Donangelok, V. Dimitrov, **S. Frauendorf**

Abstract: Neutron-rich nuclei populated in spontaneous fission are providing new tests for microscopic models. The neutron-rich $^{104-108}$Mo, $^{108-114}$Ru and $^{112-116}$Pd exibit a variety of rapidly changing collective band structures to high spins. The first evidence for chiral band doublets in any even-even nucleus are reported.

Shell stabilization and the survival of heavy compound nuclei

Nucl. Phys. A 746 (2004) 483c, http://dx.doi.org/10.1016/j.nuclphysa.2004.09.124

Heinz, A., K.-H. Schmidt, **A.R. Junghans**

Abstract: Knowledge of the influence of nuclear shell structure on the survival probability of heavy compound nuclei against fission is important for a quantitative understanding of the production rates of spherical super-heavy elements (SHE). Fission probabilities of N = 126 isotones beyond astatine can be used as test cases for the production of spherical super-heavy elements, as those isotones possess a strong shell correction energy and are

highly fissile. Here, we report on two new experimental approaches which probe the effect of the closed neutron shell at N = 126 on the competition between fission and particle evaporation using projectile fragmentation and electromagnetic-induced fission of radioactive beams. We conclude that these nuclei lose at least a great part of their stability against fission at low excitation energies and angular momenta-mostly due to the influence of collective contributions in the level density. Implications on the production of spherical SHE will be discussed.

Quadrupole moments and g factors for high-spin neutron isomers in ^{193}Pb

Phys. Rev. C 70 (2004) 034305

Ionescu-Bujor, M., A. Iordachescu, D.L. Balabanski, S. Chmel, G. Neyens, G. Baldsiefen, D. Bazzacco, F. Brandolini, D. Bucurescu, M. Danchev, M. De Poli, G. Georgiev, A. Goŕgen, H. Haas, H. Hübel, G. Ilie, N. Marginean, R. Menegazzo, P. Pavan, G. Rainovski, R.V. Ribas, C. Rossi Alvarez, C.A. Ur, K. Vyvey, **S. Frauendorf**

Abstract: The g-factors and quadrupole moments of the $21/2^-$ and $33/2^+$ isomers in ^{193}Pb have been measured by the time-differential perturbed γ-ray angular distribution method as $g(21/2^-)$ = -0.059(11), $|Q(21/2^-)| = 0.22(2)$ eb and $g(33/2^+) =$ -0.171(9), $|Q(33/2^+)| = 0.45(4)$ eb. The results support the three-neutron configurations $(1i_{13/2})^2{}_{12^+} \otimes 3p_{3/2}$ and $(1i_{13/2})^3$ for the $21/2^-$ and $33/2^+$ states, respectively. The quadrupole moment of the 12^+ isomer in ^{194}Pb described by the two-neutron $(1i_{13/2})^2$ configuration has been remeasured as $|Q(12^+)| = 0.48(3)$ eb in perfect agreement with the previous data. The experimental results are discussed within a microscopic Bardeen-Cooper-Schrieffer approach in a number-projected one- and three-quasiparticle neutron space, and in the frame of the pairing plus quadrupole tilted-axis cranking model.

High-spin states in the vibrational nucleus ^{114}Cd

Eur. Phys. J. A 20 (2004) 55

Jungclaus, A.R., A. Algora, M. Axiotis, M.J.G. Borge, M.A. Ferńandez, A. Gadea, E. Galindo, M. Hausmann, S. Lenzi, T. Martinez, D.R. Napoli, I. Piqueras, **R. Schwengner**, C. Ur

Abstract: High-spin states of the neutron-rich vibrational nucleus ^{114}Cd have been studied using the incomplete fusion reaction ^{110}Pd (^{7}Li, $p2n$) and the GASP spectrometer in conjunction with the ISIS Si ball. About 50 new states with excitation energies up to 7 MeV and angular momentum I less than or equal to (18^+) were observed and for many of them, spin and parity could be firmly assigned. The band-like stuctures in ^{114}Cd are compared to the corresponding ones in the even-even neighbour ^{112}Cd.

New determination of the ^{7}Be(p,γ)^{8}B S-factor

Nucl. Phys. A 746 (2004) 210

Junghans, A.R., E.C. Mohrmann, K.A. Snover, T.D. Steiger, E.G. Adelberger, J.M. Casandjiana, H.E. Swanson, L.R. Buchmann, A.M. Laird, S. Park, A.Y. Zyuzinc

Abstract: We present new measurements of the ^{7}Be(p,γ)^{8}B cross section from $\bar{E}_{cm} = 116$ to 2460 keV. Our new measurements lead to $S_{17}(0) = 22.1 \pm 0.6$(expt) ± 0.6(theor) eV b based on data from $\bar{E}_{cm} = 116$ to 362 keV, where the central value is based on the theory of Descouvemont and Baye. We compare our results to other $S_{17}(0)$ values extracted from both direct (^{7}Be(p,γ)^{8}B) and indirect (Coulomb dissociation and heavy-ion reaction) measurements, and show that the results of these 3 types of experiments are not mutually compatible. We recommend a "best" value, $S_{17}(0) = 21.4 \pm 0.5$(expt) ± 0.6(theor) eV b, based on the mean of all modern direct measurements below the 1^+resonance.

Transient effects in fission from new experimental signatures

Phys. Rev. Lett. 9307 (2004) 2501

Jurado, B., C. Schmitt, K.-H. Schmidt, J. Benlliure, T. Enqvist, **A.R. Junghans**, A. Kelić, F. Rejmund

A new experimental approach is introduced to investigate the relaxation of the nuclear deformation degrees of freedom. Highly excited fissioning systems with compact shapes and low angular momenta are produced in peripheral relativistic heavy-ion collisions. Both fission fragments are identified in atomic number. Fission cross sections and fission-fragment element distributions are determined as a function of the fissioning element. From the comparison of these new observables with a nuclear reaction code a value for the transient time is deduced.

Finite-width QCD sum rules for ρ and ω mesons

Prog. Part. Nucl. Phys. 53 (2004) 317

Kämpfer, B., S. Zschocke

Abstract: We present a combined analysis of the in-medium behavior of ρ and ω mesons within the Borel QCD sum rule taking into account finite widths.

Strangeness saturation: Dependence on system-size, centrality and energy

Heavy Ion Phys. 21 (2004) 207

Kämpfer, B., J. Cleymans, P. Steinberg, S. Wheaton

The dependence of the strangeness saturation factor on the system size, centrality and energy is studied in relativistic heavy-ion collisions.

HADES tracking system: First in-beam experience

IEEE Trans. Nucl. Sci. 51 (2004) 939

Kanaki, K., F. Dohrmann, W. Enghardt, C. Garabatos, **E. Grosse, J. Hutsch, B. Kämpfer**, A. Kondyurin, **R. Kotte, L. Naumann, A. Sadovsky**, J. Stroth, **M. Sobiella**

Abstract: The High Acceptance Di-Electron Spectrometer (HADES) at the heavy ion synchrotron SIS of GSI, Darmstadt, is a high-resolution second generation detector system for lepton pair spectroscopy. Its low-mass tracking system consists of two pairs of planes of trapezoidally shaped Multiwire Drift Chambers (MDC), installed on either side of a superconducting toroidal magnet. This paper summarizes some experiences with the construction and the in-beam operation of the six large-area chambers produced by Forschungszentrum Rossendorf. Studies on creeping of aluminum wires over a period of three years are presented. In addition, the observation of growth of filaments with various shapes and sizes in one of the chambers used in-beam will be discussed in detail.

Tagging the reaction $pn \to d\phi$ by backward protons in $pd \to d\phi p_{sp}$ processes

J. Phys. G: Nucl. Part. Phys. 30 (2004) 1115

Kaptari, L.P., **B. Kämpfer**, S.S. Semikh

Abstract: The reaction $pd \to d\phi p_{sp}$ is studied within the Bethe-Salpeter formalism. Under special kinematical conditions (slow backward spectator proton p_{sp} and fast forward deuteron) relevant for forthcoming experiments, e.g. at COSY, the cross section and a set of polarization observables are shown to factorize in the contribution of the pure subprocess $pn \to d\phi$ and a contribution stemming from deuteron quantities and kinematical factors. This provides a theoretical basis for studying threshold-near processes at quasi-free neutrons.

Relativistic effects in proton-induced deuteron break-up at intermediate energies with forward emission of a fast proton pair

Eur. Phys. J. A 19 (2004) 301

Kaptari, L.P., **B. Kämpfer**, S.S. Semikh, S.M. Dorkin

Abstract: Recent data on the reaction $pD \to (pp)n$ with a fast forward pp pair with very small excitation energy is analyzed within a covariant approach based on the Bethe-Salpeter formalism. It is demonstrated that the minimum non-relativistic amplitude is completely masked by relativistic effects, such as Lorentz boost and the negative-energy P components in the 1S0 Bethe-Salpeter amplitude of the pp pair.

The LSO/APD array as a possible detector for in-beam PET in hadron therapy

IEEE Trans. Nucl. Sci. 51 (2004) 1389

Kapusta, M., **P. Crespo**, D. Wolski, **K. Heidel, L. Heinrich, J. Hutsch, J. Pawelke, M. Sobiella**, A. Trzcinska, M. Moszynski, **W. Enghardt**

Abstract: We have studied the performance of finger like LSO : Ce (LSO) crystals coupled one by one to pixels of avalanche photodiode detector (APD) arrays during their operation in coincidence at ^{12}C ion beams of parameters being typical for tumor irradiations. In a first step of these experiments the parameters of the detectors and

the signal processing setup has been characterized off-beam, i.e. by means of beta$^+$ radioactive sources (^{22}Na, ^{68}Ge). Afterwards, the apparatus was installed at the medical beam line of the heavy ion synchrotron (SIS) of the Gesellschaft für Schwerionenforschung (GSI) at Darmstadt, Germany. Here, the beta$^+$ activity produced by nuclear fragmentation reactions of ^{12}C 200.3 AMeV heavy ion beams with polymerized methyl methacrylate (PMMA) phantoms were measured. Furthermore, a ^{68}Ge source was included into the in-beam experiment, in order to check the stability of the setup and to compare energy and time resolution before, during and after phantom irradiations. Additionally, it could be demonstrated by means of high resolution gamma-ray spectroscopy that LSO is not activated by the light projectile fragments escaping the patients downbeam during therapeutic irradiations. The experimental results indicate, that LSO scintillator is a suitable material for in-beam PET and, furthermore, the LSO/APD array is a feasible detector concept for in-beam monitoring of the dose application by means of PET.

Dipole and quadrupole excitations in ^{88}Sr up to 6.8 MeV

Phys. Rev. C 70 (2004) 064307

Käubler, L., H. Schnare, **R. Schwengner, H. Prade, F. Dönau**, P. von Brentano, J. Eberth, J. Enders, A. Fitzler, C. Fransen, M. Grinberg, R.-D. Herzberg, H. Kaiser, P. von Neumann-Cosel, N. Pietralla, A. Richter, **G. Rusev**, Ch. Stoyanov, I. Wiedenhöver

Abstract: Dipole and quadrupole excitations in the semimagic $N=50$ nucleus ^{88}Sr were investigated at the superconducting Darmstadt electron linear accelerator S-DALINAC with bremsstrahlung of an end-point energy of 6.8 MeV. Many new dipole excitations could be identified, and their reduced excitation probabilities were determined. The experimental findings are discussed in the context of quasiparticle-phonon-model and shell-model calculations. A breaking of the $N=50$ core is essential to describe the structure of the observed excitations. The two-phonon quadrupole-octupole $J^\pi=1^-$ state exhibits unusual features which are presently not understood.

High-spin structure of $N \simeq Z$ nuclei around the $A = 72$ region

Eur. Phys. J. A 20 (2004) 131

Kelsall, N.S., C.E. Svensson, S. Fischer, D.E. Appelbe, R.A.E. Austin, D.P. Balamuth, G.C. Ball, J.A. Cameron, M.P. Carpenter, R.M Clark, M. Cromaz, M.A. Deleplanque, R.M. Diamond, P. Fallon, D.F. Hodgson, R.V.F. Janssens, D.G. Jenkins, G.J. Lane, C.J. Lister, A.O. Macchiavelli, C.D. O'Leary, D.G. Sarantities, F.S. Stephens, D.C. Schmidt, D. Seweryniak, K. Vetter, J.C. Waddington, R. Wadsworth, D. Ward, A.N. Wilson, A.V. Afanasjev, **S. Frauendorf**, I. Ragnarsson

Abstract: High-spin states have been studied in ^{72}Kr and ^{72}Br using the ^{40}Ca + ^{40}Ca and ^{36}Ar + ^{40}Ca reactions at 164 and 145 MeV, respectively. The properties and configurations of the high-spin bands observed have been interpreted using unpaired cranked Nilsson-Strutinsky (CNS), and for ^{72}Kr, paired cranked relativistic Hartree-Bogoliubov (CRHB) calculations. In ^{72}Kr a new band has been identified that has the properties expected for the doubly aligned S-band configuration. In ^{72}Br the previously known bands have been extended to higher spin. This has lead to a re-interpretation of the configurations.

Subthreshold antiproton production in proton-carbon reactions

J. Phys. G: Nucl. Part. Phys. 30 (2004) 921

Komarov, V.I., **H. Müller**, A. Sibirtsev

Abstract: Data from KEK on subthreshold $\bar{p}$ as well as on $\pi^\pm$ and $K^\pm$ production in proton-nucleus reactions are described at projectile energies between 3.5 and 12.0 GeV. We use a model which considers a hadron-nucleus reaction as an incoherent sum over collisions of the projectile with a varying number of target nucleons. It samples complete events and allows thus for the simultaneous consideration of all particle species measured. The overall reproduction of the data is quite satisfactory. It is shown that the contributions from the interaction of the projectile with groups of several target nucleons are decisive for the description of subthreshold production. Since the collective features of subthreshold production become especially significant far below the threshold, the results are extrapolated down to COSY energies. It is concluded that an $\bar{p}$ measurement at ANKE-COSY should be feasible, if the high background of other particles can be efficiently suppressed.

Particle identification at HADES

Nucl. Phys. A 734 (2004) 78

Kugler, A., H. Agakichiev, C. Agodi, M. Alvarez-Pardo, H. Alvarez-Pol, E. Badura, A. Balanda, F. Ballester, A. Bassi, R. Bassini, G. Bellia, D. Bertini, J. Bielčik, M. Böhmer, C. Boiano, H. Bokemeyer, J.L. Boyard, S. Brambilla, P. Braun-Munzinger, S. Chernenko, R. Coniglione, M. Dahlinger, H. Daues, R. Diaz, **F. Dohrmann**, I. Duran, Th. Eberl, L. Fabbietti, O. Fateev, C. Fernandez, P. Finocchiaro, J. Friese, I. Fröhlich, B. Fuentes, J.A. Garzon, B. Genolini, R. Gernhäuser, M. Golubeva, D. Gonzales, H. Goringer, **E. Grosse**, F. Guber, J. Hehner, Th. Hennino, S. Hlavac, J. Hoffmann, R. Holzmann, J. Homolka, A. Ierusalimov, I. Iori, M. Jaskula, **B. Kämpfer, K. Kanaki**, T. Karavicheva, D. Kirschner, L. Kidon, P. Kienle, I. Koenig, W. Koenig, H.-J. Körner, B.W. Kolb, U. Kopf, **R. Kotte**, W. Kühn, T. Kurtukian, R. Krücken, R. Kulessa, A. Kurepin, J. Lehnert, E. Lins, D. Magestro, P. Maier-Komor, C. Maiolino, J. Markert, V. Metag, J. Mousa, M. Münch, C. Müntz, **L. Naumann**, A. Nekhaev, W. Niebur, W. Ott, R. Novotny, J. Otwinowski, Yu. Panebratsev, V. Pechenov, M. Petri, P. Piattelli, J. Pietraszko, R. Pleskac, M. Ploskon, W. Pryzgoda, N. Rabin, B. Ramstein, A. Reshetin, J. Ritman, P. Rosier, M. Roy-Stephan, A. Rustamov, J. Sabin, **A. Sadovski**, B. Sailer, P. Salabura, M. Sanchez, P. Sapienza, P. Senger, C. Schroeder, K. Shileev, P. Shishov, R. Simon, V. Smoliankin, L. Smykov, S. Spataro, H. Stelzer, H. Ströbele, J. Stroth, C. Sturm, M. Sudol, A. Taranenko, P. Tlusty, A. Toia, M. Traxler, H. Tsertos, I. Turzo, D. Vassiliev, A. Vazquez, V. Wagner, W. Walus, S. Winkler, M. Wiśniowski, T. Wojcik, J. Wüstenfeld, N. Yahlali, Yu. Zanevsky, K. Zeitelhack, D. Žovinec, P. Zumbruch

Abstract: none

Charged hadrons and leptons identification at HADES

Acta Physica Slovaca 54 (2004) 375

Kugler, A., H. Agakishiev, C. Agodi, H. Alvarez-Pol, A. Balanda, G. Bellia, J. Bielčik, M.Bohmer, J. Boyard, P. Braun-Munzinger, S. Chernenko, T. Christ, R. Coniglione, R. Djeridi, **F. Dohrmann**, I. Duran, Th. Eberl, L. Fabbietti, O. Fateev, P. Finocchiaro, J. Friese, I. Fröhlich, J. Garzon, R. Gernhäuser, M. Golubeva, D. Gonzales-Dias, **E. Grosse**, F. Guber, T. Hennino, S. Hlavác, R. Holzmann, A. Ierusalimov, I. Iori, M. Jaskula, M. Jurkovic, **B. Kämpfer, K. Kanaki**, T. Karavicheva, I. Koenig, W. Koenig, B. Kolb, **R. Kotte**, J. Kotulič-Bunta, R. Krücken, W. Kühn, R. Kulessa, A. Kurepin, S. Lang, J. Lehnert, C. Maiolino, J. Markert, V. Metag, J. Mousa, M. Münch, C. Müntz, **L. Naumann**, R. Novotny, J. Novotný, J. Otwinowski, Y. Pachmayer, V. Pechenov, T. Perez, J. Pietraszko, R. Pleskač, V. Pospišil, W. Przygoda, N. Rabin, B. Ramstein, A. Reshetin, J. Ritman, M. Roy-Stephan, A. Rustamov, **A. Sadovski**, B. Sailer, P. Salabura, M. Sanchez, P. Sapienza, A. Schmah, R. Simon, V. Smoliankin, L. Smykov, S. Spataro, B. Spruck, H. Ströbele, J. Stroth, C. Sturm, M. Sudol, P. Tlustý, A. Toia, M. Traxler, H. Tsertos, V. Wagner, M. Wiśniowski, T. Wojcik, J. Wüstenfeld, Yu. Zanevsky, D. Žovinec, P. Zumbruch

Abstract: The HADES spectrometer installed at GSI Darmstadt is devoted to the study of the production of di-lepton pairs from vector meson decays in relativistic nucleus-nucleus collisions, as well as proton- and pion-induced reactions. Extraction of rare lepton pairs in high hadron multiplicity events requires an efficient particle identification (PID). In HADES charged particles momentum is measured by a tracking system surrounding the toroidal super conducting magnet, and velocity and energy loss is provided by a TOF detector. Leptons are identified by a Rich as well as a Shower detector. The particle identification method is using full experimental information from all subdetectors. To demonstrate the method performance, single particle spectra of charged hadrons and leptons from C + C at 2 AGeV will be presented and compared with results of corresponding simulations. The proton and pion yields an m_{T} and rapidity distributions will be compared with existing data. Very preliminary results of lepton analysis will be shown as well.

Subthreshold antiproton production in pC, dC and αC reactions

J. Phys. G: Nucl. Part. Phys. 30 (2004) 1379

Müller, H., V.I. Komarov

Abstract: Data from KEK on subthreshold $\bar{p}$ as well as on $\pi^{\pm}$ and $K^{\pm}$ production in pC, dC and αC reactions at energies between 3.5 and 12.0 AGeV are described for the first time within a unified approach. We use a model which considers a nuclear reaction as an incoherent sum over collisions of varying numbers of projectile and target nucleons. It samples complete events and thus allows for the simultaneous consideration of all final particles including the decay products of the nuclear residues. The enormous enhancement of the $\bar{p}$ cross section, as well as the moderate increase of meson production in dC and αC compared to pC reactions, is well reproduced. In our

approach, the observed enhancement near the production threshold is mainly due to the contributions from the interactions of few-nucleon groups.

The HADES tracking system

Nucl. Instr. Meth. A 535 (2004) 242

Müntz, C., J. Markert, G. Agakichiev, H. Alvarez-Pol, E. Badura, J. Bielcik, H. Bokemeyer, J.-L. Boyard, V. Chepurnov, S. Chernenko, H. Daues, **F. Dohrmann, W. Enghardt**, O. Fateev, C. Garabatos, L. Glonti, **E. Grosse**, J. Hehner, **K. Heidel**, T. Hennino, J. Hoffmann, A. Ierusalimov, **B. Kämpfer, K. Kanaki**, W. Koenig, **R. Kotte, L. Naumann**, W. Ott, Y.C. Pachmayer, V. Pechenov, J. Pouthas, B. Ramstein, K. Rosenkranz, P. Rosier, M. Roy-Stephan, A. Rustamov, **A. Sadovski**, L. Smykov, **M. Sobiella**, H. Stelzer, H. Stroebele, J. Stroth, C. Sturm, M. Sudol, J. Wüstenfeld, Y. Zanevsky, P. Zumbruch

Abstract: The HADES dielectron spectrometer has recently launched its physics program at the heavy ion synchrotron SIS at GSI Darmstadt. The spectroscopy of vector mesons in heavy ion collisions via their dielectron decay channel makes great demands on the HADES tracking system regarding acceptance and spatial resolution. The tracking system is formed out of 24 low-mass, trapezoidal multi-layer drift chambers providing about $30\,m^2$ of active area. Low multiple scattering in the in total four planes of drift chambers before and after the magnetic field is ensured by using helium-based gas mixtures and aluminum cathode and field wires. First in-beam performance results are contrasted with expectations from simulations. Emphasis is placed on the energy loss information, exploring its relevance regarding track recognition.

Studies of β - delayed proton decays of $N \simeq Z$ nuclei around ^{100}Sn at the GSI-ISOL facility

Nucl. Phys. A 746 (2004) 66

Mukha, I., L. Batist, F. Becker, A. Blazhev, A. Brüchle, J. Döring, M. Górska, H. Grawe, T. Faestermann, C. Hoffman, Z. Janas, A. Jungclaus, M. Karny, M. Kavatsyuk, O. Kavatsyuk, R. Kirchner, M. La Commara, C. Mazzocchi, C. Plettner, A. Płochocki, E. Roeckl, M. Romoli, M. Schädel, **R. Schwengner**, S.L. Tabor, M. Wiedeking and GSI ISOL Collaboration

Abstract: Beta decays of ^{94,96}Ag and ^{103}Sn nuclei into proton channels have been studied in the recent experiments at the GSI-ISOL facility. New efficient and chemically selective ion sources provided the highest yields of light silver and tin isotopes. Large arrays of germanium γ-ray and silicon charged-particle detectors, as well as a total absorption spectrometer (TAS) were used to measure β-proton, proton-γ, β-proton-γ and proton-γ-γ spectra. For the decay of ^{94}Ag, we observed high-spin states in ^{93}Rh populated by proton emission following β decay, whose largest spin value ($\geq 39/2$) yields an experimental proof for the existence of a second high-spin isomer in ^{94}Ag with $I \geq 17$. Its β-decay energy is at least 16.8 MeV, corresponding to an excitation energy ≥ 5.5 MeV. For ^{103}Sn, the γ rays measured in coincidence with β-delayed protons allowed us to establish the β-decay properties of this isotope. In particular, a Q^{EC} value of 7.5(6) MeV is derived from the intensity ratio of protons that are preceded either by EC or by β^+ decays and populate the 2^+ state in ^{102}Cd.

On the small β-decaying (21^+) spin gap isomer in ^{94}Ag

Nucl. Phys. A 733 (2004) 20

Plettner, C., H. Grawe, I. Mukha, J. Döring, F. Nowacki, L. Batist, A. Blazhev, C.R. Hoffman, Z. Janas, R. Kirchner, M. LaCommara, C. Mazzocchi, E. Roeckl, **R. Schwengner**, S.L. Tabor, M. Wiedeking

Abstract: The small β decay of ^{94}Ag, a nucleus with three proton and three neutron holes with respect to ^{100}Sn, was investigated at the GSI on-line mass separator by using an array of germanium and silicon detectors. On the basis of a small $\beta\gamma\gamma$ coincidence measurement, the previously reported decay scheme has been considerably improved and evidence is presented for a spin-gap isomer with a spin-parity assignment of (21^+), i.e., the highest spin ever observed in small β decay. The half-life of the low-spin isomer (7^+) was remeasured to be 0.59(2) s, whereas the half-life of the high-spin isomer was determined as 0.47(8) s. For the states in ^{94}Ag and ^{94}Pd, large-scale shell-model calculations that include up to 4p-4h excitations across the $N = Z = 50$ shell gap and employ a realistic interaction were carried out. These core excitations play a crucial role in generating the $E4$ isomerism required for the interpretation of the long half-life of the (21^+) state in ^{94}Ag.

The modelling of positron emitter production and PET imaging during carbon ion therapy

Phys. Med. Biol. 49 (2004) 5217

Pönisch, F., K. Parodi, B.G. Hasch, **W. Enghardt**

Abstract: At the carbon ion therapy facility of GSI Darmstadt in-beam positron emission tomography (PET) is used for imaging the β^+-activity distributions which are produced via nuclear fragmentation reactions between the carbon ions and the atomic nuclei of the irradiated tissue. On the basis of these PET images the quality of the irradiation, i.e. the position of the field, the particle range in vivo and even local deviations between the planned and the applied dose distribution, can be evaluated. However, for such an evaluation the measured β^+-activity distributions have to be compared with those predicted from the treatment plan. The predictions are calculated as follows: a Monte Carlo event generator produces list mode data files of the same format as the PET scanner in order to be processed like the measured ones for tomographic reconstruction. The event generator models the whole chain from the interaction of the projectiles with the target, i.e. their stopping and nuclear reactions, the production and the decay of positron emitters, the motion of the positrons as well as the propagation and the detection of the annihilation photons. The steps of the modelling, the experimental validation and clinical implementation are presented.

Studying in-medium hadron properties with HADES

Acta Phys. Pol. B 35 (2004) 1119

Salabura, P., **F. Dohrmann, E. Grosse, B. Kämpfer, K. Kanaki, R. Kotte, L. Naumann, A. Sadovsky**, G. Agakichiev, C. Agodi, H. Alvarez-Pol, A. Balanda, P. Braun-Munzinger, V. Chepurnov, S. Chernenko, T. Christ, R. Coniglione, J. Diaz, R. Djeridi, G. Bellia, D. Belver, J. Bielcik, M. Böhmer, H. Bokemeyer, J. Boyard, I. Duran, T. Eberl., V. Emeljanov, L. Fabbietti, O. Fateev, C. Fernandez, P. Finocchiaro, J. Friese, I. Fröhlich, B. Fuentes, J. Garzon, R. Gernhäuser, M. Golubeva, D. Gonzales, F. Guber, T. Hennino, S. Hlavac, J. Hoffmann, R. Holzmann, A. Ierusalimov, I. Iori, M. Jaskula, M. Jurkovic, T. Karavicheva, I. Koenig, W. Koenig, B. Kolb, J. Kotulic-Bunta, R. Krücken, A. Kugler, W. Kühn, R. Kulessa, A. Kurepin, T. Kurtukian-Nieto, S. Lang, J. Lehnert, C. Maiolino, J. Marin, J. Markert, V. Metag, N. Montes, J. Mousa, M. Münch, C. Müntz, J. Novotny, J. Otwinowski, Y. Pachmayer, Y. Panebratsev, V. Pechenov, T. Perez, J. Pietraszko, R. Pleskac, V. Pospisil, W. Przygoda, N. Rabin, B. Ramstein, A. Reshetin, J. Ritman, G. Rodriguez-Prieto, M. Roy-Stephan, A. Rustamov, J. Sabin-Fernandez, B. Sailer, M. Sanchez, V. Smolyankin, L. Smykov, S. Spataro, B. Spruck, H. Stroebele, J. Stroth, C. Sturm, M. Sudol, A. Titov, P. Tlusty, A. Toia, M. Traxler, H. Tsertos, A. Vazquez, Y. Volkov, V. Wagner, W. Walus, S. Winkler, M. Wisniowski, T. Wojcik, J. Wüstenfeld, Y. Zanevsy, P. Zumbruch

Abstract: HADES is a second generation experiment designed to study dielectron production in proton, pion and heavy ion induced reactions at the GSI accelerator facility in Darmstadt. The physics programme of HADES is focused on in-medium properties of the light vector mesons. In this contribution we discuss relevance of dielectron spectroscopy to the problem of hadron mass origin. We present status of the HADES experiment, demonstrate its capability to identify rare dielectron signal and show first experimental results obtained from C + C reactions at 2 AGeV.

Study of e^+, e^- production in elementary and nuclear collisions near the production threshold with HADES

Progr. Part. Nucl. Phys. 53 (2004) 49

Salabura, P., G. Agakichiev, C. Agodi, H. Alvarez-Pol, A. Balanda, G. Bellia, D. Belver, J. Bielcik, M. Böhmer, H. Bokemeyer, J. Boyard, P. Braun-Munzinger, V. Chepurnov, S. Chernenko, T. Christ, R. Coniglione, J. Diaz, R. Djeridi, **F. Dohrmann**, I. Duran, T. Eberl, V. Emeljanov, L. Fabbietti, O. Fateev, C. Fernandez, P. Finocchiaro, J. Friese, I. Fröhlich, B. Fuentes, J. Garzon, R. Gernhäuser, M. Golubeva, D. Gonzalez, **E. Grosse**, F. Guber, T. Hennino, S. Hlavac, J. Hoffmann, R. Holzmann, A. Ierusalimov, I. Iori, M. Jaskula, M. Jurkovic, **B. Kämpfer, K. Kanaki**, T. Karavicheva, I. Koenig, W. Koenig, B. Kolb, **R. Kotte**, J. Kotulic-Bunta, R. Krücken, A. Kugler, W. Kühn, R. Kulessa, A. Kurepin, T. Kurtukian-Nieto, S. Lang, J. Lehnert, C. Maiolino, J. Marn, J. Markert, V. Metag, N. Montes, J. Mousa, M. Münch, C. Müntz, **L. Naumann**, J. Novotny, J. Otwinowski, Y. Pachmayer, Y. Panebratsev, V. Pechenov, T. Perez, J. Pietraszko, R. Pleskac, V. Pospisil, W. Przygoda, N. Rabin, B. Ramstein, A. Reshetin, J. Ritman, G. Rodriguez-Prieto, M. Roy-Stephan, A. Rustamov, J. Sabin-Fernandez, **A. Sadovsky**, B. Sailer, M. Sanchez, V. Smolyankin, L. Smykov, S. Spataro, B. Spruck, H. Stroebele, J. Stroth, C. Sturm, M. Sudol, A. Titov, P. Tlusty, A. Toia, M. Traxler, H. Tsertos, A. Vazquez, Y. Volkov, V. Wagner, W. Walus, S. Winkler, M. Wisniowski, T. Wojcik, J. Wüstenfeld, Y. Zanevsky, P. Zumbruch

Abstract: HADES is a second generation experiment designed to study dielectron production in proton, pion, and heavy ion induced reactions at the GSI accelerator facility in Darmstadt. The physics programme of HADES is

focused on in-medium properties of the light vector mesons. In this contribution we present status of the HADES experiment, demonstrate its capability to identify rare dielectron signal, show first experimental results obtained from C + C reactions at 2 A GeV and shortly discuss physics programme of up-coming experimental runs.

Modelling of dissipation in nuclear fission

Int. J. Mod. Phys. E 13 (2004) 97

Schmitt, C., B. Jurado, **A.R. Junghans**, K.-H. Schmidt, J. Benlliure

Abstract: Peripheral heavy-ion collisions at relativistic energy are proposed as a new experimental approach dedicated to nuclear dissipation studies and, in particular, to investigate transient effects which are responsible for the inhibition of fission at the beginning of the process. To extract reliable information from the data, an analytical approximation of the time-dependent fission decay width is used in connection with new experimental signatures of relaxation effects.

Infrared characterization of environmental samples by pulsed photothermal spectroscopy

Eur. Phys. J. Appl. Phys. 25 (2004) 39

Seidel, W., H. Foerstendorf, K.H. Heise, R. Nicolai, A. Schamlott, J.M. Ortega, F. Glotin, R. Prazeres

Abstract: Low concentration of toxic radioactive metals in environmental samples often limits the interpretation of results of infrared studies investigating the interaction processes between the metal ions and environmental compartments. For the first time, we show that photothermal infrared spectroscopy performed with a pulsed free electron laser can provide reliable infrared spectra throughout a distinct spectral range of interest. In this model investigation, we provide vibrational absorption spectra of a rare earth metal salt dissolved in a KBr matrix and a natural calcite sample obtained by thermal beam deflection technique and FT-IR spectroscopy, respectively. General agreement was found between all spectra of the different recording techniques. Spectral deviations were observed with samples containing low concentration of the rare earth metal salt indicating a lower detection limit of the photothermal method compared to conventional FT-IR spectroscopy.

Comment on "Electromagnetic dissociation of ^{8}B and the astrophysical S factor for ^{7}Be(p,γ) ^{8}B"

Phys.Rev.C 700(2004) 39801, http://link.aps.org/abstract/PRC/v70/e039801

Snover, K.A., **A.R. Junghans**, E.C. Mohrmann.

Abstract: Recently, Davids and Typel recommended a "low" value of $S_{17}(0)$ based on fits to published direct and Coulomb dissociation data, in which they excluded the precise result of Junghans We show that their statistical analysis is incorrect due to a substantial underestimate of the experimental uncertainties, and that there is no reason to exclude the Junghans result based on statistical arguments.

High-spin states and band terminations in ^{69}As

Phys. Rev. C 70 (2004) 044304

Stefanescu, I., L. Eberth, G. Gersch, T. Steinhardt, O. Thelen, N. Warr, D. Weisshaar, B.G. Carlsson, I. Ragnarsson, G. de Angelis, T. Martinez, A. Jungclaus, **R. Schwengner**, K.P. Lieb, E.A. Stefanova, D. Curien

Abstract: Excited levels in ^{69}As were studied using the ^{40}Ca(^{32}S, $3p$)^{69}As reaction at 95 and 105 MeV beam energy. Gamma rays were detected with the EUROBALL spectrometer operated in conjunction with the Neutron Wall and the charged-particle detector array EUCLIDES. New level sequences with positive and negative parity were identified from $3p$-$\gamma\gamma$ and $\gamma\gamma\gamma$ coincidences. Spins were assigned to many of the levels on the basis of directional correlations of oriented states measurements. The previously observed positive-parity band was extended to spin $45/2^{+}$ and it was found to exhibit a crossing with another configuration identified up to spin $53/2^{+}$. Three negative-parity bands were observed for the first time up to spins $(43/24^{-})$, $39/2^{-}$, and $(41/2^{-})$. The previously known band was extended to spin $(49/2^{-})$. No evidence for superdeformation was found, despite very high counting statistics. Configurations were assigned to each of the observed bands through comparisons to the cranked Nilsson-Strutinsky calculations.

Level structure of ^{69}Se

Phys. Rev. C 69 (2004) 034333

Stefanescu, I., J. Eberth, G. de Angelis, N. Warr, G. Gersch, T. Steinhardt, O. Thelen, D. Weisshaar, T. Martinez, A. Jungclaus, **R. Schwengner**, K.P. Lieb, E.A. Stefanova, D. Curien, A. Gelberg

Abstract: Excited levels in ^{69}Se have been studied using the ^{40}Ca(^{32}S, $2pn$)^{69}Se reaction at 95 and 105 MeV beam energy. γ-rays have been detected with the EUROBALL spectrometer operated in conjunction with the wall and the charged-particle detector array EUCLIDES. New level sequences with positive and negative parities have been identified from $n-\gamma\gamma$ and $n-\gamma\gamma\gamma$ coincidences. Spins have been assigned to many of the levels on the basis of angular distribution and directional correlation measurements. Excitation energies of the positive-parity yrast band and the branching ratios of its decay are compared with the predictions of the rigid triaxial rotor plus particle model.

Experimental evidence for chirality in the odd-A ^{105}Rh

Phys. Lett. B 598 (2004) 178

Timár, A., P. Joshi, K. Starosta, V.I. Dimitrov, D.B. Fossan, J. Molnár, D. Sohler, R. Wadsworth, A. Algora, P. Bednarczyk, D. Curien, Zs. Dombrádi, G. Duchene, A. Gizon, J. Gizon, D.G. Jenkins, T. Koike, A. Krasznahorkay, E.S. Paul, P.M. Raddon, G. Rainovski, J.N. Scheurer, A.J. Simons, C. Vaman, A.R. Wilkinson, L. Zolnai, **S. Frauendorf**

Abstract: High-spin states in ^{105}Rh were populated by the ^{96}Zr(^{13}C, $p3n$) reaction at beam energies of 51 and 58 MeV, and studied using the EUROBALL IV γ-ray spectrometer and the DIAMANT charged particle array. A pair of nearly degenerate $\Delta I = 1$ three-quasiparticle bands with the same spins and parity have been observed. Comparison of the experimental results with tilted axis cranking calculations confirms the chiral character of the two bands, while arguments based on the excitation of particles within the $\pi\, g_{9/2}\, \nu\, (h_{11/2})^2$ configuration of the yrast band and comparison with the previously observed γ band exclude the other possible interpretations. This is the first experimental evidence for three-quasiparticle chiral structure in the $A \sim 100$ region, and the first simultaneous observation of a γ band and chiral partner bands in one nucleus.

Multiplicity correlations of intermediate-mass fragments with pions and and fast protons in ^{12}C + ^{197}Au

Eur. Phys. J. A 21 (2004) 293

Turzó, K., G. Auger, M.-L. Begemann-Blaich, N. Bellaize, F. Rittiger, F. Bocage, R. Borderi, R. Bougault, B. Bouriget, J.L. Charvet, A. Chbihi, R. Dayras, D. Durand, J.D. Frankland, E. Galichet, D. Gourio, D. Guinet, S. Hudan, G. Immé, P. Lautesse, F. Lavaud, A. Le Fèvre, R. Legrain, O. Lopez, J. Lukasik, U. Lynen, W.F.J. Müller, L. Nalpas, H. Orth, E. Plagnol, G. Raciti, E. Rosato, A. Saija, C. Schwarz, **W. Seidel**, C. Sfienti, B. Tamain, W. Trautmann, A. Trzcinski, E. Vient, M. Vigilante, C. Volant, B. Zwieglinski, A.S.Botvina

Abstract: Low-energy π^+ ($E_\pi \leq 35$ MeV) from ^{12}C + ^{197}Au collisions at incident energies from 300 to 1800 MeV per nucleon were detected with the Si - Si(Li) - CsI(TI) calibration telescopes of the INDRA multidetector. The inclusive angular distributions are approximately isotropic, consistent with multiple rescattering in target spectator. The multiplicity correlations of the low-energy pions and of energetic protons ($E_p \geq 150$ MeV) with intermediate-mass fragments were determined from the measured coincidence data. The deducted correlation functions $1 + R \approx 1.3$ for inclusive event samples reflect the strong correlations evident from the common impact parameter dependence of the considered multiplicities. For narrow impact parameter bins (based on charged-particle multiplicity), the correlation functions are close to unity and do not indicate strong additional correlations. Only for pions at high particle multiplicities (central collisions) a weak anticorrelation is observed, probably due to a limited competition between these emissions. Overall, the results are consistent with the equilibrium assumption made in statistical multifragmentation scenarios. Predictions obtained with intranuclear-cascade models coupled to the Statistical Multifragmentation Model are in good agreement with the experimental data.

Intranuclear cascade plus percolation plus evaporation model applied to the ^{12}C + ^{197}Au system at 1 GeV/nucleon

Nucl. Phys. A 734 (2004) 545

Volant, C., K. Turzó, W. Trautmann, G. Auger, M.-L. Begemann-Blaich, R. Bittiger, B. Borderie, A.S. Botvina, R. Bougault, B. Bouriquet, J.-L. Charvet, A. Chbihi, R. Dayras, D. Doré, D. Durand, J.D. Frankland, E. Galichet, D. Gourio, D. Guinet, S. Hudan, G. Immé, Ph. Lautesse, F. Lavaud, A. Le Févre, 0. Lopez, J. Lukasik, U. Lynen,

W.F.J. Müller, L. Nalpas, H. Orth, E. Plagnol, G. Raciti, E.Rosato, A. Saija, C. Schwarz, **W. Seidel**, C. Sfienti, J.C. Steckmeyer, B. Tamain, A. Trzciński, E. Vient, M. Vigilante, B. Zwiegliǹski

Abstract: The nucleus-nucleus Liege intranuclear-cascade+percolation+evaporation model has been applied to the $^{12}C + ^{197}Au$ data measured by the INDRA-ALADIN collaboration at GSI. After the intranuclear cascade stage, the data are better reproduced when using the Statistical Multiframentation Model as afterburner. Further checks of the model are done on data from the EOS and KAOS collaborations.

Level scheme of ^{94}Mo at high angular momentum

High Energy Phys. Nucl. Phys. - Chinese Ed. 28 (2004) 941

Zhang, Y. H., M.L. Liu, G. de Angelis, Zs. Podolyàk, W.T. Guo, A. Gadea, C. Ur, N. Marginean, C. Rusu, **R. Schwengner**, D.R. Napoli, R. Menegazzo, S. Lunardi, D. Bazzacco, T. Martinez, M. Axiotis, A. Gargano, S. Lenzi, F. Brandolini, W. von Oertzen

Abstract: High-spin level structure of ^{94}Mo has been re-investigated using the modem multidetector array of GASP via the $^{16}O(^{82}Se, 4n\gamma)^{94}Mo$ reaction at $E(^{82}Se) = 459\,MeV$. The previously reported level scheme has been largely modified up to similar to 10 MeV in excitation energy due to identifications of some important linking transitions. The level structure of ^{94}Mo has been compared with the shell model calculations. It is suggested that the valence neutron excitation within $d_{5/2}$, $g_{7/2}$, and $h_{11/2}$ orbitals should be taken into account in order to adequately describe the high-spin level structure of ^{94}Mo above $I^{\pi} = 14^{+}$.

Stability of the N = 50 shell gap in the neutron-rich Rb, Br, Se, and Ge isotones

Phys. Rev. C 70 (2004) 024301

Zhang, Y. H., Zs. Podolyàk, G. de Angelis, A. Gadea, C. Ur, S. Lunardi, N. Marginean, C. Rusu, **R. Schwengner**, Th. Kröll, D.R. Napoli, R. Menegazzo, D. Bazzacco, E. Farnea, S. Lenzi, T. Martinez, M. Axiotis, D. Tonev, W. Gelletly, S. Langdown, P.H. Regan, J.J. Valiente Dobon, W. von Oertzen, B. Rubio, B. Quintana, N. Medina, R. Broda, D. Bucurescu, M. Ionescu-Bujor, A. Iordachescu

Abstract: The low- and medium-spin states of the $N = 50$ neutron-rich, $^{87}_{37}$Rb, $^{85}_{35}$Br, $^{84}_{34}$Se and $^{82}_{32}$Ge isotones have been populated in deep-inelastic processes produced by the interaction of 460 MeV ^{82}Se ions with a ^{192}Os target. The subsequent gamma decay has been investigated at the Laboratori Nazionali di Legnaro using the GASP gamma-ray detector array. The comparison of the experimentally observed excited states with shell-model calculations performed with and without neutron degrees of freedom has allowed the investigation of the role of the neutron-core breaking excitations and therefore of the $N = 50$ shell gap. The inclusion of neutron configurations in the shell-model calculations results in an improved agreement between the experimental and calculated level energies at medium and high spin. These results highlight the considerable contribution of neutron-core particle-hole excitations across the $N = 50$ shell gap to the level configurations. The overall agreement of the measured excited states with the shell-model predictions is indicative of the persistence of the $N = 50$ shell gap down to $Z = 32$.

$\rho - \omega$ splitting and mixing in nuclear matter

Phys. Rev. C 70 (2004) 035207

Zschocke, S., B. Kämpfer

Abstract: We investigate the splitting and mixing of ρ and ω mesons in nuclear matter. The calculations were performed on the basis of QCD sum rules and include all operators up to mass dimension-6 twist-4 and up to first order in the coupling constants. Special attention is devoted to the impact of the scalar four-quark condensates on both effects. In nuclear matter the Landau damping governs the $\rho - \omega$ mass splitting while the scalar four-quark condensates govern the strength of individual mass shifts. A strong in-medium mass splitting causes the disappearance of the $\rho - \omega$ mixing.

Proceedings and Reports

Altstadt, E., C. Beckert, H. Freiesleben, V. Galindo, **E. Grosse, A. Junghans**, B. Naumann, F.-P. Weiss
Design of a photoneutron source for time-of-flight experiments at the radiation source ELBE
12th International Conference on Nuclear Engineering ICONE-12, Washington D.C., USA,
April, 2004, Proceedings on CD-ROM paper 49456

Barz, H.W., B. Kämpfer, L. Naumann, Gy. Wolf, M. Zetenyi
Calculations $K\pm$ and ϕ Production in Near-Threshold Proton-Nucleus Collisions,
International Workshop on Hot and Dense Matter in Relativistic Heavy-Ion Collisions,
Budapest, Hungary, March, 2004,
arXiv nucl-th/0405075

Barz, H.W., M. Zetenyi
Medium effects on ϕ production in near-threshold proton-nucleus collisions,
Proc. NPDC18 conference, Prague, Czech Republic, August 2004

Crespo, P., T. Barthel, H. Frais-Koelbl, E. Griesmayer, **K. Heidel, K. Parodi, J. Pawelke, W. Enghardt**
Suppression of random coincidences during In-beam PET measurements,
Conference Record NSS 45-6 from the Nuclear Science Symposium and Medical Imaging Conference NSS-MIC 2004, Rome, Italy, Oct. 2004

Dekorsy, Th., **K. Fahmy, E. Grosse**, P. Michel, **W. Seidel**, A.Wolf, **R. Wünsch**
An electromagnetic undulator for the far infrared at ELBE
Proc. 26th Int. Free-Electron Laser Conf. and 11th FEL Users Workshop, Trieste, Sept 2004, p. 389
http://accelconf.web.cern.ch/accelconf/f04/fel2004proceedings.pdf

Dohrmann, F., D. Abbott, A. Ahmidouch, P. Ambrozewicz, C.S. Armstrong, J. Arrington, R. Asaturyan, K. Assamagan, S. Avery, K. Bailey, O.K. Baker, S. Beedoe, H. Bitao, H. Breuer, D.S. Brown, R. Carlini, J. Cha, N. Chant, E. Christy, A. Cochran, L. Cole, G. Collins, C. Cothran, J. Crowder, W.J. Cummings, S. Danagoulian, F. Duncan, J. Dunne, D. Dutta, T. Eden, M. Elaasar, R. Ent, L. Ewell, H. Fenker, H.T. Fortune, Y. Fujii, L. Gan, H. Gao, K. Garrow, D.F. Geesaman, P. Gueye, K. Gustafsson, K. Hafidi, J.O. Hansen, W. Hinton, H.E. Jackson, H. Juengst, C. Keppel, A. Klein, D. Koltenuk, Y. Liang, J.H. Liu, A. Lung, D. Mack, R. Madey, P. Markowitz, C.J. Martoff, D. Meekins, J. Mitchell, T. Miyoshi, H. Mkrtchyan, R. Mohring, S.K. Mtingwa, B. Mueller, T.J. O'Neill, G. Niculescu, I. Niculescu, D.H. Potterveld, J.W. Price, B.A. Raue, P.E. Reimer, J. Reinhold, J. Roche, P. Roos, M. Sarsour, Y. Sato, G. Savage, R. Sawafta, R.E. Segel, A.Yu. Semenov, S. Stepanyan, V. Tadevosian, S. Tajima, L. Tang, B. Terburg, A. Uzzle, S. Wood, H. Yamaguchi, C. Yan-1, C. Yan-2, L. Yuan, M. Zeier, B. Zeidman, B. Zihlmann
Electroproduction of Strangeness on Light Nuclei
Proc. of SENDAI 03, Int. Symposium on Electrophoto-production of Strangeness on Nucleons and Nuclei,
June 16-18 2003, Sendai, Japan to be published by World Scientific, New Jersey, Singapore 2004

Kolomeitsev, E.E., C. Hartnack, **H.W. Barz**, M. Bleicher, E. Bratkovskaya, W. Cassing, L.W. Chen, P. Danielewicz, C. Fuchs, T. Gaitanos, C.M. Ko, A. Larionov, M. Reiter, Gy. Wolf, J. Aichelin
Transport theories for heavy-ion collisions in the 1 AGeV regime,
Proc. of Strange Quark Matter 2004, Cape Town, South Africa

Kotte, R.
Hadron production in C + C at 2 AGeV measured by the HADES spectrometer
P. Tlusty for the HADES Collaboration,
Proc. XLII Int. Winter Meeting on Nucl. Physics, Vol. 120, p. 171
Bormio, Italy, 2004

Kotte, R.
Dipleton Analysis in the HADES Spectrometer for C + C at 2 AGeV
J. Otwinowski for the HADES Collaboration
Proc. XLII Int. Winter Meeting on Nucl. Physics, Vol. 120
Bormio, Italy, 2004

Michel, P., F. Gabriel, **E. Grosse**, P. Evtushenko, T. Dekorsy, M. Krenz, M. Helm, U. Lehnert, **W. Seidel, R.Wünsch, D.Wohlfarth**, A.Wolf
First lasing of the elbe mid-ir fel
Proc. 26th Int. Free-Electron Laser Conf. and 11th FEL Users Workshop, Trieste, Sept 2004, p. 8
http://accelconf.web.cern.ch/accelconf/f04/fel2004proceedings.pdf

Panteleeva, A., W. Enghardt, E. Lessmann, J. Pawelke, W. Wagner, W. Dörr
Determination of RBE of 10 kV and 25 kV X-rays
33rd Annual Meeting of the ESRB, 2004,
Central Eur. J. of Occupational and Environmental Medicine 10 (2004) 150

Parodi, K., P. Crespo, F. Fiedler, J. Pawelke, F. Pönisch, T. Haberer, C. Kausch, M. Krämer, D. Schardt
The application of PET to the monitoring of heavy ion therapy
Proc. from Workshop "Imaging in Radiotherapy: present and future", Rome, Italy,
Dec. 8-11, 2002,
ISS Report, Rapporto ISTISAN 04/25 (2004) 63

Parodi, K., F. Pönisch, W. Enghardt
The feasibility of in-beam PET for accurate monitoring of proton therapy:
Results of a comprehensive experimental study
Conference Record NSS 43-5 from the Nuclear Science Symposium and Medical Imaging Conference NSS-MIC 2004, Rome, Italy, Oct. 2004

Poljanc, K., **F. Sommerer, K. Parodi**, H. Aiginger, **W. Enghardt**
Positronenemissionstomographie in der Therapie mit Kohlenstoffionen und Validierung des FLUKA Monte Carlo Codes für die Vorhersage der bei Tumorbestrahlungen mit Ionen erzeugten β^+-Aktivität,
Abstract of the OGMP Annual Meeting, Wiener Neustadt, Austria,
June 4-5, 2004

Schneider, C., H. Büttig, **W. Enghardt**, F. Gabriel, D. Janssen, P. Michel, F. Pobell, H. Prade, A. Kudryavtsev, C. Haberstroh, W. Sandner, I. Will
Machbarkeitstudie für einen industriellen supraleitenden Table Top Elektronenbeschleuniger
Wissenschaftlich-Technische Berichte FZR-410 (2004)

Seidel, W., H. Foerstendorf, F. Glotin, M. Ortega, A. Prazeras
Exploring the spatial resolution of the photothermal beam deflection technique in the infrared region
Proc. 26th Int. Free-Electron Laser Conf. and 11th FEL Users Workshop, Trieste, Sept. 2004, p. 679
http://accelconf.web.cern.ch/accelconf/f04/fel2004proceedings.pdf

Sommerer, F., W. Enghardt, K. Parodi, K. Poljanc, H. Aiginger
Simulationsrechnungen zur Validierung des Monte Carlo Codes FLUKA für die Vorhersage der bei Tumorbestrahlungen mit Ionen erzeugten β^+-Aktivität,
Contribution to 54. Jahrestagung der Österreichischen Physikalischen Gesellschaft, Linz, Austria,
Sept. 2004

Wolfring, E.
Untersuchung strahleninduzierter Chromosomenaberrationen
Wissenschaftlich-Technische Berichte FZR-404 (2004)

Talks at Conferences and other Institutes

Barz, H.W.
Contribution of the nucleon-hyperon reaction channels to K^- production in proton-nucleus collisions
DPG Frühjahrstagung, Köln,
March 8-12, 2004

Barz, H.W.
BUU calculations for K^+, K^- and ϕ production for proton-nucleus collisions in the GeV region
International Workshop on Hot and Dense Matter in Relativistic Heavy-Ion Collisions, Budapest, Hungary,
March 24-27, 2004

Bluhm, M.
Quasi-particle model for deconfined matter
Strangness in Quark Matter 2004, Cape Town, South Africa,
Sep. 15-20, 2004

Crespo, P.
In-situ monitoring with PET: Suppression of random coincidences during in-beam PET measurements
ENLIGHT Workpackage 5, Curie Institute, Paris, France,
Jun. 06, 2004

Crespo, P.
In-beam PET for hadron therapy using LSO/APD-array detectors
41th General (Open) Meeting of the Crystal Clear Collaboration, CERN, Geneva, Switzerland,
Sep. 29, 2004

Crespo, P.
Suppression of random coincidences during in-beam PET measurements
2004 IEEE Nuclear Science Symposium and Medical Imaging Conference, Rome, Italy,
Oct. 21, 2004

Dohrmann, F.
Testing new time of flight detectors at ELBE: Status report
CBM Collaboration Meeting, GSI Darmstadt, Darmstadt,
Feb. 13, 2004

Dohrmann, F.
Productions of antikaons in $p + \mathrm{Au}$ and $p + \mathrm{C}$ collisions
DPG Frühjahrstagung, Köln,
March 10, 2004

Dohrmann, F.
Die besondere Rolle der seltsamen Quarks in Kernen und Kernmaterie
Physikalisches Kolloquium der TU Dresden, Dresden,
June 22, 2004

Dohrmann, F.
Electroproduction of $^{3,4}\mathrm{H}$ - λ states on Helium
19th European Conference on FEW-Body Problems in Physics, Groningen, Netherlands,
Aug. 23, 2004

Dohrmann, F.
Testing novel time of flight detectors at ELBE: Status report
CBM Collaboration Meeting, GSI Darmstadt, Darmstadt,
Oct. 7, 2004

Dohrmann, F.
Testing novel time of flight detectors at ELBE: Overview
HADES Collaboration, Meeting, GSI Darmstadt, Darmstadt,
Oct. 30, 2004

Enghardt, W.
Tomographische Rekonstruktion beim in-beam PET Monitoring der Schwerionentherapie
DKFZ, Heidelberg,
Jan. 21, 2004

Fahmy, Karim
Proteinstruktur und Funktion: Ein Infrarot-Blick auf Membranproteine
ISAS, Berlin,
May 5, 2004

Fahmy, Karim
Metallisierung von Proteinen: Wege zu neuen Materialien
Bruker-Anwendertreffen, Ettlingen,
Nov. 11, 2004

Fahmy, Karim
Topology of conformational changes in photoreceptor activation
Uni. Frankfurt am Main,
Dec. 20, 2004

Frauendorf, S.
Exotic phenomena at high spin
Workshop on AGATA physics, CNRS Orsay, France,
March 2004

Frauendorf, S.
Chirality of nuclear rotation
Annual meeting of the Division of Nuclear Physics, Chinese Physical Society, Bejing, China,
Apr. 2004

Frauendorf, S.
Nuclear tidal waves
Bejing University, China,
Apr. 2004

Frauendorf, S.
Tilted rotation
Bejing University, China,
Apr. 2004

Frauendorf, S.
Symmetries of the cranked mean field
Niels Bohr Institute, University of Copenhagen, Danmark,
June 2004

Frauendorf, S.
Experimental evidence for chirality
Niels Bohr Institute, University of Copenhagen, Danmark,
June 2004

Frauendorf, S.
Symmetries of the cranked mean field
Invited talk, International Nuclear Physics Conference, Goeteborg, Sweden,
June 2004

Frauendorf, S.
Probing shape coexistence by dipole excitations
FZ Rossendorf, Institut für Kern- und Hadronenphysik, Dresden,
July 2004

Frauendorf, S.
Normal persistent currents and gross shell structure at high spin
Workshop on mesoscopic physics, Michigan State University, USA,
Oct. 2004

Frauendorf, S.
Spontaneous symmetry breaking and rotational bands
Invited talk, Fall meeting of the Div. of Nucl. Phys. of the American Physical Society, Chicago, USA,
Oct. 2004

Junghans, A.
Precise measurement of the ^{7}Be(p,γ)^{8}B S-factor
Bothe-Kolloquium, MPI Heidelberg,
May 19, 2004

Junghans, A.
Status of the ^{7}Be(p,γ)^{8}B S-factor
Advances and Challenges in Nuclear Astrophysics, ECT, Trento, Italy,
May 24-28, 2004

Kämpfer, B.
Baryon resonances and the production of light vector mesons near thresholds
Internat. Workshop, Hirschegg, Austria,
Jan. 11-17, 2004

Kämpfer, B.
QCD equation of state above and below Tc
XLII Int. Winter Meeting on Nucl. Physics, Bormio, Italy,
Jan. 25-31, 2004

Kämpfer, B.
Phantastische Ausblicke auf unser Universum
TU Dresden, Urania-Seniorenakademie, Dresden,
May 05, 2004

Kämpfer, B.
Quasiparticle model of QCD matter above and below Tc and at large μ
Int. Symp. "The QCD phase diagramme: from theory to experiment", Skopelos, Greece,
May 28 - June 3, 2004

Kämpfer, B.
Dipletons and charm as probes of chiral restoration
Int. Conf. High Energy Phys., Bejing, China,
Aug. 16-22, 2004

Kämpfer, B.
Strangeness and charm in QCD matter
Strangness in Quark Matter 2004, Cape Town, South Africa,
Sept. 15-20, 2004

Kämpfer, B.
Electromagnetic probes of strongly interacting matter
Workshop on In-Medium Hadron Physics, Giessen,
Nov. 11, 2004

Kotte, R.
Two-proton small-angle correlations in central heavy-ion collisions: A beam-energy- and system-size-dependent study
FOPI collaboration meeting, Darmstadt,
Apr. 2, 2004

Naumann, L.
FAIR an international accelerator facility for antiproton and ion beam research in Darmstadt
INTAS TRD Collaboration Meeting, Gatchina, Russia,
July 1, 2004

Naumann, L.
Testing of X-ray sensitive detectors at ELBE
CBM Collaboration Meeting, Darmstadt,
Oct. 7, 2004

Panteleeva, A.
Determination of RBE of low-energy X-rays at ELBE
DPG Frühjahrstagung, Köln,
March 8, 2004

Panteleeva, A.
Determination of RBE of 10 kV and 25 kV X-rays for cell survival and micronuclei induction
7. Jahrestagung der Gesellschaft für Biologische Strahlenforschung (GBS), GSI Darmstadt,
March 31 - Apr. 2, 2004

Parodi, K.
The feasibility of in-beam PET for proton therapy
BROWN BAG - physics seminar, Massachusetts General Hospital, Boston, USA,
Feb. 2, 2004

Parodi, K.
In-beam PET for in-situ dose quantification in cardon ion therapy and posible extension to proton therapy
DPG Frühjahrstagung, München
March 22, 2004

Parodi, K.
The feasibility of in-beam PET for accurate monitoring of proton therapy:
Results of a comprehensive experimental study
IEEE Nuclear Science Symposium and Medical Imaging Conference, Rome, Italy,
Oct. 21, 2004

Parodi, K.
Feasibilty of dose quantification with in-beam PET data in radiotherapy with ^{12}C and proton beams
BROWN BAG - physics seminar, Massachusetts General Hospital, Boston, USA,
Dec. 12, 2004

Pawelke, J.
The ELBE Microbeam
Microbeam-Workshop an der GSI Darmstadt,
Mar. 30.-31., 2004

Reichelt, U.
Monte-Carlo-Methoden für den Elektronentransport mit Einzelstreumodellen
68. DPG Frühjahrstagung, München,
March 23, 2004

Rusev, G. (group report)
Photon scattering from ^{92}Mo, ^{98}Mo and ^{100}Mo up to the neutron-seperation energy
DPG Frühjahrstagung, Köln,
March 8-12, 2004

Wagner, A.
A position-sensitive heavy-ion detector for time-of-flight applications
Annual NUSTAR Meeting, GSI Darmstadt,
Febr. 19, 2004

Wagner, A. (group report)
Photon scattering from heavy nuclei up to energies well above particle emission thresholds
DPG Frühjahrstagung, Köln,
March 11, 2004

Wagner, W.
Channeling X-rays at the ELBE radiation source
Internat. Workshop on Charged and Neutral Particle Channeling Phenomens, Channeling 2004, Frascati, Italy,
Nov. 2-6, 2004

Zschocke, S.
$\rho - \omega$ splitting and mixing in nuclear matter
DPG Frühjahrstagung, Köln,
March 8-12, 2004

Zschocke, S.
Mass-shift of the ρ and ω meson and their mixing in nuclear matter
Inst. f. Theoret. Physik, Dresden, TU Dresden,
Jun. 6, 2004

Zschocke, S.
Splitting and mixing of the ρ and ω in nuclear matter
KFKI-RMKI, Budapest, Hungary,
Nov. 19, 2004

Zschocke, S.
Splitting and mixing of the ρ and ω in nuclear matter
FIAS, Frankfurt am Main,
Dec. 3, 2004

Zschocke, S.
An algebraic approach to bare nucleon matrix elements
Inst. f. Theoret. Physik, TU Dresden,
Dec. 10, 2004

Talks of Visitors

Bayer, W., TU Darmstadt:
Channeling Experimente am Institut für Kernphysik der TU Darmstadt, Jul. 7, 2004

Biro, T.S., KFKI Budapest:
Peculiar equilibria in heavy ion physics, Oct. 15, 2004

Fuchs, C., Uni Tübingen:
Vektormeson- und Dileptonproduktion, Apr. 16, 2004

Gernhäuser, R., TU München:
Segmented diamond detectors, Jun. 18, 2004

Gönnenwein, F., Uni Tübingen:
Überblick über den derzeitigen Stand der Spaltforschung, Jun. 11, 2004

Hübel, H., Uni Bonn:
Wobbling-Anregungen in Triaxialen Kernen, Dec. 3, 2004

Knöpfle, T., MPI Heidelberg:
Silizium Detektoren: Helix-Auslesechip und die Suche nach Pentaquarks am HERA-B Experiment, Jul. 2, 2004

Knoll, J., GSI Darmstadt:
Fluid dynamics multifragmentation and flavour kinetics, Oct. 15, 2004

Lantukh, Y., Uni Orenburg:
Investigation biological materials by means of holographic materials, Aug. 8, 2004
Infrared holography of DNA films, Aug. 26, 2004

Leupold, S.K., Uni Giessen:
The ρ-meson spectral function at finite nuclear density, Nov. 19, 2004

Nesterenko, V., MPI - Physik komplexer Systeme:
Electric dipole modes in nuclei and atomic clusters, March 6, 2004

Rafelski, J., Uni Arizona:
Strangness and the discovery of quark-gluon plasma, Jun. 25, 2004

Rauscher, T., Uni Basel:
Kernphysikalische Aspekte der Nukleosynthese in schweren Sternen, May 14, 2004

Reisdorf, W., GSI Darmstadt:
Kollektive Flüsse bei partieller Transparenz in Schwerionenreaktionen: Der schwere Weg zur Zustandsgleichung, Apr. 23, 2004

Ring, P., TU München:
Kovariante Dichtefunktionaltheorie zur Beschreibung von angeregten Zuständen in exotischen Kernen, Dec. 10, 2004

Simon, H., GSI + TU Darmstadt:
Towards dead-time free multi-parameter data acquisition for future experiments at GSI, Jul. 16, 2004

Speth, J., FZ Jülich GmbH:
Effektive Theorien für die Struktur stabiler und instabiler Kerne, Okt. 29, 2004

Strieder, S.K., Uni Bochum:
LUNA - Nukleare Astrophysik im Untergrund, Nov. 26, 2004

Vlassenbroeck, J., Gent University:
Multidisciplinary research at the Gent University 15 MeV linear electron accelerator, Jun. 6, 2004

Teaching Activities

Enghardt, W.
Radiotherapie mit Photonen, Elektronen und schweren geladenen Teilchen (Teletherapie)
TU Dresden, Jan. 29, 2004, Febr. 5, 2004

Enghardt, W.
Technologie für die Radiotherapie
TU Dresden, Dez. 9 and 16, 2004

Fahmy, K., F. Schwille
Struktur und Funktion in Biomolekülen
TU Dresden, Sommersemester 2004

Fahmy, K.
Physikochemische Grundlagen von Struktur und Funktion in Biomolekülen
Universität Freiburg, Oberseminar 2004

Grosse, E., F. Dohrmann
Schlüsselexperimente der Kern- und Teilchenphysik
TU Dresden, Sommersemester 2004

Grosse, E., A. Wagner
Kerne und Sterne
TU Dresden, Sommersemester 2004

Grosse, E., A. Wagner, B. Kämpfer
Kerne und Sterne
TU Dresden, Wintersemester 2004/2005

Kämpfer, B.
Relativistische Astro-und Teilchenphysik
TU Dresden, Sommersemester 2004

Kämpfer, B.
Allgemeine Relativitätstheorie
TU Dresden, Wintersemester 2004/2005

Awards

Katia Parodi
Doktorandenpreis 2004, Forschungszentrum Rossendorf

Prof. Stefan Frauendorf
"Fellow of the American Physical Society", Denver, USA, 2004

Ph.D. Theses

Nicole Lehmann
Investigation of receptor G protein coupling in vision
Uni. Freiburg, July 2004

Werner Scheinast
Schwellennahe Erzeugung von Kaonen und Antikaonen in Proton-Kern-Stößen
TU Dresden, August 2004

Katia Parodi
On the feasibility of dose quantification with in-beam PET data
in radiotherapy with ^{12}C and proton beams
TU Dresden, November 2004

Diploma Theses

Torsten Mikuletz
Dosimetrische Charakterisierung einer für strahlenbiologische Experimente
als Referenzstrahlungsquelle dienenden Röntgenanlage
Hochschule Mittweida (FH), April 2004

Florian Sommerer
Validierung des FLUKA-Codes für Anwendungen in der Ionentherapie
Atominstitut der östereichischen Universitäten, Wien, August 2004

Thomas Barthel
Experimentelle Verifikation eines Verfahrens zur Unterdrückung zufälliger
Koinzidenzen bei der in-beam Positronen-Emissions-Tomographie
Hochschule Mittweida (FH), 2004

Personnel

Departments of the IKH

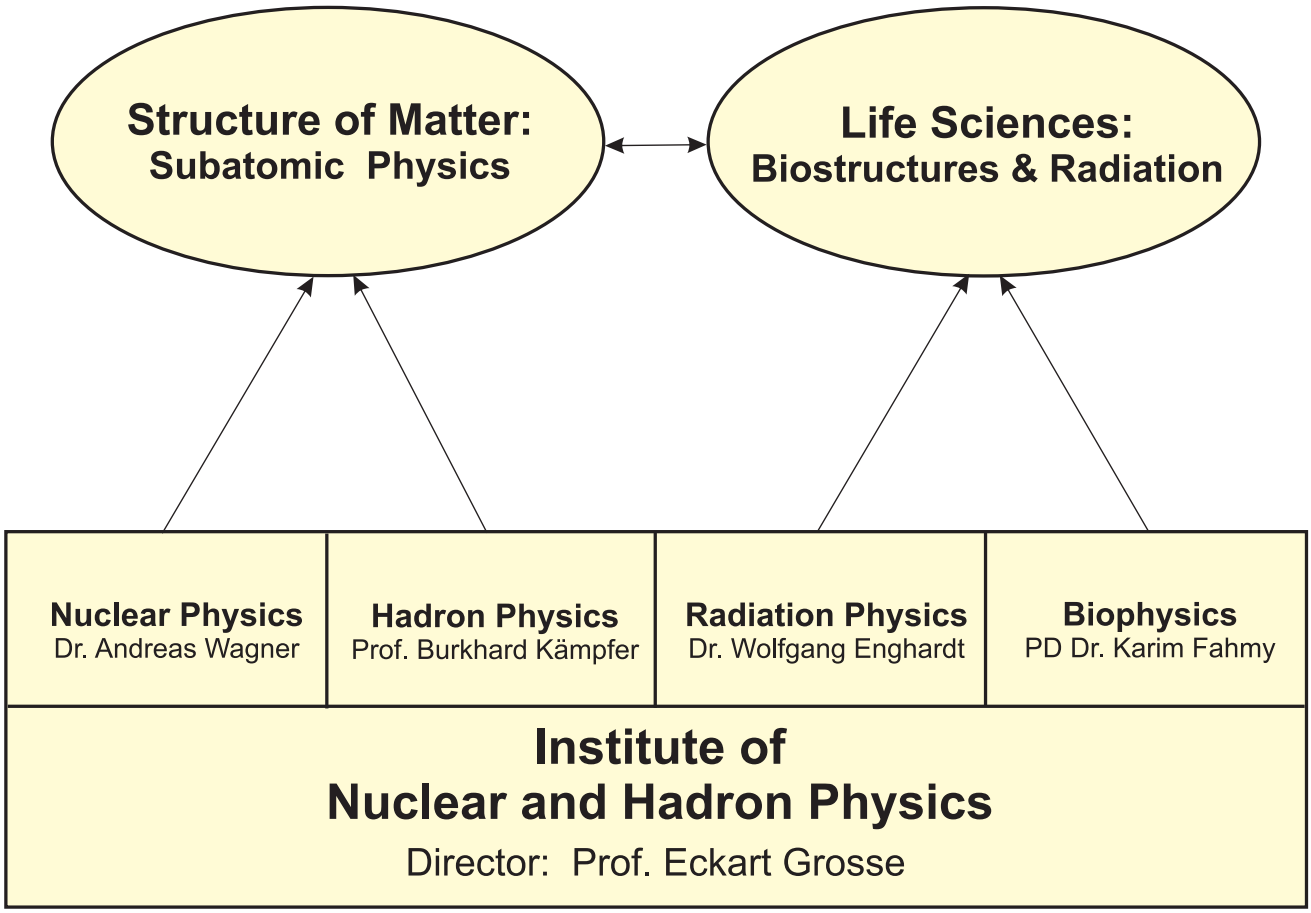

Personnel of the Institute for Nuclear and Hadron Physics

Director: Prof. Dr. E. Grosse [1]

Scientific Personnel

PD Dr. H.W. Barz
Dr. F. Dönau
Dr. F. Dohrmann
Dr. W. Enghardt
PD Dr. K. Fahmy
Prof. S. Frauendorf [2]
Dr. A. Junghans
Prof. B. Kämpfer
Dr. J. Klug
Prof. H. Kötzle
Dr. R. Kotte
PD Dr. K. Möller
Dr. H. Müller
Dr. N. Nankov
Dr. L. Naumann
Dr. W. Neubert
Dr. J. Pawelke
Dr. J.A. Piest
Dr. F. Pönisch
Dr. O. Savchuk
Dr. K.D. Schilling
Dr. R. Schwengner
Dr. M. Sczepan
Dr. W. Seidel
Dr. A. Wagner
Dr. W. Wagner
Dipl. Phys. D. Wohlfarth
Dr. R. Wünsch
Dr. S. Zschocke

PhD Students

B. Azadegan
T. Barthel [3]
R. Beyer [3]
M. Bluhm
P. Crespo
M. Erhard
F. Fiedler
G. Furlinski
K. Kanaki
N. Lehmann
S. Madathil
D. Möckel
T. Mikuletz [3]
C. Nair
A. Panteleeva
K. Parodi
U. Reichelt
G. Rusev
A. Sadovsky
W. Scheinast
G. Shakirin
F. Sommerer [3]
R. Thomas
T. Würschig [3]

Technical Personnel

J.U. Berlin
M. Boeck
M. Böse
D. Hachenberger
A. Hartmann
K. Heidel
L. Heinrich
R.R. Hensel
M. Hoff
J. Hutsch
K. Krüger
M. Langer
E. Leßmann
M. Paul
J. Philipp
B. Rimarzig
S. Schaller
C. Schneidereit
W. Schulze
M. Sobiella
J. Steiner
U. Wolf
E. Wolfring

[1] also TU Dresden
[2] also University of Notre-Dame, Indiana, USA
[3] Diploma Student

Guest Scientists

Dr. Kaptari, L.P.	JINR Dubna, Russia
Dr. Kapusta, M.	Soltan Institute for Nuclear Studies, Department of Electronics, Otwock-Swierk, Poland
Dr Klug, J.	Uppsalla University, Sweden
Dr. Kostov, L.K.	Institute for Nuclear Research and Nuclear Energy, Sofia, Bulgaria
Lantukh, J.	Universität Orenburg, Russia
Sommerer, F.	Atominstitut der Österreichischen Universitäten Wien, Austria
Dr. Wolf, G.	KFKI, RMKI, Budapest, Hungary
Zetenyi, M.	KFKI Budapest, Hungary